HIGH-PRESSURE, HIGH-TEMPERATURE SINTERING OF POLYCRYSTALLINE CUBIC BORON NITRIDE WITH IMPROVED THERMOSTABILITY AND MECHANICAL PROPERTIES FOR HIGH TEMPERATURE APPLICATIONS

by

Xian Yao

A dissertation submitted to the faculty of
The University of Utah
in partial fulfillment of the requirements for the degree of

Doctor of Philosophy

Department of Metallurgical Engineering

The University of Utah

August 2014

The University of Utah Graduate School

STATEMENT OF DISSERTATION APPROVAL

The dissertation of **Xian Yao**

has been approved by the following supervisory committee members:

Zhigang Zak Fang	, Chair	**April 25, 2014** Date Approved
Ravi Chandran	, Member	**April 25, 2014** Date Approved
Sivaraman Guruswamy	, Member	**April 25, 2014** Date Approved
J. Daniel Belnap	, Member	**April 25, 2014** Date Approved
Charles Elliot	, Member	**April 25, 2014** Date Approved

and by **Manoranjan Misra** , Chair of

the Department of **Metallurgical Engineering**

and by David B. Kieda, Dean of The Graduate School.

ABSTRACT

Polycrystalline cubic boron nitride (PCBN) is one of the few materials suitable for friction stir welding (FSW) of hardened steels, which demands tool materials to possess high temperature strength, toughness, abrasion resistance, thermal and chemical stabilities.

In FSW process at temperatures higher than 980°C PCBN consisting of AlB_2, as one of the major reaction products, underwent a reverse peritectic reaction: $AlB_2 \rightarrow Al_{(l)} + AlB_{12}$ and released liquid Al, which was believed to cause inter-cBN-granular cracking in the PCBN tool during FSW of hardened steel.

In the present research, PCBN starting with decreased Al additive and addition of fine cBN powder, was HP/HT-sintered at higher B:Al ratio and increased available BN surface area for fast in situ reaction with liquid Al in favor of forming AlB_{12} instead of AlB_2. Titanium powder in HP/HT-sintering of PCBN under the same pressure and temperature conditions resulted in cBN, TiN, and TiB_2 reaction products but could not achieve the densification comparable to the Al additives. However, using Ti-coated cBN particles with addition of the fine cBN powder led to PCBN with highly packed reaction products of cBN, TiN, and TiB2 and strong mechanical properties.

Applying electron backscattered diffraction (EBSD) method, the PCBN with 10vol%Al additive was detected to consist of 0.5vol% and finely dispersed AlB_2 in addition to AlB_{12} as the major borides in addition to cBN and AlN. Such PCBN was

shown to possess high thermostability measured at 1000°C and measureable increases in flexural strength at temperatures up to 1100°C, while room temperature fracture toughness value was retained up to 1100°C as well. Combine x-ray diffraction (XRD) and EBSD results revealed the increase in high-temperature strength was resultant of high residual compressive-stress on cBN grains applied by thermal expansion of the AlN-AlB_{12} grainboundary phase. The PCBN sintered from cBN with 10vo%Al powder, possessing improved thermostability and mechanical strength at temperatures up to 1100°C benefiting from significantly reduced AlB_2 and increased cBN vol%, is suitable for high temperature applications. The PCBN sintered using the Ti-coated cBN particles showed significant decrease in strength and toughness measured in 900°C to 1100°C range, due to oxidation reactions of TiN and TiB_2 at high temperatures.

TABLE OF CONTENTS

ACKNOWLEDGEMENTS

I would like to express my deep gratitude to Dr. Zak Fang for giving me a chance to fulfill my dream as a Ph.D. in metallurgy. His professional guidance and patient supervision made the study and completion of the project possible. My appreciation, from the bottom of my heart, goes to Dr. J. Daniel Belnap for his consistent advising, mentoring, and supervision not only in this study but also in my professional career. My thanks also go out to Dr. Sivaraman Guruswamy and Dr. Ravi Chandran for their academic teaching, supervision, and guidance in this study. I particularly would like to thank Dr. Charles Elliott for his guidance and challenges to me both as a graduate student previously and a committee member for this study.

I owe my career and professional achievements to Megadiamond for its continued support in studying PCBN material and funding for this project. The valuable technical discussions and suggestions from my fellow material scientists at Megadiamond also gave me the encouragement and confidence to finish the project.

It is with my greatest respect to my late father, a lifelong teacher and metallurgist, that I dedicate this dissertation. My late mother's love and persistency in acquiring knowledge inspired me to achieve and be the best I can be.

1 INTRODUCTION

Friction stir welding (FSW) is a new welding process utilizing a milling type of machinery and tool setup to plastically stir and mix materials resulting in a submelting temperature, solid-state welding process. During FSW, high torque load and high temperatures are experienced by tool materials because of the significant friction stir action leading to superplastic deformation in the materials in forming the weld. Polycrystalline cubic boron nitride (PCBN) composite, owing to its unique high-temperature hardness, high abrasion resistance, oxidation resistance, and chemical stability, has been used in FSW-processing of hardened steels and ferrous materials otherwise very difficult or impossible to process. One of the first PCBN composites for FSW tools was ultrahigh pressure and high-temperature (HP/HT) sintered from cBN and 20vol%Al as starting powder mixtures.

During FSW, cracking was experienced in the PCBN tool shoulder area although the tools showed only slight abrasion wear and could still carry out the FSW process. Analysis of the cracked PCBN tool revealed, in addition to the primary cubic boron nitride (cBN) and reacted AlN phases, the existence of AlB_2 which decomposes at 980°C via the reverse peritectic reaction: $AlB_2 \rightarrow Al_{(l)} + AlB_{12}$. Plastic dimples, rich in Al, were found on the fracture surfaces of the PCBN tool after FSW of hardened steel tool at 1000°C or higher and under the thermal and mechanical loading.

Aluminum is used as a common PCBN sintering additive, because of its low melting point, highly-reactive nature, and reaction products such as AlN, AlB_2, and AlB_{12} formed with cBN particles. It will be ideal to modify the cBN + Al system as a sintering precursor to promote the formation of high melting-temperature AlB_{12} while minimizing the intermediate AlB_2 in the PCBN composite with improved thermostability, high temperature strength, and toughness. It can be more beneficial if the intermediate AlB_2 and other aluminum borides are replaced by using Ti as additive in a cBN+Ti system to HP/HT-sinter PCBN with stable and stronger TiN and TiB_2 reactive products besides the primary cBN particles for high temperature applications.

The present study focused on understanding the mechanisms of HP/HT-sintering of PCBN composites from cBN+Al and cBN+Ti systems and high-temperature mechanical property characterization of the new PCBN composites. In the cBN+Al powder system, the goal was to modify the system to produce PCBN with the minimum amount of AlB_2 possible to enhance the thermostability and maintain high strength and toughness at elevated temperatures. In the cBN+Ti system, the aim was to evaluate the system and to study a valid method to bring Ti into HP/HT sintering PCBN at cBN+Al comparable sintering conditions without the Al-containing reaction products for high temperature applications. The microstructures, reaction phases, thermal and mechanical properties, high temperature flexural strength and fracture toughness of the HP/HT-sintered PCBN composites from cBN+Al and cBN+Ti systems were evaluated and compared.

2 LITERATURE REVIEW

2.1 Friction Stir Welding a High Temperature Application for PCBN

Friction stir welding (FSW) technique was developed in 1991 by The Welding Institute, UK with the first patent issued to Wayne M. Thomas et al., on Nov. 8, 1995.[1] FSW uses a milling type of tool and apparatus with the tool pin first penetrating the two materials to be joined and then traveling along the seam in forming the joint, as demonstrated in

Figure 2-1. It shows that tremendous heat was generated by mechanical stirring actions caused by the friction between the tool and materials thus enabling significant plastic deformation as well as mixing of the two metals. This results in a sub-melting, solid-state joint thus reducing many of the disadvantages associated with welds formed from molten metal pool. Indeed, FSW of ferrous materials requires a tool material that possesses a combination of exceptional high temperature properties such as high strength (hot hardness), toughness, abrasion resistance, high thermostability, oxidation resistance, and least affinity to the materials welded.[2] Some of the exploratory work on steels was conducted using tungsten alloys,[3, 4] tungsten-rhenium alloy,[5] and lately the new tungsten-rhenium-cBN composites[6] with some success. Commercial applications have been accomplished using PCBN to FSW-process hardened steels.[2,7-10] It has been found that for non-PCBN materials, abrasion was the major wear pattern[11] but for PCBN tool material cracking or fracturing was the dominant failure mode.[12, 13]

2.2 Modeling of FSW Tool

2.2.1 Temperatures in FSW of stainless steels

High temperature in workpiece is needed in FSW processing to maintain the superplastic deformation and material flow from one side to the other to form the weld. Two types of heat sources were considered in modeling: a) the frictional work at the tool-workpiece interface and b) the deformation work in the workpiece.[14] Finite element modeling predicted close to 50% of the total mechanical energy from the machine was transferred to increasing the temperature of the 304L stainless-steel workpiece during FSW processing.[15] Studies and simulations on 304L stainless steel predicted the maximum temperature in the stirred welding zone could reach 1056°C[16] to 1157°C.[15] Increasing the tool rotational speed resulted in increase in maximum temperature up to 1200°C.[14] The maximum temperature in the tool during the FSW processing was experienced in the tool shoulder area instead of the stirring pin.[15]

2.2.2 Forces and stresses in FSW tool

Common FSW tool failure was proposed as starting with the pin failure because the pin was under large bending moment and torsion in typical FSW process.[17] The total traverse force, F, consists of two portions: F_s - force carried by tool shoulder and F_p – force carried by the pin. It can be calculated as:[17]

$$F = F_s + F_p \tag{2-1}$$

$$F_s = \oint_A \delta \cdot \mu P \cdot d_A \tag{2-2}$$

$$F_p = \oint_A \sigma \cdot d_A \tag{2-3}$$

where: δ is spatial fractional slip, μ is the coefficient of friction, P is the normal pressure, σ is temperature-dependent yield strength of the work material, and d_A is the projected contact area of the pin. Experimental study of varying friction stirring pin length showed that as the pin length decreased to zero, the axial force approached a constant limit. This limiting force was believed to be carried by the shoulder rather than the pin and appeared to be more than 50% of the total axial force.[18]

During FSW process two types of load apply to the tool pin, in addition to the normal compression load: bending and torque. The prior is introduced from the resistance of jointed materials in the welding direction and the latter is from the spindle rotation.[17]

2.3 Cubic Boron Nitride

2.3.1 Synthesis of cubic boron nitride

As an essential and major constituent of PCBN materials, cBN crystals are man-made and, unlike diamonds, are not found in nature.[19] After the first successful and commercial conversion from graphite to diamond in 1954,[20] General Electric scientists invented synthetic cBN in 1957.[21, 22] Similar to high-pressure and high-temperature (HP/HT) diamond synthesis, Robert H. Wentorf Jr.[21] and colleagues substituted graphite with hexagonal boron nitride (hBN) and successfully forced hBN to cBN lattice change, under ultra-high pressure of 6GPa at temperatures higher than 1350°C, as illustrated in Figure 2-2. Since then, the exact pressure-temperature phase diagram and equilibrium conditions in B-N system have been explored and modified.[23, 24] It was found originally that, parallel to diamond synthesis, under the HP/HT conditions and assisted by catalysts such as alkali- and alkaline-earth metals such as Li, Mg, Ca, Al[25] and their nitrides, BN

crystal lattice underwent a transformation from hexagonal to cubic (zincblende) arrangement, as illustrated in Figure 2-3. The pressure effect in hBN/cBN equilibrium was summarized[26] as $P(GPa)=0.00273T(K)$[27] but under the assistance of the catalysts, the equilibrium line could be lowered to $P(GPa)=0.0029T(K)-1.2$.[28]

Since the first synthesis of cBN, large discrepancies exist between experimental results and thermal dynamic calculations as to where exactly is the cBN-hBN phase transformation line positioned. New thermodynamic data and experiments suggested the cBN to hBN phase transformation line to a much lower pressure and higher temperature region such that cBN was the stable phase at room pressure and at temperatures up to 1300°C.[28,29] Kinetics was another deciding factor to the phase transformation temperature at room pressure,[30] which was found to be dependent on cBN's grain size, purity, and defect concentration.[29] Regardless where exactly the equilibrium line is, a significant kinetic barrier exists that hinders the direct transition from the sp^2 to sp^3 bonding under ambient atmosphere and temperature.[31]

Besides cubic and hexagonal crystal lattice arrangements, a wurzite[32] structure (wBN) was also discovered by compressing pure hBN samples to pressures higher than 12.5GPa without applying heat. Other methods of synthesizing cBN include chemical and physical vapor deposition as well dynamic compaction techniques.[24, 33, 34] Today, most cBN crystals in sizable quantity for industrial applications are still produced by HP/HT synthesis method.

A unit-cell crystal structure of cBN is similar to that of diamond, having strong and short (1.5Å) covalent bonds, and each atom is a part of a rigid tetrahedral network equidistant to its neighboring atoms. The difference is that in cBN lattice, the larger N

atoms occupy the face centered cubic sites and B atoms fill in half of the tetrahedral interstitial spaces. Because of these short and periodic tetrahedral-shaped covalent (sp^3-hydridized) bonds[31] between B and N, cBN possesses hardness second only to diamonds.

2.3.2 Advantages of cBN over diamond

cBN exhibits significantly higher oxidation resistance than diamond at temperatures higher than 700°C in ambient atmosphere.[35] This, combined with lower solubility of BN into Fe[36] than C (diamond), makes cBN composites preferred over diamond in dry and high-speed machining of hardened steels and other ferrous materials where the cutting tips often reach 1000°C or even higher temperatures.[37] One theory for the high thermostability of c-BN in air or oxygen was proposed that protection by continuous B_2O_3 layer prevented cBN from further oxidation up to 1300°C. Reverse phase transformation from cubic to hexagonal lattice in ambient pressure was proposed as: 1320°C ± 380°C.[29]

2.4 Polycrystalline Cubic Boron Nitride

Since the late 1960s to 1970s, cBN particles have been further HP/HT-sintered into polycrystalline cBN composites[34, 37-40] and used as an ultra-hard cutting-tool material for dry and high speed machining hardened ferrous materials including cast iron, superalloys, and sintered powder metallurgy parts. These type of operations were previously carried out by wet grinding – a slow, costly, and environmentally less-friendly operation. Commonly, PCBN composites are HP/HT-sintered using cBN powder with Al-containing catalysts,[41, 42] under pressures and temperatures equal to or slightly lower

than the cBN-hBN equilibrium condition established by R.H. Wentorf, Jr.[39, 43]

Advantages of polycrystalline materials over single crystals are that the polycrystalline materials are macroscopically homogeneous and uniform without specific weak directions or planes owing to the random crystal orientations. Another significant advantage of PCBN is that, as a composite, it can be designed using different cBN grain sizes and volumes balanced with different metallic or ceramic additives to achieve properties which cannot be obtained by using pure cBN crystals alone. Figure 2-4 is a SEM image of microstructure of PCBN from a FSW tool, HP/HT-sintered from cBN + 20 vol%Al as starting powder mix,[44] showing cBN (dark grains), AlN (grey intergranular phase), and AlB_2 (dark, fine, irregular phase).

2.4.1 Basics of PCBN sintering

Pure or binderless PCBN, practically 100% cBN content without an additive, was sintered[45-47] and demonstrated improved cutting performances.[48] However, to sinter such a binderless PCBN, extremely high pressure (7.7 GPa) and high temperatures (2200° – 2400°C) have to be maintained in facilitating solid-state boundary diffusion and even cBN lattice diffusion.[49] Such ultra-high pressure and high temperature conditions are extremely difficult and costly to obtain compared to the already demanding 5 GPa or higher pressure and 1200° - 1400°C temperature range under the assistance of the sintering additives. PCBN composites are more commonly HP/HT-sintered by reactive liquid sintering mechanism in which a liquid is present during sintering at high temperatures to provide the same type of driving force as in liquid phase sintering. During sintering, the liquid reacts and disappears as the sintering progresses or as it is

completed.[50] Typical sintering additives are metallic elements in *III A* and *IV A* as well as transitional *IV B* to *VIII B* groups of the Periodic Table of Elements such as: Al, Si, Ti, Fe, Co, Ni, W etc. or their compounds such as: AlN, Si_3N_4, TiN, TiC, Al-Ti, Al-Co, Al-Ni, and so forth. As a result, most commercial PCBN composites[51-53] are sintered using cBN crystals with additives most commonly elemental Al, for reactive liquid sintering, and/or Ti-containing compounds as the starting powder mixture. To initiate the reactions, heat is needed but sufficient heat produced by the exothermic reactions, in cBN and Ti-containing system for instance, in turn may make the reaction self-sustained and sufficient to sinter the product.[54, 55]

Commercial raw cBN crystals, as the major starting powder for PCBN composites, may not be obtained having the stoichiometric B/N atomic ratio of exactly 50/50. Instead, there were often more B atoms than N atoms in the compound, i.e., B: N>50:50, because of the existence of oxides such as B_2O_3. Reducing B_2O_3 (T_m=*480°C*) was viewed as one of the steps in preparing cBN crystals for HP/HT-sintering of PCBN, because it may prevent the critical direct-contact between B and/or N atoms of the separate grains.[56] For this purpose, metallic elements such as Al, Ti, Mg, Ca, etc. that form stronger oxides with more -ΔG such as TiO_2, Al_2O_3, MgO, CaO etc. are suitable candidates. The reactions happen in two stages.[57] First, Al reduces with B_2O_3 in the reaction of:

$$6B_2O_3 + 13Al = AlB_{12} + 6Al_2O_3 \qquad 2\text{-}4$$

and releases fine B, Al_2O_3 and AlB_{12}. The second stage is marked by direct reaction of B with Al in forming AlB_2 at temperature up to 500°C.

A major sintering driving force comes from reduction in surface energy of the powders. The material flow during pressure-assisted sintering can be further accelerated by the stress applied. The most effective factor, that affects or enhances the degree of sintering among other parameters, is temperature. Rapid densification close to theoretical values can be quickly achieved with small particles, high pressures, and high temperatures.[54] Therefore, the ultrahigh pressure and high temperature applied to sintering PCBN create a condition that is not only necessary in keeping the cubic lattice as the stable structure but also beneficial in accelerating the kinetic process.

2.4.2 B-N-Al system and reactions

As a PCBN sintering additive, Al has been the element of choice[19, 25] because of its low melting point (T_m=660°C) and rapid reaction nature. In the B-N-Al ternary system, X-ray diffraction conducted[58] did not reveal existence of a ternary compound. In the B-N-Al cross-section at 900°C, with a given composition close to the high BN volume region and particularly if B:N>50:50, equilibrium compounds of BN, AlN, AlB_2 and AlB_{12} were found at room temperature, as shown in Figure 2-5.

2.4.2.1 B-Al binary system

Study of Al-B binary reactions revealed[59-61] two intermetallic compounds: AlB_2 and AlB_{12} with a peritectic reaction during cooling from $T \geq 980$°C:

$$Al_{(L)} + AlB_{12} \rightarrow AlB_2 \qquad 2\text{-}5$$

At room temperature AlB_2 is one of the stable phases, as shown in Figure 2-6. However, due to the sluggish nature of the peritectic reaction between AlB_{12} and $Al_{(l)}$, AlB_{12} core

were found inside the AlB_2 particles.[60] The solubility of B in solid Al (FCC) is less than 0.025 at% and in liquid Al starts at 0.055 at%. The reaction between B and Al in atomic scale was proposed as alumination of boron, which is different from boriding of transition metal. Boriding of metal starts with gradual saturation of B atoms from the metal surface, therefore, the first phase formed will be with the least B content in the initial stage. Alumination of boron mechanism, on the other hand, involves Al entering the boron lattice, therefore, forming a phase with the highest boron content, such as AlB_{12}, in the initial stage of alumination.[62]

Based on the equilibrium phase diagram and phase lever rule, the reverse peritectic reaction, starts with decomposing of AlB_2 upon heating. Decomposition of one mole of AlB_2 leads to 0.28 mole of Al(B) liquid solution and 0.72 mole of stable solid AlB_{12} at the peritectic temperature of 980°C. As temperature increases, the fraction of Al liquid increases as well.

In addition to the temperature and composition requirements, the complexity of the aluminum-boride lattice structures is also a factor in determining their crystallinity. AlB_2 has a hexagonal structure with B and Al atoms in alternating layers, whereas AlB_{12} has a complex orthorhombic arrangement, hence, requiring significant ordering from the Al-B liquid to form.[63] B atoms have to diffuse and find their positions in the lattice from the dilute solution. If the cooling rate is sufficiently high, long range order of AlB_{12} may be disturbed resulting in defects in crystal lattice and higher solid energy. This, in turn, leads to a reduced AlB_{12} compound's stability and lesser tendency to form.[63] In a Al-B liquid modeling, if considering the interface kinetics is dominated by collision between B and Al atoms, the probability of forming AlB_2 and AlB_{12} can be modeled as:[63]

$$P_{AlB_2} = (1 - x_B)x_B^2 \quad 2\text{-}6$$

$$P_{AlB_{12}} = (1 - x_B)x_B^{12} \quad 2\text{-}7$$

where: P_{AlB_2} is the probability for forming AlB_2, $P_{AlB_{12}}$ is the probability for forming AlB_{12}, and $x_B$is the molar fraction of B atoms. Comparing the equations shows that for a given B molar fraction x_B, the probability of forming $AlB_2$is much greater than forming AlB_{12}.

2.4.2.2 N-Al binary system

Nitrogen is practically insoluble in both liquid and solid Al, as shown in Figure 2-7. At 1200-1500°C, AlN's solubility was reported to be less than 0.004wt%[64], which did not change significantly between 900° and 1600°C. This provided the basis for separating the reactions in B-N-Al ternary system into two independent systems: Al-B and Al-N.

Theoretical calculation for a BN:Al=9:1 molar ratio mix indicated that[65], at temperatures from 1227° to 1527°C and pressure at $1x10^7$ Pa, the reaction products were BN, AlN, and AlB_{12} in a molar ratio of approximately $BN:AlN:AlB_{12}=8:1:0.1$.

In summary, there are two reactions in cBN+Al system at elevated temperatures in ambient atmosphere:[66]

$$BN + \frac{3}{2}Al = AlN + \frac{1}{2}AlB_2 \quad 2\text{-}8$$

$$(\Delta G = -142.6+0.0197T, kJ/mol), when\ T \leq 980°C)$$

$$BN + \frac{13}{12}Al = AlN + \frac{1}{12}AlB_{12} \quad 2\text{-}9$$

$$(\Delta G = -68.0+0.0253T, kJ/mol), when\ T \geq 980°C)$$

2.4.2.3 Wetting and reaction of Al to BN surface

One of the important criteria for selecting PCBN sintering additive is its liquid contact angle to cBN surface. As illustrated in Figure 2-8, Al is observed to have one of the least contact angles to cBN, with $\theta=0^{\circ}$ reported after treating Al and cBN at 1200°C for 30 min in vacuum[67] or 1138°C in another case.[68]

The wetting of Al to BN was controlled by its interfacial reaction. Al surface oxidation, although only a few tens of nm, may substantially affect the contact angle, as illustrated in Figure 2-9. Only at temperatures higher than 900°C, in vacuum or reducing atmospheres, can the oxidation effect be negligible partially because of the reaction product of Al_2O_3 was a gaseous phase. Another study concluded that the degree of decreasing in contact angle depended on the quantity of oxide film on Al surface and when the oxide film was minimized the contact angle then became zero degree.[69] It was proposed, as illustrated in Figure 2-9, that γ_{SL} became Al-AlN interfacial energy and θ_f was then the final contact angle, instead of the contact angle between pure Al to BN, assuming the reaction developed at the same rate as the wetting at the triple junction.[70]

Another experiment[71] indicated that after heating cBN+Al powder mixture at 1100° - 1200°C for 60 min, without applying ultrahigh pressure, there was still a detectable amount of unreacted Al in the mix. Complete Al and cBN reactions were observed at 1300°C for 60 min. Depending on the initial mix compositions, reaction products of AlN, Al_2O_3 and AlB_2 were detected by X-ray diffraction. At reaction temperatures up to 1300°C, the quantity of AlN increased with the temperature, which was attributed to the surface reaction of BN with Al in reducing the pore channel diameters, thereby, slowing down the rate for further reacting. The surface oxide B_2O_3 on

fine BN particle surface was found to greatly diminish the wetting and infiltration by Al.[72] The effect of ultrahigh pressure to Al wetting of cBN was proposed to follow a slope of $dT/dP = 68K/GPa$[73] from the onset of Al liquid infiltration into a cBN compact under the HP/HT condition.

2.4.3 B-N-Ti system and reactions

Solid state reactions between BN and Ti powder were found to begin at 1200°C and lead to the formation of Ti-borides and Ti-nitrides and solid solutions of B and N in Ti.[74] In B-N-Ti ternary system, the solubility of TiB_2 in TiN_{1-x} reached 8mol%, whereas the solubility of TiN_{1-x} in TiB_2 wsa negligible.[74] Solubility of B in TiN_{1-x} was less than 1at% and there was no solubility of N in TiB or TiB_2 at 1400°C. Solubility of Ti in BN, mutual solubility of Ti-borides and Ti-nitrides in BN was quite restricted at temperatures up to 1500°C. As a result, B-N-Ti ternary system can be treated as two separated reaction systems: Ti-B and Ti-N.

Comparable to cBN+Al system of reactions, TiN and TiB_2 are reaction products in a cBN+Ti system. Thermodynamic calculations of 1:1 molar cBN:Ti mixture, at 1000°C and 1400°C under $3x10^{-3}$Pa vacuum, predicated formation of TiB_2, TiN, and N_2 at approximately TiB_2:TiN:N_2 = 0.45:0.45:0.1.[75]

Synthesis of in situ TiB_2/TiN from dense BN-Ti established the temperature for both pressureless displacement reaction and self-propagating high-temperature sintering is less than 1200°C[76], which is well below the melting point of Ti(T_m=1660°C). Based on the 1090°C isothermal cross-section in the B-N-Ti phase diagram,[77] as shown in Figure 2-10, in the composition close to BN+10vol%Ti, TiN_{1-x}, BN, and TiB_2 exist[74] and

may remain at room temperature.

Studies of bonding structure between BN and Ti as well as Ti-coated cBN suggested a transition similar to: BN-TiB_2-TiB-TiN_{1-x} -(αTi)-Ti(pure).[78, 79] A different study of cBN+Ti system[80] under atmospheric pressure suggested diffusion of B from cBN into the Ti at 1400°C and resulting to stoichiometric TiB_2 and TiN, without formation of other borides or nitrides such as Ti_2N and TiB.

2.4.3.1 B-Ti binary system

As shown in Figure 2-11, in a B-Ti system the lowest liquid eutectic between Ti and TiB is T_m=1540°C, which is much higher than Al-B system's liquidus temperature of 660°C or peritectic temperature of 980°C. The solubility of B in Ti(α) was reported at <1.7at% and < 1at% in Ti(β), respectively, on the other hand, the solubility of Ti in B is also very low and it can be treated as pure B.[81] TiB_2(T_m=3225°C) is not a naturally occurring compound but it can be prepared by a variety of high-temperature methods, such as the direct reactions of Ti or its oxides/hydrides, with elemental B over 1000°C.[82]

2.4.3.2 N-Ti binary system

In contrast to the Al-N system, there are wide ranges of mutual solubility between Ti and N in forming many different TiN solid solutions with different N concentrations, as shown in Figure 2-12. In fact, TiN phase includes a stoichiometric TiN and a wide range of N from 30 to more than 54 at%.[83] The ratio of N diffusion coefficient in β-Ti, α-Ti, and δ-TiN is of the order of 100:10:1.[84] It was then suggested that Ti was rapidly saturated with N limited only by dissolution reaction followed by TiN formation at a

much slower rate which was increasingly diffusion controlled. Some of the reactions in the Ti-N system are:[83] allotropic change of α-Ti to β-Ti at 883 ± 3°C; fusion reaction of β-Ti to liquid at 1670 ± 6°C; eutectic or peritectic reaction of TiN to α-Ti + Ti_2N at 1050±60°C; and allotropic change of Ti_2N to TiN(cubic) at ~1100°C.

In summary, the reaction of cBN+Ti was proposed as:

$$BN + \frac{3}{2}Ti = TiN + \frac{1}{2}TiB_2 \qquad 2\text{-}10$$
$$(\Delta G^0 = -226.5+0.0163T,\ kJ/mol)$$

2.4.4 Reactive sintering of PCBN in HP/HT conditions

Reactive sintering mechanisms of PCBN in HP/HT conditions were considered with focuses on cBN+Al and cBN+Ti systems.

2.4.4.1 Reactive liquid sintering of cBN+Al system

TEM evaluation[42] of PCBN composite HP/HT-sintered from cBN+Al starting material revealed a structure with a continuous thin layer of AlN surrounding cBN grains. Outside the AlN was a layer of AlB_2 which was comparatively unstrained with little dislocations. Unreacted Al or hBN was not detected in the PCBN. The sintering mechanism was proposed that, as Al melted between the load-bearing cBN network, reaction between Al liquid and cBN led to a continuous, oriented, and solid skin of AlN except the areas that cBN grains were in direct contact under the ultra-high pressure. The B liberated from BN lattice then formed AlB_2 or even AlB_{12} outside the AlN layer to consume the remaining Al.[85] There was no evidence of recrystallization of cBN from the solvent/catalyst (Al). Some fine AlN particles observed inside AlB_2 areas may have been

formed by complete reaction of fragmented cBN or even hBN with the Al melt. Another TEM study[85] suggested that at 900°C, in HP/HT sintering of PCBN, Al liquid reacted with cBN but did not proceed to completion at 900°C. At temperature higher than 1200°C, Al metal completely reacted with cBN leading to reaction products of AlN, AlB_2 and AlB_{12}. It also suggested that as result of the reaction, AlN was always surrounding cBN grains with AlB_2 and AlB_{12} next to the AlN, therefore, B was believed to diffuse through the AlN layer to reach unreacted metallic Al to form AlB_2 and/or AlB_{12}.

Particle to particle bonding mechanisms for PCD and PCBN are different.[86] In PCD sintering, fast dissolving of C into catalysts, such as Co, Fe, and Ni, in forming solutions and fast precipitating onto diamond crystals surfaces was recognized as the major diamond to diamond intergranular-bonding mechanism.[30, 51, 87, 88] This results in a continuously bonded diamond skeleton. However, direct contact or bonding between cBN crystals was only found at the points where cBN crystals were crushed against each other, which were then surrounded immediately by AlN and AlB_2.[42]

In recent scanning transmission electron microscopy (STEM) conducted on binderless, practically 100% pure PCBN sintered at temperature higher than 2000°C and pressure higher than 7.5GPa,[46, 47] directly bonded cBN crystals[89] were observed via solid-state boundary diffusion or cBN lattice diffusion.[49]

2.4.4.2 Reactive sintering of cBN+Ti system

Compared to the cBN+Al system, study of mechanism and reactions of cBN+Ti under HP/HT conditions was very limited. One transmission electron microscopy (TEM) study of HP/HT sintered cBN+Ti system showed formation of columnar TiB_2 directly

covering cBN grains and TiN was observed to grow on the TiB_2 surface.[75] Sintering temperature of 1000°C was found insufficient to form TiB_2 phase until further heating up to 1400°C. The reactively formed TiB_2 was suggested as a determining factor in obtaining a high microhardness of the composite. The TEM observation confirmed the reaction sintering between cBN and TiN, TiC binders under 7GP and 1750°C via formation of TiB_2.[90] Compared to the cBN + Al powder system, these reaction temperatures and pressure conditions were much higher and more difficult to achieve.

2.4.5 PCBN sintering process

General PCBN processing steps included powder mixing, pre-reaction, HP/HT sintering, and finish machining. Two methods have been employed to bring molten Al to react with cBN particles. One was liquid infiltration of the highly-compacted cBN crystals under the HP/HT condition and another was premixing cBN crystals with fine-powdered Al. The Al infiltration was shown to be dependent on the cBN particle size, compaction, and reaction kinetics[91]. As observed, a complete Al liquid supply by liquid Al infiltrating and reacting with cBN particles through a densely compacted cBN powder mass may not be achieved.[72] For the purpose of in situ and complete reaction of cBN with Al, fine Al powder mixed with cBN powder as a precursor to sintering PCBN was preferred.

It was demonstrated that just mix final reaction products as detected by analyzing PCBN composites without the pre-alloying processing and in situ HP/HT reactions could not achieve the mechanical properties and performance in metal cutting comparing to PCBN processed otherwise.[92, 93] Reaction or pre-alloying on the mixtures prior to

sintering and the parameters employed during HP/HT-sintering were both critical factors determining the PCBN composites' sintering characteristics and final properties.

2.4.6 Properties of common reaction compounds in PCBN

Reported physical properties of reaction products found in HP/HT-sintered PCBN composites are summarized in Table 2-1, with diamond as reference.

2.5 Variables Affecting PCBN Properties

In addition to the additive types, cBN volume, grain size, and particle packing play important roles in determining the properties, particularly high cBN volume-content PCBN for high temperature applications.[6, 94]

2.5.1 cBN volume %

The volume fraction of cBN particles in PCBN composites have been found to vary from 50 to 95vol%[95-98] depending on the materials being machined.[94, 99] It was suggested that the forces applied to PCBN were carried mostly by the cBN grain structure or the bonded skeleton which determined the PCBN's mechanical properties.[100] The non-cBN phase or binder phase was the first to be abraded by workpiece followed by removal of cBN grains and contributing to further abrasion.[101] As a result, high cBN volume fraction was needed in maintaining the PCBN's high mechanical strength and abrasion wear resistance.

2.5.2 cBN grain size

It was demonstrated in PCD system that as the fracture toughness increased with increase of diamond grain size, as a trade-off, strength declined.[102, 103] Based on failure analyses of worn PCBN tools, the grain boundaries filled with reactive sintering phases[104] were detected as weak points both in terms of mechanical strength and chemical stability. The number of grain boundaries per unit length or the discontinuity(flaw) size on the tool cutting-edge was also found to affect the mechanical and chemical tool wears[105] marked by diffusion wear between the binder phase and the work piece.[101, 106] Additionally, because of fine grains' lower packing density compared to large grains', there was a tendency for a fine-grained PCBN composites to inherently consist more second phase and grain boundaries under comparable HP/HT synthesis conditions.

2.5.3 cBN particle packing

Theoretical modeling predicated that in the case of packing unit spheres, the smallest possible hole in a randomly packed structure was a triangular pore among three spheres in close contact, which has a radius of approximately 0.154 of the sphere's diameter. This led to the condition that the secondary spheres should be at least approximately 7 times smaller than the primary ones if they were to slip through the packed spheres and fill all the interstitial spaces.[107] Based on this model, when two sized spheres were mixed at the ratios of 7:1 size and 73:27 volume ratio, a highest theatrical packing fraction of 0.86 could be obtained for the bimodal distribution.[108]

Under the ultrahigh (4-6GPa) cold-pressure without heat, significant crushing of cBN crystals occurred and led to reduction in grain size, with larger cBN crystals more

sensitive to the ultrahigh pressure than smaller-sized.[109] Increasing the applied ultrahigh pressure resulted in a decreasing of the porosity% and diameter of pores of the cBN compacts. Under a given and constant applied ultrahigh pressure, the pore diameter increased with increasing cBN grain sizes.

2.5.4 Reaction phase and compound

No commercially available PCBN materials had been found consisting of Ti alone as the sintering additive, instead, Al was often added together with Ti to lower the reaction temperature and provide some level of liquid sintering assistance.

2.6 Material Evaluation

PCBN composites' densification, degree of reactive sintering, effects of sintering temperature and time, effects of different reactive sintering additives were examined and studied by mechanical, microstructural, and thermal property measurements on PCBN sintered with different parameters.

2.6.1 Flexural strength by three-point-bend and four-point-bend methods

Flexural strength, indication of cBN's bonding strength via the reaction compounds under tensile stress was evaluated using four-point-bending method at room temperature, as shown in Figure 2-13. The maximum fracture load obtained was used for calculating the flexural strength using the equation of: [110]

$$\sigma = \frac{3F(L-l)}{2bw^2} \qquad 2\text{-}11$$

where: σ is the maximum stress of extreme outside fiber of the specimen at its rupture in

the four-point-bend test *(Pa); F* is the maximum load applied to the specimen at the rupture *(N); L* is the distance between the two outside support pins *(m); l* is the distance between the two inside loading pins *(m); b* is the specimen width *(m);* and *w* is the specimen thickness *(m).*

Because of sample size limitations, a three-point-bend test method was used as well in assessing brittle materials' flexural strength at high temperatures,[110] as illustrated in Figure 2-14:

$$\sigma = \frac{3FL}{2bw^2} \qquad 2\text{–}12$$

Compared to four-point-bend testing, three-point-bend testing gave synthetically high strength values. In one test, the mean flexural strength of 925MPa was obtained using three-point-bend method, whereas the same material tested using four-point-bend method yielded a mean value of 724MPa.[50] It was because the area and volume under the tensile stress in the four-point-bend sample was much bigger than that of the three-point-bend sample, as illustrated in the schematics, resulting in an increased probability of a larger discontinuity being exposed to the high-tensile stress.

2.6.2 Vickers hardness and fracture toughness by indentation method

Vickers hardness, measurement of PCBN composite's resistance to plastic deformation under compressive load was measured and calculated using formula (ASTM E384):

$$H_v = \frac{1.8544P}{d^2} \qquad 2\text{-}13$$

where: H_v is the Vickers hardness *(Pa); P* is the load applied *(N);* and *d* is the Vickers

indentation's diagonal length *(m)*.

Limited publications[111, 112] were found using single-edge v-notch bending test in measuring PCBN materials' plane-strain fracture toughness *(K_{IC})*. Using this method, K_{IC} values of 6.8 to 8.0 $MPa\sqrt{m}$ for a PCBN composite were reported.[113]

Fracture toughness, K_C, for ultra-hard materials such as PCBN[114, 115] were commonly estimated by indentation cracking method modified from Palmqvist indentation method on cemented WC-Co[116] using Vickers hardness indenter, as illustrated in Figure 2-15, with equation of:[117]

$$K_c = \frac{\xi\sqrt{E/H_v}P}{c^{3/2}} \qquad 2\text{-}14$$

where: ξ is the material independent constant for Vickers-indenter produced radial cracks; E is the Young's modulus *(Pa)*; H_v is the Vickers hardness *(Pa)*; P is max load applied *(N)*; and c is the radial/median crack *(m)*. The value of the constant $\xi = 0.016 \pm 0.004$ is obtained, when $c/a > 2.5$, found from evaluating various materials including: glass-ceramic, soda-lime glass, aluminosilicate glass, Al_2O_3, Si_3N_4, ZrO_2, and WC-Co.[117]

Tested by the indentation method, K_{IC} for PCBN materials was estimated as $5.0 \pm 0.5\ MPa\sqrt{m}$.[118] PCBN with larger cBN grain size yielded higher K_C[49] under the same HP/HT sintering temperature and without sintering additives.

2.6.3 Fracture toughness measurement by diametral compression method

Plain strain fracture toughness, K_{IC}, values of ceramic materials and PCD have been measured using a diametral disc with a center crack.[103,119] To concentrate the crack nucleation in the tip of the opening and in a planar propagation mode, chevron notch at

each end of the slot can be implemented, as shown in Figure 2-16. The disc was loaded with a diametral compression force perpendicular to the center crack and K_{IC} can be calculated using equation: [119]

$$K_I = \frac{P}{(\pi R)^{1/2} B} Y \qquad 2\text{-}15$$

where: P is the diametral compression load applied to the disc, R is the radius of the disc, B is the thickness of the disc, and Y is a dimensional parameter. When crack length $a > a_1$ then:[119]

$$Y = \alpha^{1/2} N_1(\alpha) \qquad 2\text{-}16$$

where: $N_1(\alpha) = 0.991 + 0.141\alpha + 0.863\alpha^2 + 0.886\alpha^3$. In case of pure mode I, $N_1(\alpha)$ is a function only of the relative crack length $\alpha = a/R$.

2.6.4 High temperature mechanical property measurement

High temperature mechanical property measurements, including microhardness, flexural strength have been conducted up to 1200°C.[47,120] The hardness values were shown to decrease as the temperature increases.[35] For PCBN with 90wt% cBN balanced with AlN and AlB_2, the room temperature hardness was reduced by about 50% when the temperature reached 1200°C and higher.[121] The reason for decrease in microhardness was proposed because as the active slip systems of cBN crystal of $\{111\}\langle 110\rangle$[100] was readily energized, it leads to slip deformation within cBN grains. Another high temperature Knoop indentation study found that the indentation mechanism was through intracrystalline and intercrystalline gliding at high temperatures compared to the development of twining and shear cracks at low temperatures.[122] Study of PCBN sintered

with different cBN volumes (50wt% to 80wt%) and binder types (Al, Ti, TiC) suggested that the brittle to ductile transition started at 800°C for all these compsoites.[123] Flexural strength values of submicron grain-sized and high purity PCBN may increase with rising of testing temperature beyond 800°C.[47] The increase of flexural strength with temperature was believed to be due to small plastic deformation at the crack tips inside cBN grain which relaxed the localized stresses at a crack tip and prevented further development of the crack.[47] Direct measurement of fracture toughness values of PCBN using the three-point-bend method[124] showed that fracture toughness of a 25μ average-grain-sized PCBN decreased approximately by 1/3 with increase of temperature up to 800°C.

2.6.5 Weibull distribution and modulus

Applicability of strength and fracture toughness values measured on small PCBN samples in the laboratory in predicting mechanical failure of FSW tools can be attempted by adapting Weibull distribution and modulus. The probability of failure of brittle ceramic materials can be expressed as: [125]

$$P_f = 1 - \exp\left[-\frac{V}{V_0} \frac{(\sigma)^m}{\sigma_o} \right] \qquad 2\text{-}17$$

where: P_f is the probability of failure, σ is the applied stress over volume V, V_o is the test sample volume, σ_o is the characteristic strength (measured flexural strength or fracture toughness), m is the Weibull modulus. In order to find the value of the Weibull modulus *(m),* the equation can be rearranged and taken natural logarithm on both sides:

$$\ln\left[\ln(\frac{1}{1-p}) \right] - \ln(\frac{V}{V_0}) = m \ln\sigma - m \ln\sigma_0 \qquad 2\text{-}18$$

for a constant test sample volume the equation can be reduced to:

$$\ln\left[\ln\left(\frac{1}{1-p}\right)\right] = m\ln\sigma + const. \qquad 2\text{-}19$$

which is a linear function of $y=ax+b$ format, therefore, the Weibull modulus *(m)* can be obtained as the slope in plotting *ln(ln(1/(1-P))) vs. ln* σ.

If the probability of failure P_f value is held at a constant, then by measuring mean strength the equation can be reduced to:

$$\frac{\sigma_2}{\sigma_1} = \left[\frac{V_1}{V_2}\right]^{\frac{1}{m}} \qquad 2\text{-}20$$

which gives a scaling factor corresponding the measured mechanical property on small samples to a larger volume.

2.6.6 Reactivity and thermal behavior evaluation

Thermostability, oxidation behavior, possible decomposition of AlB_2, or even unreacted residual Al in the PCBN materials were analyzed by thermo-gravimetric analysis (TGA) during heating up and high-temperature holding at the peritectic reaction temperature of 980°C. TGA analysis can also reveal the cBN crystals', additives', precursor mix's reactivity,[54] thermostability, and oxidation behaviors.[126]

2.6.7 Electron backscattered diffraction (EBSD) analysis

Kikuchi patterns were generated when a large number of electrons were incoherently scattered and traveling in all directions in the specimen; these can then be Bragg-diffracted by the atomic planes.[127] Kikuchi patterns were also found by electron

backscattered diffraction (EBSD) on the surface of a polished and highly tilted sample, which was bombarded with high-intensity electron-beam in a SEM chamber,[128] as illustrated in Figure 2-17.

In conjunction with SEM imaging and EDS spectra collected simultaneously, the Kikuchi patterns can be analyzed in identifying crystal orientations, lattice structure, and grain size by true crystal orientation and lattice differences. This technique became commercially available in 1986 and combined the EBSD patterns obtained in SEM with on-line computer-assisted indexing of the EBSD patterns.[129] Numerous publications were available in analyzing FSW-processed metal welds and the EBSD technique was also found in analyzing grain size and orientations of polycrystalline diamond.[130] The present literature review did not find any publication for applying EBSD technique in analyzing PCBN microstructure or composition.

2.6.8 Modeling of stresses on two-phase grains structure

2.6.8.1 Modeling of thermal stresses on two-phase grains structure

Researchers[131] adapted elastic stresses for a pressure cylinder with diameter a and b[132], as illustrated in Figure 2-18, for modeling of thermal expansion stress for intergranular two-phase composites. The assumptions were: a) external pressure acting on the outer phase-II $P_o = 0$ and b) the interfacial stress between phase I inner and outer II $P_i = \sigma_a$. Then the stress components, σ_r – radial stress and σ_t tangential stress at the interface, when $r = a$, were obtained[132]:

$$\sigma_{1,r} = \sigma_a \qquad 2\text{-}21$$

$$\sigma_{1,t} = \sigma_a \qquad 2\text{-}22$$

$$\sigma_{2,r} = \frac{a^2(b^2-r^2)}{r^2(b^2-a^2)}\sigma_a \quad 2\text{-}23$$

$$\sigma_{2,t} = \frac{-a^2(b^2+r^2)}{r^2(b^2-a^2)}\sigma_a \quad 2\text{-}24$$

where: $\sigma_{1,r}$, $\sigma_{2,r}$ is the radial stress acting on phase I and phase II, respectively, at radius r; $\sigma_{1,t}$, $\sigma_{2,t}$ are the tangential stress acting on the phase I and II at the interface when $r=a$.

When temperature change induced thermal stresses were considered, Hooke's law can be expressed as:

$$\epsilon_{1,t} - \alpha_1 T = \frac{1}{E_1}(\sigma_{1,t} - \nu_1\sigma_{1,r}) \quad 2\text{-}25$$

$$\epsilon_{2,t} - \alpha_2 T = \frac{1}{E_2}(\sigma_{2,t} - \nu_2\sigma_{2,r}) \quad 2\text{-}26$$

where: α_1, α_2 are the coefficient of thermal expansion of phase I and phase II, respectively; ν_1, ν_2 are the Poisson's ratio for phase I and phase II; E_1, E_2 are the elastic modulus for phase I and phase II, respectively.

Based on continuity condition at the interface, i.e., the radial displacement at the interface was the same for both phase I and phase II, the strain was proportional to the radial displacement at $r = a$:

$$\varepsilon_{1,t} = \varepsilon_{2,t} \quad 2\text{-}27$$

Rearranging and solving Equations 2-21 through 2-27 gave the equation for calculating interfacial residual stress as a result of thermal expansion differences between phase I and II: [131]

$$\sigma_a = \frac{(\alpha_2-\alpha_1)\Delta T}{\frac{1-\upsilon_1}{E_1} + \frac{\frac{b^2+a^2}{b^2-a^2}+\upsilon_2}{E_2}} \quad 2\text{-}28$$

where: ΔT is the temperature change.

Applying this model using finite element analysis to different polycrystalline grain-structure arrays concluded that when the intergranular phase had a greater coefficient of thermal expansion than the free standing grain, the intergranular phase and the particle inside were subjected to hydrostatic tension and compression, respectively. In the intergranular phase, the hydrostatic pressure was found less tensile in the multigrain junction regions. The highest tensile component of stresses was shown parallel to the grain boundary and could become compressive in the direction normal to the grain boundary.[131]

2.6.8.2 Modeling of interfacial stresses on two-phase grains structure

Further, the phase boundary stress for a two-dimensional cylindrical system with a core (phase I) and sheath (phase II), as shown in Figure 2-19, was derived as:[133]

$$\sigma_{\varphi m} = \frac{E_k E_m}{E_m(1-\nu_k)+E_k(1-\nu_m)} a\rho^{-2} \qquad 2\text{-}29$$

where: E_k, E_m, are the modulus of elasticity for core and sheath, respectively; α is the dilation difference per unit length between materials of the core and sheath; $\rho = r/R_k$ is the distance r to core radius R_k ratio in a cylindrical coordinates; ν_k, ν_m are the poison's ratio for core and sheath, respectively; α is the dilation difference per unit length between the core and sheath, and $\rho = R_m/r_k$.

2.6.9 Residual stress and compositional analyses by XRD method

In x-ray diffraction (XRD) theory, it was demonstrated that the planar stress σ_ϕ, as illustrated in Figure 2-20 can be calculated as:[134]

$$\varepsilon_\psi = \frac{d_i - d_0}{d_0} = \frac{1+\nu}{E}\sigma_\phi sin^2\psi - \frac{\upsilon}{E}(\sigma_1 + \sigma_2) \quad 2\text{-}30$$

or

$$\sigma_\phi = \frac{E}{2(1+\nu)sin^2\psi} cot\theta(2\theta_n - 2\theta_i) \quad 2\text{-}31$$

or

$$\sigma_\phi = k(2\theta_n - 2\theta_i) = k(\Delta 2\theta) \quad 2\text{-}32$$

where: $k = \frac{E}{2(1+\nu)sin^2\psi} cot\theta$

By measuring the quantity of $(\Delta 2\theta) = (2\theta_n - 2\theta_i)$ the shift in diffraction-line position due to stress as the angle ψ is changed, the planar stress can be calculated.

Quantitative compositional analysis using Rietveld refinement[135] is a whole-pattern fitting method to a multiphase polycrystalline XRD pattern, hence, it requires data and knowledge of all crystal structures in the pattern. It worked particularly well in the case of overlapping peaks by using profile intensities instead of the integrated quantities in the refinement procedure. The principle of the profile refinement method was to minimize the least square residual of function M:[135]

$$M = \sum_i W_i \left\{ y_i(obs) - \frac{1}{c} y_i(calc) \right\}^2 \quad 2\text{-}33$$

where: Σ_i is the sum over the independent observations; W_i is the statistical weight; c is an overall scale factor; y_i(obs) is the intensity observed; and y_i(calc) is the intensity calculated.

Computer programs using the least-squares refinement can be carried out for XRD patterns. For the first cycle of iteration all parameters were required. These were further refined in subsequent refinement cycles until a certain convergence criterion have been reached.[135]

2.7 Evaluation of Cracked FSW PCBN Tool

In many FSW applications, one of the common failure modes of the PCBN (80-20Al) was observed to start as fine cracking on the tool shoulder area.[44] As a part of failure analysis conducted on the cracked PCBN tools, fracture toughness was measured using indentation method with varying loads from 50N to 200N and K_c values measured was rather constant in a given PCBN material. Fracture toughness values from 3.5 to 5.2 $MPa \cdot m^{1/2}$ were obtained. However, the PCBN with a lower fracture toughness value yielded longer tool life, leading to the belief that the fracture toughness value alone was not a determining factor in PCBN's tool life in the FSW processing. [44]

In spite of the only detectable compounds of cBN, AlN, and AlB_2 in the PCBN (80-20Al) before the FSW processing, fractography revealed sizeable liquid Al seeping out during the continued FSW processing in temperatures exceeding 1000°C and the formation of plastic dimple-type of deformation, [44] as shown in Figure 2-21.

As predicted by the Al-B phase diagram, reverse-peritectic decomposition of AlB_2 occurs at temperatures of 980°C or higher:

$$AlB_2 \rightarrow Al_{(l)} + AlB_{12} \qquad 2\text{-}34$$

It was concluded that during FSW process of steels, the PCBN (80-20Al) tool was under mechanical stresses and temperature equal or higher than 1000°C throughout the tooling and resulting in the reverse peritectic reaction and the release of $Al_{(l)}$ led to the dimple type of fracture surface in the PCBN tool.[2, 44]

2.8 Hypothesis for PCBN Cracking in FSW Application

The PCBN tool HP/HT-sintered using 20vol%Al additive for FSW applications was found consisting of AlB_2 as a reacted boride in addition to cBN and AlN. During FSW of steels, temperatures in the PCBN (80-20Al) tools exceeded 1000°C and led to reverse peritectic decomposition of $AlB_2 \rightarrow Al_{(l)} + AlB_{12}$, which caused cracking under the thermo-mechanical loading condition.

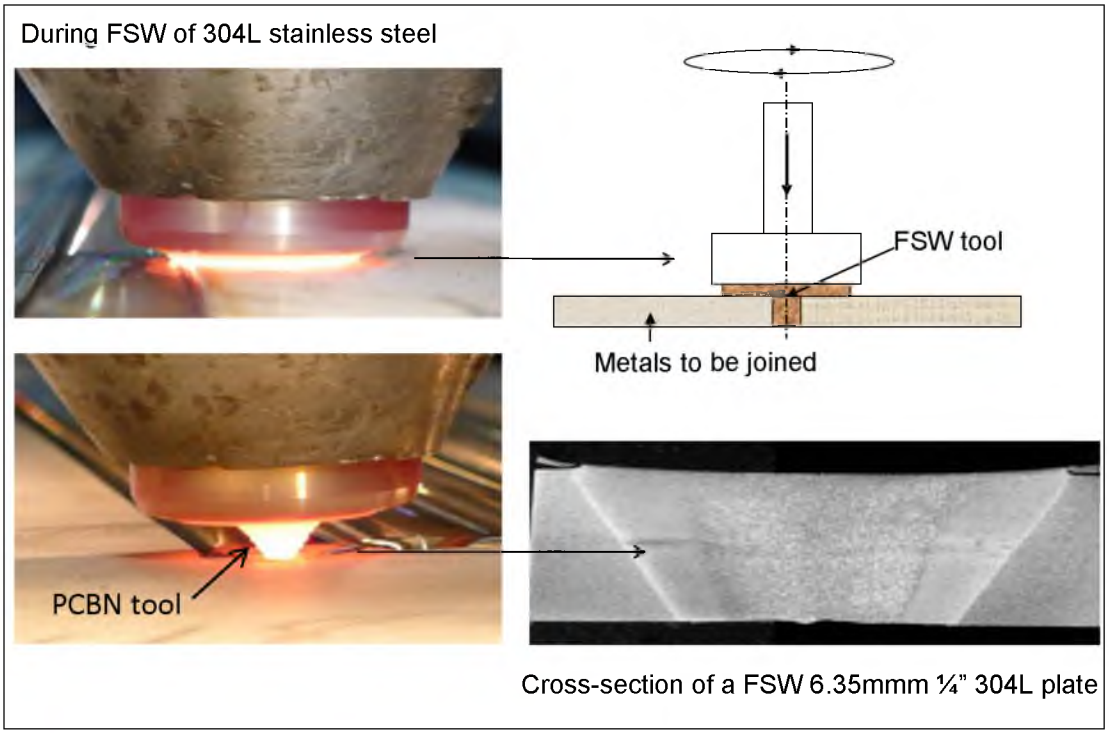

Figure 2-1. FSW ¼" thick 304L stainless steel plate using a PCBN tool

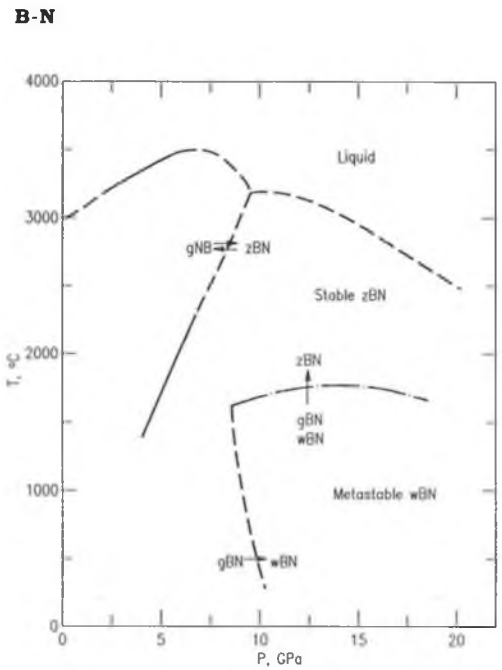

Figure 2-2. P-T phase diagram for B-N, showing graphite (hexagonal) gBN (hBN), zincblende zBN(cBN), and wurzite (wBN) lattice stable regions and conditions. (Reprinted with permission from the Am. Ceram. So., Fig. 8877,[77] originally published by Rapoport, E., Ann. Chim. (Paris). 1[7], 1985, 607-638.)

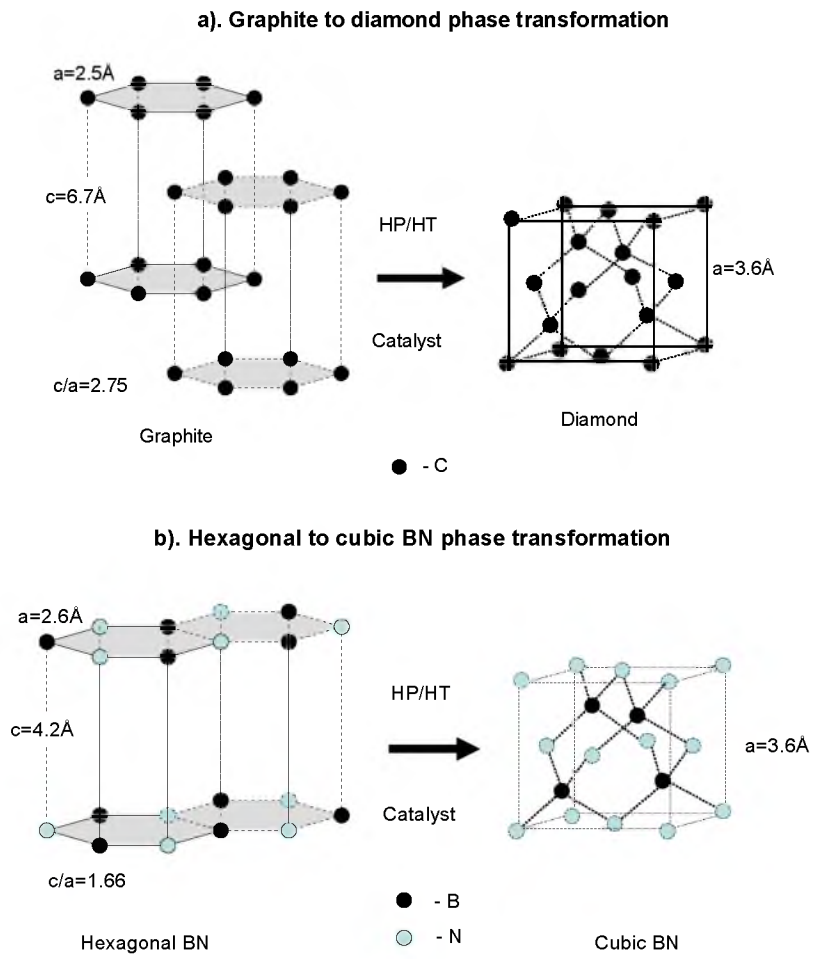

Figure 2-3. Illustration of lattice change: a) from graphite to diamond and b) hBN to cBN.

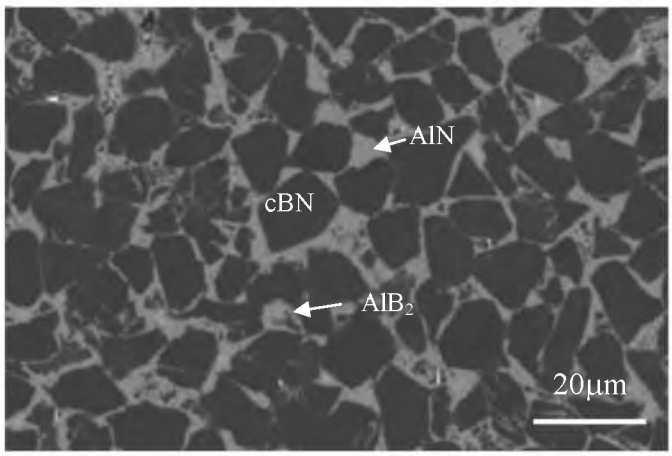

Figure 2-4. PCBN composite HP/HT-sintered using cBN+20vol%Al as a starting powder.

B-N-Al

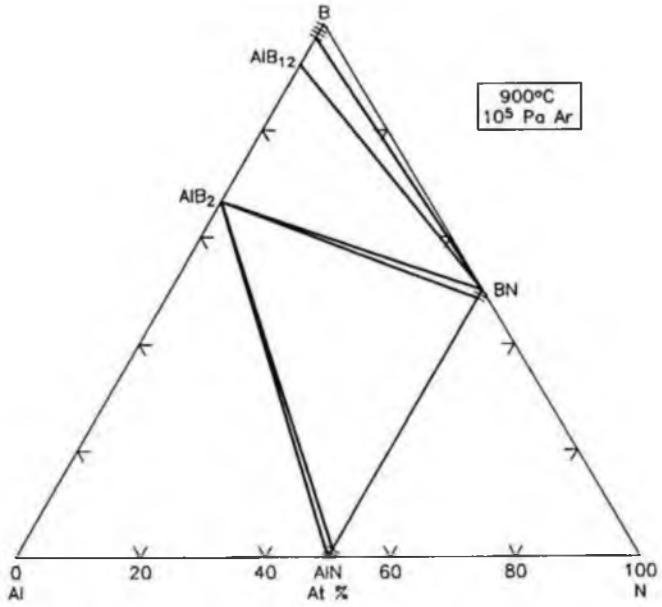

Figure 2-5. B-N-Al phase diagram, at 900°C isothermal section, under 10^5 Pa Ar. (Reprinted with permission from the Am. Ceram. So., Fig. 8880,[77] originally published by Rogl, P. and Schuster, J. C.: Phase Diagram of Ternary Boron Nitride and Silicon Nitride Systems. Monograph Series on Alloy Phase Diagrams, 1992, 3-5. ASM Int'l, Materials Park, OH.)

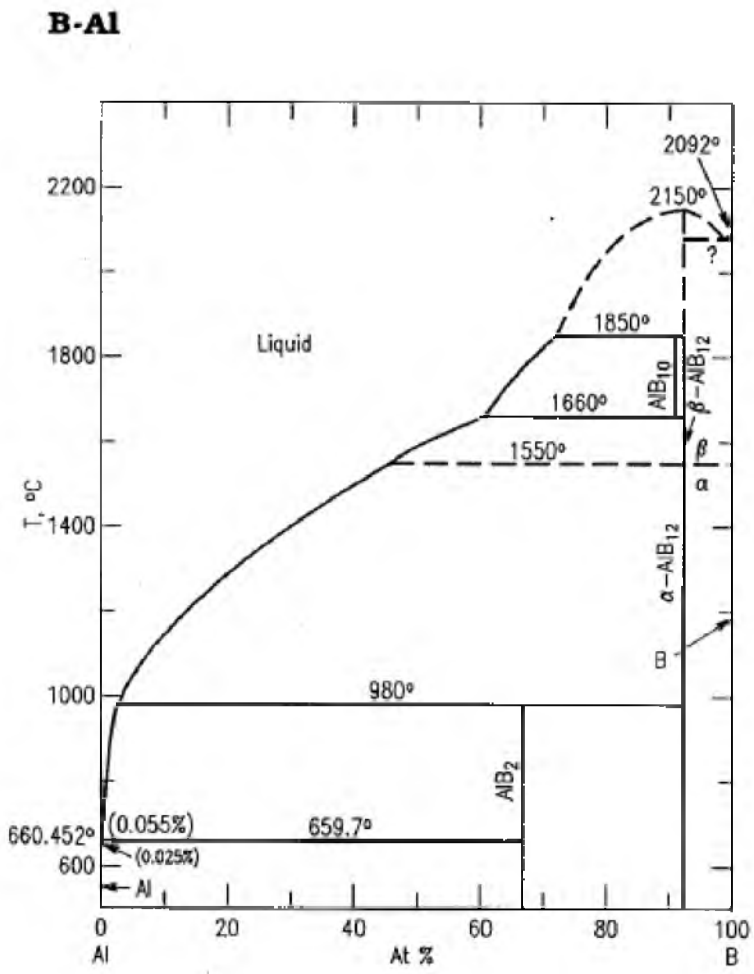

Figure 2-6. B-Al phase diagram. (Reprinted with permission from the Am. Ceram. So., Fig. 8801,[77] originally published by Carlson, O. N. Bull. Alloy Phase Diagrams, 11[6], 1990, 560-566.)

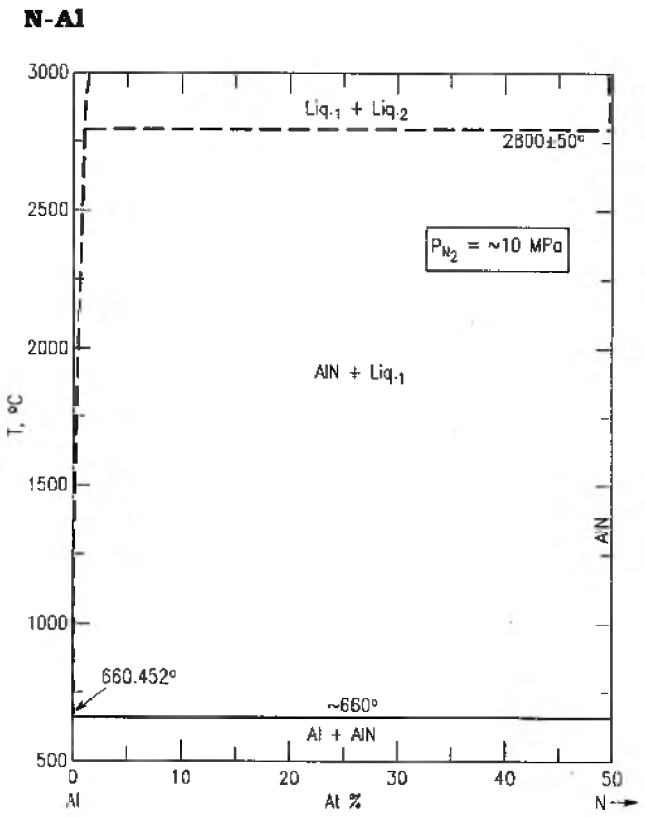

Figure 2-7. N-Al phase diagram. (Reprinted with permission from the Am. Ceram. So., Fig. 9072,[77] originally published by Wriedt, H. A., Bull. Alloy Phase Diagrams, 7[4], 1986, 329-333; 395-396.)

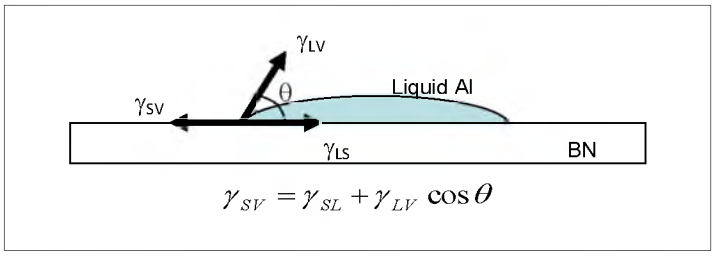

Figure 2-8. Illustration of contact angle of liquid Al wetting on a solid cBN surface.

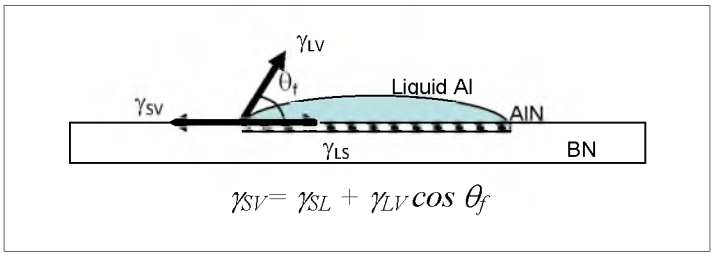

Figure 2-9. Illustration of contact angle of liquid Al wetting on BN considering the fast AlN reaction at the Al-BN interface.

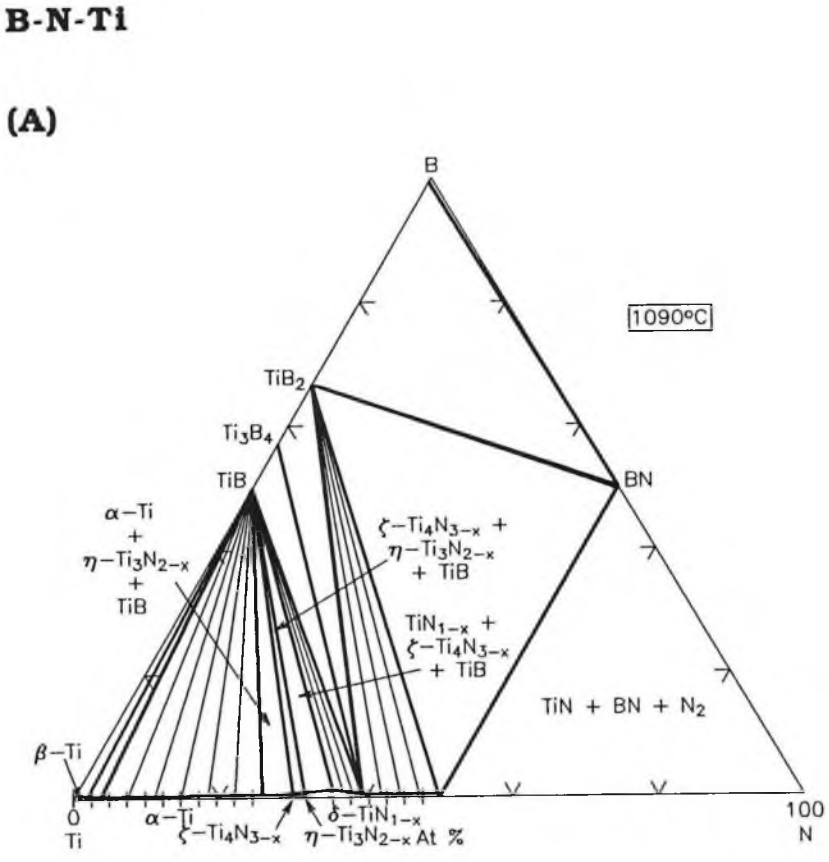

Figure 2-10. B-N-Ti isothermal section at 1090°C. (Reprinted with permission from the Am. Ceram. So., Fig. 8917,[77] originally published by Rogl, P. and Schuster, J. C.: Phase Diagram of Ternary Boron Nitride and Silicon Nitride Systems. Monograph Series on Alloy Phase Diagrams, 1992, 103-106. ASM Int'l, Materials Park, OH.)

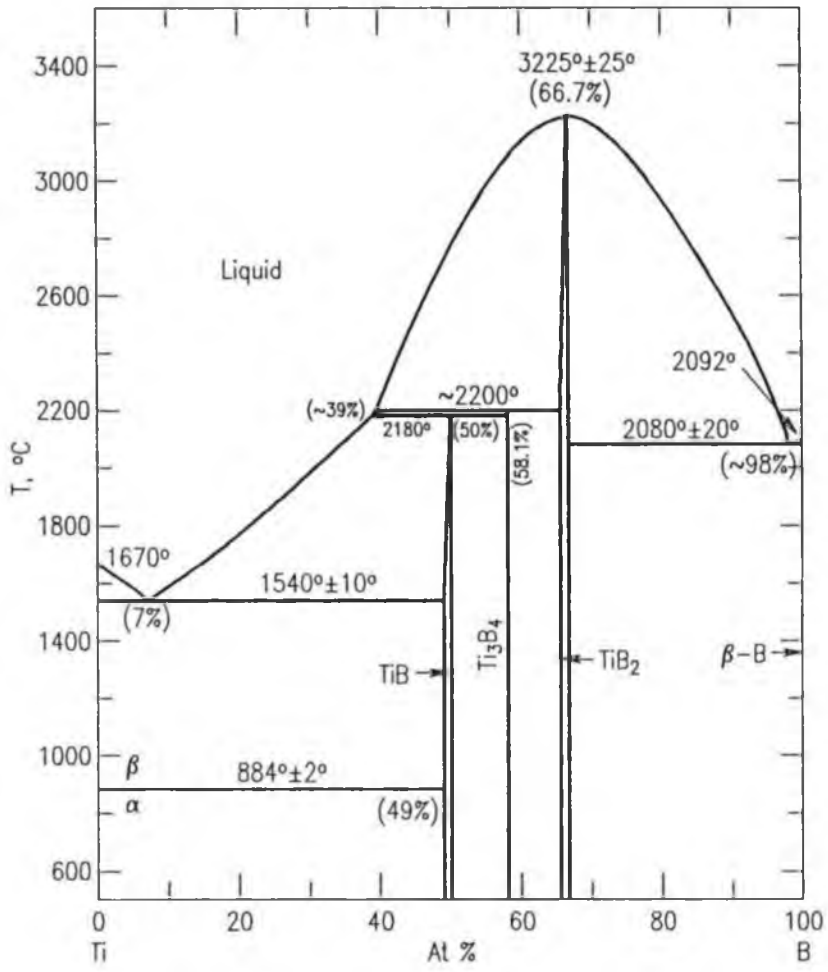

Figure 2-11. B-Ti phase diagram. (Reprinted with permission from the Am. Ceram. So., Fig. 8820,[77] originally published by Murray, J. L.; Liao, P. K.; and Spear, K. E.; Bull. Alloy Phase Diagrams, 7[6] 1986, 550-555; 587-588.)

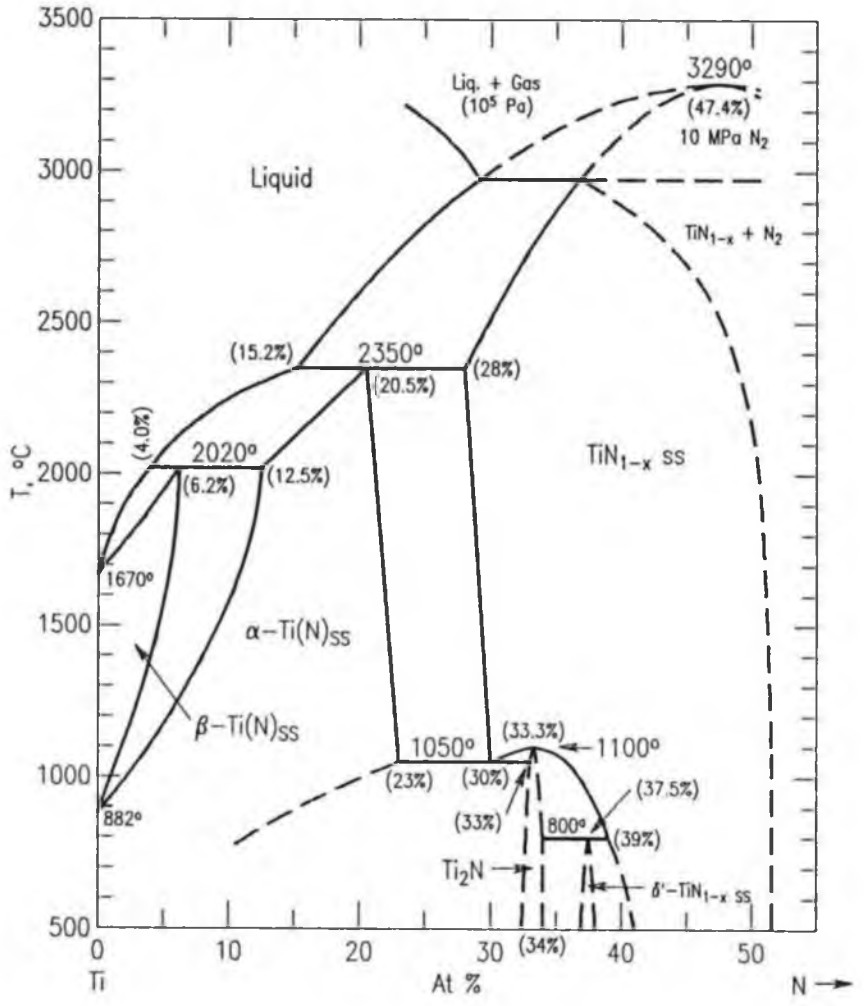

Figure 2-12. N-Ti phase diagram. (Reprinted with permission from the Am. Ceram. So., Fig. 9088,[77] originally published by Wriedt, H. A. and Murray, J. L., Bull. Alloy Phase Diagrams, 8[4], 1987, 378-388.)

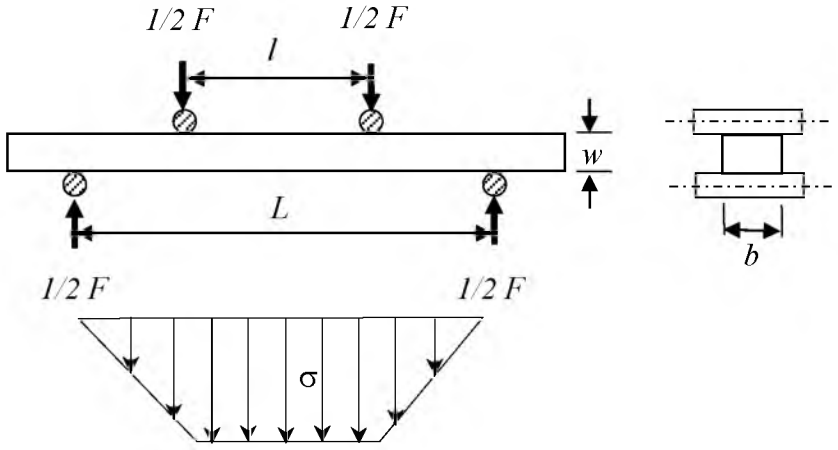

Figure 2-13. Four-point-bend test setup and distribution of maximum fiber tensile-stress.

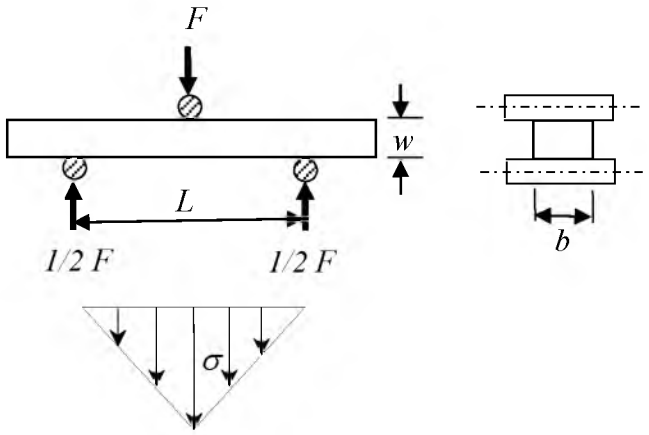

Figure 2-14. Three-point-bend test setup and maximum fiber tensile-stress distribution.

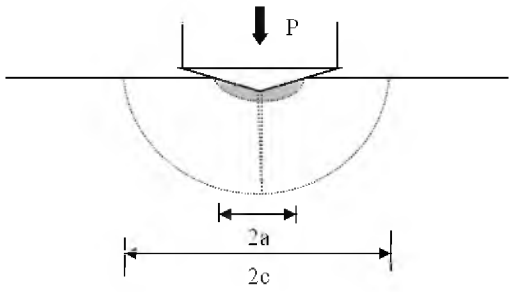

Figure 2-15. Schematic of Vickers indentation test for K_C measurements.

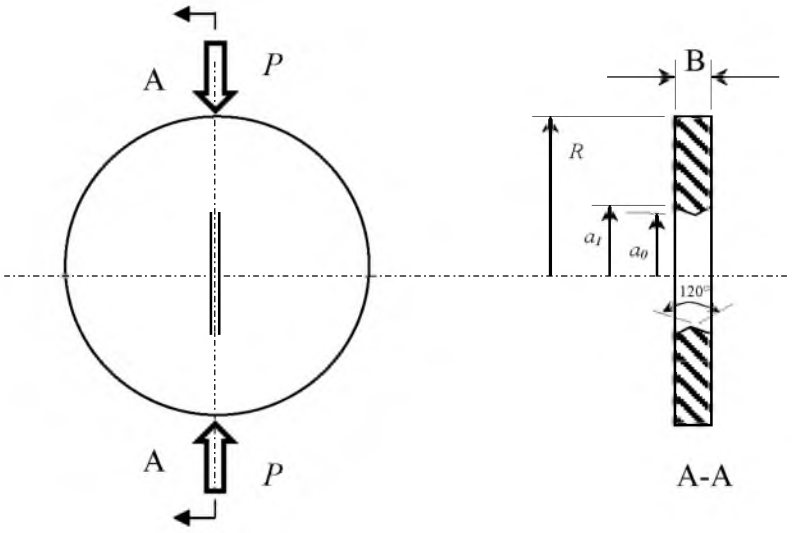

Figure 2-16. Schematic of diametral compression sample with a chevron notched crack pins for fracture toughness test.

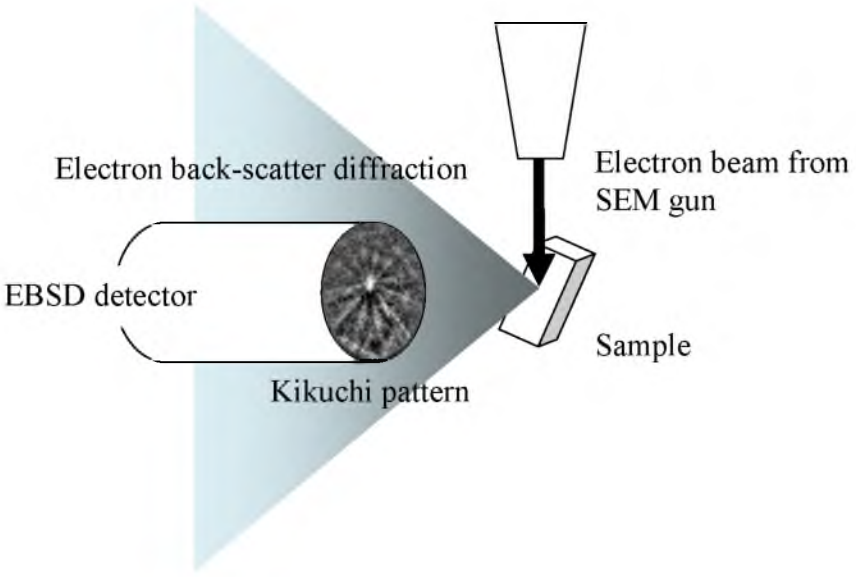

Figure 2-17. Illustration of EBSD (Kikuchi) pattern collected and detected inside a SEM chamber. Modified from the reference.[136]

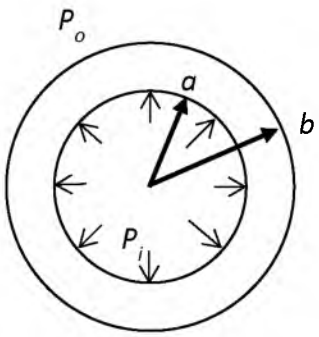

Figure 2-18. A hollow cylinder subjected to uniform pressure on the inner and outer surfaces. Modified from the reference.[131]

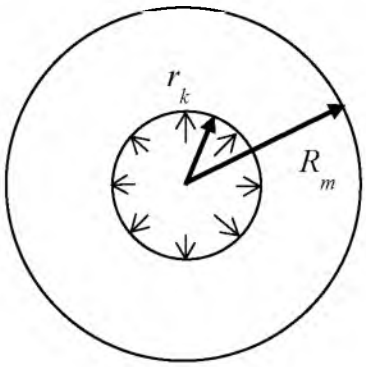

Figure 2-19. Modeling of the dilation effect of a disk surrounded by a cylinder. Modified from the reference.[133]

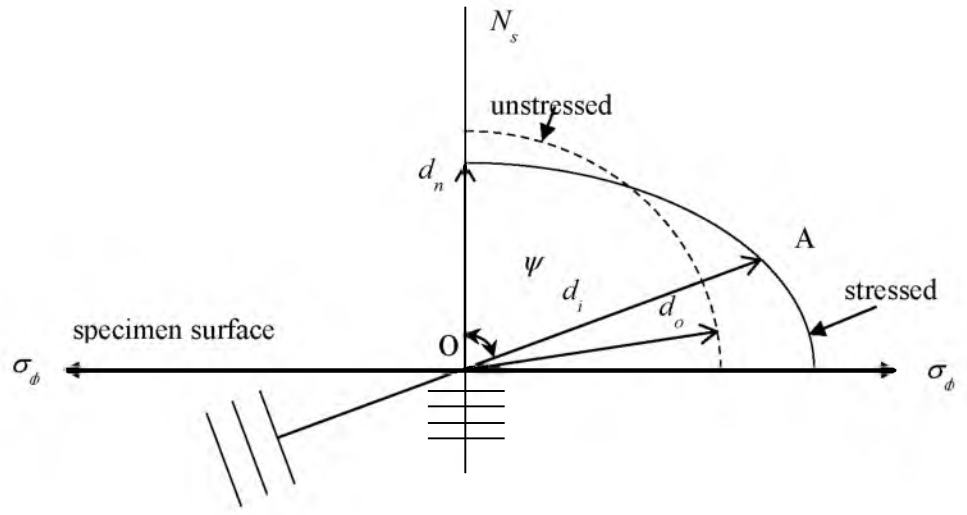

Figure 2-20. Vector diagram of plane spacing of d under a tensile stress σ_ϕ.Modified from the reference. Modified from the reference.[134]

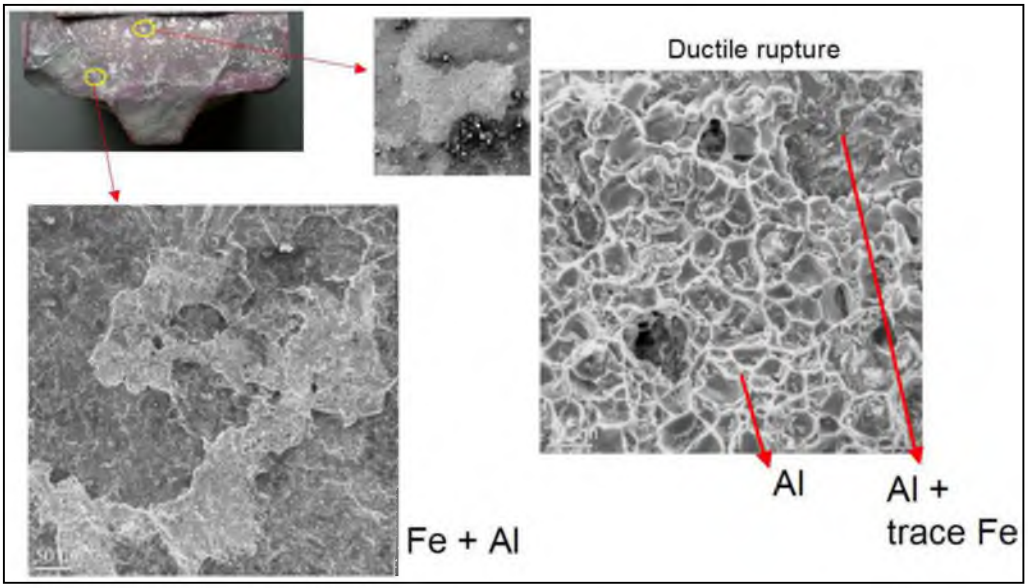

Figure 2-21. SEM image of fractured PCBN (80-20Al) FSW-tool, showing ductile rupture of Al metal. Reprinted with permission from Teledyne Scientific Company as a report for Office of Naval Research. (Marshall, D. B. Reducing Fracture Tendencies in PCBN FSW Tools, Base Effort Final Report for Office of Naval Research, Code 332; Teledyne Scientific and Imaging LLC, Thousand Oaks, CA: July 25, 2010.)[44]

Table 2-1. Typical physical properties of reaction products in PCBN materials. Data collected from the references.[114, 137-142]

Properties	Lattice	ρ	E	σ flex	K_{IC}	HV	T_m	T.C.	α
Unit		g/cc	GPa	MPa	MPa $m^{1/2}$	GPa	°C	$Wm^{-1}K^{-1}$	$10^{-6}K^{-1}$
Diamond (ref.)	*Cubic*	*3.52*	*950*	*1050*	*3.4*	*115*	*3800*	*2200*	*1*
cBN	Cubic	3.49	870	650	5.0 ± 0.5	65	3097	800	1.15
AlB_2	Hex.	3.19	448	-	1.5 ± 0.3	19	980*	-	-
AlB_{12}	Tetra.	2.6	405	-	2.8 ± 0.2	27	2092	5	-
AlN	Hex.	3.20	305	302	4.4	11	2054	110	5
Al_2O_3	Cubic	3.97	393	445	4.0 ± 0.5	21	2047	39	8.4
TiB_2	Hex.	4.52	560	450	6.0 ± 2.0	33	3225	90	6.6
TiN	Cubic	5.4	465	400	5	18	2950	66	9.4
TiO_2	Tetra.	4.25	270	426	6.0 ± 2.0	11	1893	12	8.5

* - Peritectic decomposition and partial melting.

3 RESEARCH SCOPE AND OBJECTIVE

The scope of the present study is to promote the formation of high B to Al ratio and thermally more stable AlB_{12} instead of intermediate AlB_2, as the major boride in PCBN HP/HT-sintered using the cBN+Al system, in order to minimize the effect of AlB_2's decomposition at 980°C. Also to evaluate the validity of utilizing Ti additive to cBN in forming stronger and more stable products of TiN and TiB_2 together with cBN, hence, completely eliminating AlB_2 as a reaction product in the PCBN composite for high temperature applications.

The objectives of the current research are as following:

- to study the effect of HP/HT reactive-sintering of PCBN in the cBN-Al system with reduced Al starting content in minimizing AlB_2 as one of the common reactive sintering products and promote stronger and thermally more stable AlB_{12} in addition to cBN and AlN compounds;
- to evaluate mechanical and thermal properties of the PCBN with decreased initial Al volume and hence the reacted AlB_2 content; for a better understanding of the roles of AlB_2 in the PCBN composites particularly at high temperatures; and
- to study using Ti additive in solid-state HP/HT-sintering of PCBN with stronger TiN and TiB_2 as reactive sintering products in addition to cBN particles, consequently, completely eliminating the possible AlB_2 decomposition in the PCBN at high temperatures in the PCBN composite.

4 EXPERIMENTAL PROCEDURE

4.1 HP/HT Sintering of PCBN Using Al and Ti Additives

4.1.1 cBN grain size and ratio

As the major constituent, cBN particles provide the mechanical strength, thermostability, and abrasion wear resistance which make PCBN composites so unique. To achieve a close particle packing and provide extra reactive sintering sites and surface areas between cBN and additives, a bimodal cBN particle size distribution was employed with the primary particle size of 12-22μ cBN (average size=14.1μ) and secondary particle of 2-4μ, (average size=2.2μ). Both were BMP-400 grade supplied by Diamond Innovations. The size distribution and surface area of cBN powders were measured using Malvern Mastersizer 2000, while the bulk oxygen content was measured with LECO Oxygen Analyzer. The results are summarized in Table 4-1 and pictured in Figure 4-1. The volume ratio of the primary 14.1 μ to the secondary 2.2μ cBN particle in the mix was selected as 9:1.

4.1.2 Al additive to cBN

Pure Al powder (CERAC A-1183), as pictured in Figure 4-2 was selected as the additive to the bimodal cBN mix for liquid-phase-assisted sintering of PCBN. The Al and cBN starting compositions for Mix I are indicated on the ternary phase diagram Figure 4-3 and summarized in Table 4-2.

4.1.3 Approach in promoting AlB_{12} and minimizing AlB_2

The addition of fine 2.2μ cBN powder provided an extra cBN surface area of 79% compared to the 14.1μ alone, as in the baseline PCBN (80-20Al) composition. The purpose was to promote fast alumination reaction of liquid Al to reach high B:Al=12:1 ratio in favor of AlB_{12} formation at high temperatures on cBN surfaces, instead of low B:Al=2:1 ratio. Compared with the baseline 80-20vol%Al mixture, the 90-10vol%Al not only cut the Al vol% by 50% but also increased the B:Al atomic ratio from 2.8:1 to 6.3:1 which would greatly enhance the chance for AlB_{12} formation as well. The amount of Al powder addition was also selected based on the assumption of a complete wetting or coating of Al onto the available cBN grain surfaces upon melting. Based on the measured cBN particle surface areas with a spherical approximation that: $V=\pi/6D^3$, $A=\pi D^2$, and $\rho=W/V$, then the surface area per unit weight of given sized spheres can be calculated as: $A/W=6/(\rho D)$. Following this calculation, if the 10vol% of Al added was fully molten and coating the bimodal cBN grain surfaces, the Al layer thickness would be ranging from 50nm (calculated using the measured areas from the bimodal cBN powders) to 200nm (calculated using the spherical approximation), as summarized in Table 4-3.

4.1.4 Ti additives to cBN

In this study, two methods were experimented with in carrying Ti additive to the bimodal cBN mix: a) adding pure Ti powder and b) starting with Ti-coated cBN grains. The total Ti content was maintained at 10vol% level in the two mixes, as indicated on the B-N-Ti ternary phase diagram in Figure 4-4.

4.1.4.1 Pure Ti powder

In Mix II (cBN+10vol%Ti), pure average diameter of 2.2μ Ti powder (CERAC T-1191) was blended with the bimodal cBN particles in formulating the composition as listed in Table 4-4.

4.1.4.2 Ti-coated cBN

In Mix III, Ti was presented as a uniform coating layer on the coarse cBN powder supplied by Diamond Innovations (12-22μ BMP-Ti), consisting of 15.8wt% Ti-coating with median diameter of 16.3μ. The two types of Ti sources, pure Ti and Ti-coated cBN particles are pictured in Figure 4-5. XRD analysis conducted on the Ti-coated cBN revealed the Ti-coating on the cBN actually was comprised of Ti, TiN, and TiB_2, as shown in Figure 4-6. Similar to Mix I and II, to further react with the relatively thick Ti-containing coating, provide more reaction surfaces, and strengthen the intergranular phases, the 9vol% of 2-4μ cBN was also added to the primary Ti-coated cBN powder in Mix III, as summarized in Table 4-4.

4.1.4.3 Comparison of TiB_2 to AlB_2

Compared with AlB_2, TiB_2 did not display decomposition or melting behavior up to 1500°C in argon in TGA analysis, as shown in Figure 4-7, whereas AlB_2 displayed an endothermic reaction starting at 1001°C corresponding to the reverse-peritectic decompositions, as described in Equation 2-32.

4.2 Powder Mixing

Mixing of cBN and the additives was carried out in a Turbula shaker-mixer (Willy A. Bachofen, AG, Swiss) in a sealed container, without mixing medium, and under protection of Ar gas. This method combines rotational and shaking motions to provide a uniform blending without contamination from mixing media.

4.3 Mixture Reaction Prior to HP/HT Sintering

After the mixing, the three cBN+Al and cBN+Ti mixes were heat-treated at 1000°C for 90 min in 10^{-5} to 10^{-6} Torr vacuum prior to HP/HT sintering to partially react (pre-alloy) elemental Al and Ti with the cBN.[65, 68, 70, 143, 144]

4.4 HP/HT Sintering

4.4.1 Sintering apparatus

A cubic type of press for diamond synthesis, evolved from the original design by Tracy Hall in the late 1950s,[145] was utilized to achieve the high-pressure and high temperature (HP/HT) conditions for PCBN sintering. In the present study, the high pressure was set as constant at approximately 5.5GPa and the temperature varies in the range of 1200 to 1500°C. A schematic cross-sectional view of the sintering cell inside the cubic press[30] is illustrated in Figure 4-8.

In this HP/HT sintering apparatus, the ultrahigh pressure was applied by six simultaneously hydraulic-driven anvils made of cemented tungsten-carbide. The pressure from these anvils was transmitted to the sintering chamber through a ceramic type of gasket material[30, 146] possessing high thermal and electrical insulating properties. After

reaching the set ultrahigh pressure, the high temperature was obtained by resistance heating via high electrical current flowing through the metal conductors and the graphite tube surrounding the enclosed powder-mix assembly. Inside the graphite heating-tube, a pressure transmitting medium of pure NaCl was used to completely surround the refractory-metal enclosed powder-mix for the purpose of achieving a near hydrostatic pressure condition. The sintering temperature was recorded via a thermocouple in contact with the graphite tube throughout HP/HT sintering cycle. Upon completion of the designed sintering time, the temperature was then lowered by decreasing the power input and by strong cooling of the anvils. After the cell was cooled down to close to room temperature, the applied pressure was then gradually decreased to zero, as illustrated in Figure 4-9. Depending on the volume of the powder-mix charge in the cell, multiple PCBN samples can be sintered with each HP/HT cycle.

4.4.2 Sintering pressure

The sintering pressure was selected and kept as a constant in the cBN stable region according to the B-N pressure-temperature phase diagram. Such applied pressure was determined previously on the HP/HT apparatus by converting hBN to cBN using Al as catalyst. The actual pressure for this phase transformation has been reported as higher than 5GPa.[30,39, 147]

4.4.3 Sintering temperature

The effect of sintering temperatures in 1200°C to 1450°C range monitored by Pt/Pt-Rh (Type-R) thermocouple was studied, as listed in Table 4-5, with a constant 15

min of sintering time.

4.4.4 Sintering time

Reactive-sintering kinetic was studied at 1350°C range, while varying sintering time from 2 to 30 min, as shown in Table 4-6.

4.5 Material Evaluation

4.5.1 Microstructure evaluation

After HP/HT sintering, the PCBN samples' microstructure, reacted compounds, and thermostability were evaluated using SEM, XRD, and TGA.

4.5.2 Microstructure and phase identification by EBSD method

Kikuchi patterns generated by electron backscattered-diffraction (EBSD) on polished PCBN samples were collected using a TSL® Orientation Imaging Microscope (OIM) attached to a FEI® Inspect-F field-emission SEM, as displayed in Figure 4-10. At the same time, EDS mapping was also collected by EDAX Genesis Software allowing simultaneously detection of chemical composition and crystallographic patterns.[129, 148] The Kikuchi patterns mapped over the area scanned were further processed and analyzed by OIM Analysis Software for crystallography, inverse pole figures, phase identification, mapping, and grain size measurements.

4.5.3 Mechanical property evaluation

As-HP/HT-sintered PCBN density values were measured using the Archimedes method and compared with theoretically calculated values based on fully reacting the initially added Al and Ti additives with cBN particles. Flexural strength and fracture toughness at room temperature were measured using four-point-bending method and diametral compression method, respectively, on a screw-driven load frame made by Interactive Instrument, as shown in Figure 4-11.

Fracture toughness, K_{IC}, was measured both using Vickers indentation and diametral compression methods. To validate the diametral compression test apparatus and procedure, a commercial grade (TCM 406) of cemented tungsten carbide samples were tested. The cemented carbide was made of mean WC grain size of 4μ and 6wt% Co with a published K_{IC} value[149] of 11.88$MPa{\cdot}m^{1/2}$ tested following the ASTM standard B771-11 (Standard Test Method for Short Rod Fracture Toughness of Cemented Carbides). Applying the diametral compression method on six such cemented-carbide samples returned a mean of K_{IC} = 11.99 $MPa{\cdot}m^{1/2}$, with the range of 11.78 to 12.28 $MPa{\cdot}m^{1/2}$, which produced an excellent agreement with the published value.

4.5.4 High temperature flexural strength and fracture toughness

The PCBN composites' flexural strength and fracture toughness, at 25°C, 900°C and 1100°C, were measured using three-point-bend and diametral compression methods, respectively. These temperatures were selected above and below AlB_2 peritectic reaction and around the predicated temperatures of PCBN tool in FSW 304L steels.[14, 15,16] The high temperature was achieved by resistance heating in a Severn Thermal Solution split-

furnace mounted on a MTS® FlexTest electro-mechanical tester, as shown in Figure 4-12. In order to prevent sample oxidation, the entire furnace chamber was charged with continued Ar gas flow at 20L/min for the net furnace cavity of 1.2L throughout the test. All test samples were weighed before and after the high temperature tests to record the relative weight changes after the testing. Test temperature was monitored and controlled by three thermocouples in three heating zones. The push rods and three-point-bend fixture were all made of high-purity sintered SiC and the holder for fracture toughness test by the diametral compression method was made of a thin sheet of pure 125μm-thick niobium, as pictured in Figure 4-12.

4.5.5 Residual stress measurement by XRD

Planar residual stresses in PCBN before and after flexural strength testing were evaluated using cBN (ICDD 01-089-1498) $hkl=331$ at $d=0.830Å$ and $2\theta=136.41°$ on Rigaku Ultima IV XRD equipment and calculated using Rigaku PDXL-2 software.

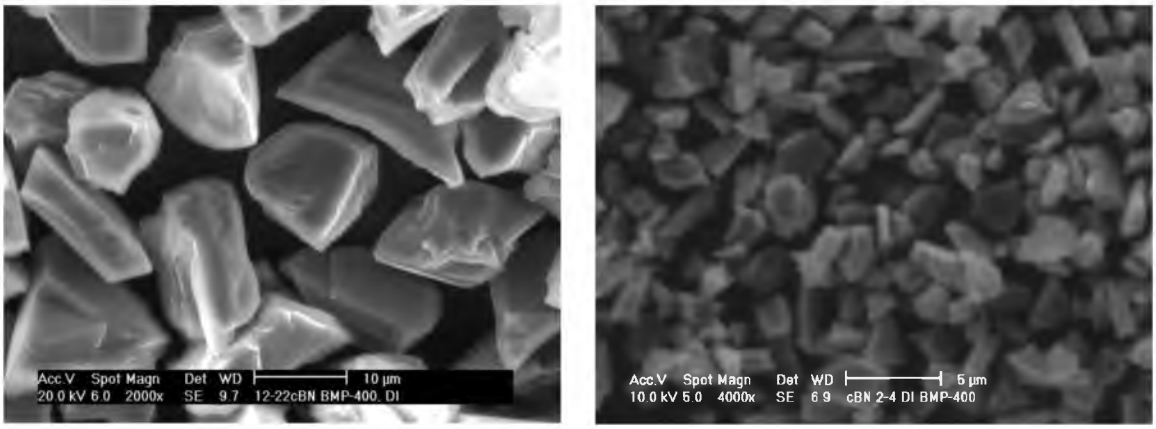

a) b)

Figure 4-1. SEM images of: a) primary 12-22 µ cBN (median=14.1µ) and b) finer 2-4 µ cBN (median=2.2µ) particles; both were BMP-400 grade from Diamond Innovations.

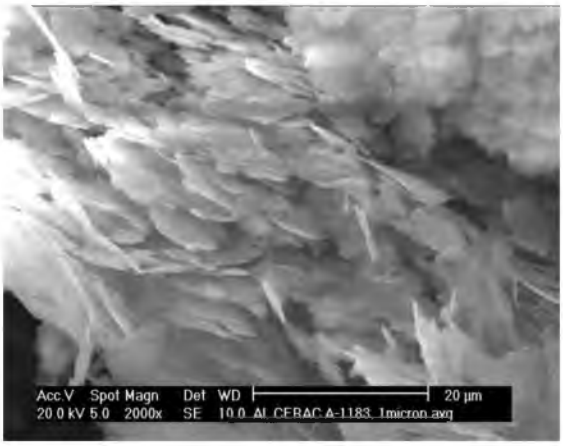

Figure 4-2. Pure Al (CERAC A-1183), as the additive in the cBN+10vl%Al mix.

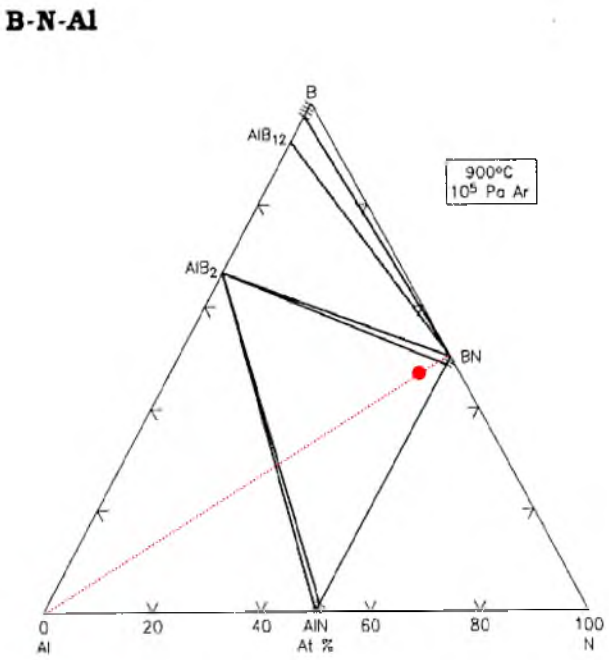

Figure 4-3. The cBN+Al mix composition for HP/HT sintering of the PCBN, as indicated in the Al-B-N system. (Modified from the Am. Ceram. So., Fig. 8880,[77] originally published by Rogl, P. and Schuster, J. C.: Phase Diagram of Ternary Boron Nitride and Silicon Nitride Systems. Monograph Series on Alloy Phase Diagrams, 1992, 3-5. ASM Int'l, Materials Park, OH.)

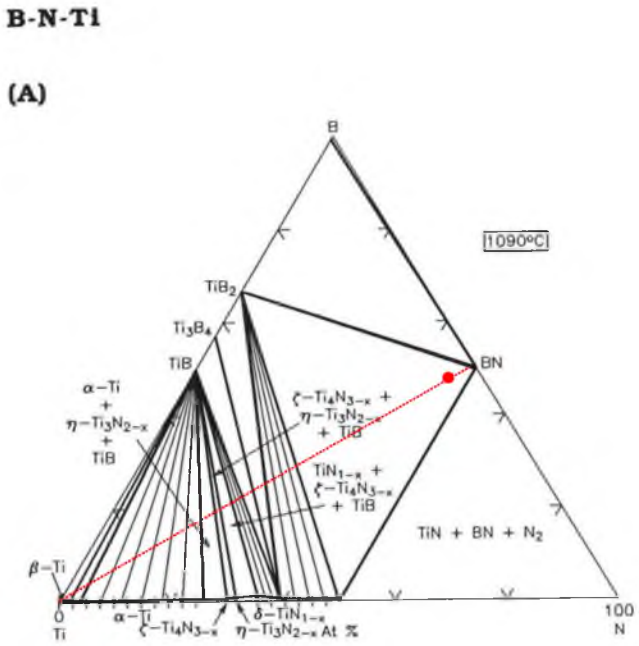

Figure 4-4. The BN+Ti mix composition for HP/HT sintering of the PCBN, as indicated in the B-N-Ti ternary system at 1090°C cross-section. (Modified from the Am. Ceram. So., Fig. 8917,[77] originally published by Rogl, P. and Schuster, J. C.: Phase Diagram of Ternary Boron Nitride and Silicon Nitride Systems. Monograph Series on Alloy Phase Diagrams, 1992, 103-106. ASM Int'l, Materials Park, OH.)

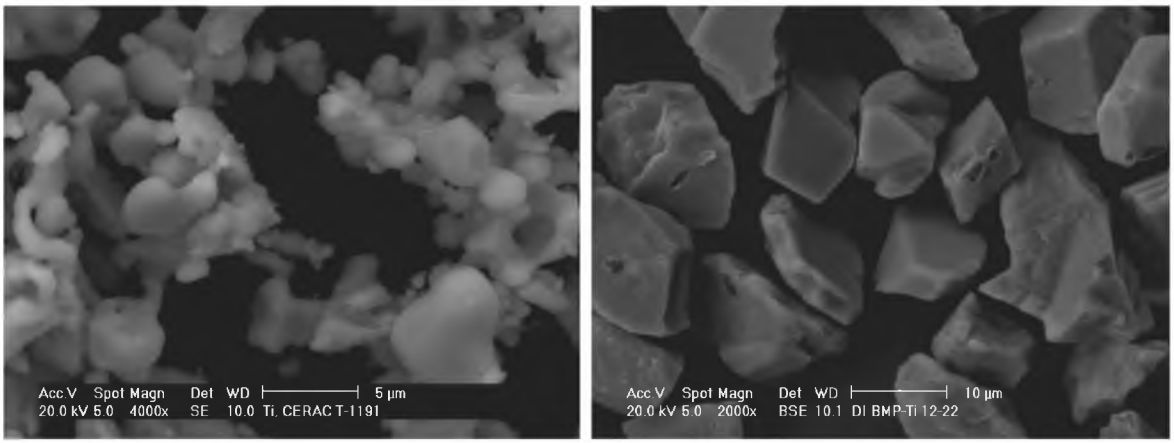

a) b)

Figure 4-5. Image of: a) Ti powder (CERAC T-1191) used in Mix II and b) Ti-coated 12-22µ c-BN (Diamond Innovations, BMP-Ti) used in Mix III.

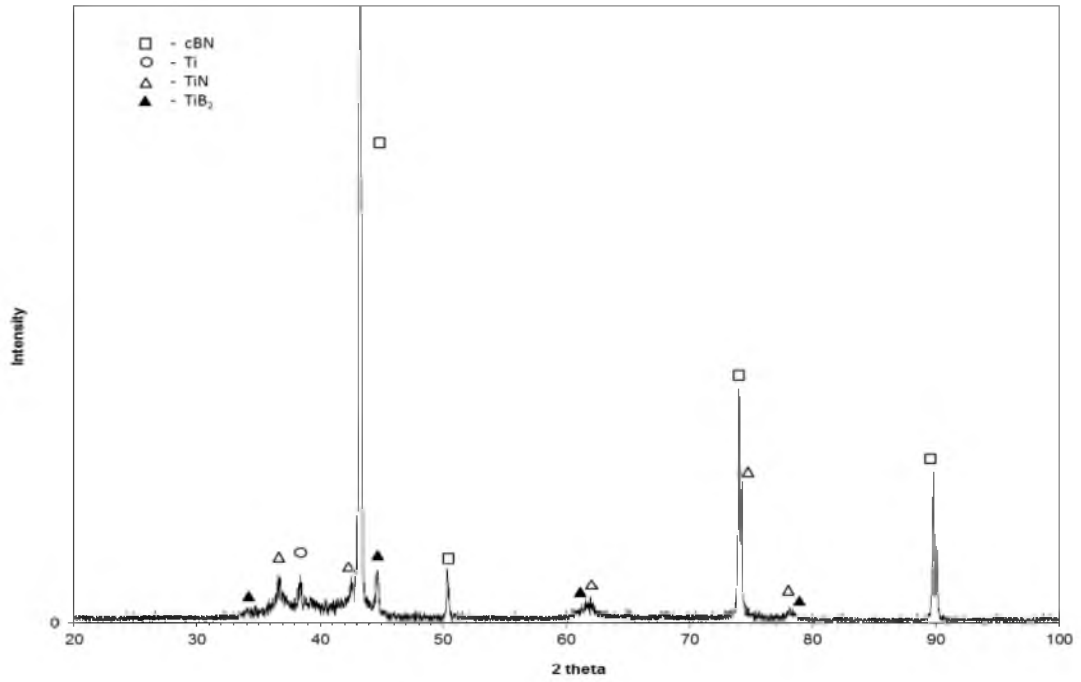

Figure 4-6. XRD pattern collected on the Ti-coated cBN powder (Diamond Innovations BMP 12-22Ti).

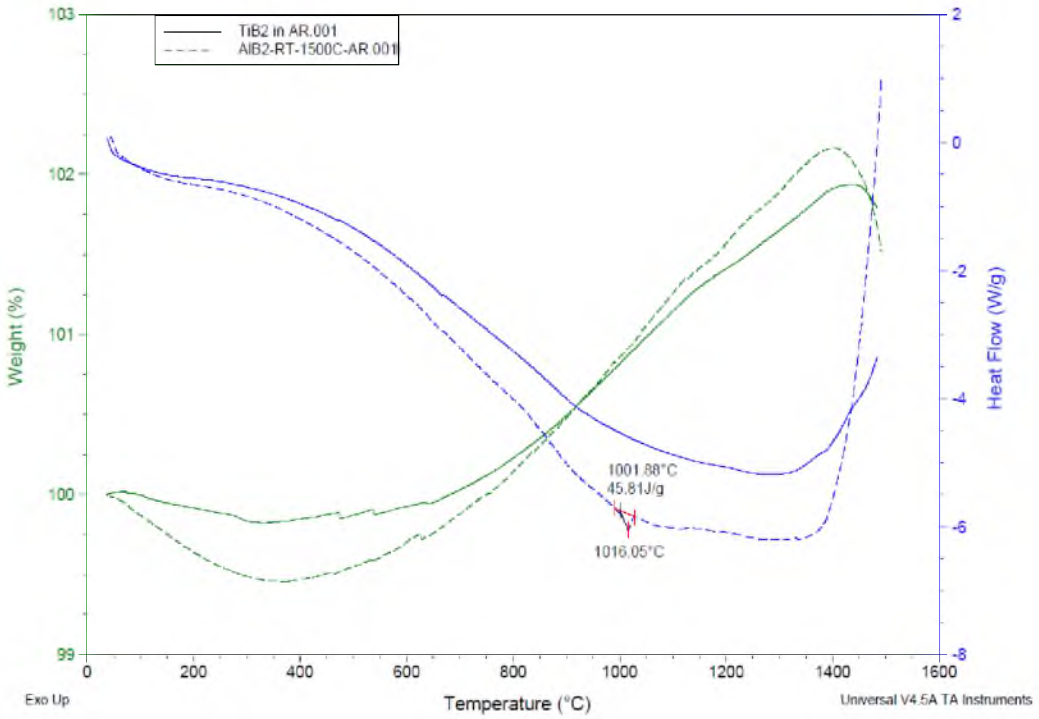

Figure 4-7. TGA response of TiB_2 (CERAC® T12601 -325mesh) and AlB_2 (CERAC® A-1006 -200mesh) powders in argon.

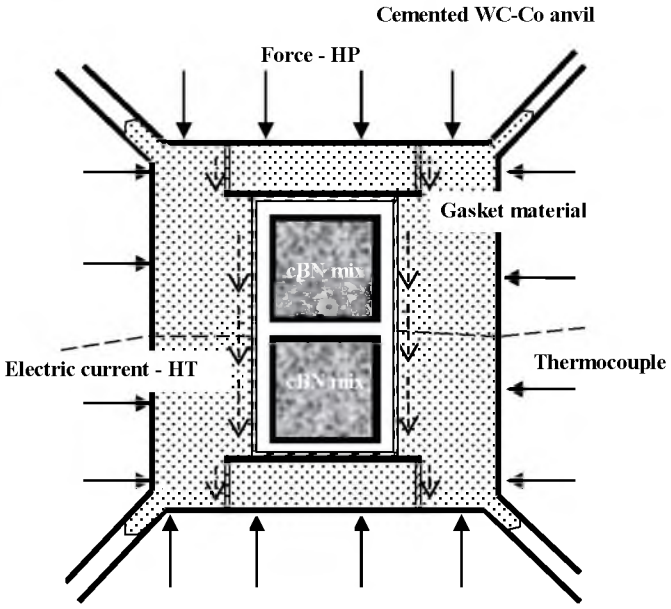

Figure 4-8. Cross-sectional view of a HP/HT-sintering cell configuration in a cubic press for sintering the PCBN.

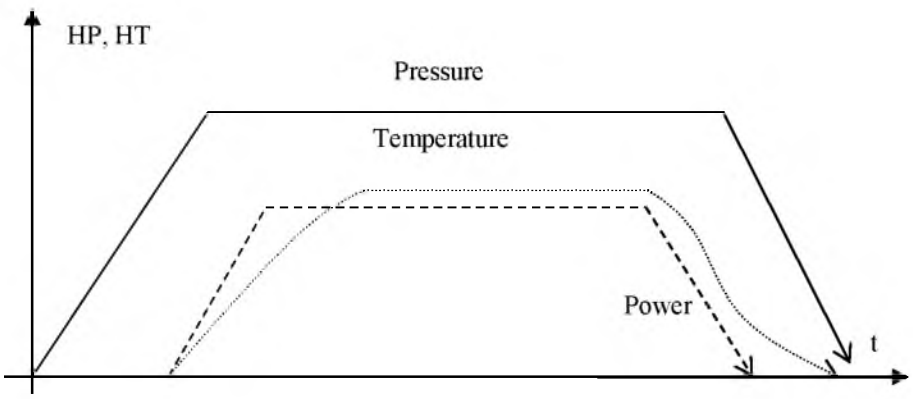

Figure 4-9. Illustration of HP/HT sintering pressure, power inputs, and temperature applied in sintering PCBN composites.

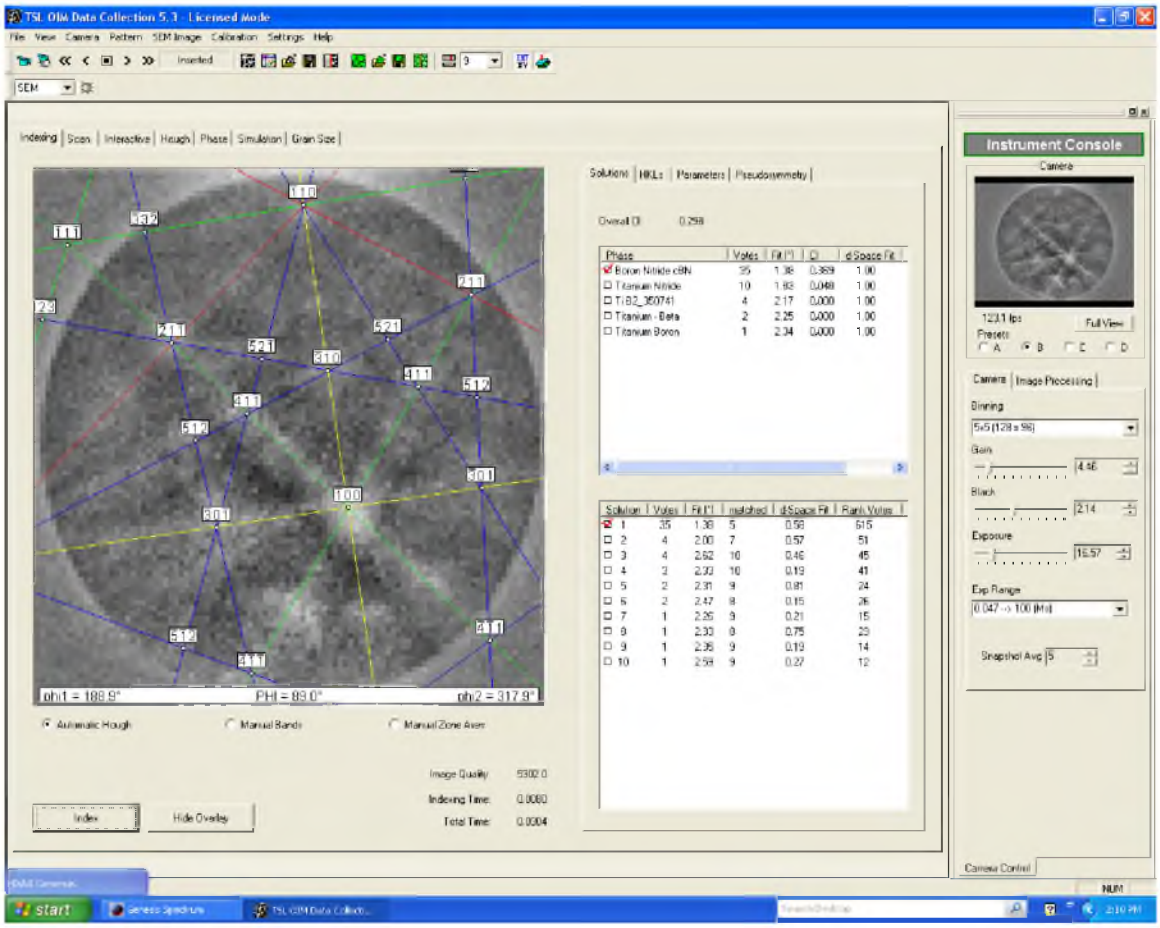

Figure 4-10. TSL® OIM Data Collection software used in identifying Kikuchi patterns generated by EBSD from the PCBN.

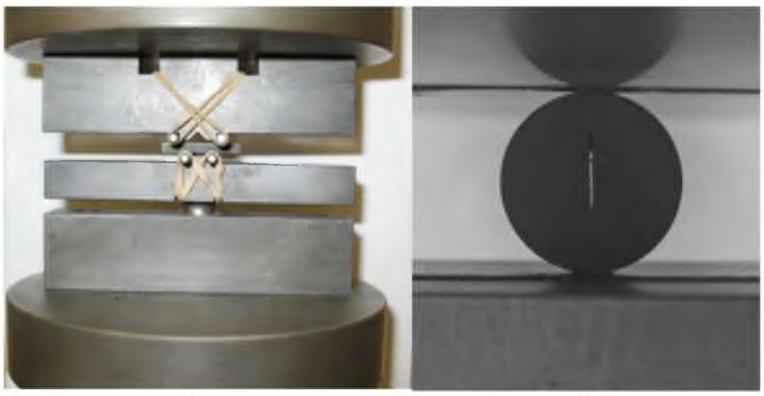

a) b)

Figure 4-11. Test setups of: a) four-point-bend for flexural strength and b) diametral compression for fracture toughness measurements of the PCBN composites.

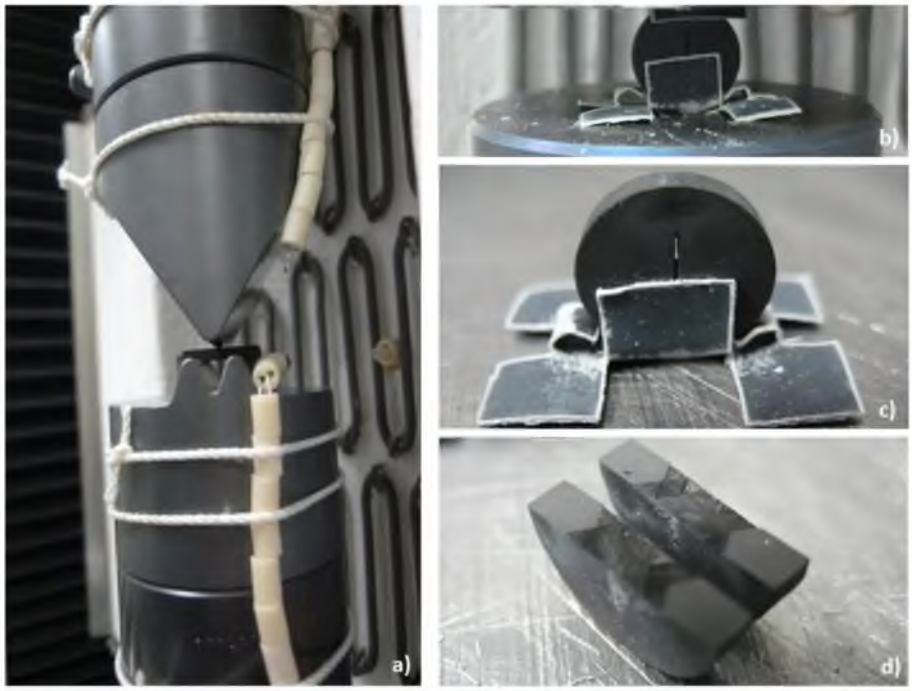

Figure 4-12. The high-temperature testing setup: a) flexural-strength test by three-point-bend method, b) fracture toughness test by diametral compression method, c) and d) a fractured PCBN sample tested at 900°C.

Table 4-1. Characteristics of cBN powder.

Size range	Average diameter (D_{50}%)	Specific area
12-22μ	14.1μ	0.443 m^2/g
2-4μ	2.2μ	2.96 m^2/g

Table 4-2. Composition and properties of starting powders in the cBN+10vo%Al system.

Starting Powder	cBN		Al
Powder Size	D_{50}%=14.1μ	D_{50}%=2.2μ	Typical (~1μ)
Surface Area	0.443m^2/g	2.96m^2/g	-
Bulk Oxygen	0.06wt%	0.2wt%	0.4 wt%
Mix I	81vol%	9vol%	10vol%

Table 4-3. Estimate of Al liquid spreading thickness on cBN surface, in Mix I (cBN+10vol%Al).

	cBN (D50%=14.1μ)	cBN (D50%=2.2μ)	Al (~1μ)	Al coating thickness(nm)
Fraction (vol%)	81	9	10	
Measured (m^2/g)	0.443	2.96	-	50
Spherical approach (m^2/g)	0.122	0.78	-	200

Table 4-4. cBN + Ti additives as starting mixes for PCBN sintering.

Powder	c-BN			Ti
	12-22μ	12-22μ Ti-coated	2-4μ	
	$D_{50\%}$=14.1μ	$D_{50\%}$=16.3μ	$D_{50\%}$=2.2μ	<3μ
Oxygen	0.06wt%	0.6wt%	0.2wt%	4.1wt%
Mix II	81vol%	-	9vol%	10vol%
Mix III	-	91vol (incl. 15.8wt% Ti-coating)	9vol%	-

Table 4-5. Temperature range for HP/HT sintering of PCBN.

Starting mix	1250°C	1300°C	1350°C	1400°C	1450°C
Mix I (cBN+10vol%Al)	x	x	x	x	x
Mix II (cBN+10vol%Ti)	x		x	x	x
Mix III (Ti-coated cBN)	x		x	x	x

Table 4-6. Sintering time for HP/HT sintering of PCBN.

Starting mix	2 min	5 min	10 min	15 min	30 min
Mix I (cBN+10vol%Al)	x	x	x	x	x
Mix II (cBN+10vol%Ti)	x			x	x
Mix III (Ti-coated cBN)	x			x	x

5 RESULT AND DISCUSSION

5.1 Oxidation of Powders Used in Sintering of PCBN

Since the PCBN are used in dry and high speed machining applications such as high-speed turning and FSW, it is important to characterize individual constituent's oxidation behavior.

5.1.1 Oxidation of cBN powder

Thermal and oxidation behaviors of the 12-22μ cBN powder (BMP-400 Diamond Innovations) were evaluated using TA Instrument STD Q600 thermo-gravimetric analyzer (TGA) from room temperature to 1500°C with a 5°C/min heating rate in still air. As shown in Figure 5-1, there was little evidence of oxidation from room temperature up to 1200°C. A strong oxidation and exothermic reaction started from around 1228°C with 4% weight gain up to the peak reaction temperature of 1315°C, followed by a fast 10% weight loss as the temperature increased up to 1500°C.

The TGA result showed that the cBN powder was thermally stable and oxidation resistant up to 1200°C, above which a strong exothermic oxidation-reaction happened in forming B_2O_3[150] reflected by the weight gain. The oxidation of cBN at temperature higher than 1200°C can be summarized in Equation 5-1:

$$2BN + \frac{3}{2}O_2 = B_2O_{3(l)} + N_{2(g)} \qquad 5\text{-}1$$

As temperature continued to rise, intense evaporation of the B_2O_3 and N_2 as well as lattice conversion from cBN to hBN happened and was reflected by the fast and significant specimen weight-loss beyond 1350°C. The solidified remaining glassy B_2O_3 on cBN can be seen on the cBN surface in Figure 5-2 after the TGA test. The evidence of preferential evaporation on some cBN grains was also revealed because of losing N atom from cBN lattice[150] and evaporation of lighter hBN phase.[151] The TGA result of cBN to hBN lattice conversion and fast volatilization agreed well with the reported at 1320°C ± 380°C temperature, depending on cBN's grain sizes and impurities.[29]

5.1.2 Oxidation of AlN powder

The oxidation behavior of AlN powder (CERAC A1120-Mega, -325mesh) was evaluated using TGA from room temperature to 1500°C with a 5°C/min heating rate in still air. The exothermic oxidation reaction,[152] as given in Equation 5-2, started at 1108°C and reached the maximum reaction rate at 1171°C with a significant weight gain up to 1500°C, as shown in Figure 5-3.

$$2AlN + \frac{3}{2}O_2 = Al_2O_3 + N_{2(g)} \qquad 5\text{-}2$$

5.1.3 Oxidation and decomposition of AlB_2

Oxidation of AlB_2 was a complex process without a single control mechanism[153] because of partial molten and peritectic decomposition of AlB_2, oxidation of Al and B to products of Al_2O_3 and B_2O_3, further reaction of Al_2O_3 with B_2O_3 in forming $2Al_2O_3{\cdot}B_2O_3$, and liquidizing followed by vaporizing of B_2O_3, as shown in Figure 5-4.

The decomposition of AlB_2 was measured by TGA in argon, as shown previously in Figure 4-7, with the reverse peritectic decomposition of AlB_2 powder observed to start at 1001°C.

5.1.4 Oxidation of Ti-coated cBN powder

Thermal-oxidation response of the Ti-coated cBN (Diamond Innovations, 12-22μ BMP-Ti) was measured by TGA in still air as well, as shown in Figure 5-5. Contrast to the pure 12-22 μ cBN powder's oxidation response, as displayed in Figure 5-1, two exothermic oxidation reactions were observed starting at above 700°C, 1100°C and were associated with significant weight gains corresponding to oxidation of TiN,[154] pure Ti[155] and TiB_2.[156] The likely reactions are:

$$2TiN + O_2 = 2TiO + N_2 \quad 5\text{-}3$$

$$Ti + O_2 = TiO_2 \quad 5\text{-}4$$

$$TiB_2 + 5/2O_2 = TiO_2 + B_2O_3. \quad 5\text{-}5$$

When temperature reached 1300°C and higher, an exothermic reaction and weight-loss was detected as the bulk cBN particles disintegrated, as shown in Figure 5-1.

5.2 Reactive Sintering PCBN from cBN+Al Powder

5.2.1 cBN+Al reactions prior to HP/HT sintering

In preparation of Mix I (cBN+10vol%Al) as a precursor to HP/HT sintering of PCBN, the mixture was pre-alloying treated at 1000°C for 90 min in 10^{-5} to 10^{-6} Torr vacuum. As shown in Figure 5-6, after the vacuum treatment, simultaneous Al wetting or bonding with multiple fine cBN grains was detected in the mixture and most likely

through the newly formed AlN which was detected by the XRD pattern shown later. Complete wetting or spreading of Al onto large and smooth cBN particle surfaces was not evident partly because the 1000°C temperature was below the reported complete wetting temperature of 1200°C and the existence of surface oxides such as Al_2O_3 on the fine Al powder or B_2O_3 on the cBN surface prevented pure Al's wetting on cBN.[69] There was no detectable amount of AlB_2 or AlB_{12} found in the XRD pattern, which may result from evaporation of highly soluble B in vacuum with liquid Al[157] and, during cooling, there was not sufficient time for B to precipitate and form equilibrium AlB_2.[60]

TGA analysis conducted on Mix I (cBN+10vol%Al) after the pre-alloying displayed a clear endothermic reaction at 660°C corresponding to the melting of residual Al, followed by an immediate weight gain due to oxidation and formation of Al_2O_3, as shown in Figure 5-7. The TGA response in addition to the XRD result, shown later, confirmed the existence of residual elemental Al in the precursor mix after the vacuum treatment, which prepared the cBN+Al mixture for fast partial liquid-phase reactive sintering and contributed to the initial shrinkage due to capillary-induced rearrangement[54] in the HP/HT conditions applied.

5.2.2 Initial high-pressure cold compaction

As an initial step in HP/HT sintering, when Mix I (cBN+10%Al) was subjected to full sintering pressure (5.5 GPa) without heat input, the pre-alloyed Al was observed to be largely compressed and confined to the intergranular spaces of the ultra-hard cBN crystals, as shown in Figure 5-8. The ultrahigh pressure applied also resulted in a significant amount of transgranular cBN cracking which was substantially absent before

the HP cold-compaction. In one location, fracturing was observed between two adjacent large cBN crystals with flat facets caused by small cBN grains slipping in between and acting as point contact for significant bending stresses leading to the fracture in the large crystals.

5.2.3 Effect of HP/HT sintering temperature

5.2.3.1 Effect of sintering temperature on reaction phases

PCBN HP/HT-sintered in 1200°C to 1500°C temperature range with a constant 15 min sintering-time were examined by XRD method. This confirmed the existence of compounds of cBN, AlN, and AlB_{12} as described in Equation 2-9:

$$BN + \frac{13}{12}Al = AlN + \frac{1}{12}AlB_{12}$$

Commonly reported AlB_2 product was not detected, as summarized in Figure 5-9. As a reference, AlB_2 compound's major d-spacing, diffraction peak intensity ratios, *hkl*, and 2θ are listed in Table 5-1. In fact, the strongest diffraction peak of AlB_2 (101) I/I_0=100% was only observed previously in PCBN (80-20Al) when the Al additive was higher.

Peaks corresponding to residual Al in the precursor mix disappeared after sintering at 1245°C for 15 min. The peak intensity ratio of $I_{AlN(100)}/I_{cBN(111)}$ shows a linear increase with rising sintering temperature, as plotted in Figure 5-10. The XRD patterns demonstrated that at sintering temperatures above 1200°C range, Al reacted with cBN in favor of forming large amount of AlN and measurable AlB_{12} with continued reaction and densification up to 1500°C. Because AlN was observed to grow on the cBN surface, which supplied N atoms, the increase of AlN peak intensity reflected a corresponding increasing AlN amount and thickness with the consumption of B and N atoms on the

cBN grain surfaces. The observed growth of AlN and disappearance of pure Al but weak signal of peak height for AlB_{12} suggested that B solution in Al[144] was fast, but AlB_{12} formation was a slow process because of the requirement for B and Al to rearrange in forming complex crystal lattice.[61, 63] The AlB_{12} formed possessed a poor crystallinity because of its complex crystal lattice.

The AlB_{12} detected in the XRD patterns, in addition to EDS spectra and EBSD analyses later, suggested a fast alumination of BN surface by Al liquid to reach high B:Al=12:1 atomic ratio. A ratio that was much higher than the 20-40at% as predicted by the Al-B phase diagram in a closed environment during sintering. Upon fast cooling at 300 to 400°C/min in the end of HP/HT sintering, because of small amount of residual Al liquid available, any AlB_2 precipitated out via the peritectic-reaction would be difficult to detect. As a result, only a small amount of AlB_{12} formed at high temperature was detected by XRD in the PCBN (90-10Al). Based on these findings and the assumption of all Al-added was fully reacted with BN in forming AlN and AlB_{12}, theoretical density of the PCBN was calculated for the reacted cBN+Al system, as predicted by Equation 2-9. Based on this reaction, in PCBN (90-10vol%Al) the initially-added 90vol% cBN particles were partially consumed to 83.5vol%, balanced with newly reacted products of 11.8vol% AlN and 4.6vol% AlB_{12}, as listed in Table 5-2.

5.2.3.2 Effect of sintering temperature on mechanical properties

Mechanical properties including relative density, flexural strength, Vickers hardness, and indentation fracture toughness were measured, with respect to the sintering temperatures in 1250°C to 1500°C range with 15 min sintering time, as displayed in

Figure 5-11. Although increases in relative density and Vickers hardness continued, further increase of flexural strength beyond 1350°C sintering temperature was not observed.

As observed in Figure 5-12, cBN grains are shown mostly surrounded by the reacted AlN and AlB_{12} without substantial cBN to cBN grain contact or bonding. As a result, the crack propagation path induced by Vickers indentation under 294.3N of load was intergranular-dominant through AlN and AlB_{12} region in the PCBN (90-10Al) sample sintered 1350°C for 15 min. Without a substantial cBN-cBN grain bonding or growth, cBN particles' higher strength and fracture toughness over AlN's also favored a cBN-AlN intergranular fracture path, which was more preferred with thickening of the reacted AlN-AlB_{12} phase.

The relatively flat flexural-strength response to the increase of sintering temperatures supported the finding that cracks nucleated and propagated through the intergranular AlN and AlB_{12} layer on cBN crystals. Namely, further increase in sintering temperatures did not change the bonding mechanism from an indirect cBN-AlN-cBN dominant structure to a more direct cBN-cBN bonding structure. To the contrary, as reaction temperature increases, the thickening of AlN as the major reaction product increased leading to less chance for direct cBN-cBN bonding and resulting to a preferred intergranular crack propagation path.

5.2.3.3 Effect of sintering temperature on microstructure

The PCBN (90-10Al) microstructures HP/HT-sintered at different temperatures with constant 15 min time, as compared in Figure 5-13, consisted of individual cBN

grains mostly surrounded by AlN and AlB_{12} phases. At sintering temperature of 1245°C the cBN grain boundaries were more distinct, jagged, and separated with thin and less-well-defined reaction products of AlN and Al-boride with visible cBN internal cracks, as displayed in Figure 5-13 a) and b). At 1350°C, as shown in Figure 5-13 c) and d), the cBN grain boundaries became smoother and separated by well-defined reaction phases, although some of the cBN internal cracks were still visible. At 1490°C, the microstructure showed smoother cBN grain boundaries with well-defined reaction phases while some cBN internal cracks still remained, as shown in Figure 5-13 e) and f). The increased amount of reaction products of AlN and AlB_{12} on the cBN grain boundaries, as detected by XRD and microstructures, may be accountable for the observed drop in fracture toughness values with increase of sintering temperatures, because of the lower fracture toughness values of the thickening intergranular phase.

5.2.4 Effect of HP/HT sintering time

5.2.4.1 Effect of sintering time on reaction phases

XRD patterns collected on HP/HT-sintered PCBN using the pre-alloyed Mix I (cBN+10vol%Al) revealed the disappearing of Al peaks after merely 2 min sintering time and presence of low intensity peaks corresponding to AlB_{12} in the 1350°C range, as summarized in Figure 5-14. This showed the quick reaction kinetic of Al's wetting and reacting to cBN resulting in AlN; solution of B into Al; and continued formation of AlB_{12} largely happened during the first 2 min of sintering in the 1350°C range. The intensity ratio of $I_{AlN(100)}/I_{cBN(111)}$, revealed a slight increase with sintering time, as shown in Figure 5-15, but the response was not as significant as observed with raising the temperatures'

suggesting the reactive sintering was more responsive to sintering temperatures than time.

5.2.4.2 Effect of sintering time on mechanical properties

As plotted in Figure 5-16, in spite of detecting AlN and AlB_{12} formation after 2 min of HP/HT sintering time, most significant increases in relative density, Vickers hardness, and flexural strength were measured in samples up to 20 min sintering time. This suggests a continued cBN densification and reaction with sintering time as liquid Al was consumed. As the sintering time extended from 20 to 30 min, further increase of the mechanical properties was not obtained.

5.2.4.3 Effect of sintering time on microstructures

Typical microstructures of the PCBN (90-10Al) sintered from 2 to 30 min in the 1350°C range are displayed in Figure 5-17. In the fields of a) and b) of the PCBN with 2 min sintering time, pools of B-rich Al-solution are visible, as indicated by the arrows, revealing transient stage of the reactions $Al+12B=AlB_{12}$ on the jagged and porous cBN grain boundaries. Such B-rich Al-solution was further minimized in samples sintered with 15 min and 30 min as more stoichiometric AlB_{12} compound was crystalized.

The intra-cBN-cracking and discontinuities resulting from the initial cold HP-compaction were more pronounced in the 2 min sintered sample and became less with increase of sintering time to 30 min. This suggests such discontinuities were further cured with sintering time. Compared to the 2 min sintered sample, the 15 min sintered sample displays smoother cBN grain boundaries and more AlN and AlB_{12} formation on the grain boundaries, as shown in Figure 5-17 c) and d). Further increase of the sintering time to 30

min seemed to reduce the cBN internal cracks and discontinuities even more, as shown in Figure 5-17 e) and f). The 30 min sintered microstructure shows reduced pores and discontinuities on cBN grain boundaries but did not show to increase cBN to cBN grain contact or direct bonding.

5.2.5 Formation of AlB_{12} in PCBN (cBN+10vol%Al)

The SEM image, as displayed in Figure 5-18, shows a structure of AlN surrounding cBN grains and AlB_{12} concentrated in pockets enclosed by AlN, as detected by EDS listed in Table 5-3.

Compared to the baseline PCBN (80-20Al) using single modal cBN (D_{50}=14.1μ), the 9vol% addition of fine cBN (D_{50}=2.2μ) in the PCBN (90-10Al) mixture provided an extra source of B and N atoms in facilitating fast forming AlN on cBN particle surfaces. It also increased the chance for metalizing (alumination) by liquid Al onto cBN surfaces to reach the B:Al=12:1 ratio required for AlB_{12} nucleation, instead of AlB_2. Following the AlB_{12} formation close to the cBN surfaces, AlB_2 is likely to form in Al liquid phase a further distance from the cBN surface where the lower B:Al=2:1 ratio is easily reached.

X-ray line-scan conducted across the cBN grain boundary region, as shown in Figure 5-19, revealed the intensity of Al, B, and N from a cBN-AlN-AlB_{12}-AlN-cBN grain boundary structure. It was also noticeable that higher O and Al intensities detected at the cBN grain boundaries between cBN and AlN indicated Al_2O_3 formed by reducing of B_2O_3 on the cBN grain boundaries.

In Mix I (cBN+10vol%Al), the 10vol%Al added was equivalent to 7.9wt%Al into the cBN mix. Based on Equation 2-9, if the initially added 7.9wt% of Al was completely

reacted in forming AlN and AlB_{12}, 0.61wt%Al would be combined with B in reacting to 3.52wt% of AlB_{12} in the final PCBN (90-10Al) composition.

Following Al-B phase diagram and the Mix I (90-10vol%Al) composition, as shown in Figure 5-20, using rule of lever at T=1350°C, for example, the ratio of $Al_{(l)}$:AlB_{12}=15.7:84.3 existed in an equilibrium condition. As the 90cBN+10vo%Al composition cooled down to just above 980°C, the liquid fraction shrank to $Al_{(l)}$:AlB_{12} = 13.5:86.5. At T = 980°C, the peritectic reaction $Al_{(l)} + AlB_{12} \rightarrow AlB_2$ happened and led to complete consumption of $Al_{(l)}$ in forming AlB_2. At T $\leq$ 980°C, with the Mix I (90-10vol%Al) composition, there should be no liquid Al phase remaining but solid phase of AlB_{12} and little AlB_2, as summarized in Table 5-4. The final reaction products were then calculated as: 0.02wt% of AlB_2 and 3.47wt% of AlB_{12}, in the Al-B binary system, in addition to 10.17wt% of AlN balanced with cBN in the HP/HT sintered PCBN, as summarized in Table 5-5. Due to its poor crystallinity[61] and small quantity, AlB_{12} peaks appeared very weak in the XRD pattern collected on PCBN (90-10Al) HP/HT sintered at 1350°C for 15 min, as shown in Figure 5-21. Quantitative Rietveld analysis revealed the PCBN (90-10Al) consisting of cBN=87.8wt%, AlN=8.6wt%, and AlB_2=3.6wt%, which agreed well with the quantities calculated by the lever rule.

5.2.6 Reaction products in PCBN (cBN+Al) determined by EBSD method

5.2.6.1 EBSD results on the PCBN sintered at 1245°C

Results of electron backscattered-diffraction (EBSD) analysis on the PCBN (90-10Al), HP/HT-sintered at 1245°C for 15 min, are displayed in Figure 5-22. The orientation mapping of all phases and their inverse pole figures, as presented in Figure

5-23, did not reveal particular preferred orientation of all the phases detected. Area fractions of reaction phases identified in the field were listed in Table 5-6.

Because the field of analysis was highly localized, the exact area fractions of the phases identified may not match the bulk quantities calculated, measured by density, and detected by XRD later in the PCBN (90-10Al). A small quantity (0.5vol%) of isolated and fine AlB_2 precipitates were detected, mostly scattered among the AlN and AlB_{12} matrix with a few observed in contacting cBN surfaces. The inverse pole figure mapping, as shown in Figure 5-23, revealed some transgranular fracturing within cBN grains identified by different crystal-lattice orientations otherwise difficult to distinguish solely based on the SEM image. Minor cBN lattice distortions reflecting the crystal lattice distortions were detected within some of the large grains reflected by the slight variation in the color shades from grain boundary to the center of cBN. As expected, the rotation angles on the grain boundaries were much larger, 5° and higher, than the intragranluar twist angles (mostly 2° to 5°) within cBN grains. Such small twist and gradual change in lattice orientation angles within cBN grains was the result of high residual stresses between contacting cBN crystals during HP/HT sintering. The EBSD analysis together with the XRD results validated the dominant chemical reaction initially described in Equation 2-9 for PCBN sintered using the cBN+10vol%Al system at 1245°C for 15 min.

As shown in Figure 5-24, identified by the crystal lattice differences, the reactive sintering products of AlN, AlB_2, and AlB_{12} were fine and submicron-sized rather than a continuous layer in the cBN intergranular regions. The identification of the reactions phases were assisted by the simultaneously collected x-ray elemental mapping of B, N, and Al, as shown in Figure 5-25.

5.2.6.2 EBSD results on the PCBN sintered at 1420°C

To evaluate the effect of sintering temperature in forming AlB_{12} and AlB_2, EBSD was also conducted on PCBN sample sintered at 1420°C for 15 min using Mix I (90-10vol%Al). The result still revealed the existence of AlB_2 at about 0.6% by area fraction together with a slight decrease in total cBN area fraction, as shown in Figure 5-26 through Figure 5-29. This confirmed the difficulty in completely eliminating the AlB_2 which precipitated as the last liquid Al solution solidified via the peritectic reaction at 980°C and lower. The EBSD result also showed increased amounts of AlN and AlB_{12} associated with the consumption of cBN, as summarized in Table 5-7, which corresponds to the intensity increase of AlN peaks in XRD patterns and supported the continued reactions between cBN and Al-added.

Undetected by XRD and SEM imaging methods, EBSD was able to differentiate, by crystal lattice differences, approximately 0.5% area fraction of AlB_2 existing in PCBN HP/HT sintered in 1245°C and 1420°C for 15 min, as a result of the peritectic reaction during cooling through 980°C. The grain sizes of the reaction products of AlN, AlB_{12} and the small quantity of AlB_2 determined by crystal lattices were mostly in the submicron range, as shown in Figure 5-24 and Figure 5-28. Such fine and inter-cBN-granular phases provided grainboundary channels for liquid Al to metalize the cBN surfaces, instead of diffusing through a continuous AlN layer to reach the cBN surfaces. The polycrystalline particle nature of the micron-sized AlN particles were not as dense and uniform of a layer surrounding the cBN grains as previously observed by SEM and TEM.[85] Distributions of B, N, Al, and O simultaneously mapped by EDS in the field of analysis are shown in Figure 5-25 and Figure 5-29, and were considered and referenced in the phase

identification. In the small areas analyzed, increased area fractions of AlN and AlB_{12} were detected in the grain boundary areas with the sintering temperature increased from 1245°C to 1420°C under 15 min of sintering time, indicating a continued reaction. The locations where AlB_2 particles were detected indicated last solidification spots of boron-containing Al solution.

5.2.7 Stability of the PCBN in high temperature exposure

Thermostability of the PCBN (90-10Al) was evaluated at 1000°C for 300 min holding time using TGA in argon. Possible decomposition of AlB_2 into AlB_{12} and liquid Al was not detected during the prolonged exposure at 1000°C, which was just above the reverse peritectic decomposition temperature. Approximately, 1% weight gain owing to oxidation was picked up during the TGA test, as shown in Figure 5-30.

The thermostability of the PCBN (90-10Al) on a 25mm diameter and 3.2mm thick sample was heat-treated at 925°C for 90 min and then again at 1000°C for 90 min in vacuum, respectively. XRD patterns conducted on the heat-treated sample, as shown in Figure 5-31, did not reveal detectable peaks of AlB_2 or pure Al. Such high temperature heat treating of PCBN sample at the temperatures below and above peritectic temperature of 980°C demonstrates the thermostability of the AlB_{12} and insignificant or slow reaction kinetic of the reverse peritectic reaction from about 0.5vol% of $AlB_2 \rightarrow AlB_{12}+Al_{(l)}$ solution. Although, at low intensity the peaks corresponding to AlB_{12} seemed to be more distinguishable after the 1000°C heat cycle indicating its increased crystallinity. These results demonstrated the PCBN (90-10Al) was thermally stable at temperatures up to 1000°C without a detectable quantity of reverse peritectic reaction of AlB_2.

5.3 Reactive Sintering PCBN from cBN+Ti Powder

5.3.1 cBN+Ti reactions prior to HP/HT sintering

Parallel to the cBN+10vol%Al experiment, Mix II (cBN+10vol%Ti), consisting of the bimodal cBN and Ti powder additive, was pre-alloyed in vacuum at 1000°C for 90 min as a precursor for HP/HT-sintering into PCBN. Compounds of $TiN_{0.3}$ and TiB_2 were detected in the XRD pattern collected on the pre-alloyed mixture, as displayed in Figure-5-32.

5.3.2 Effects of HP/HT sintering temperature

5.3.2.1 Effect of sintering temperature on reaction phases

XRD patterns collected on the PCBN sample HP/HT sintered from mid-1200°C to low 1400°C temperatures using Mix II (cBN+10vol%Ti) revealed the complete disappearance of the sub-stoichiometric $TiN_{0.3}$ from the pre-alloyed mix and replacement by more balanced TiN, as shown in Figure-5-32. After sintering, increases in intensity ratios of both $I_{TiN(111)}/I_{cBN(111)}$ and $I_{TiB2(100)}/I_{cBN(111)}$ with rising temperatures suggest the reactions' temperature-activated diffusion process, as plotted in Figure 5-33. The HP/HT sintering was carried out simultaneously inside the same HP/HT cell with the PCBN (90-10Al) mix. The sintering temperatures studied were all below the melting point of pure Ti (T_m=1660°C).

The reaction was shown to start with enrichment of N, released from cBN, to the $TiN_{0.3}$ towards more stoichiometric TiN. At the same time, available B atoms formed TiB_2. The combined reactions, in the B-N-Ti system studied, were confirmed as predicated by Equation 2-10:

$$BN + \frac{3}{2}Ti = TiN + \frac{1}{2}TiB_2$$

A trace amount of hBN was detected in samples sintered at temperatures higher than 1350°C with 15 min sintering time. This suggests that some cBN lattice underwent the transformation from cubic to hexagonal, as observed in the TGA test on the raw cBN crystals. This occurred because some of the cBN particle surfaces were not completely surrounded by hydrostatic pressure supposedly supplied by soft and fine Ti powder, as observed in the microstructures later. Such undesirable cBN to hBN lattice transformation was likely caused by high melting temperature of Ti and difficulties in spreading the Ti powder evenly to cover the cBN surfaces which can otherwise be achieved by spreading liquid Al at same the sintering temperatures. However, such cBN to hBN conversion was not observed in the PCBN (cBN+10Ti) sintered at 1245°C for 15 min. This indicates the stability of cubic lattice of cBN crystals under such temperature and sintering time as predicated by the P-T phase diagram of BN, previously shown in Figure 2-2. In the XRD patterns, broadening of the cBN peaks were observed suggesting varying degree of high residual stresses[158, 159] in the cBN grains, resultant of the 5.5GPa applied high pressure. Such broadening from the initial powder mixture to sintered PCBN was less apparent in XRD patterns from the cBN+Al mix. This reflects the cBN+Ti mix's more rigid packing, less cBN slipping, and high residual stresses stored in the cBN crystals in the HP/HT sintering conditions due to lack of the liquid-assisted sintering.

5.3.2.2 Effect of sintering temperature on microstrcutres

Microstructure of PCBN sintered using MIX II (cBN+10vol%Ti) powder, as displayed in Figure 5-34, shows uneven spreading of Ti powder on cBN grain surfaces

led to a large degree of voids and dry compaction of cBN particles in many places in the temperature range of 1245°C to 1420°C with 15 min sintering time. These were locations of cBN to hBN lattice transformation, due to lack of hydrostatic pressure surrounding the cBN grains, at temperatures higher than 1350°C as detected by the XRD.

Compared to cBN with Al as additive, PCBN sintered with Ti powder showed: a) lack of a high degree of densification from the liquid-phase-assisted sintering by Al; b) appearance of hBN at temperatures higher than 1350°C; and c) a large amount of porosity found up to 1420°C temperature.

5.3.2.3 Reaction products in PCBN sintered from cBN+Ti

In the cBN grain boundary areas that cBN and Ti reacted in PCBN sintered at 1350°C for 15 min, as shown in Figure 5-35, the TiB2 was observed to be mostly fine needle-shaped growing out of the cBN surfaces with submicron-sized TiN particles spreading out as a TiN matrix among cBN particles.

The microstructure evaluations showed that the reactions between the pure Ti powder and cBN grains were solid state in nature, which did not match the liquid-phase-assisted sintering results, in the temperature and time range studied. To promote a uniform dispersion of pure Ti among cBN grains and in situ cBN+Ti reactions, submicron-sized Ti powder would be a better candidate. Because of the difficulties in achieving high densifications, further study of using Ti powder as a starting powder for PCBN sintering was not pursued.

5.4 Reactively Sintering PCBN from Ti-coated cBN

5.4.1 Ti-coated cBN reactions prior to HP/HT sintering

As an alternative to the pure Ti powder, the Ti-coated 12-22μ cBN powder was used as a uniformly distributed Ti source for PCBN sintering. XRD conducted on the Ti-coated cBN particles showed the coating layer consisting of Ti, TiN, and TiB_2 instead of pure Ti as suggested by the commercial grade name. After adding 9vol% of 2.2μ pure cBN powder and following the vacuum pre-reaction at 1000°C for 90 min, Mix III (Ti-coated cBN) showed a mixture of loose powder with adhesions of small pure cBN to the large Ti-coated cBN particles at some locations, as observed in Figure 5-36. As evident by XRD patterns later, Ti on the cBN coating surface was mostly consumed in forming new TiN and TiB_2 during the pre-alloying in vacuum, which was done as a precursor prior to HP/HT sintering.

5.4.2 Initial high pressure cold compaction

After being subjected to ultrahigh pressure compaction (5.5GPa) without heat input, Mix III (Ti-coated cBN) showed highly-compacted cBN grains with some transgranular cracking; sticking of fine cBN particles to the large coated cBN; and rubbing-off of the Ti-coating layer from some cBN surfaces. The Ti-coating layer thickness was measured directly on the fractured cBN crystals in the order of 150 to 250nm, as shown in Figure 5-37. It is also noticeable that the Ti-coating on cBN particles seemed to be made of nano-sized granular structure.

5.4.3 Effects of HP/HT sintering temperature

5.4.3.1 Effect of sintering temperature on reaction phases

XRD patterns collected on PCBN HP/HT-sintered with the pre-alloyed Mix III (Ti-coated cBN) displayed reactive products of cBN, TiN, TiB_2, and trace amounts of Ti_2O_3 at different sintering temperatures, as shown in Figure 5-38. The intensity ratios of $I_{TiN(111)}/I_{cBN(111)}$ and $I_{TiB2(100)}/I_{cBN(111)}$, plotted in Figure 5-39, illustrated the reactive sintering products' significant response to sintering temperature. This is characteristic of the temperature activated diffusion process.

5.4.3.2 Effect of sintering temperature on mechanical properties

The relative density and flexural strength measured on PCBN using Mix III (Ti-coated-cBN) showed a significant increase from 1250°C to 1350°C with 15 min sintering time, but rather horizontal beyond 1350°C, indicating the reaction as described in Equation 2-10 was largely completed at temperatures higher than 1350°C with 15 min sintering time. Compared with the porous microstructure from the PCBN starting with the pure Ti powder, a remarkably high relative density and packing of the large Ti-coated cBN particles were achieved under the same HP/HT sintering conditions although without assistance of liquid phase Al.

The fracture toughness measured by Vickers indentation method decreased noticeably with increase of sintering temperature, as shown in Figure 5-40 d). This reflected the continued reactions between metallic Ti and cBN and formation of harder ceramic TiB_2 and TiN particles on cBN grain boundaries associated with further consumption and separation of the cBN particles. Both led to PCBN's lower overall

toughness values. The mode of crack propagation induced by the Vickers indentation method at 294N was observed as a mixed mode of intergranular and transgranular, through cBN/TiB_2-TiN grain boundaries and through cBN grains in some places, as shown in Figure 5-41. The large field of view shows that all cBN grains were well-packed and separated by a rather uniform coating layer consisting of reacted TiN and TiB_2 with little cBN to cBN grain bonding or growth.

5.4.3.3 Effect of sintering temperature on microstrcutres

Compared to directly adding Ti powder to cBN particulates, highly close-packed large cBN particles were observed with little evidence of grain boundary porosity in PCBN using Mix III consisting of Ti-coated cBN with addition of fine and pure cBN powder, as shown in Figure 5-42. All cBN grains were uniformly surrounded with approximately 1μ or less coating layer consisting of cBN-Ti reaction products, which may act as a low-viscosity sintering lubricant allowing the large cBN particles to slip and pack without significant crushing with 15 min sintering time. Benefiting from the uniform coating and packing, no cBN to hBN lattice reverse transformation was detected by the XRD patterns in the 1245°C to 1420°C temperature range. The finer 2.2μ pure cBN-added seemed to fill in the spaces among the large coated-cBN particles and reacted with the coating consisting initially Ti and $TiN_{0.3}$ in forming stable and stoichiometric TiN and TiB_2 products. Some microfracturing and discontinuities inside cBN grains, resulting from the initial HP cold compaction, were still visible in the PCBN sintered at 1245°C. Such discontinuities were more cured in the samples sintered at 1350°C and particularly at 1420°C, which showed the least cBN internal cracks. With these findings

and the assumption that all Ti, existing as a part of coating on cBN particles, had been fully-reacted with B and N atoms in forming TiN and TiB_2, the PCBN's theoretical density value was then calculated.

5.4.4 Effects of HP/HT sintering time

5.4.4.1 Effect of sintering time on reaction phases

XRD patterns collected on PCBN starting with the pre-alloyed Mix III (Ti-coated cBN) sintered at 2 min, 15 min, and 30 min at 1350°C range displayed reaction products of TiN, TiB_2, and a trace of Ti_2O_3, as shown in Figure 5-43. However, the peak intensity ratios of $I_{TiN(111)}/I_{cBN(111)}$ and $I_{TiB2(100)}/I_{cBN(111)}$, as plotted in Figure 5-44, were rather unchanged with the sintering temperatures studied. Namely, reactions between cBN and the Ti-containing coating layer, as described in Equation 2-10, were more responsive to the sintering temperature than sintering time which, again, was characteristic of diffusion controlled reaction process.

5.4.4.2 Effect of sintering time on mechanical properties

Similar to the reaction compounds' XRD peak intensities, the PCBN's relative density, Vickers hardness, flexural strength, and indentation fracture toughness, as plotted in Figure 5-45, did not show significant changes with respect to the sintering time from 2 to 30 min at 1350°C temperature range. These showed that the reactions between cBN and the Ti-containing coating as described in Equation 2-14 proceeded with fast kinetics at the temperature.

5.4.4.3 Effect of sintering time on microstrcutres

The microstructure of the PCBN sample, with 2 min sintering time using the Ti-coated cBN, exhibited some internal cracks and discontinuities that were not cured with the short sintering time at 1350°C temperature range, as shown in Figure 5-46 a) and b). The appearance of such discontinuities was reduced noticeably after 15 min sintering time and was even less in the sample sintered with 30 min time. The reaction products of TiN and TiB_2 on the cBN grain surfaces seemed to increase with sintering time from 2 min to 30 min, as indicated by the well-defined and thickening layer on the cBN grain boundaries. Although, increase in relative density and mechanical properties with sintering time were not measured. The fracture toughness values of K_c measured by Vickers indentation method showed a very slight decrease with increase of sintering time instead of the significant decline with increase in sintering temperature. Rather flat responses of TiN and TiB_2 to cBN intensity ratios with increase of sintering time were detected, as shown in Figure 5-44.

5.4.4.4 Reaction phases in PCBN sintered using Ti-coated cBN

Detailed interaction between the Ti-coating and cBN grains in the PCBN HP/HT-reacted at 1350°C for 2 min is displayed in Figure 5-47 and reveals a mixture of TiB_2 (dark grey) visible inside the TiN matrix. It is different than what was observed in the cBN+Ti powder system in that the fine TiB_2 formed directly on the cBN surfaces and TiN particles spread in the cBN grain boundary spaces, as shown in Figure 5-35. It was because the Ti-coating layer on the cBN powder consists of a large amount of TiN initially, before the HP/HT sintering, as shown in Figure 5-43. The 9vol% of 2.2μ pure

cBN added into the Ti-coated 16.3μ cBN provided new sources of B and N for in situ reactions with the Ti-containing coating by reducing the diffusion distance for B and N atoms migrating in the Ti matrix to reach stoichiometric concentration, thereby, providing conditions for faster reaction kinetics.

The results of x-ray diffraction, microstructure, and XRD showed that all Ti coating on cBN particles were fully reacted with cBN in forming TiN and TiB_2 phases. Such reactions consumed part of the starting cBN from 88.5vol% down to 85.8vol% in Mix III (Ti-coated16.3cBN+9vol%2.2cBN), as listed in Table 5-8. Based on these numbers, the theoretical density of the PCBN using Mix III (Ti-coated cBN) was calculated.

Quantitative composition analysis with Rietveld refinement on the XRD pattern collected on sintered PCBN (Ti-coated cBN), as shown in Figure 5-48, resulted in a higher TiN content and TiN:TiB_2 more than 2:1. This was attributed to the initial TiN that existed in the as received Ti-coated cBN particles. The reaction products in PCBN (Ti-coated cBN) were determined by the EBSD method.

EBSD results on PCBN HP/HT-sintered at 1350°C for 15 min using Mix III (Ti-coated cBN) are displayed in Figure 5-49, and show reaction products of TiN and TiB_2 among cBN particles with the phase area ratios listed in Table 5-9. Although lattice structure and parameter of TiB was also included in the EBSD scan, it did not detect any measureable quantity in the field analyzed. Both TiN and TiB_2 were observed in contact with cBN grain boundaries. Minor crystal lattice distortions and strains were observed in large cBN grains reflected by the slight variation in the color shades and high density 2-5° rotation angles from grain boundary to the center. Identification of cBN, TiN, and

TiB_2 lattices and crystal structures again verified the reaction as described in Equation 2-10.

All compounds detected in the field did not exhibit a preferred orientation, as revealed by the orientation mapping and inverse pole figure in Figure 5-50. Submicron-sized TiN particles were observed to form a matrix dispersed with fine TiB_2 particles, as distinguished by the crystal lattice as well as orientation differences as displayed in Figure 5-51. The EBSD analysis revealed that the uniform Ti-containing coating on cBN surfaces, after HP/HT sintering, was reacted to produce mostly submicron TiN and TiB_2 particles, which provided direct and faster grain boundary diffusion channels for B and N atoms to diffuse into the remaining Ti instead of through the TiB_2 or TiN particles. The x-ray mapping of the elements collected simultaneously with the EBSD scan is displayed in Figure 5-52 and was used in EBSD data processing.

5.5 PCBN Sintering Mechanism

5.5.1 cBN+Al system

5.5.1.1 Initial cBN+Al powder reactions prior to HP/HT sintering

During the pre-alloying treatment at 1000°C for 90 min in vacuum, the molten Al should react with cBN to form AlN and Al-boride, however, besides cBN and AlN, there was no detectable amount of AlB_2 or AlB_{12} in the mixture after the vacuum treatment. This indicated that light B atoms dissolved from the cBN surface, traveled through the liquid Al and volatilized with some of the liquid Al at 1000°C in the 10^{-5} to 10^{-6} Torr vacuum before being cooled down to solidify as AlB_2 from the Al-B solution. Under the vacuum and 1000°C temperature, wetting of liquid Al to cBN surface and the reaction

product of AlN were observed to be localized and discontinuous on the cBN particle surfaces before HP/HT sintering.

5.5.1.2 cBN+Al reactions during PCBN sintering

Microscopically, upon heating in the initial stage of HP/HT sintering Al started melting and wetting of the cBN surfaces followed by breaking of N-B bonds, dissolving of B and reacting between Al with N atoms. Stable solid AlN was immediately formed on the cBN surface because of the near insolubility of N in liquid Al, at the same time, Al liquid metalizing of BN happened at temperatures higher than 980°C leading to AlB_{12} formation. As identified by the EBSD analysis, the AlN formed was found to be fine and polycrystalline in nature and not as a continuous layer as previously thought. This enhanced continued B enrichment coming off the cBN surface and contacting by Al liquid via the fast AlN grain-boundaries transportation, instead of much slower diffusion through solid AlN lattice. Such process is illustrated in Figure 5-53 using a simplified cBN-Al contact-surface reaction model.

At temperatures higher than 660°C and time at t_1, Al liquid started to form on the cBN and the cBN-Al interface consisted of cBN and $Al_{(l)}$ containing B and N. AlN forms immediately after the N:Al=1:1 ratio is satisfied. As the temperature increased to 980°C at time of t_2, AlB_{12} start to form at a molecular ratio of $AlN:AlB_{12}$=12:1 with 12 times more AlN molecules already reacted. The interface was comprised of cBN and $Al_{(l)}$ with dissolved B as well as AlN and AlB_{12} that had just formed. More fine particulate AlN and AlB_{12} were formed as the temperature and time increased until most of the Al liquid was consumed at time of t_4. Finally, during the cooling stage when temperature was at and

below 980°C, the remaining $Al_{(l)}$–B solution would solidify as AlB_2 via the peritectic reaction determined by the Al-B phase diagram at time of t_5. The interface of the final reactive sintering was cBN/(AlN, AlB_{12}, and approximately 0.5% area fraction of AlB_2).

Because of the Al metal's low melting point and highly reactive nature, most cBN grains were shown to be surrounded by AlN and AlB_{12} or AlB_2 without substantial cBN to cBN direct bonding observed in SEM or EBSD. As the sintering temperature and time increased, the continued reactions further thickened the AlN and AlB_{12} on cBN grain boundaries and consumed B and N atoms coming off the cBN's surface layer and led to a further divided cBN to cBN grain structure.

5.5.1.3 Enhancement of AlB_{12} formation instead of AlB_2

Equation 2-8 describes the reaction that, when temperature is at or below 980°C, for every two AlN molecules produced one AlB_2 will be formed. At temperatures higher than 980°C, only AlB_{12} should be formed, as described in Equation 2-9; but for every 13 Al atoms 12 will be consumed in forming AlN and only one will be available in forming AlB_{12}, resulting in molar ratio of AlN:AlB_{12}=12:1. It is reasonable to assume the reaction kinetic controls the reaction process. Instead of B atoms breaking free from BN lattice and dissolving into Al liquid, AlB_{12} can be formed by the mechanism of alumination of B rather than boriding of Al.[62] In such process, Al enters the BN lattice which supplies abundant B atoms favoring the compound with the highest B content such as AlB_{12} to form in the initial stage. With this model, the difference in AlB_2 content between cBN with 20vol%Al and 10vol%Al can be explained. After initial alumination of cBN by Al, the AlN and AlB_{12} formed on cBN surfaces significantly slowed down the further contact

of large amounts of Al liquid behind the reaction front in the 20vol%Al outside the AlN particle layer; thereby, resulting in a rather deficient B in the Al liquid farther away from the cBN particle surface. Upon cooling to below 980°C, without reaching the B:Al=12:1 ratio, such Al-B solution some distance away from cBN surfaces underwent peritectic reaction and formed AlB_2, as observed in the fractured FSW tool.[44] Whereas in Mix I (cBN+10vol%Al) not only was the total liquid Al available reduced from 27.8at% to 8.9at% at 1350°C, as shown in Table 5-10 and Figure 5-54, but the surface area of cBN was increased by 57%, from 0.443m^2/g to 0.695m^2/g, benefiting from the addition of the fine 2.2μ cBN. The increased B to Al ratio and shorter migration distance for Al to reach the cBN surface, owing to the 9vol% of fine and dispersive cBN addition, both promoted a fast and in situ formation of AlB_{12} to exhaust the liquid Al at temperatures higher than 980°C.

5.5.2 cBN+Ti system

Without the liquid-phase assisted reactive-sintering by Al, reactions between cBN and Ti were a solid state sintering process controlled by diffusion and chemical reaction kinetics. Comparable to the cBN+Al system, similar metal boride and nitride reaction products, TiN and TiB_2, were obtained in the cBN+Ti system, in the HP/HT sintering temperature and time studied. Contrasting to the cBN+Al system, because of the narrow solubility of B in Ti and wide solubility of N in Ti, N needed to dissolve and diffuse into the Ti further away from the cBN surface to form TiN.

5.5.2.1 Reaction of B with Ti

Although B-N-Ti is a ternary system, interdiffusion among B, N and Ti was not reported, instead, diffusion of B and N atoms into Ti was considered fast and interstitial.[160, 161] In the present study, assumptions were made that: a) diffusion of B and N atoms into Ti were individual events and b) the effect of high pressure applied to diffusion was ignored. The general equation for calculating the effect of temperature to the diffusion coefficient was given as:[162]

$$D = D_0 \exp(-\frac{Q_d}{RT}) \qquad 5\text{-}6$$

where: D is the diffusion coefficient at the given temperature (m^2/s), D_0 is a temperature independent pre-exponential (m^2/s), Q_d is the activation energy for diffusion (J/mol), R is the gas constant ($8.13J/mol/K$), and T is temperature (K).

Because of the limited solubility of B in Ti and also the fast reaction nature in forming TiB_2, the diffusivity value of B in pure Ti was extremely difficult to measure.[160] It was very likely the reason that the literature search in the present study yielded only one publication in which the equation for B diffusion in α-Ti in the temperature range of 1033 to 1117K (760 to 1090°C) was given as:[161]

$$D = (4.2^{+38}_{-3.7}) \times 10^{-6} \exp[-\frac{(113 \pm 21)kJ/mol}{RT}]\frac{m^2}{s} \qquad 5\text{-}7$$

Using Equation 5-6, the diffusion coefficient of B in Ti was calculated at its highest valid temperature of 882°C(1155°K), at which α-Ti to β-Ti phase transformation happens, $D = 3.2610^{-11}\ m^2/s$ value was be extrapolated, as shown in Figure 5-55.

With the calculated D value, the formation time and distance for B to diffuse and reach the concentration for TiB_2 from cBN grain surface to the Ti matrix was calculated by applying Fick's second law of diffusion:[162]

$$\frac{\partial D}{\partial t} = D\frac{\partial^2 C}{\partial x^2} \qquad 5\text{-}8$$

where: D is the diffusion coefficient (m^2/s); t is time (s); C is concentration of solute ($wt\%$); and x is distance (m). Applying the boundary conditions as listed in Table 5-11, Fick's second law can be expressed as:[162]

$$\frac{C_x - C_0}{C_s - C_0} = 1 - erf\left(\frac{x}{2\sqrt{Dt}}\right) \qquad 5\text{-}9$$

where: C_x, C_0, and C_s are boundary conditions as defined in Table 5-11, the expression of $erf\left(\frac{x}{2\sqrt{Dt}}\right)$ is a Gaussian error function. The value of $erf(z)$ can be calculated or is given in mathematic tables with varying (z) values.[162]

Here an assumption was made that in order for the $2B+Ti=TiB_2$ reaction to fully complete, B concentration needed to reach the C_X=31.1wt%, the stoichiometric value of B wt% in TiB_2. Also for estimation, 1μ to 5μ range was used as the distance that B atoms have to diffuse to satisfy the concentration of C_X=31.1wt% requirement. The calculation showed, as plotted in Figure 5-56, that even at the temperature of 882°C (1155°K) which was well below the HP/HT temperatures in the study, the time required was only in the order of seconds for B to diffuse through up to 5μ distance in α-Ti and to reach the concentration required forming TiB_2.

It was shown that diffusion coefficient for Ti self-diffusion exhibited a significant step-increase upon the phase transformation from α-Ti to β-Ti above 882°C. Such

diffusivity enhancement also suggested corresponding enhancement of solute diffusion leading to deeper surface coatings of boride and nitride on surface of β-Ti.[160] It is, therefore, reasonable to believe the diffusion coefficient of B in β-Ti (BCC) will be higher than α-Ti (HCP) in addition to the well-known effect of increasing temperature on diffusivity. This will promote more of the fast formation of TiB_2 as-detected in less than the 2 min sintering time in the 1350°C temperature range of the present study.

5.5.2.2 Reaction of N with Ti

It is reasonable to assume the formation of TiN was controlled by the available N diffusing through the remaining channels of Ti in direct contact with cBN surfaces. As observed both in the SEM images and EBSD results, the reacted TiB_2 was not a uniform and dense layer completely surrounding the cBN surfaces but rather submicron-sized particles leaving open channels for N atoms to diffuse directly into the Ti in contact with cBN or via the TiB_2 grain boundaries. Using the reported diffusion coefficient of $D=2.9x10^{-13}m^2/s$ for N diffusion in α-Ti at temperatures of 1350°C[163] and the boundary conditions listed in Table 5-12, the diffusion distance (1μ to 5μ range) and time for N = 22.6wt% concentration required in forming stoichiometric TiN was estimated and is shown in Figure 5-57.

Since the diffusion coefficient of N in Ti, at 1350°C was two orders of magnitude less than that of B in Ti at much lower temperature (882°C), B atoms diffused much faster than N in the Ti matrix. This resulted in TiB_2 formation first and close to the cBN surface and TiN a further distance away, as shown in Figure 5-35. Based on the pre-exponent of N self-diffusion in TiN[164] at $D_0=5.4x10^{-7}$ (m/s^2) for 1000-1500°C

temperature range, N diffusion through the newly formed TiN to reach stoichiometric or higher N/Ti ratio can be fast, thereby, exhausting the remaining Ti. Based on these calculations and assumptions the reaction process of cBN+Ti, with respect to temperature and time was illustrated in Figure 5-58.

5.5.2.3 Comparison of cBN+Ti powder and Ti-coating systems

The cBN+Ti reactive sintering may benefit from the $Ti+2B=TiB_2$ reaction on cBN surface, which releases heat at 293kJ/mole,[54] leading to rapid localized self-heating and densification under both the heat from the reaction and external pressure. This was possible in the continuous Ti-coating surrounding the cBN particles; as a result, the reactions can be continuous and sustained with localized self-heating and enhancement of N atoms' diffusion into remaining Ti. This resulted in softening of the Ti-coating on cBN surfaces and hence the lubrication effect. There was no evidence of such continued reaction happening in sintering the cBN + Ti-powder system, which was observed to be very porous and therefore unable to sustain and propagate the exothermic self-heating reaction.

5.5.3 Comparison of cBN+Al and cBN+Ti systems

Both cBN+Al and cBN+Ti systems were examples of reactive sintering of PCBN starting from powder metal additive and reactively forming much higher melting points and stronger nitrides and borides. However, substantial differences existed between the two systems. The cBN+Al system utilized the Al's low melting point for fast liquid-phase-assisted reactive-sintering and formation of AlN and AlB_{12} as well as little AlB_2,

whereas cBN+Ti system's reactive-sintering may benefit from the exothermic $Ti+2B=TiB_2$ reaction[54] leading to rapid localized self-heating and densification under both the heat from the reaction and applied ultra-high pressure. However, this reaction may be limited if the Ti medium was not continuously surrounding the cBN particles, as demonstrated in the cBN+Ti powder system.

Increased room temperature K_{IC} values, measured by diametral compression method as listed in Table 5-13, were obtained in PCBN using Mix I (cBN+10vol%Al) over the baseline PCBN (80-20vol%Al)'s, although the initial Al additive was reduced from 20vol% to 10vol%. In spite of missing the liquid-phase-assisted sintering, PCBN sintered using Mix III (Ti-coated cBN) still possessed a baseline PCBN (cBN+20vol%Al)-equivalent mean K_{IC} value at room temperature, benefiting from the high degree packing of Ti-coated cBN particles and higher fracture toughness values of TiN and TiB_2 over Al reaction compounds'.

In the present study, comparable fracture toughness values measured using the Vickers indentation and the diametral compression methods were obtained on the PCBN composites sintered at 1350°C for 15 min. As shown in Table 5-14, for the PCBN materials studied, both methods can be employed for fracture toughness estimates.

If Weibull modulus is considered for scaling from the small test sample volume to large FSW tools, one noticeable difference is that the Weibull modulus *(m=16.8)* of flexural strength obtained on PCBN (cBN+10vol%Al) is more than twice of the PCBN (Ti-coated cBN)'s *(m=7.6),* as shown in Figure 5-59. This predicted that failure load of the PCBN (cBN+10vol%Al) in larger volume tools may occur at a more predictable and narrower load range than that of the PCBN (Ti-coated cBN)'s. The Weibull moduli of

fracture toughness distributions, measured using the Vickers indentation method, were very similar for the PCBN (90-10Al) and PCBN (Ti-coated cBN).

5.6 High Temperature Flexural Strength and Fracture Toughness of PCBN

Three-point-bend and diametral compression methods were carried out in characterizing the sintered PCBN composites' strength and fracture toughness at temperatures of 25°C, 900°C, and 1100°C in continuous argon flow-through atmosphere.

5.6.1 High temperature strength and toughness of PCBN (90-10vol%Al)

5.6.1.1 High temperature flexural strength

Increase of mean strength values of 16% and 15% were measured in PCBN (90-10Al) at 900°C and 1100°C, respectively, over the 25°C measured results, as displayed in Figure 5-60. The three mean values and individual data of the flexural strength obtained at 25°C, 900°C, and 1100°C, are listed in the Appendix and were compared using two-sample T-test.[165] The null hypothesis was made that there was no significant difference in sample's mean values between the 25°C to 900°C and 1100°C results. The T-test results concluded, with 95% and higher confidence, that the null hypothesis was rejected, as summarized in Table 5-15. Namely, the mean flexural strength values obtained at 900°C and 1100°C were statistically, significantly different than that of the 25°C result.

After cooling down to room temperature, the remainder and unstressed portion of the long bend-bars extended outside the span on the initially high-temperature-tested PCBN (90-10Al) were bending-tested at room temperature. As shown in Figure 5-61, the high-temperature increase of the strength was largely retained at room temperature with a

slight decrease on samples initially tested at 900°C, which was still approximately 10% higher than the room-temperature tested mean value.

The T-test was applied also to compare the mean values of room-temperature retested using the unstressed portion of the long bend-bars after first exposing to 900°C and 1100°C. The two sample T-test results are summarized in Table 5-16 and are based on the flexural strength data collected initially at 900°C and 1100°C, respectively, and then retested again at 25°C (Reference the Appendix.)

The T-test confirmed, with 95% of confidence, that the null hypothesis was true. Namely, the mean flexural strength values initially tested at 900°C and 1100°C were statistically similar to the mean value collected after cooling down to room temperature. The slight increases of high temperature flexural strengths were largely retained to room temperature.

Fractography close to the tensile side on the room-temperature tested samples showed a mixed intergranular and transgranular fracturing mode as well as secondary cracks along the cBN-AlN/AlB_{12} grain boundaries, as shown in Figure 5-62 a). A slightly more intergranular cracking mode was observed in the 900°C tested sample, as revealed in Figure 5-62 b). At 1100°C, the fracture surface appeared to be mixed with intergranular and transgranular fracturing and a visible pocket of molten and re-solidified spherical aluminum-oxide very close to the tensile surface, as shown in Figure 5-62 c). Closer examination of the fractography, as shown in Figure 5-63, revealed intergranular fracturing with secondary cracking at room temperature; more damaged AlN-AlB_{12} phases with cBN particle pullouts at 900°C; and increased transgranular fracturing through cBN grains at 1100°C. Localized phase transformation of the small amount of

$AlB_2 \rightarrow Al_{(l)} + AlB_{12}$ was visible on the fracture surface of 1100°C tested samples, both in Figure 5-62 c) and Figure 5-64 c).

XRD patterns collected on the PCBN (90-10Al) before and after the flexural strength test at 1100°C did not reveal detectable amount of AlB_2, as shown in Figure 5-65. However, increases in both AlN and AlB_{12} were measured on the surface of bend-bars after the 1100°C tests. Compared to as-is bend-bar surface before the flexural strength testing, larger sized and more clusters of AlN-AlB_{12} phase appeared on cBN grain boundaries on the free surface of 1100°C-tested bend-bar, as shown in Figure 5-66. It was the consequence of the inter-cBN-grainboundary phase of AlN and AlB_{12} seeping out of the free surface at 1100°C, driven by the thermal expansion stress and the surrounding bulk residual-stresses. Such spots of reverse peritectic reaction were also observed on fracture surfaces of 1100°C tested samples.

5.6.1.2 High temperature fracture toughness

Fracture toughness, K_{IC}, measured using the diametral compression method at 900°C and 1100°C, revealed consistent K_{IC} values comparable to those measured at room temperature; namely, no appreciable declining with increasing of temperature, as shown in Figure 5-67. This demonstrated again the PCBN (90-10Al)'s high temperature stability up to 1100°C.

Fractography of the PCBN (90-10Al) K_{IC}-tested at 25°C, 900°C and 1100°C revealed mostly intergranular fracturing mode with isolated pockets of disintegration of AlN/AlB_{12} grain-boundary phases observed at 900°C and localized $AlB_2 \rightarrow Al_{(l)} + AlB_{12}$ decomposition in 1100°C-tested samples indicated by the oxidized Al spheres, as shown

in Figure 5-68 through Figure 5-70. Such reverese peritectic phase transformation from low temperature stable and higher density AlB_2 (ρ=3.19g/cc) phase to high-temperature stable and lower density AlB_{12} (ρ=2.6g/cc) resulted in some localized plastic deformation, which was evident from some of the localized ductile dimples at 1100°C as a result of cBN grain pull-outs.

5.6.1.3 High temperature strength and toughness

Observed in another high temperature study,[47] three-point-bending strength of the PCBN made of pure and fine cBN grains increased more than 20% from 800°C to 1200°C. Study of pure AlN[166] also showed that AlN's strength at 1000°C was slightly higher than that of the room tempeature's and it only dropped about 5% when tested at 1250°C. Hence it was not unexpected that PCBN (90-10Al), being made of high volume cBN grains and the reacted $AlN+AlB_{12}$ grain boundary phases, would exhibite high initial room temperature strength and a 15% increase at temperatures up to 1100°C.

High temperature phases are normally of lower density than their lower temperature counterparts.[167] In the Al-B binary system, density of AlB_2 (ρ=3.19g/cc) and (AlB_{12} ρ=2.6g/cc) were reported, as listed in Table 2-1. The density difference corresponds to 22.7 vol% increase from lower-temperature-stable AlB_2 phase to the high-temperature-stable AlB_{12} phase. At 980°C or higher temperature, the reverse peritectic reaction of $AlB_2 \rightarrow Al_{(l)} + AlB_{12}$ under equilibrium condition produces 53.2wt% of $Al_{(l)}$ (ρ=2.38g/cc) and 46.8wt% of AlB_{12} at ambient atmosphere; both lead to significant increase of volume over the AlB_2 in cBN-intergranular junctions. Both hardness and toughness values of the high-temperature-phase AlB_{12} are higher than those of the low-

temperature-phase AlB_2. These compressive strains from the transformation zone resulting around the crack tip and along its faces could partially counteract or shield the crack from the normal stress levels, making it more difficult for the crack to propagate.[167]

At room temperature, the cracking mode, as shown in Figure 5-68, was observed to have more cBN pullouts and intergranular secondary cracking via weak grain-boundary phases (AlN and AlB_2). As the temperature increased to 900°C and 1100°C, the fractography close to the crack origin revealed increased transgranular fracturing through cBN particles, as shown in Figure 5-69 and Figure 5-70. To cause transgranular cBN fracturing, more energy is needed because, on average, boundary fracture energy was found to be about half that of the cleavage energy.[168]

Ceramic microstructures can be modified to achieve increased crack deflection and impediment as well as increased fracture toughness. Approaches include controlled grain boundary phases and multimodal grain structures[169] and introduction of second phase with different elastic modulus and thermal expansion coefficient.[170, 171] Due to the higher coefficient of thermal expansion from AlN over cBN, AlN intergranular phase expands more than cBN grains at high temperatures resulting in a high compressive stress to the cBN grains as measured and calculated using XRD method and displayed in Figure 5-71. The planar residual compressive stresses were measured on the as-is PCBN (90-10Al) bend-bars and after 900°C and 1100°C tests on cBN crystals' $hkl=331$, $d=0.830\text{Å}$ (ICDD 01-089-1498). The intensity plots at different (ψ) angles, $2\theta \sim sin^2(\psi)$ plots, and linear regression results are shown in Figure 5-71 and the residual stress values are listed in Table 5-17.

Compared to the as-is bend-bars, the extra compressive residual-stresses induced at high temperatures reflected the thermal expansion differences between the cBN particles and the intergranular phase, mostly AlN, surrounding them. Based on the two-dimensional thermal stress model, Equation 2-28 for two phase materials in Section 2.6.8, the thermal expansion stresses on the cBN-AlN interface was estimated and is illustrated in Figure 5-72. Assumptions made for the estimate were: a) the cBN particles were spherical-shaped and b) the outer layer consisted only AlN phase uniformly surrounding the cBN particle. The mean cBN grain size of 13.4μ (r_{cBN}=*6.7μ)* was used for the modeling, which was obtained by measuring of the cBN mixture consiting of 90% of 14.1μ and 10% 2.2μ particles. The AlN layer thickness of t_{AlN} = 0.28 ± 0.10μ was obtained by measuring intergranluar AlN thickness at 12 spots in three different SEM images taken at different field of views and mangfications on the PCBN (90-10Al) sintered at 1350°C for 15 min. The poisson's ratio of v_1 for cBN and v_2 for AlN was selected at 0.15 and 0.24, respectively. The temperature difference, ΔT, was selected as 875°C (900°C-25°C) and 1075°C (1100°C-25°C) individually.

$$\sigma_a = \frac{(\alpha_2-\alpha_1)\Delta T}{\frac{1-v_1}{E_1}+\frac{\frac{b^2+a^2}{b^2-a^2}+v_2}{E_2}} \qquad 2\text{-}28$$

As shown in Figure 5-73, the compressive stress acting on cBN particle surfaces ranged from -27MPa to -55MPa (points *a* and *a'*) depending on the AlN layer thickness at 900°C; and from -33MPa to -68MPa at 1100°C (points *b* and *b'*). The same magnitude of thermal stresses, but in tension, was acting on the AlN surface in contact with the cBN particles.

In simulating the phase-boundary dilation stress caused by the reverse peritectic

phase transformation of $AlB_2 \rightarrow AlB_{12} + Al_{(l)}$, Equation 2-29 for a two-dimensional fitted cylindrical system[133] was adapted for an AlB_2 core and cBN sheath, as shown in Figure 5-74. Then Equation 5-10 can be obtained as:

$$\sigma_{\varphi m} = \frac{E_{AlB_2} E_{cBN}}{E_{cBN}(1-\nu_{AlB_2})+E_{AlB_2}(1-\nu_{cBN})} a\rho^{-2} \qquad 5\text{-}10$$

where: E_{AlB2}, E_{cBN}, is the modulus of elasticity for the AlB_2 core and the cBN sheath, respectively; α is the dilation difference per unit length between the AlB_2 core and the cBN sheath; $\rho=r/R$ is the distance r to core radius R ratio in a cylindrical coordinates; ν_{AlB2}, ν_{cBN} are poison's ratio for the AlB_2 core and the cBN sheath, respectively, α is the dilation difference per unit length between the AlB_2 core and the cBN sheath, and $\rho = R/r$.

Assume for a disk with a volume $V=\pi r^2 h$ (h=height of the disk) the interfacial dilation difference per unit length is:

$$a = \varepsilon = \frac{dr}{r} = \frac{dV}{2V} \qquad 5\text{-}11$$

$$\rho = \frac{w}{v}$$

For a fixed mass of AlB_2 as the core disk, the volume change due to $AlB_2 \rightarrow AlB_{12} + Al_{(l)}$ phase transformation can be expressed as:

$$dV = V_{AlB_{12}} - V_{AlB_2} = w_{AlB_2}\left(\frac{1}{\rho_{AlB_{12}}} - \frac{1}{\rho_{AlB_2}}\right) \qquad 5\text{-}12$$

In case I, consider only volume change caused by the phase transformation from AlB_2 to AlB_{12}, then:

$$\frac{dV}{V} = \frac{V_{AlB_{12}} - V_{AlB_2}}{v_{AlB_2}} = w_{AlB_2}\left(\frac{1}{\rho_{AlB_{12}}} - \frac{1}{\rho_{AlB_2}}\right) \cdot \frac{\rho_{AlB_2}}{w_{AlB_2}} \qquad 5\text{-}13$$

Using the density values of ρ_{AlB_2}= 3.19g/cc and $\rho_{AlB_{12}}$=2.60g/cc, as listed in Table 2-1, the $dV/V=0.2269$ and $\varepsilon=0.1135$ can be obtained. Substituting these values into Equation 5-10, and using $r_{cBN}=6.7\mu$ for r and $r_{AlB2}=0.25\mu$ for R_k core as measured by EBSD; $E_{cBN}=870GPa$ for E_m and $E_{AlB2}=448GPa$ for E_k; $\nu_{cBN}=0.15$ and $\nu_{AlB2}=0.274$ for ν_m and ν_k, respectively; the $\sigma_{\varphi m}$ can be calculated as: σ=59.6MPa.

This stress is tensile on the AlB_2 core (the stress for volume expansion from AlB_2 to AlB_{12}) and compressive in the sheath (the cBN particles surrounding and constraining the phase transformation from happening freely).

In case II, consider phase transformation from AlB_2 to AlB_{12} + $Al_{(l)}$ at T ≥ 980°C via the reverse peritectic reaction of $AlB_2 \rightarrow AlB_{12} + Al_{(l)}$. By the lever rule, 1 wt% of AlB_2 produces 53.2wt% of $Al_{(l)}$ (ρ==2.38g/cc) and 46.8wt% of AlB_{12}. The combined density of AlB_{12} and $Al_{(l)}$ is ρ_{AlB_2}= 2.478g/cc. Applying Equation 5-10, the stress $\sigma_{\varphi m}$ was calculated as: σ=75.4MPa. This stress is, again, tensile in the AlB_2 core (the stress for volume expansion from AlB_2 to AlB_{12} and $Al_{(l)}$) and compressive in the sheath (the cBN particles surrounding/constraining the phase transformation from happening).

As shown in Figure 5-75, adding the estimated compressive interfacial thermal-expansion-stress on cBN particles in addition to the room temperature's flexural strength value at 900°C, and the extra dilation stress resulting from the AlB_2 pockets gave the same range of measured flexural strength values at 900°C and 1100°C for PCBN (90-10Al). Since the AlN-AlB_{12} phase was under tensile stress, opposed to the compressive stresses acting on the cBN gains, it perspired out of the free surface on the bend-bars at 1100°C, as shown in Figure 5-66. The effect of thermal expansion mismatch was reserved to room temperature and led to additional residual stresses over the room

temperature tested mean values as detected by the XRD method. Superimposing the residual stresses measured after the initial high temperature testing to the strength measured at 25°C also yielded similar increase effects at 900°C and 1100°C for PCBN (90-10Al) tested.

In summary, upon heating to 900°C the thermal expansion stresses caused by mostly AlN grain-boundary-phase applied compressive stresses on cBN particles in PCBN (90-10Al). This leads to extra energy required to fracture at high temperatures. Further heating up to 1100°C may lead to $AlB_2 \rightarrow AlB_{12} + Al_{(l)}$ reverse peritectic decomposition in localized and confined pockets dispersed among the cBN grains, which induced additional compressive stress onto cBN grains. Such beneficial compressive stresses were largely retained after the samples were cooled down to room temperature, as reproduced by the follow-up bend-testing at room temperature using the extra-long unstressed portion. The residual stresses measured by XRD method on the 900°C and 1100°C tested bend-bars revealed compressive stress levels agreeable to the extra strength increase after the high temperature exposure.

5.6.2 High temperature response of PCBN (Ti-coated cBN)

5.6.2.1 Effect of temperature on flexural strength

The flexural strength by three-point-bend testing on the PCBN (Ti-coated cBN) showed a significant drop with increasing of test temperature, as displayed in Figure 5-76. Compared with the mean value obtained at room temperature, more than 20% of the room-temperature flexural strength was lost at 900°C and 50% at 1100°C. XRD conducted on the bending-tested samples revealed strong oxidation product of TiO_2 in

consumption of TiB_2 and TiN on the surface of the PCBN samples, as shown in Figure 5-77.

The fractography of bending-tested PCBN (Ti-coated cBN) at room temperature exhibited a mostly transgraular fracturing pattern, as shown in Figure 5-78 a) and b). As the test temperature incrased to 900°C, the fracture surface became intergranluar-dominant with damages to the reacted and intergranluar TiN and TiB_2 phase and formation of the oxidation product of TiO_2, as shown in Figure 5-78 c) and d). At 1100°C the fracture surface exhibited an intergranlular-dominant fracture mode with cBN grain pullouts and a complete disintigration of the TiN-TiB_2 layer into spherical TiO_2 particle, as shown in Figure 5-78 e) and f). The oxidation of TiN-TiB_2 was also reaveled by the EDS spectrum and the XRD pattern in Figure 5-77, with an almost complete comsumption of TiB_2 and about half of the TiN orginally reacted and formed on cBN particles surfaces. The disintigration of the cBN-grain-boundary phases by oxidation and pulveriztion of TiN and TiB_2 was shown to be the cause for the decrease of the flexural strength for PCBN (Ti-coated cBN) at 900°C, and more siginificantly, at 1100°C.

Such oxidation and TiN-TiB_2 disintegration happened mostly on the free surfaces of the bend-bars during the high temperature testing or on the fractured surfaces after samples break. As shown in Figure 5-79, the subsurface microstructure obtained by polishing on the cross-sectioned, tested bend-bar revealed TiO_2 particles on top of the free surface and the depth of damage to TiN-TiB_2 intergranular phase was less than 50μ on the tensile surface. The microstructure on bulk PCBN (Ti-coated cBN) was largely intact after heating upto 1100°C.

5.6.2.2 Effect of temperature on fracture toughness

Fracture toughness values of PCBN (Ti-coated cBN), measured using the diametral compression method, also exhibited a slight decreasing trend as the temperature reached 900°C and a further decline at 1100°C in comparison to the room-temperature tested samples, as shown in Figure 5-80.

The fractography close to the crack of origin of the K_{IC}-tested sample at room temperature showed a transgranular dominant fracture mode with well-bonded TiN/TiB_2 cBN grain boundary phases, as shown in Figure 5-81. At 900°C, the rather uniform coating layer was visibly damaged and granulated, as shown in Figure 5-82, with fracture mode turning to a mixed intergranular and transgranular mode. At 1100°C, complete oxidation and pulverization of the TiN/TiB_2 coating on cBN grains occurred, as detected by the XRD and EDS, with the fracture mode turning to mostly intergranular, as shown in Figure 5-83. The oxidation and disintegration of the uniform and strong TiN-TiB_2 grain-boundary phases on the cBN crystals was responsible for the decrease in fracture toughness values at 900°C and 1100°C in PCBN (Ti-coated cBN).

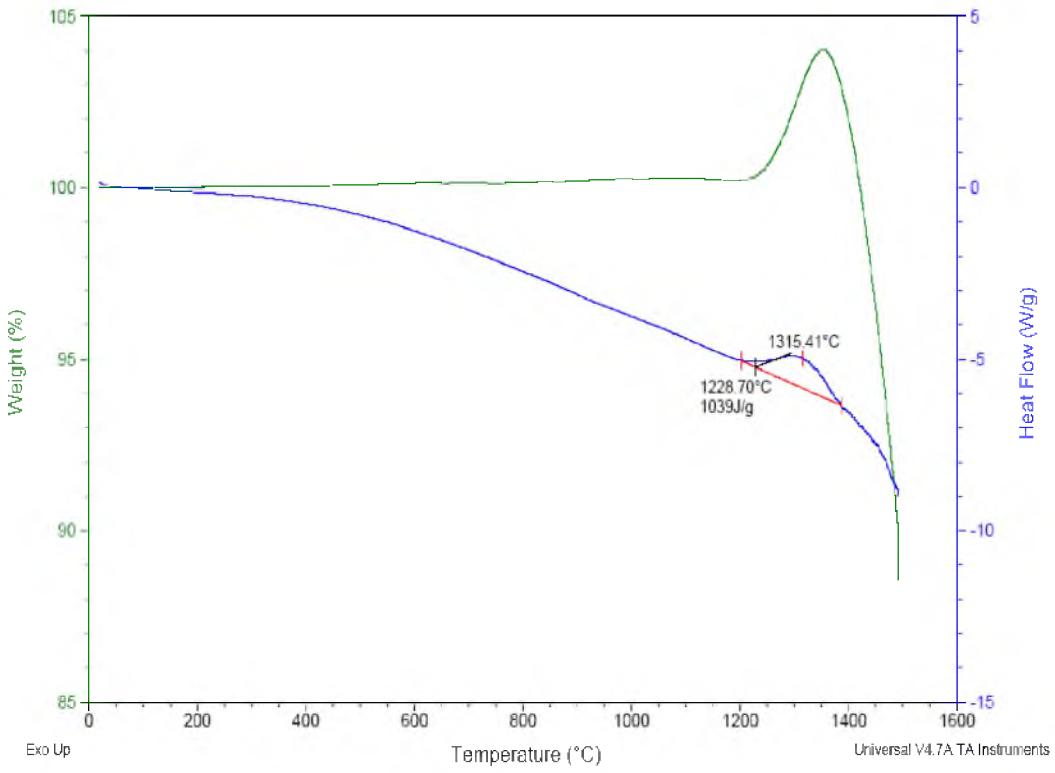

Figure 5-1. TGA response of cBN powder in air.

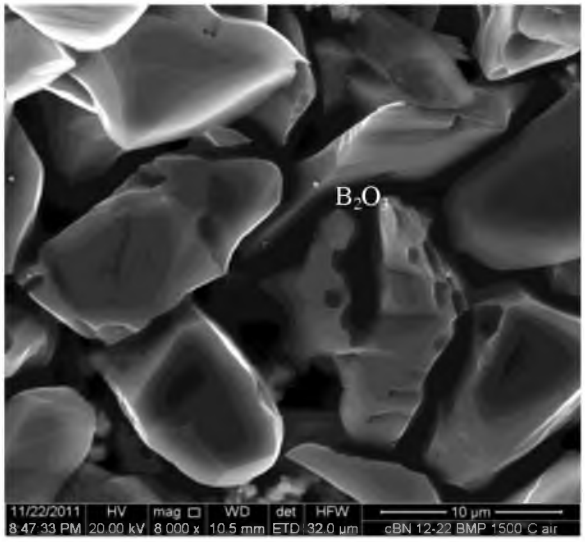

Figure 5-2. Morphology of cBN crystals after being heated up to1500°C in air.

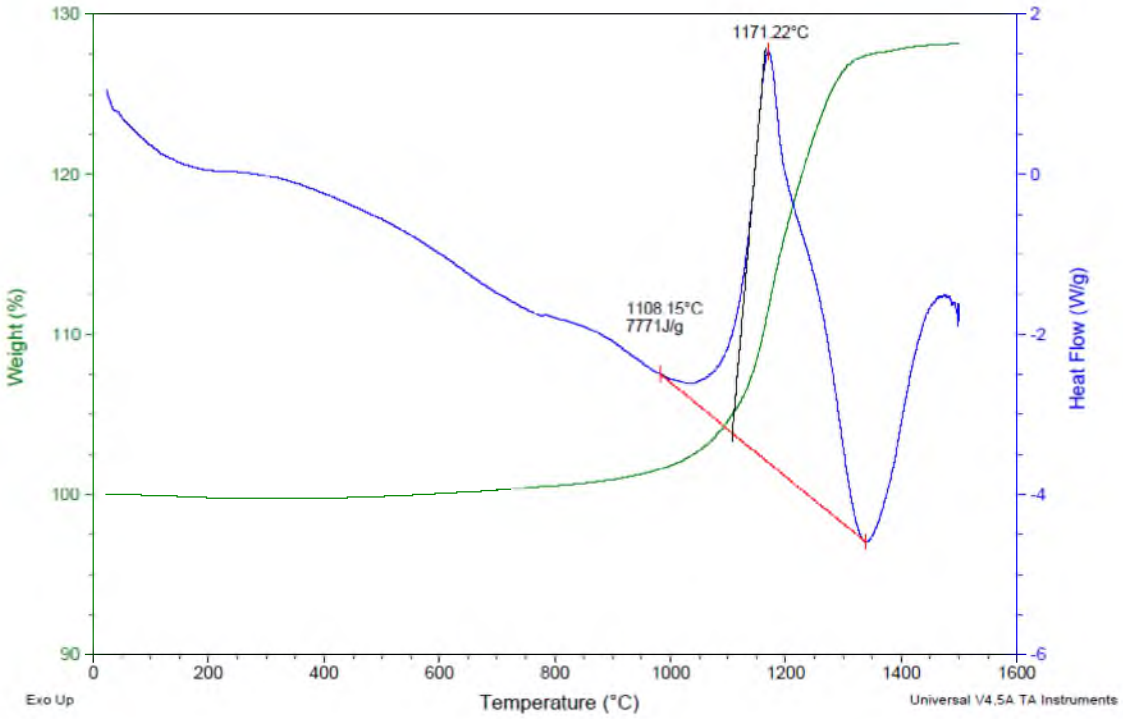

Figure 5-3. TGA response of AlN powder in air.

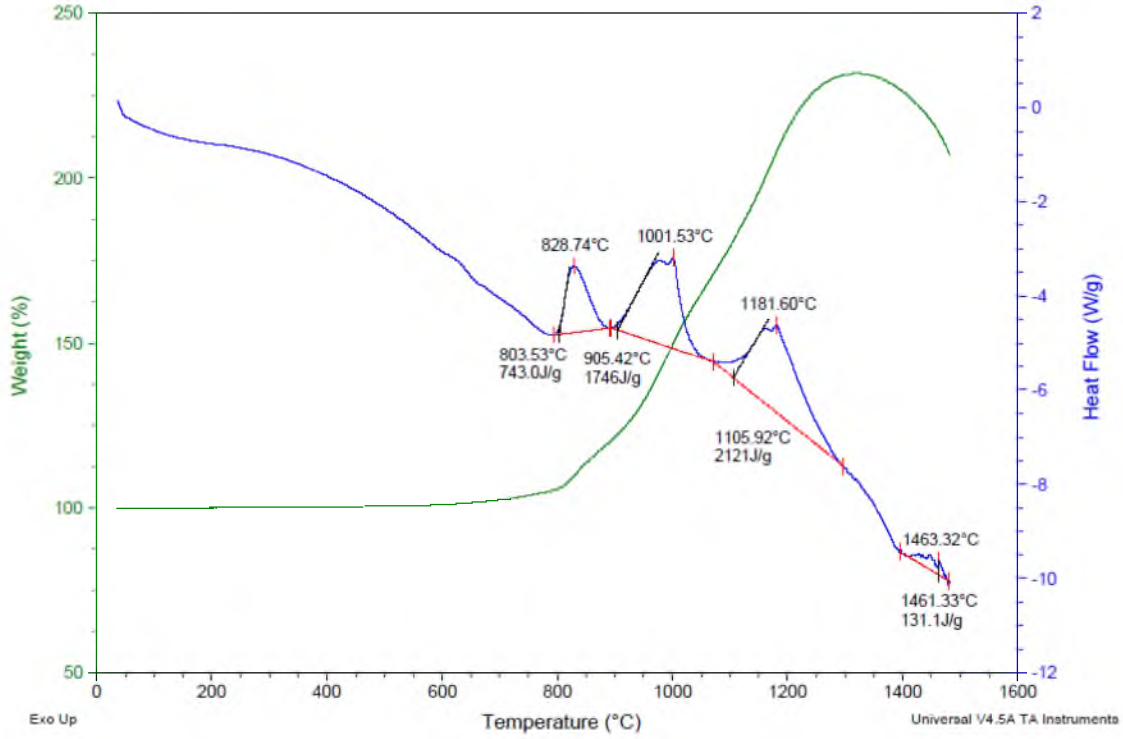

Figure 5-4. TGA response of AlB_2 in air.

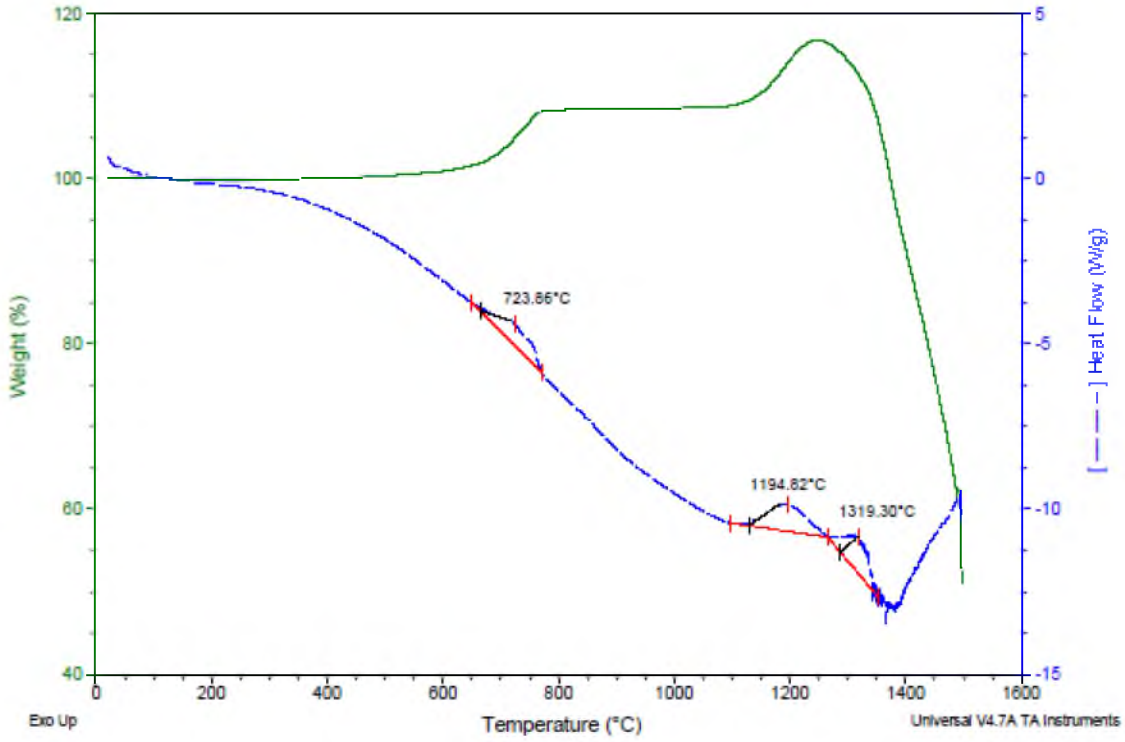

Figure 5-5. Thermal and oxidation responses of the Ti-coated cBN powder (Diamond Innovations, 12-22 BMP-Ti).

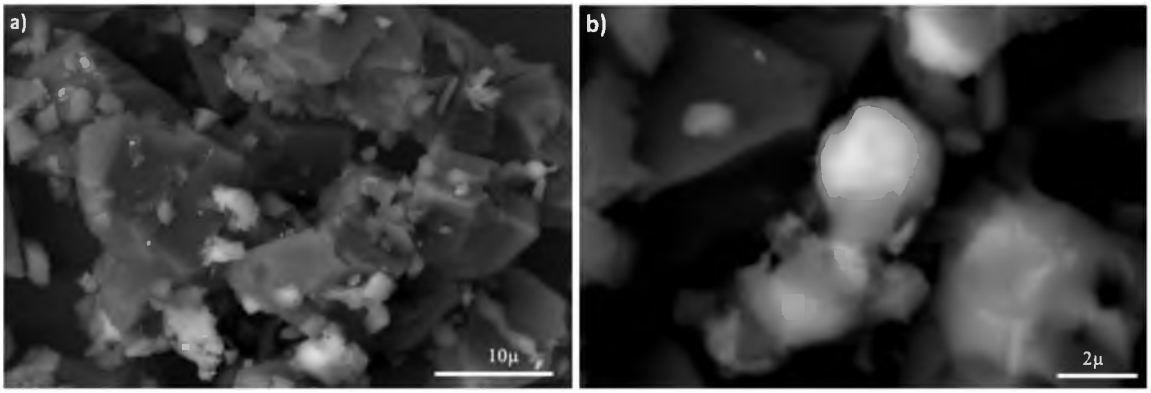

a) b)

Figure 5-6. Mix I (cBN+10vol%Al) after 1000°C for 90 min vacuum treatment showing: a) reacted Al on cBN grains and b) spherical Al bonded with fine cBN particles.

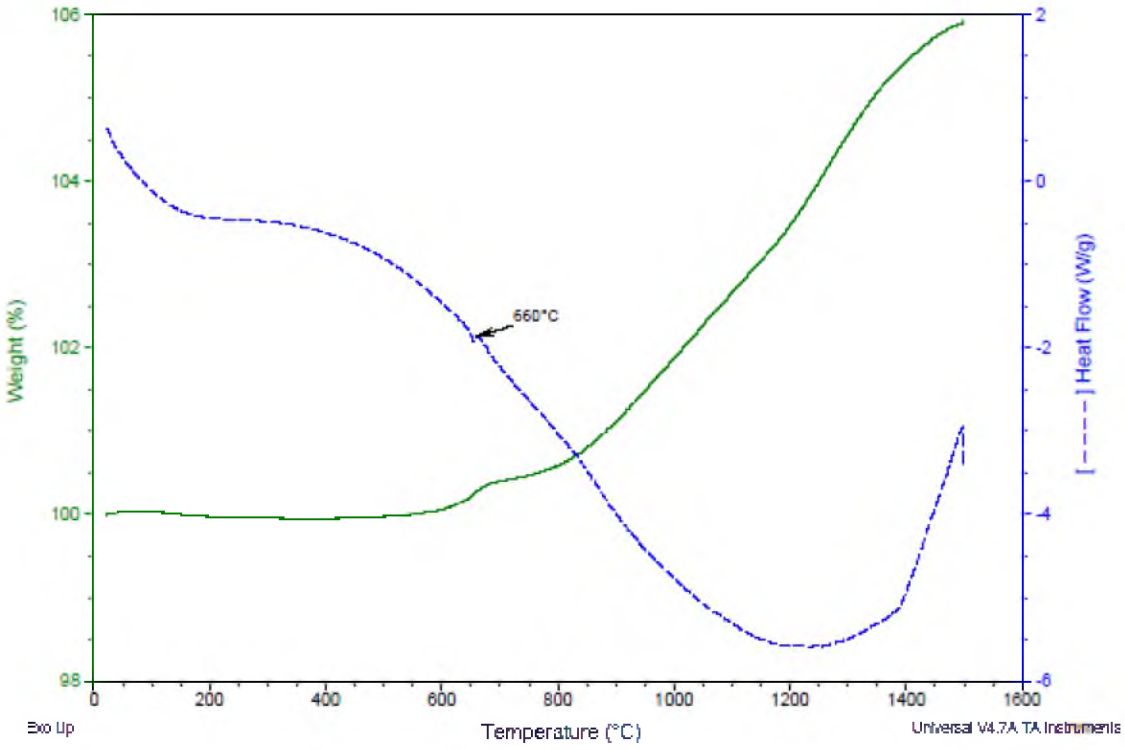

Figure 5-7. TGA response of Mix I (cBN+10vol%Al) in Ar, after pre-reaction in vacuum at 1000°C for 90 min.

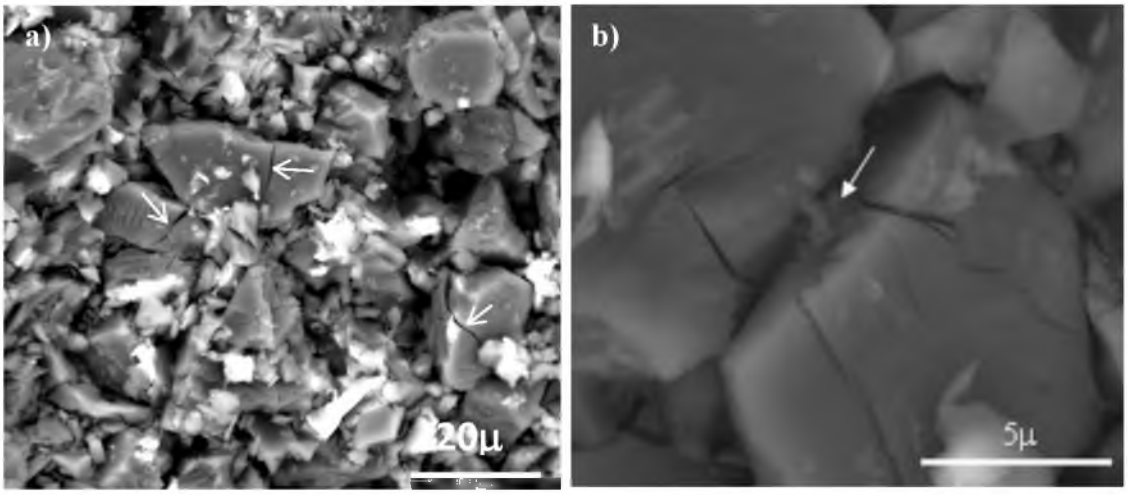

Figure 5-8. High pressure (HP=5.5GPa) cold-compacted Mix I (cBN + 10vol%Al): a) SE image of the compacted mixture and b) BSE image of two fractured cBN particles.

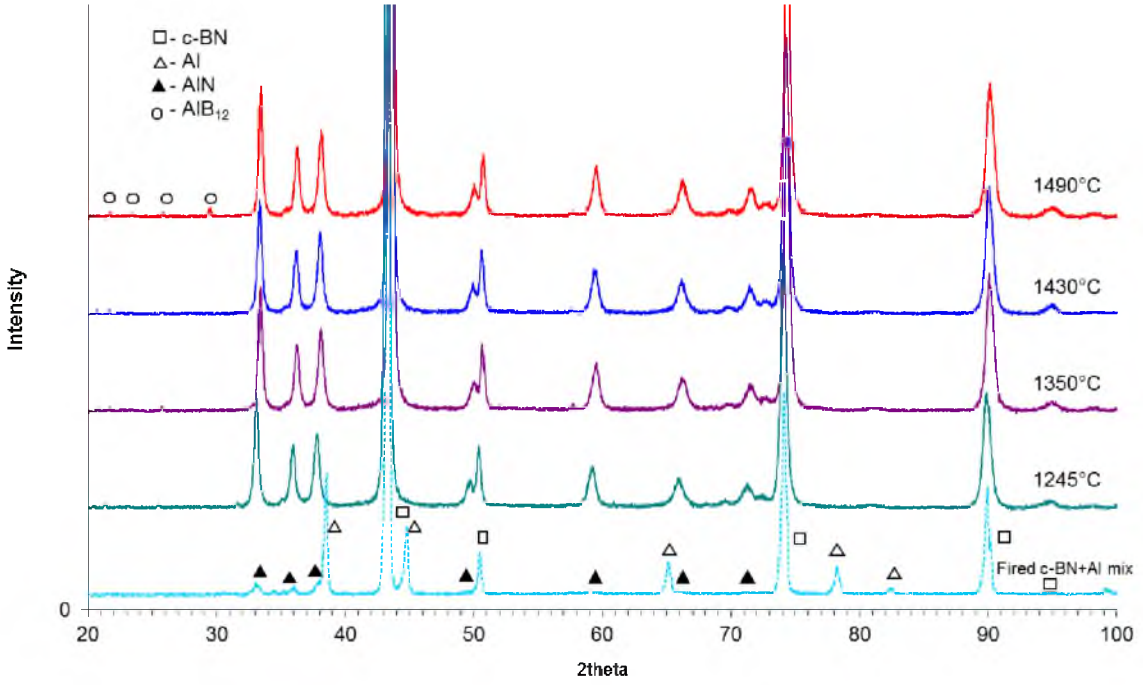

Figure 5-9. XRD patterns of PCBN HP/HT-sintered using Mix I (cBN + 10vol%Al) with 15 min sintering time.

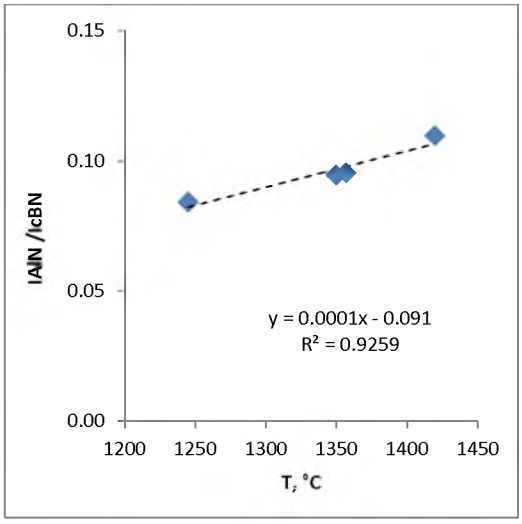

Figure 5-10. Effect of sintering temperature to XRD intensity ratio of $I_{AlN(100)}/I_{cBN(111)}$ in PCBN (90-10Al) sintered for 15 min.

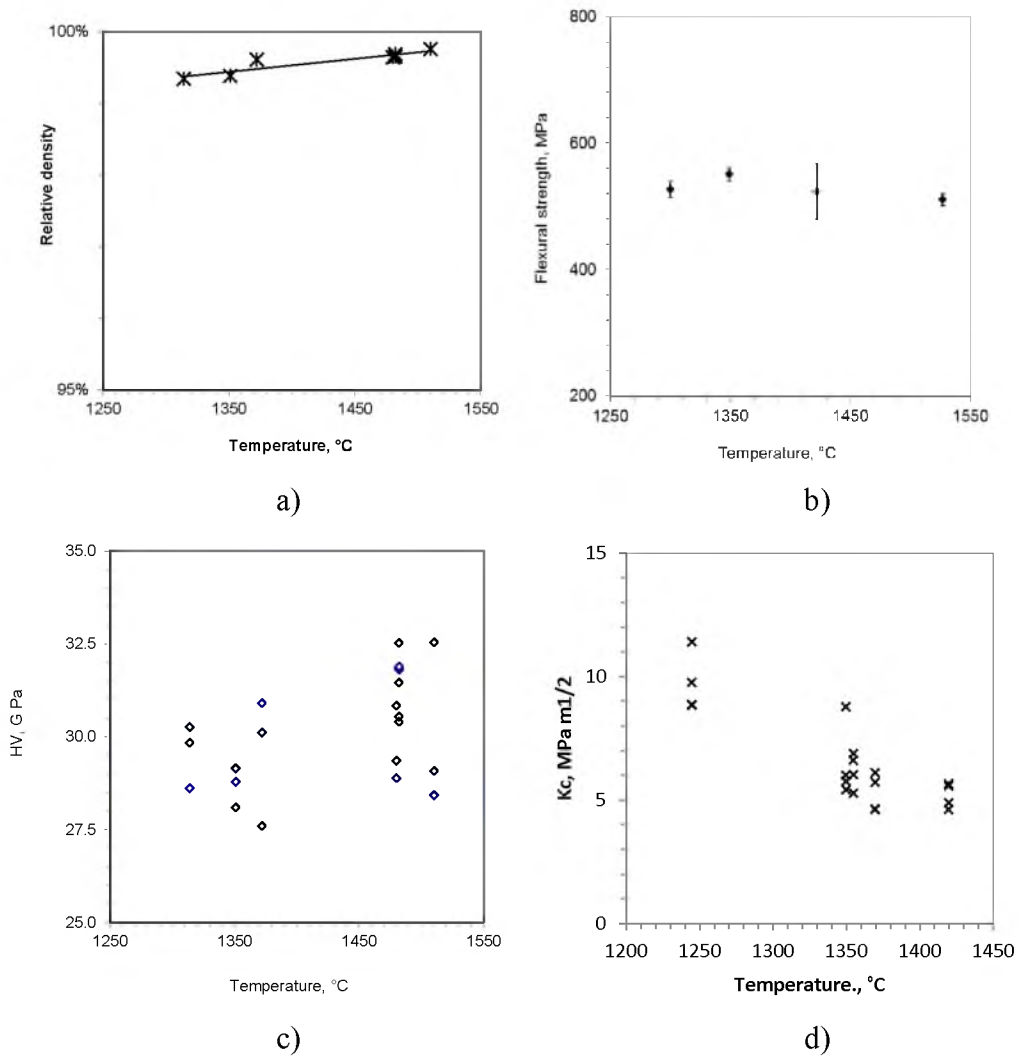

Figure 5-11. Effect of HP/HT-sintering temperature on properties of PCBN (90-10Al): a) relative density, b) four-point-bend flexural strength, c) Vickers hardness, and d) fracture toughness measured by indentation method, all with 15 min sintering time.

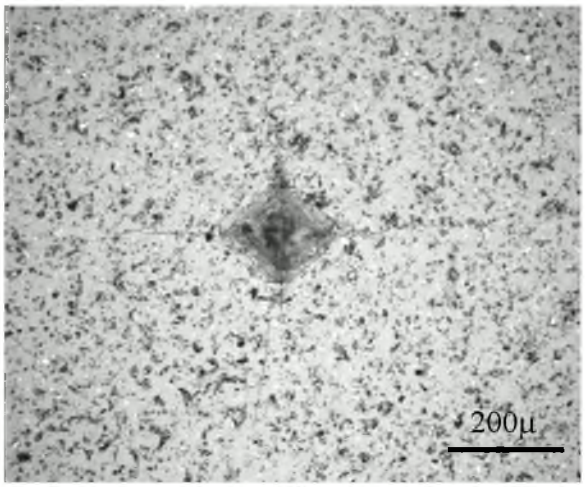

a)

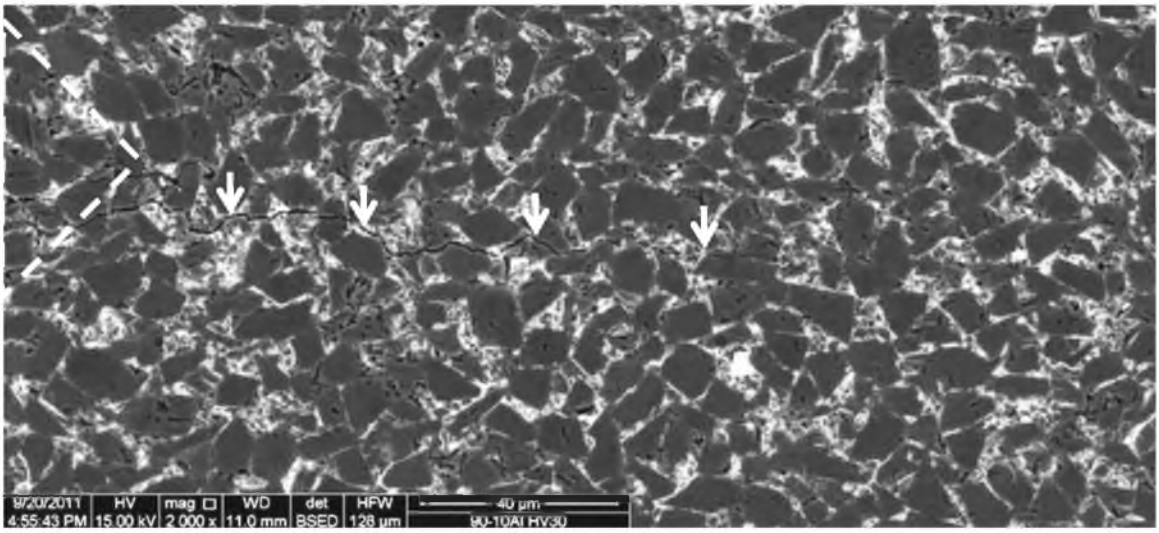

b)

Figure 5-12. Images of: a) Vickers indentation in PCBN (90-10Al) and b) SEM image of one of the Vickers indentation cracks.

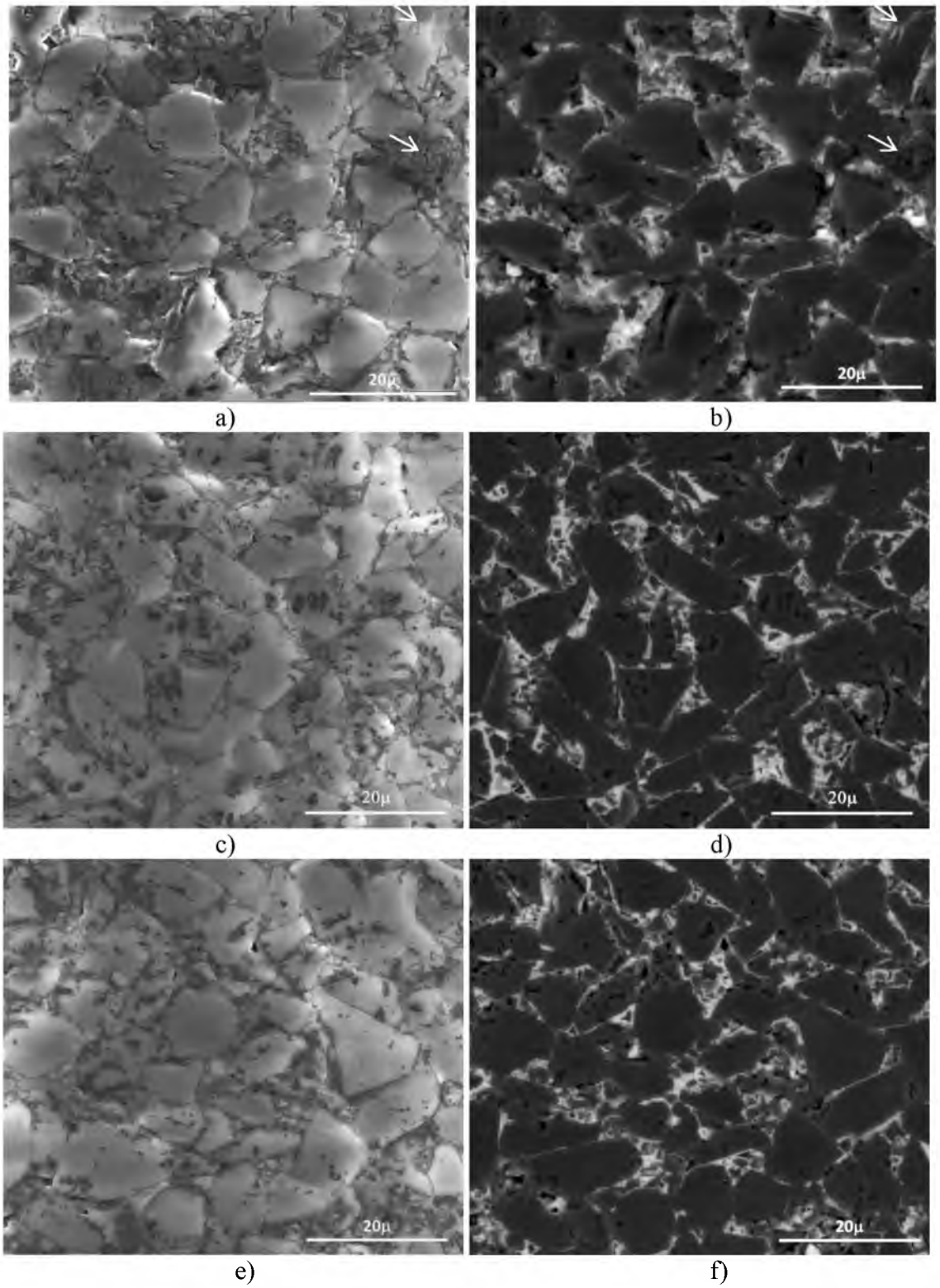

Figure 5-13. SE and BSE images of PCBN sintered using Mix I (cBN + 10vol%Al): a) and b) at 1245°C; c) and d) at 1350°C; e) and f) at 1490°C; all sintered for 15 min.

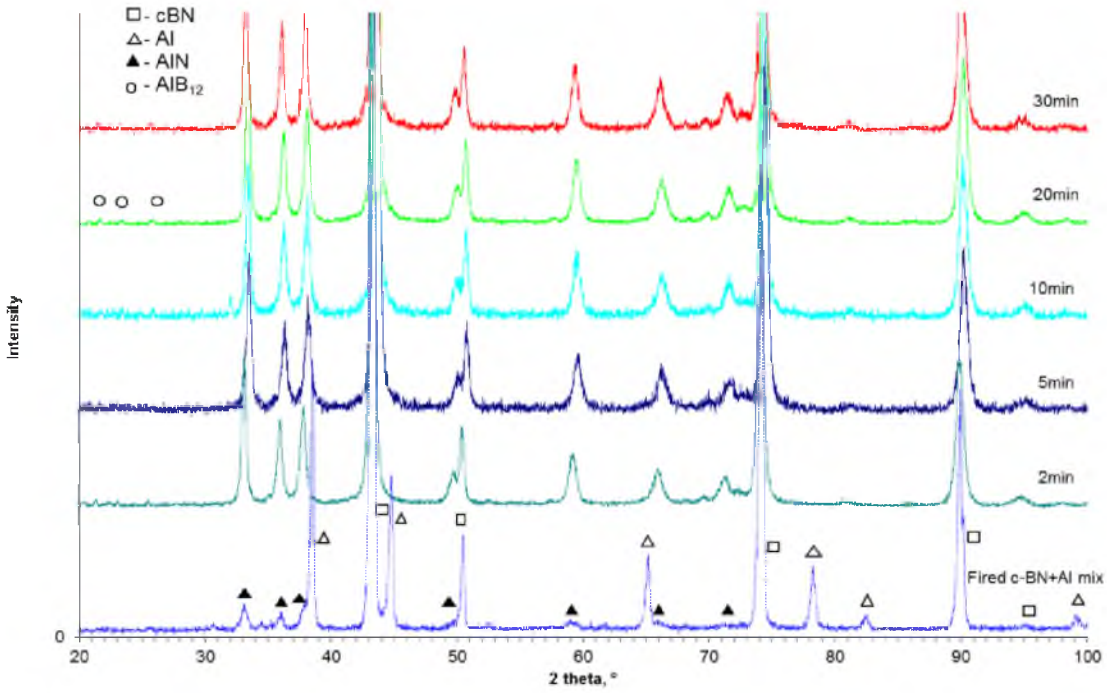

Figure 5-14. XRD patterns of PCBN HP/HT-sintered using Mix I (cBN + 10vol%Al) with different sintering times in the 1350°C range.

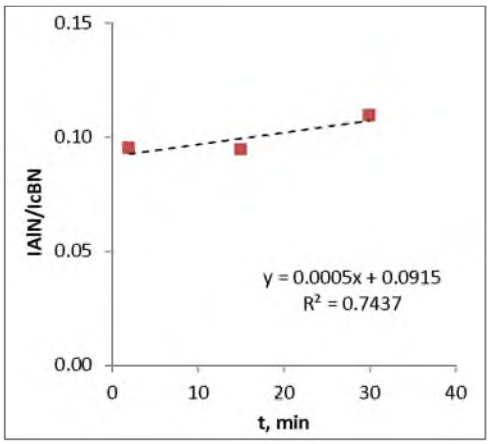

Figure 5-15. XRD intensity ratio of $I_{AlN(100)}/I_{cBN(111)}$ in the PCBN (90-10Al) sintered with different sintering time in the 1350°C temperature range.

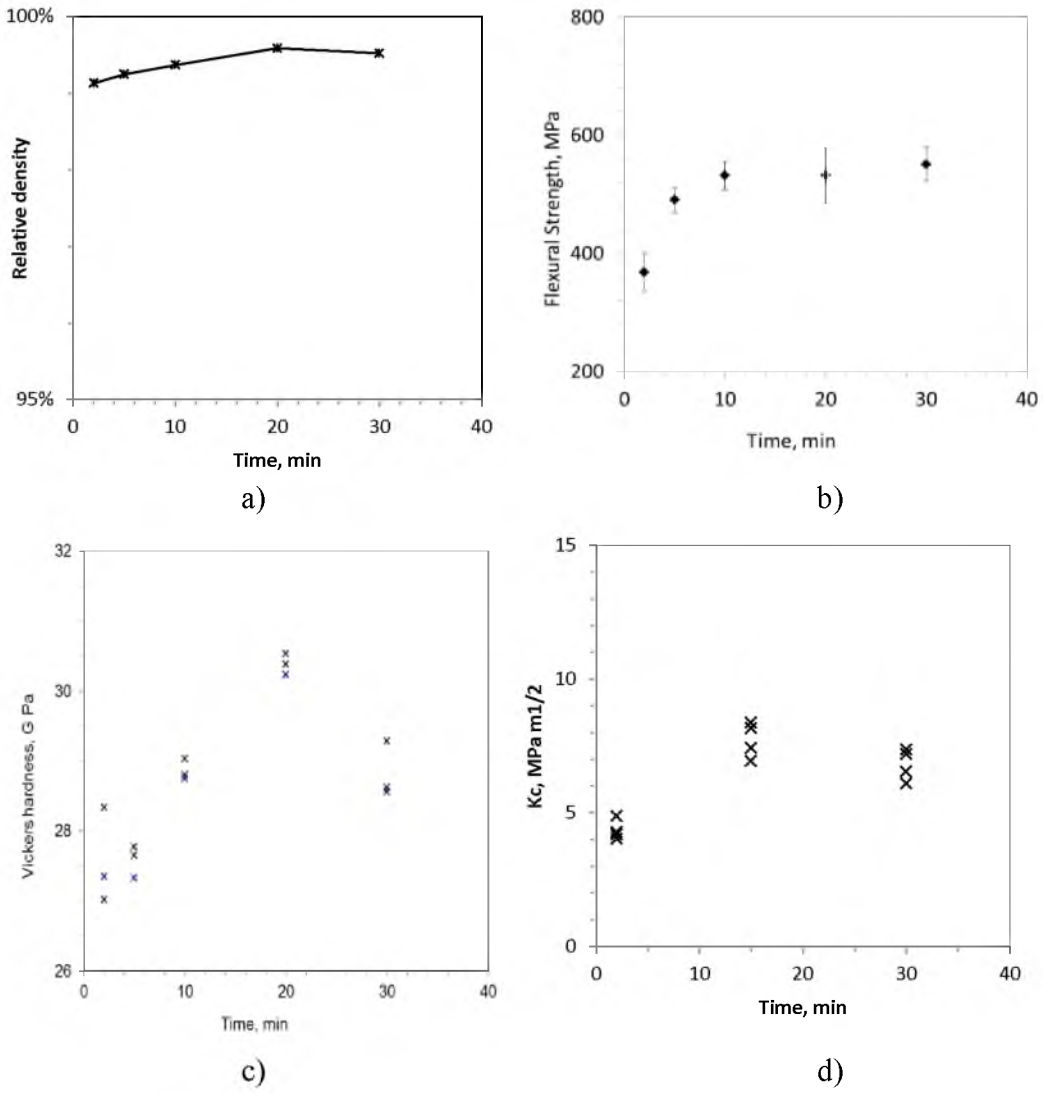

Figure 5-16. Effect of sintering time on properties of PCBN (90-10Al) sintered in the 1350°C range: a) relative density, b) four-point-bend flexural strength, c) Vickers hardness, and d) fracture toughness measured by indentation method.

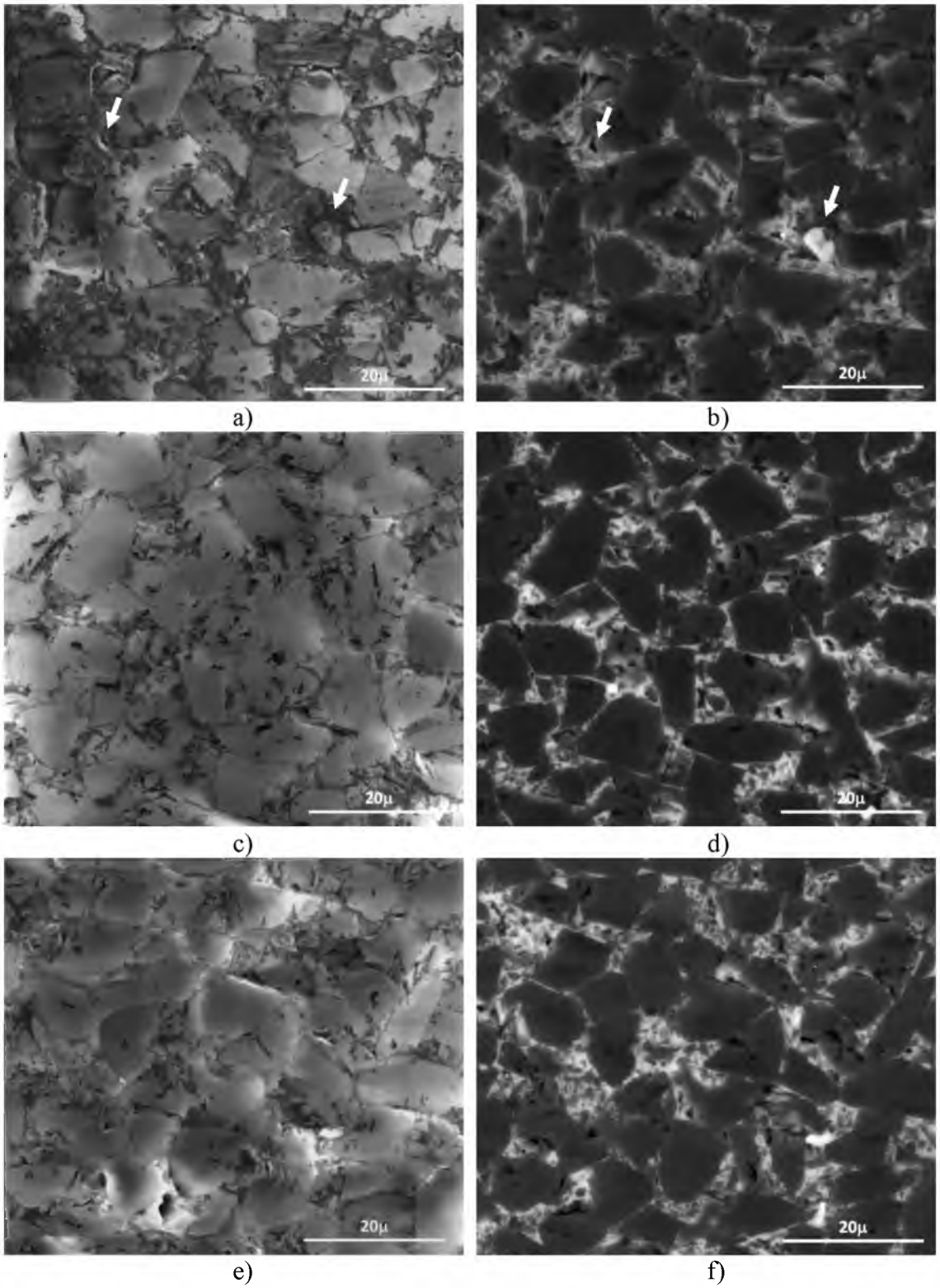

Figure 5-17. SE and BSE images of PCBN HP/HT(90-10Al) sintered at: a) and b) 2 min; c) and d) 15 min; e) and f) 30 min; all in the 1350°C temperature range.

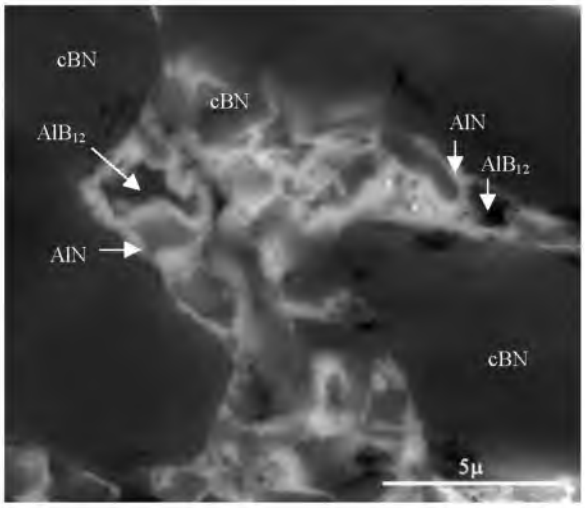

Figure 5-18. BSE image PCBN (90-10Al) showing cBN grains surrounded by AlN and AlB_{12}.

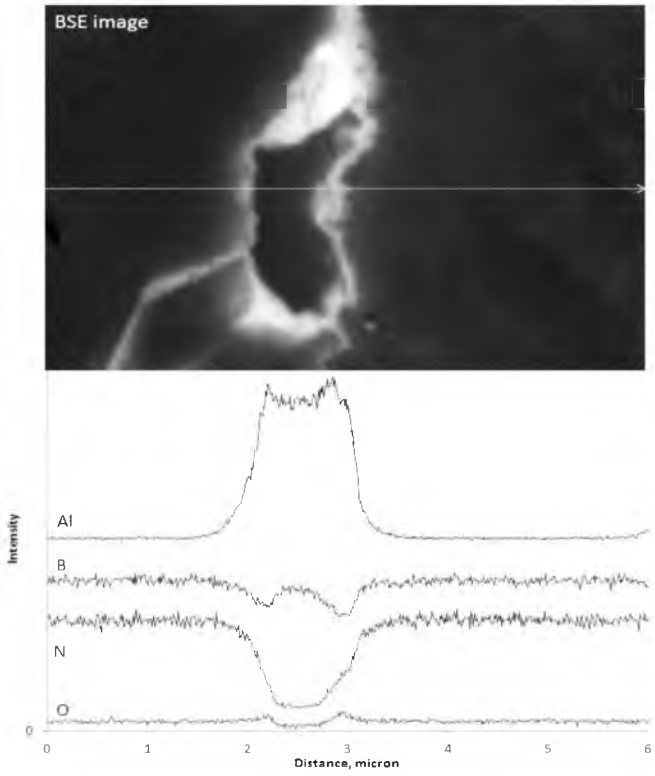

Figure 5-19. X-ray line-scan across the cBN grain boundary area and the relative intensity of the elements.

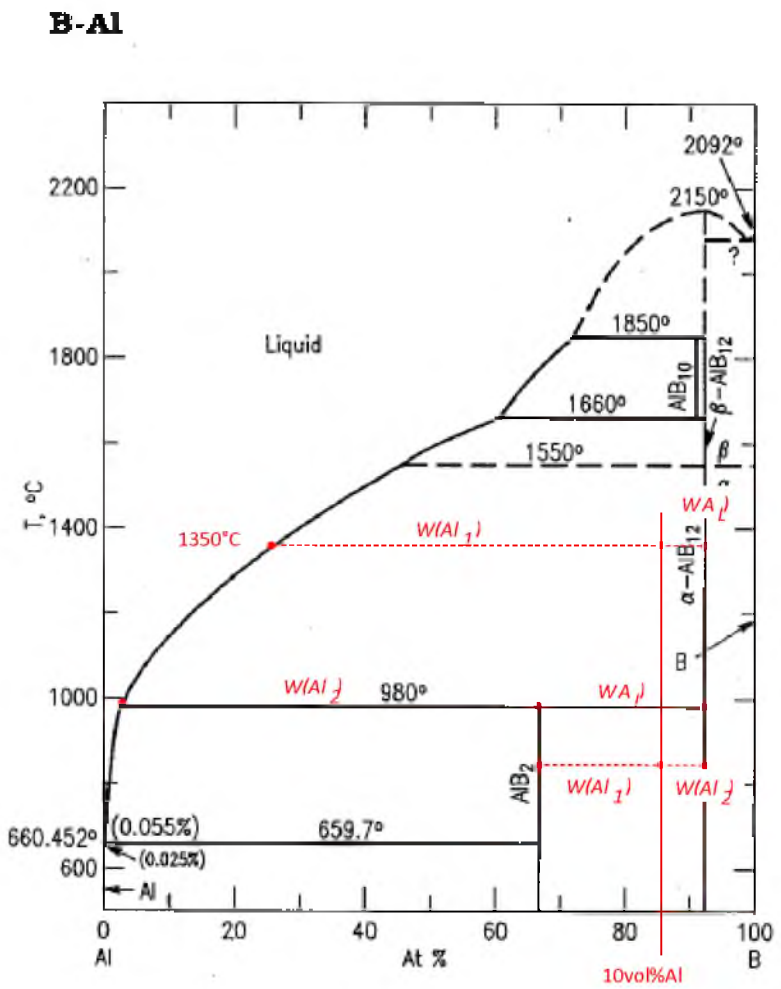

Figure 5-20. Mix I (90-10vol%Al) composition superimposed on Figure 2-6. B-Al phase diagram. (Reprinted with permission from the Am. Ceram. So., Fig. 8801,77 originally published by Carlson, O. N. Bull. Alloy Phase Diagrams, 11[6], 1990, 560-566.)

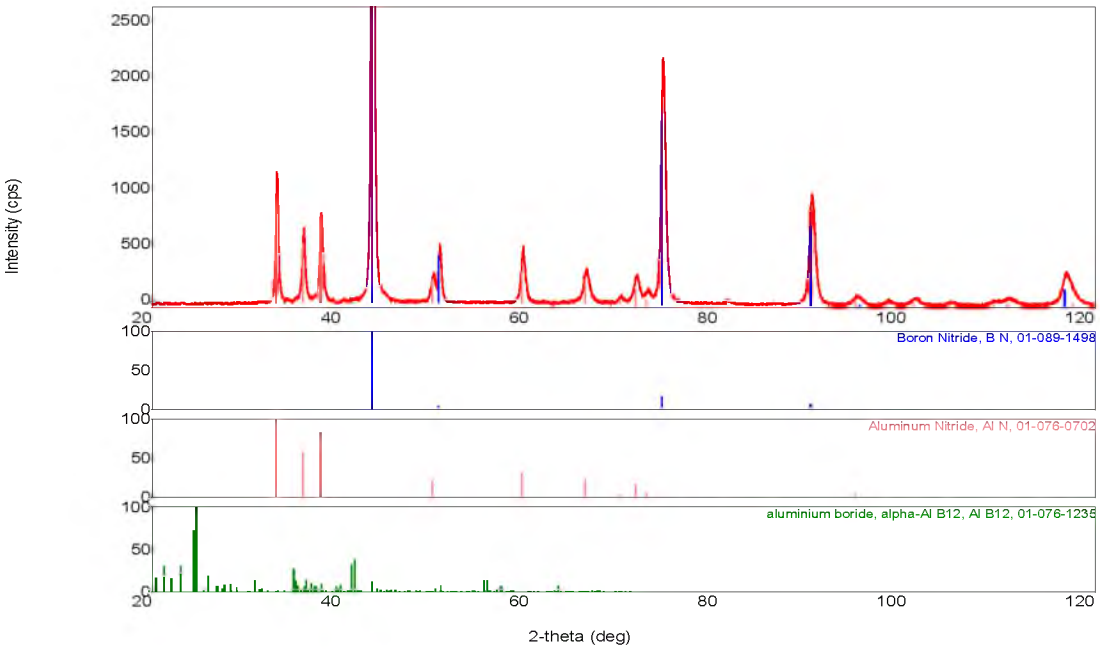

Compound	cBN	AlN	AlB_{12}
Wt%	87.8	8.6	3.6

Figure 5-21. XRD on PCBN (90-10Al) HP/HT sintered at 1350°C for 15 min.

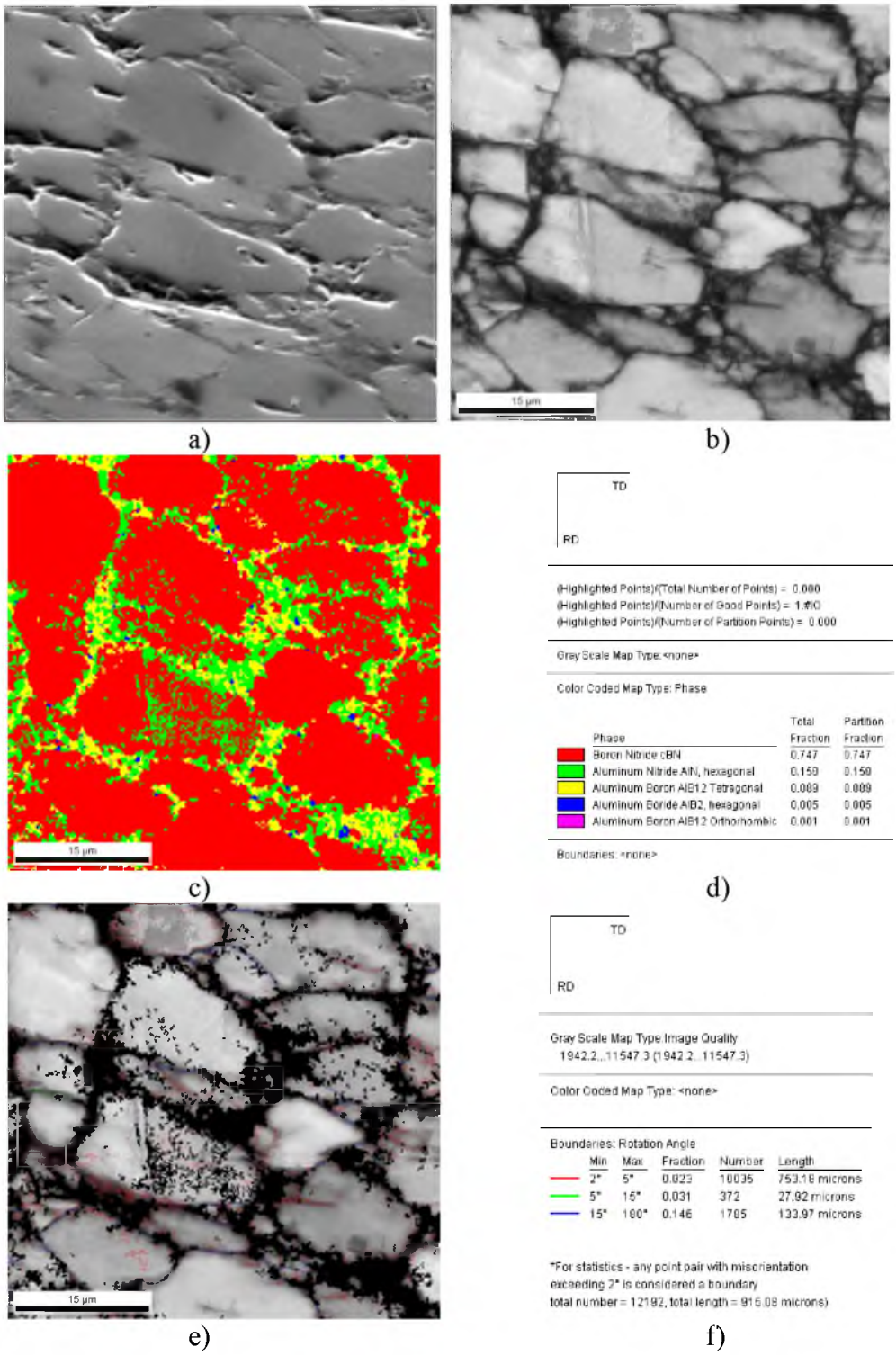

Figure 5-22. EBSD result of PCBN (90-10Al) sintered at 1245°C for 15 min: a) SEM image; b) EBSD image quality map; c) phase map; d) area fraction of all phases; e) cBN grain image-quality map superimposed with grain-boundary rotation angles; and f) rotation-angle range of cBN grain-boundaries marked.

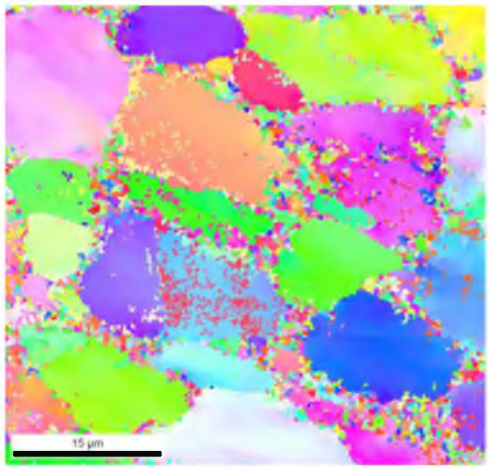

a)

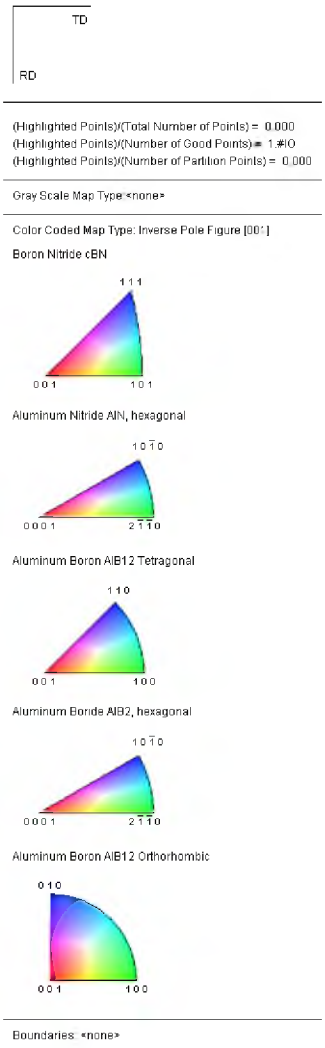

b)

Figure 5-23. EBSD results: a) orientation mapping of all phases in the PCBN analyzed and b) inverse pole figures of each phase, in PCBN (90-10Al) sintered at 1245°C for 15 min.

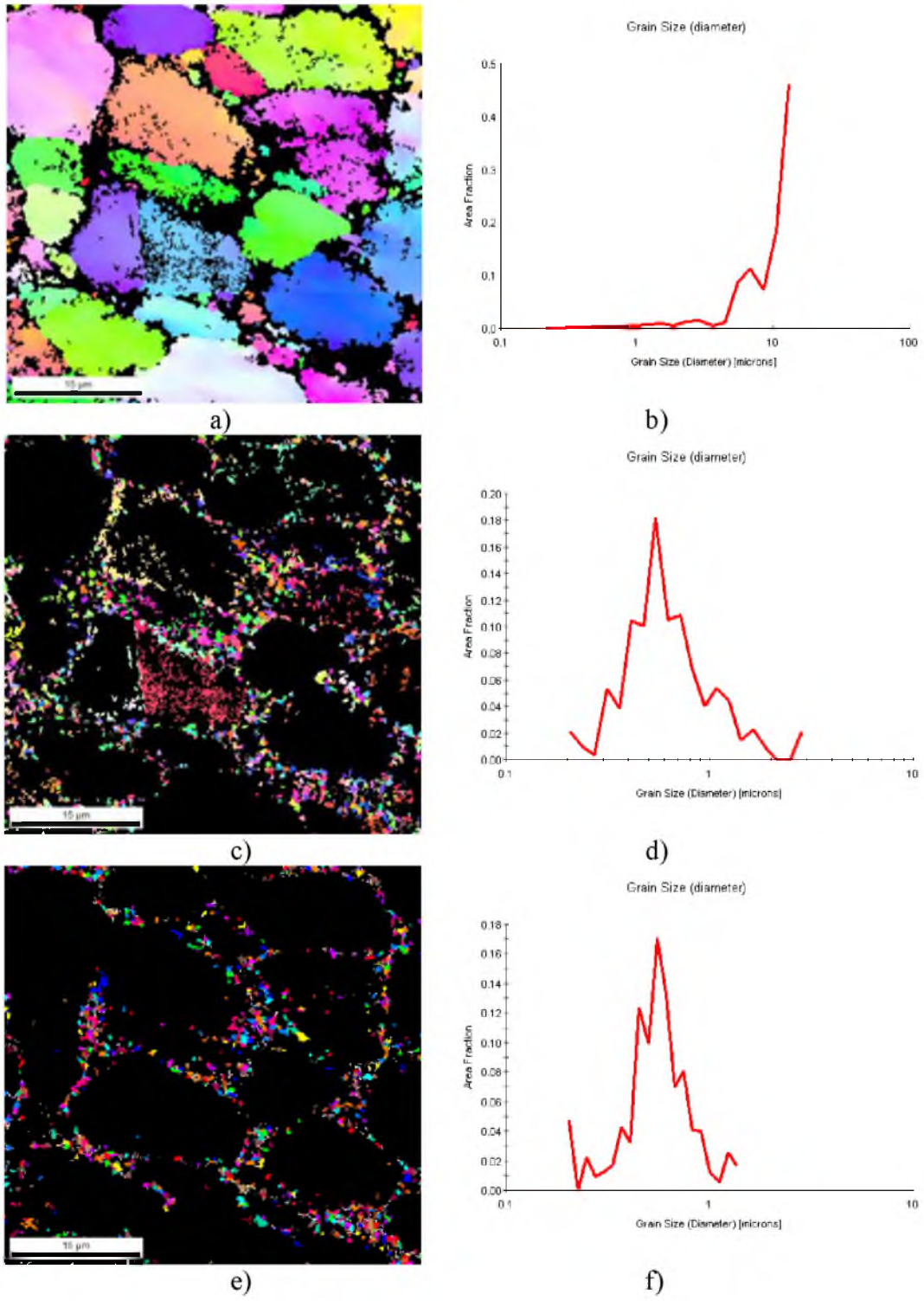

Figure 5-24. Phase and orientation map, grain size: a) and b) cBN; c) and d) AlN; e) and f) AlB_{12}; and g) and h) AlB_2 in PCBN (90-10Al) HP/HT-sintered at 1245°C for 15 min.

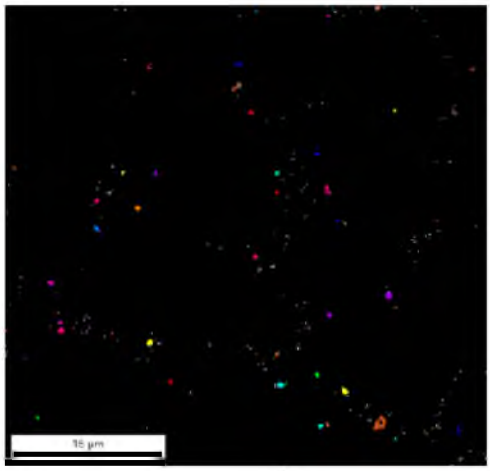

g)

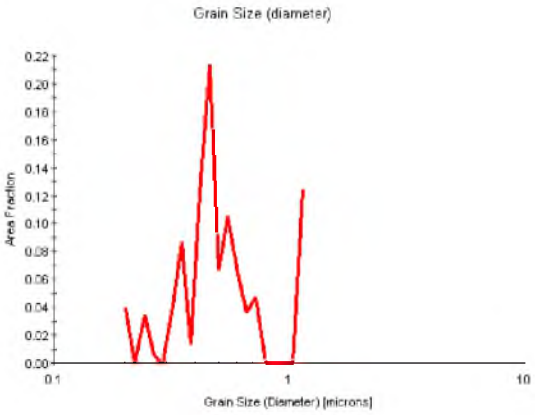

h)

Figure 5-24. Continued.

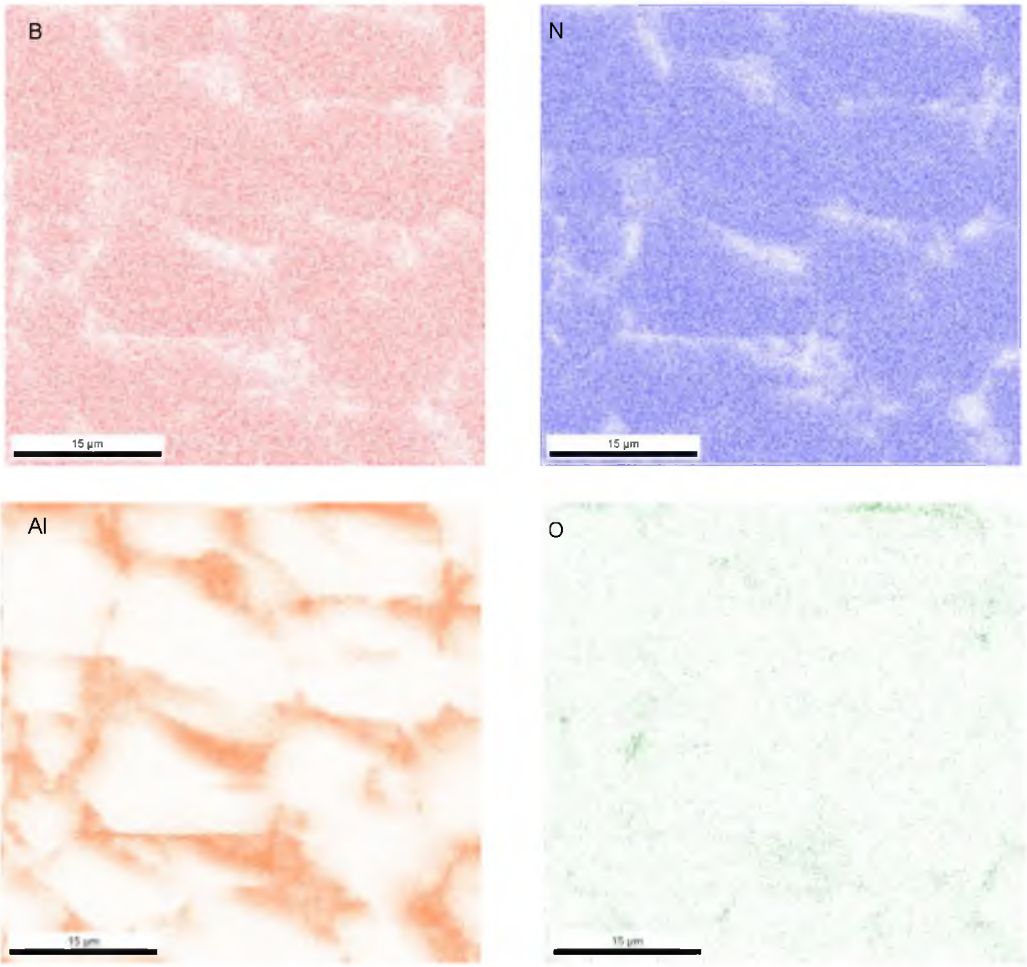

Figure 5-25. Boron (B), nitrogen (N), aluminum (Al), and oxygen (O) mapping collected simultaneously with the EBSD, in PCBN (90-10Al) sintered at 1245°C for 15 min.

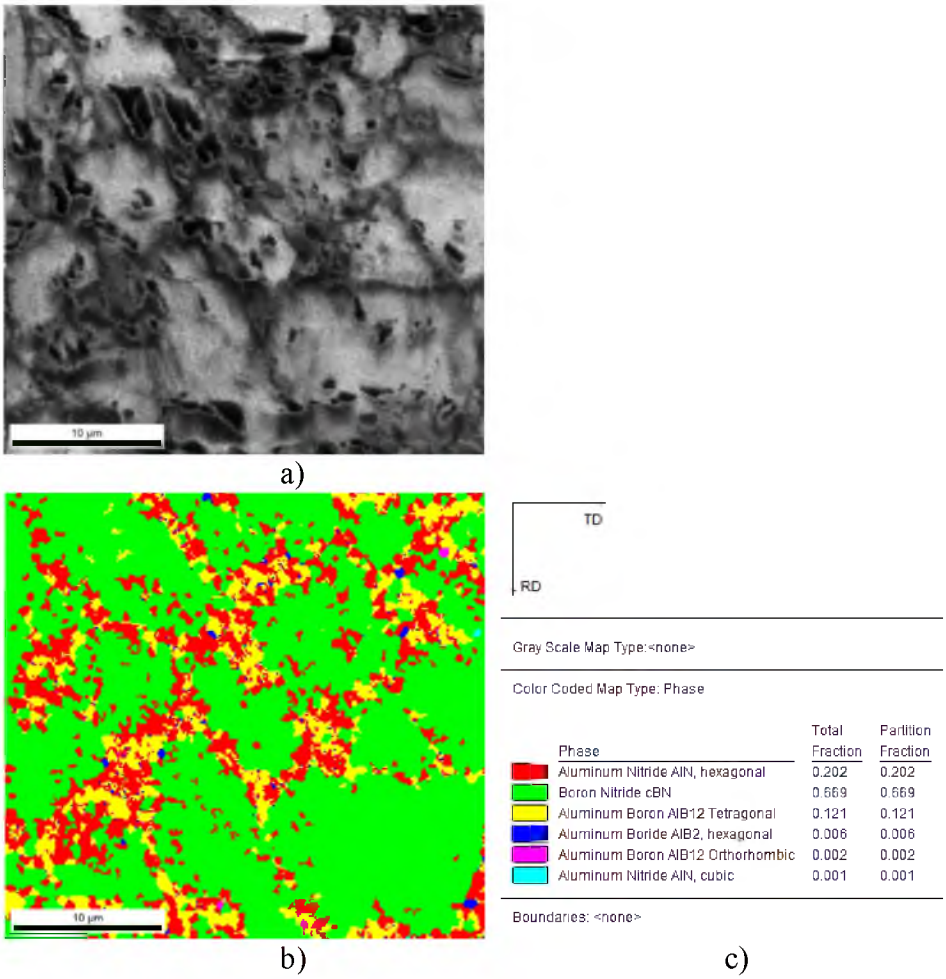

Figure 5-26. EBSD result: a) image quality map, b) phase map, and c) area fractions of phases in PCBN (90-10Al) HP/HT-sintered at 1420°C for 15 min.

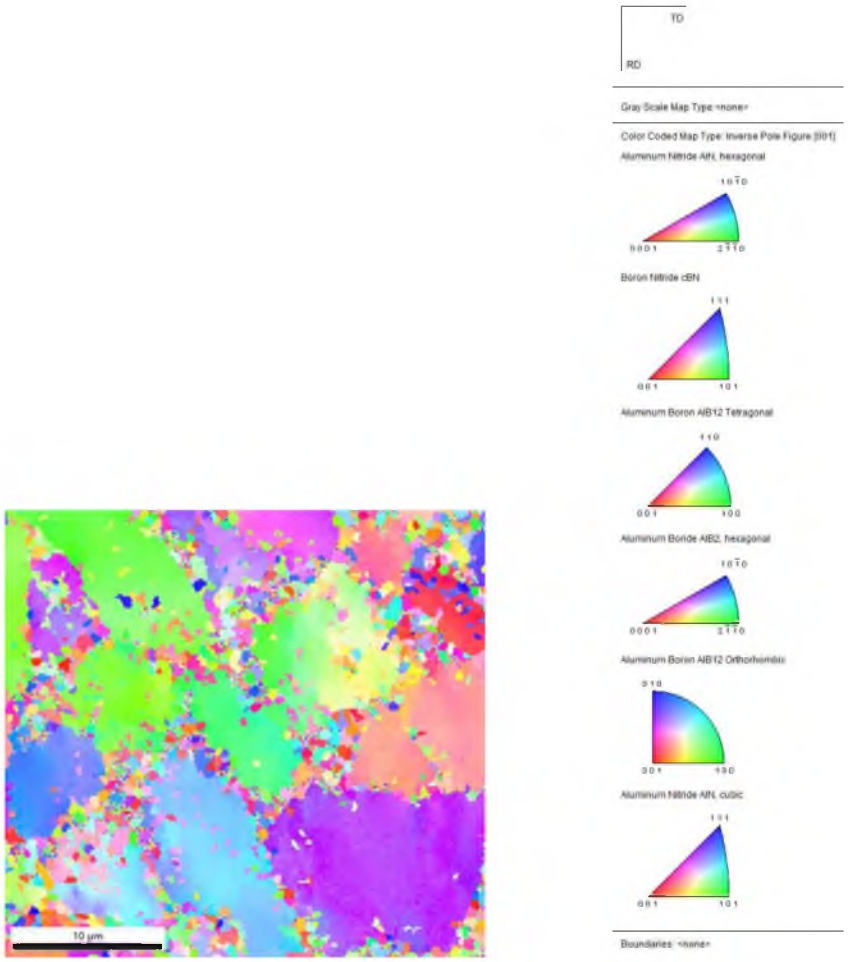

a) b)

Figure 5-27. EBSD results: a) orientation mapping of all phases in the PCBN analyzed and b) inverse pole figures of each phase in PCBN (90-10Al) sintered at 1420°C for 15 min.

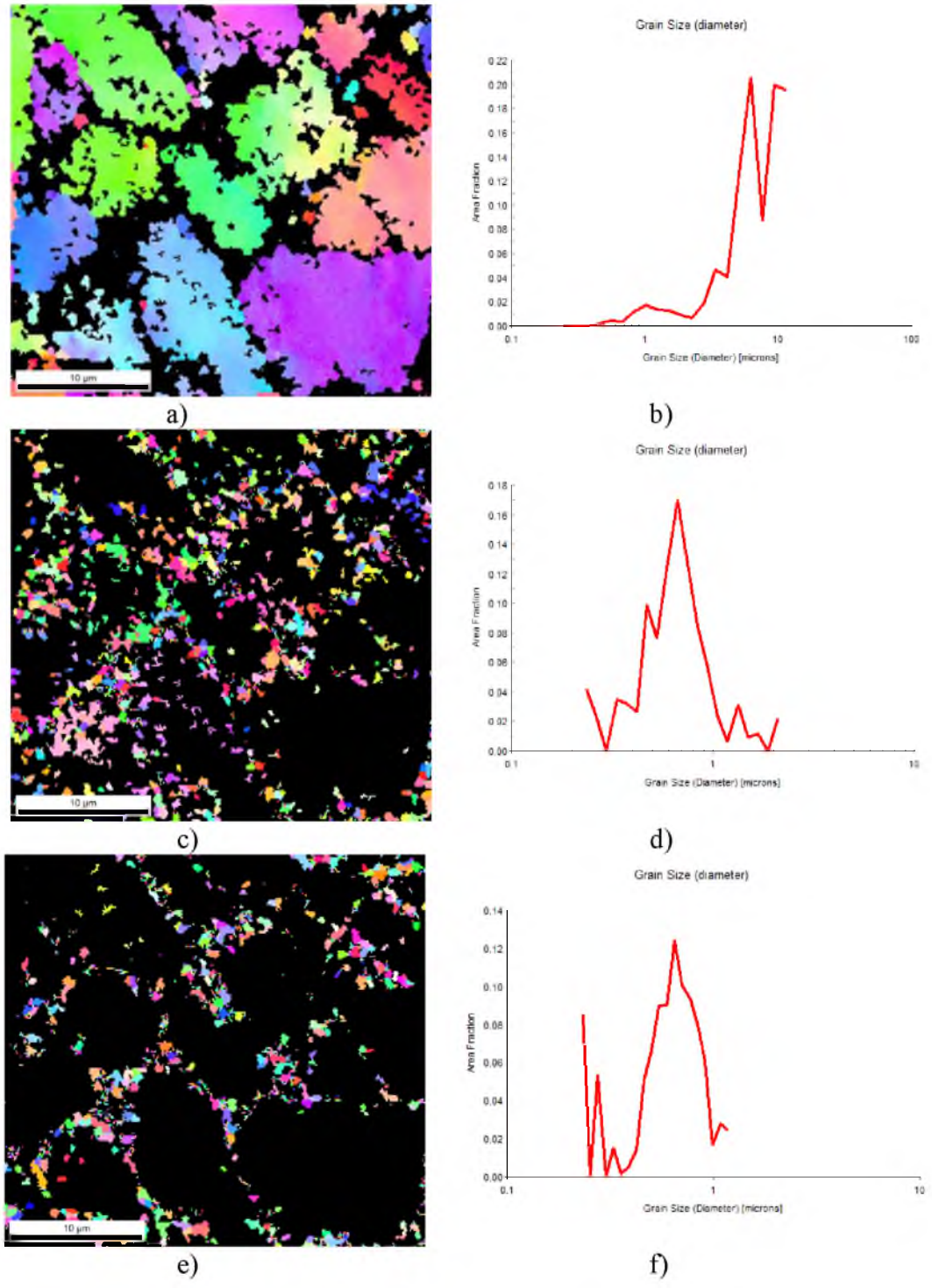

Figure 5-28. Phase and orientation map and grain size distribution of: a) and b) cBN; c) and d) AlN; e) and f) AlB_{12}; and g) and h) AlB_2 in PCBN (90-10Al) sintered at 1420°C for 15 min.

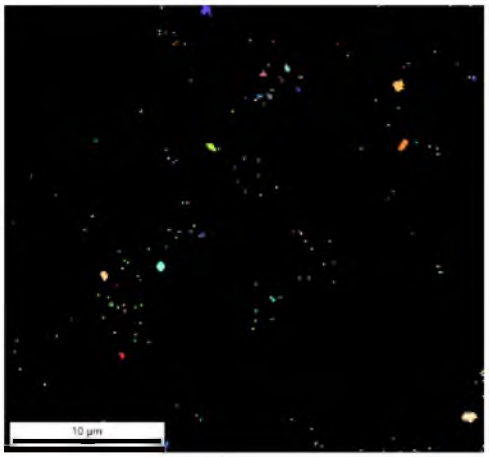

g)

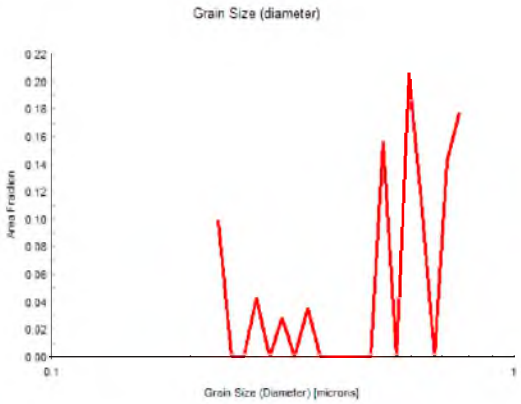

h)

Figure 5-28. Continued.

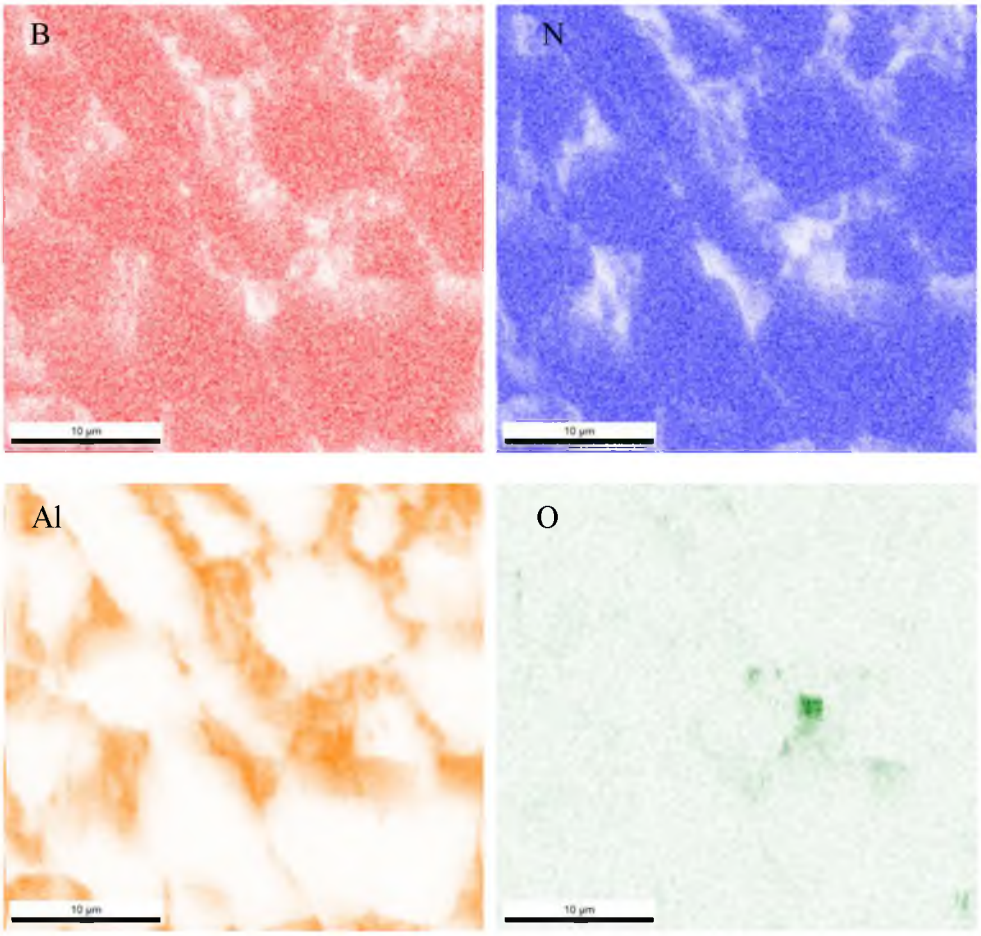

Figure 5-29. Boron (B), nitrogen (N), aluminum (Al), and oxygen (O) mapping collected simultaneously with the EBSD, in PCBN (90-10Al) sintered 1420°C for 15 min.

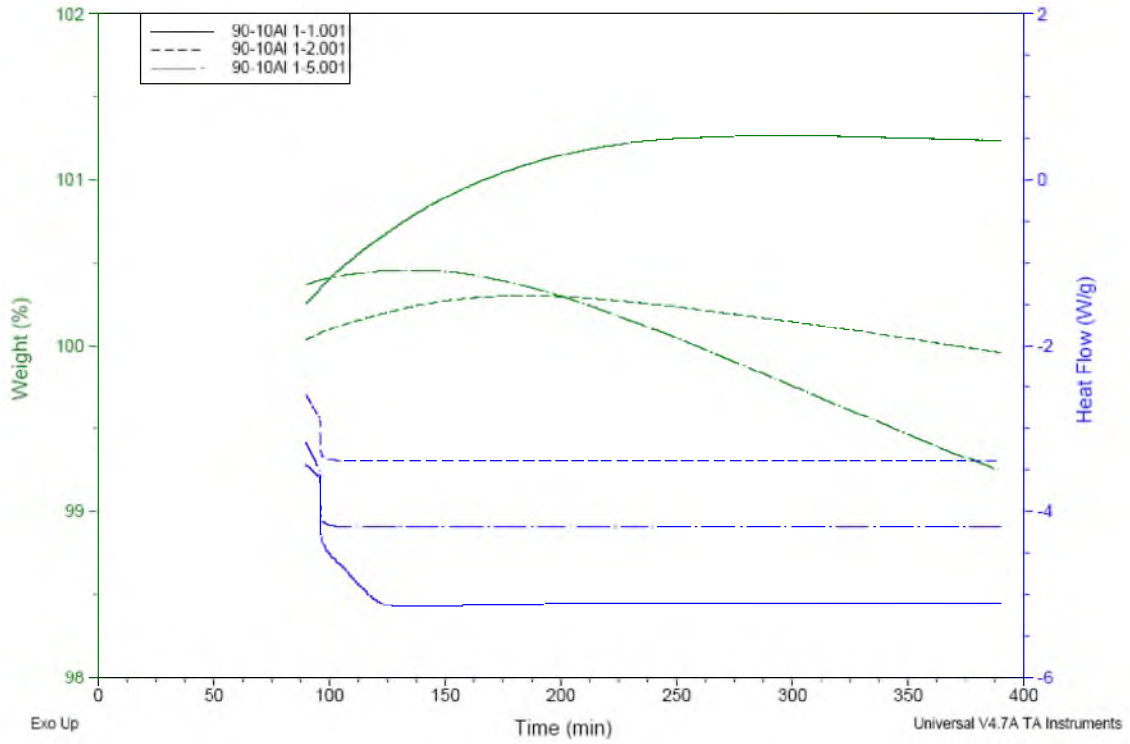

Figure 5-30. TGA response of PCBN (90-10Al), at 1000°C for 300 min in air, where sample 1-1 was sintered at 1350°C for 2 min; 1-2 at 1245°C for 15 min; and 1-5 at 1420°C for 15 min.

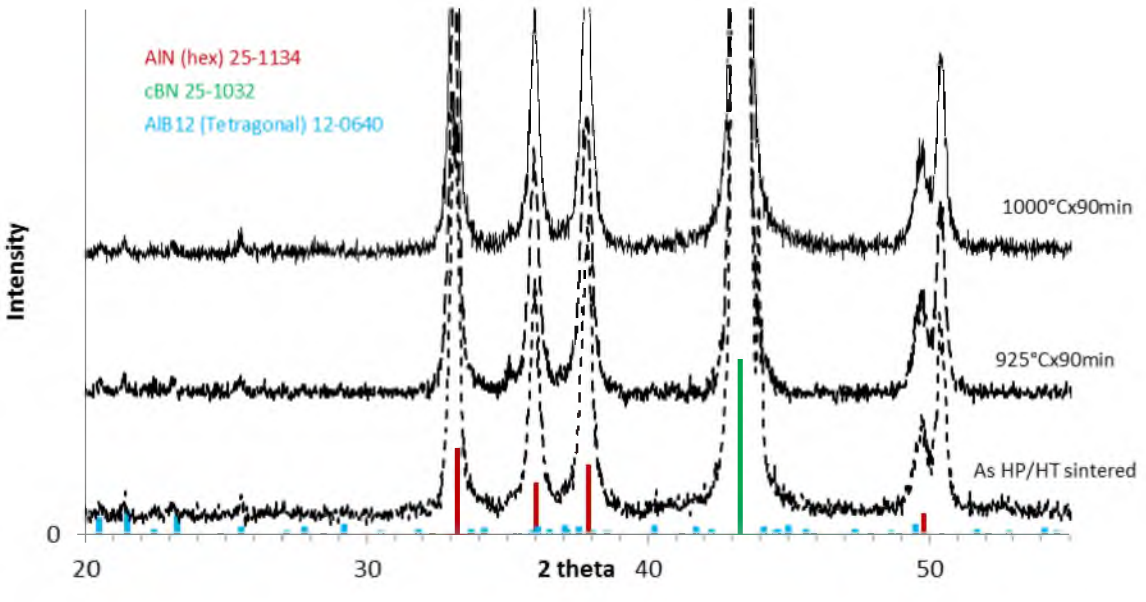

Figure 5-31. XRD patterns of PCBN (90-10Al) before and after heat treating at 925°C and 1000°C for 90 min in vacuum.

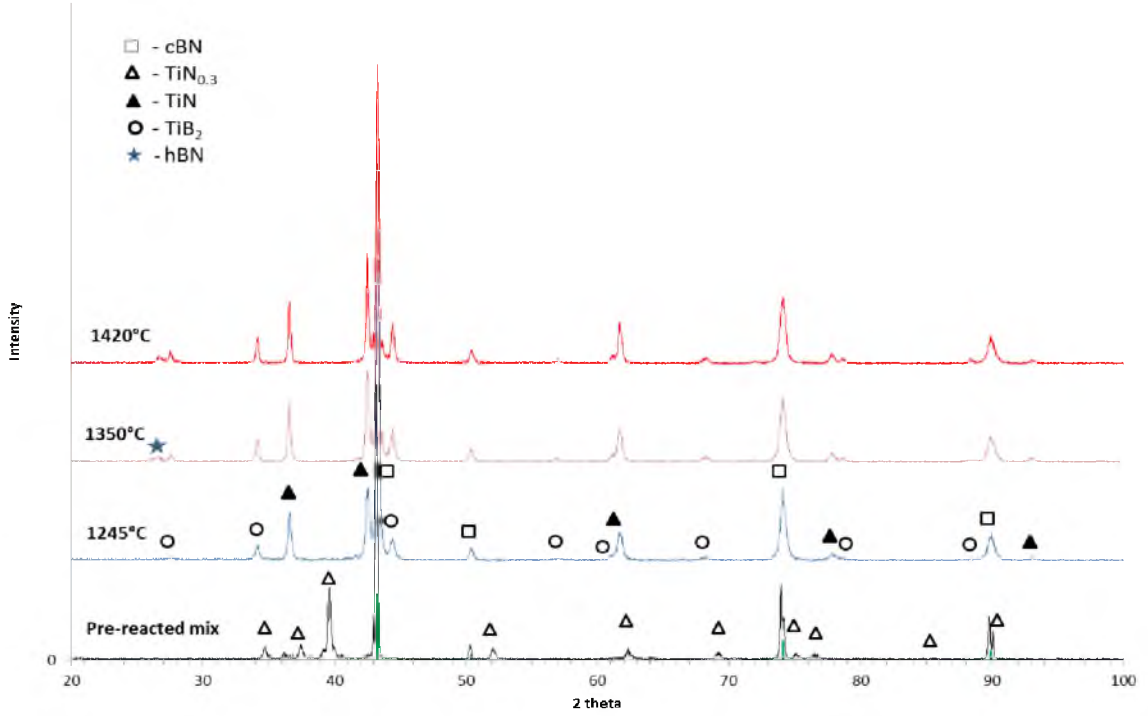

Figure-5-32. XRD patterns of PCBN HP/HT-sintered at different temperatures with 15 min sintering time, from Mix II (cBN+10vol%Ti).

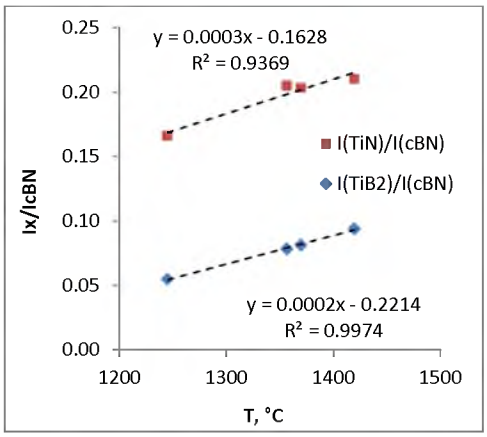

Figure 5-33. XRD intensity ratios of $I_{TiN(111)}/I_{cBN(111)}$ and $I_{TiB2(100)}/I_{cBN(111)}$ with respect to sintering temperature, in PCBN sintered using cBN+Ti powder.

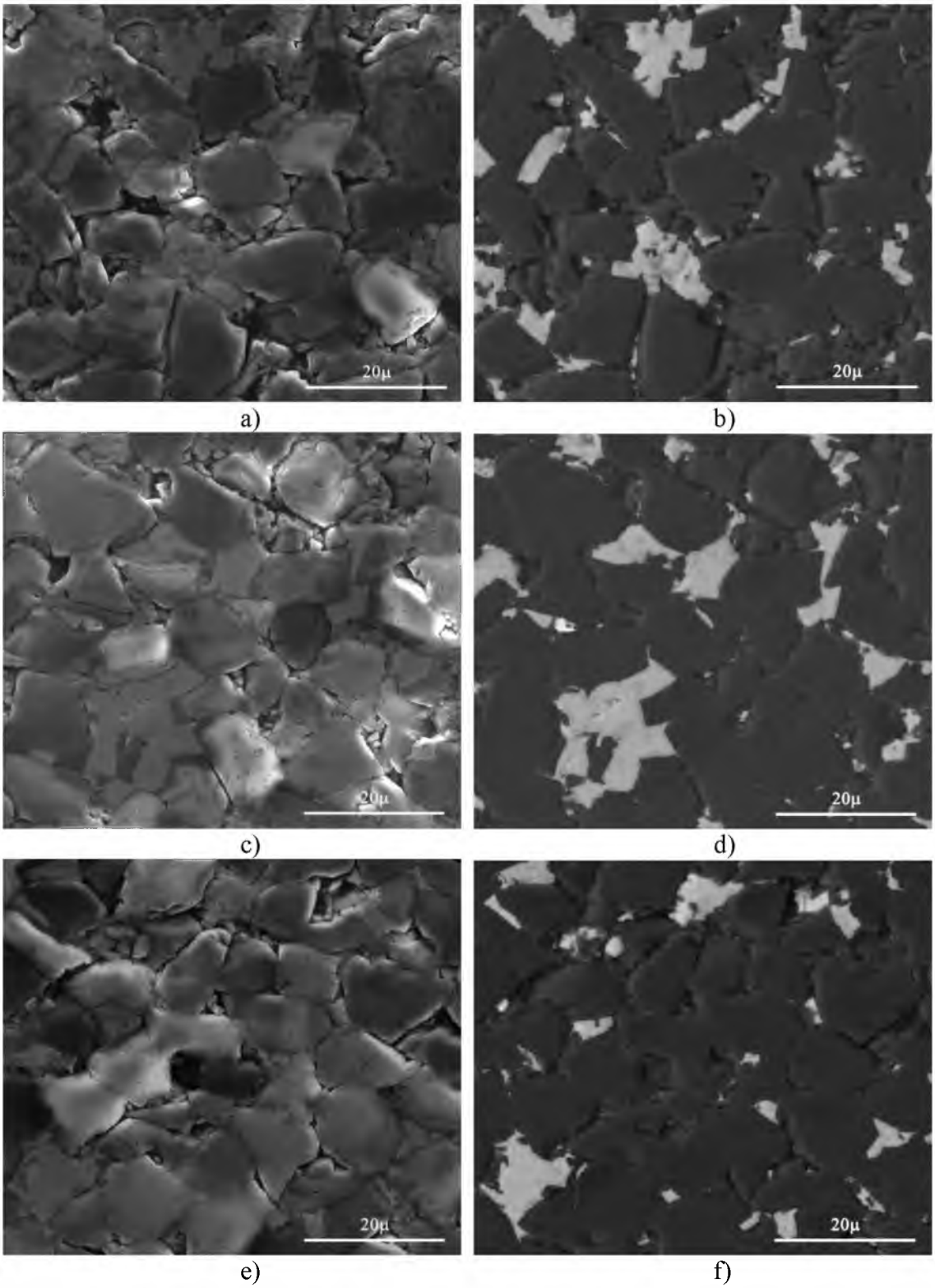

Figure 5-34. SE and BSE images of PCBN sintered using Mix II (cBN+10vol%Ti): a) and b) at 1245°C; c) and d) at 1350°C c); e) and f) at 1420°C, all sintered for 15 min.

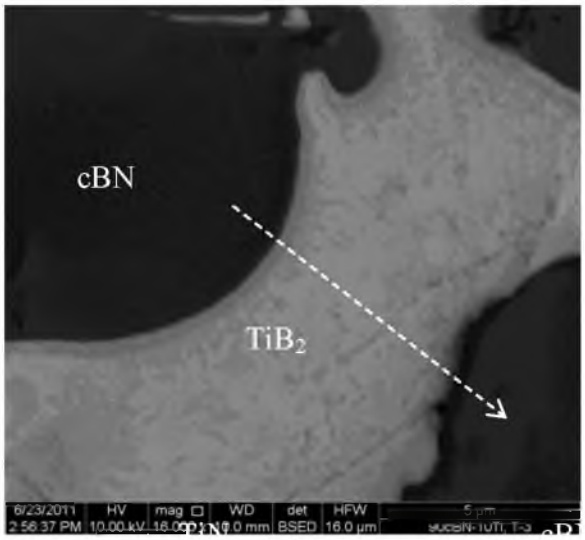

a)

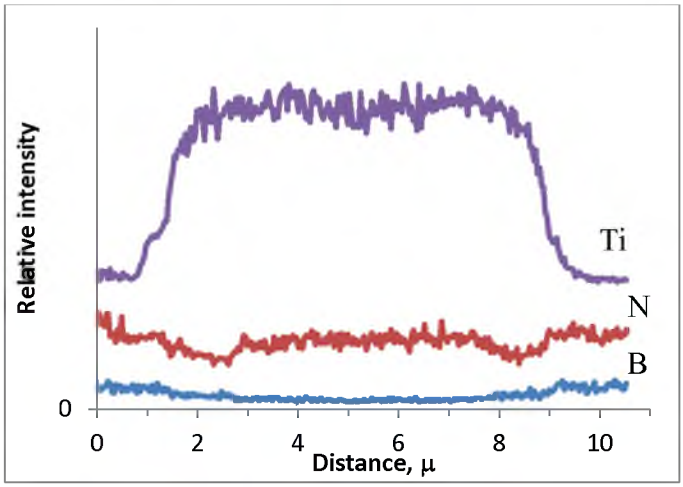

b)

Figure 5-35. Intergranular cBN-Ti boundary area in PCBN (90-10Ti): a) SEM image of the cBN grain boundaries and b) x-ray line scan as indicated by the arrow.

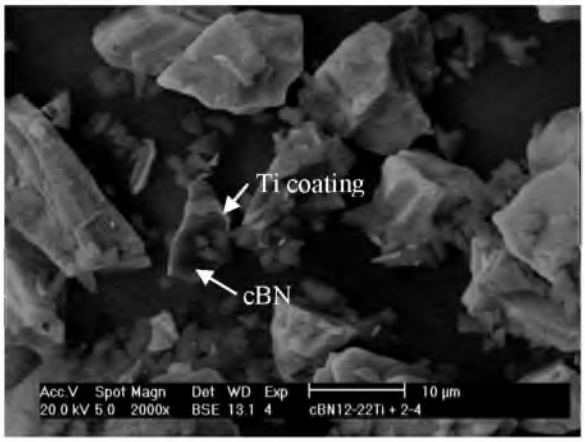

Figure 5-36. Mix III (Ti-coated cBN), after 90 min at 1000°C pre-reaction in vacuum.

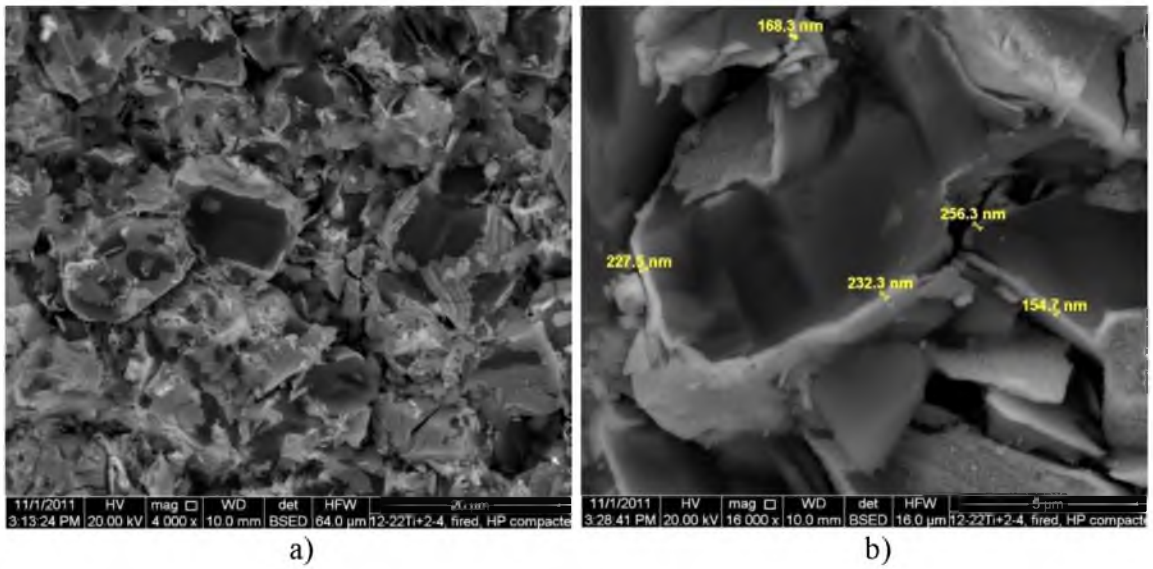

a) b)

Figure 5-37. Ultrahigh-pressure (5.5GP) cold-compacted Mix III (Ti-coated cBN): a) as compacted mix and b) measurements of the Ti-coating layer on cBN grains.

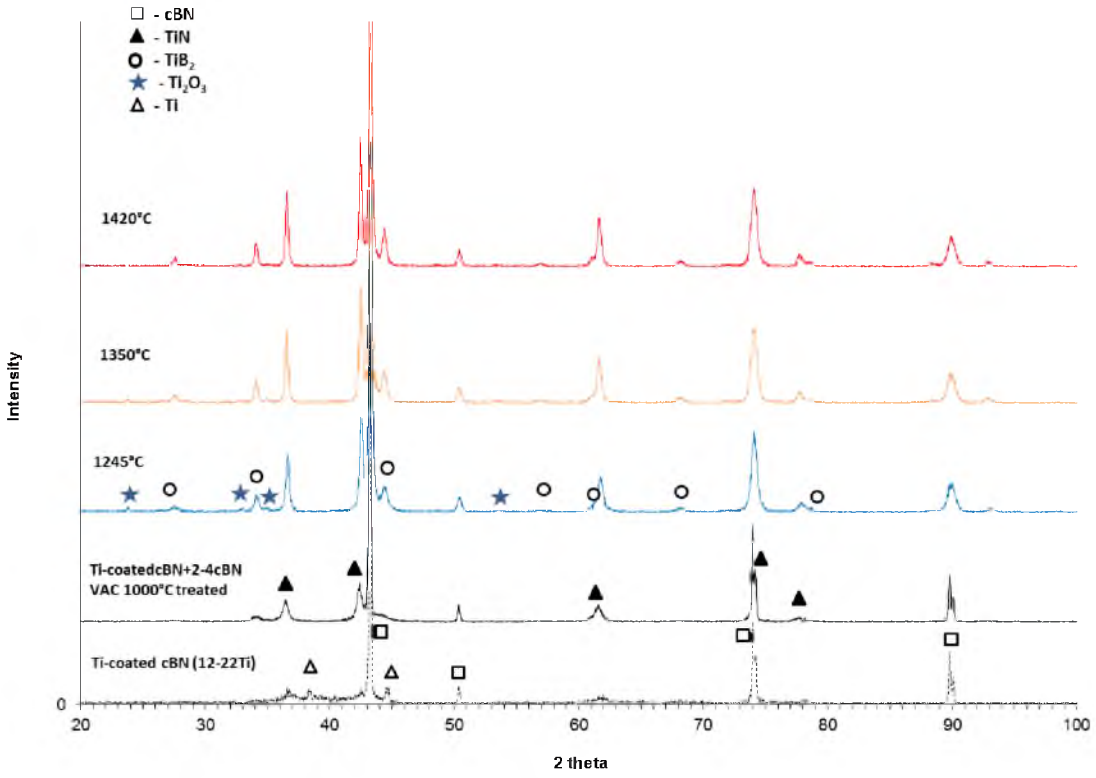

Figure 5-38. XRD patterns of PCBN HP/HT-sintered at different temperatures from Mix III (Ti-coated cBN) with 15 min sintering time.

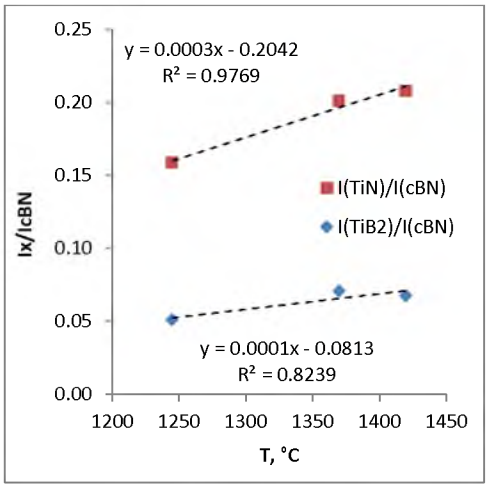

Figure 5-39. Intensity ratios of $I_{TiN(111)}/I_{cBN(111)}$ and $I_{TiB2(100)}/I_{cBN(111)}$, in PCBN (Ti-coated cBN), with respect to sintering temperature under 15 min sintering time.

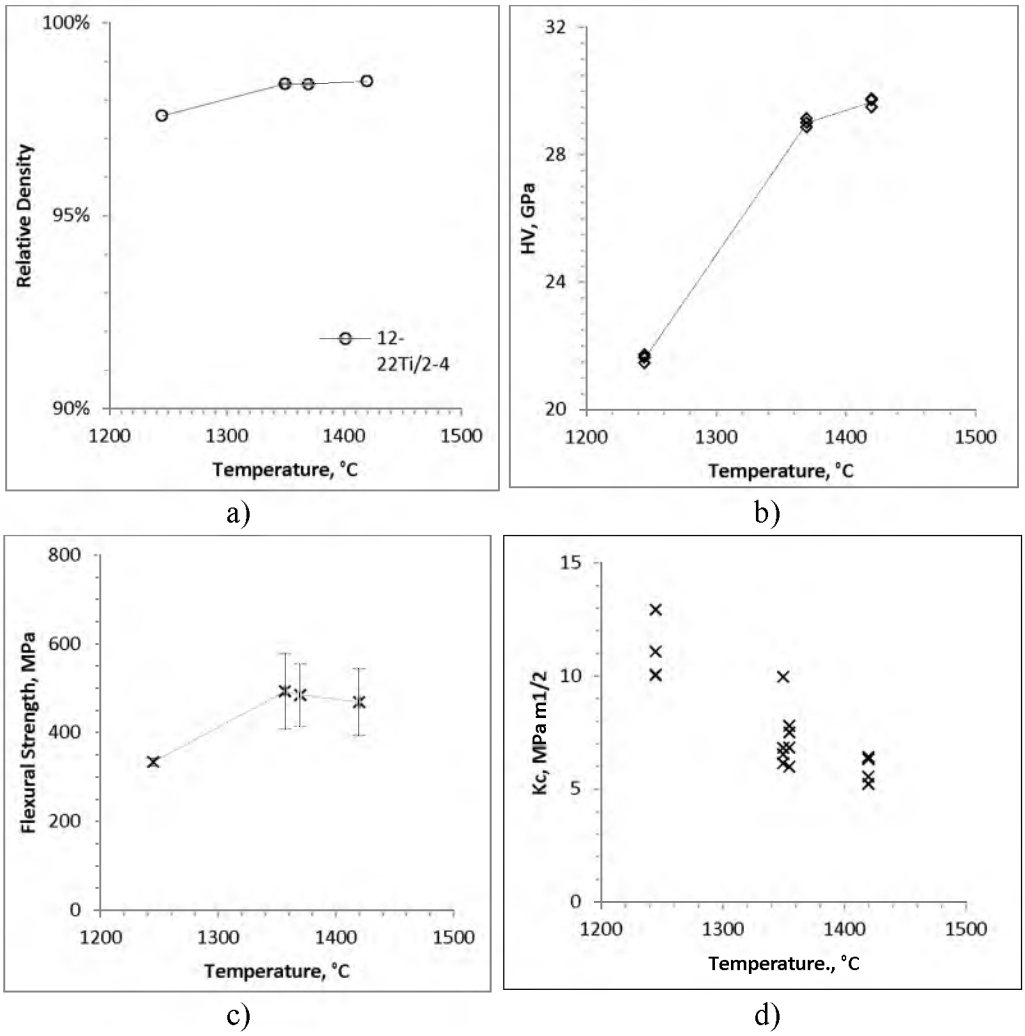

Figure 5-40. Effects of sintering temperature on PCBN (Ti-coated cBN): a) relative density; b) Vickers hardness; c) four-point-bend flexural strength; and d) indentation fracture toughness.

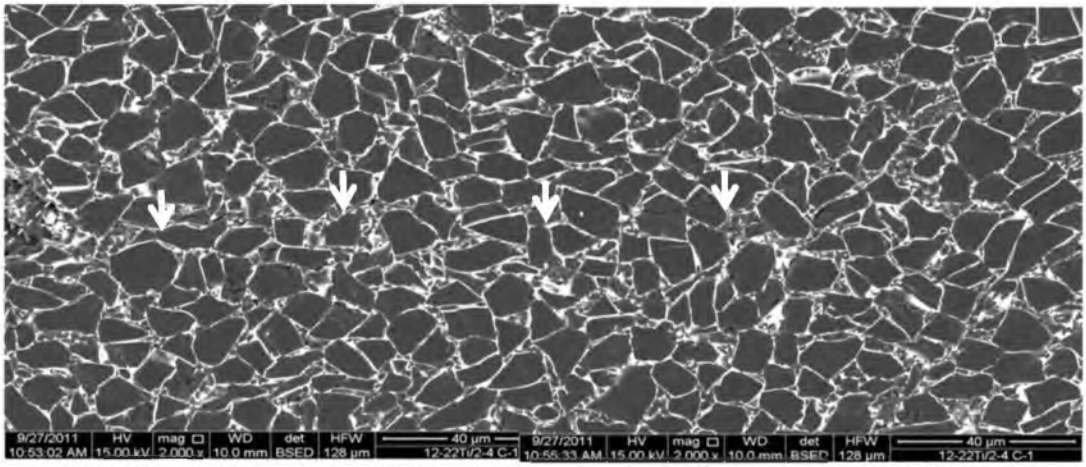

Figure 5-41. Crack induced by Vickers indentation in PCBN (Ti-coated cBN).

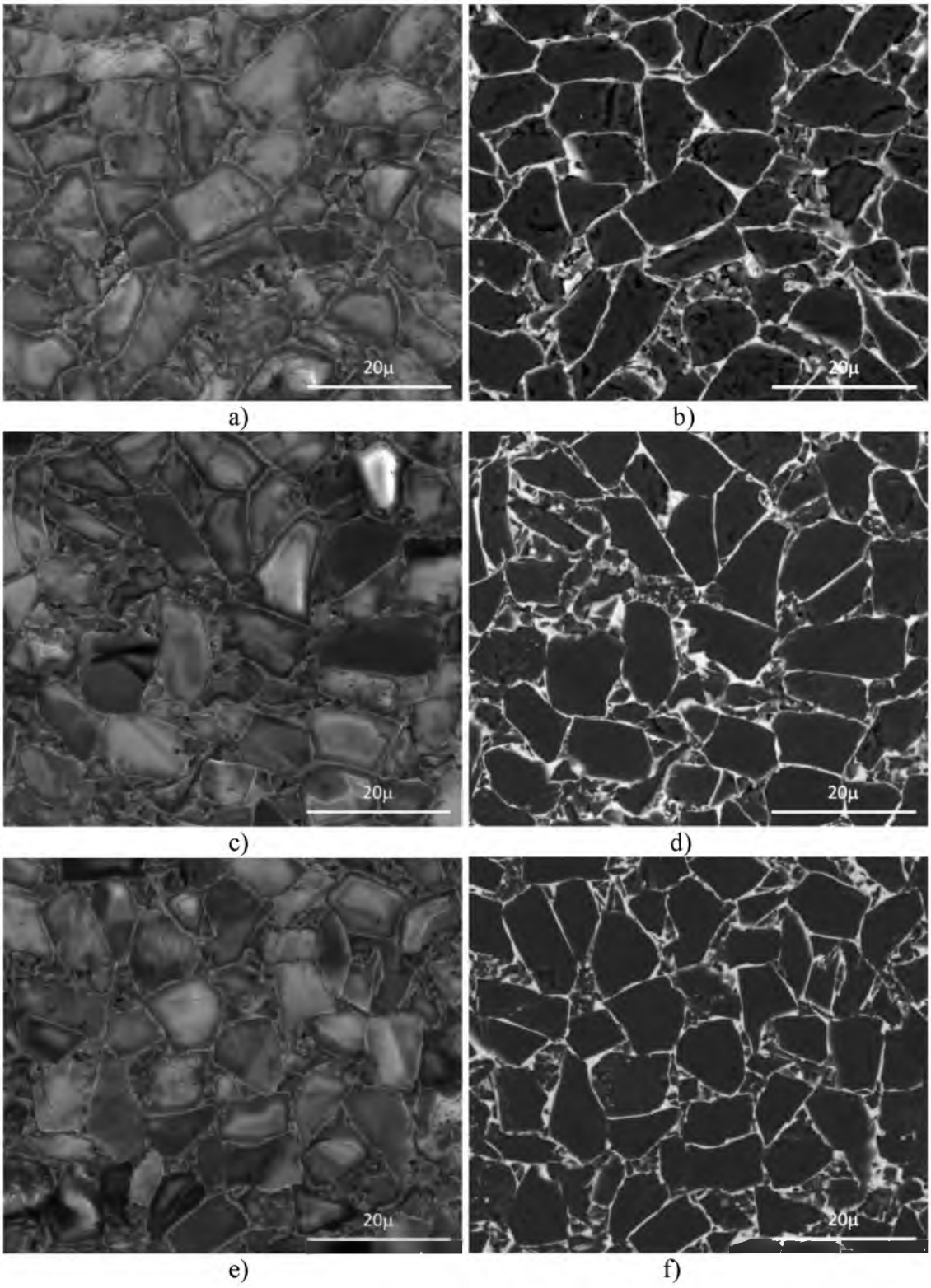

Figure 5-42. PCBN (Ti-coated cBN) sintered under different temperatures: a) SE and b) BSE images of 1245°C, c) an d) 1350°C, e) and f) 1420°C, with 15 min sintering time.

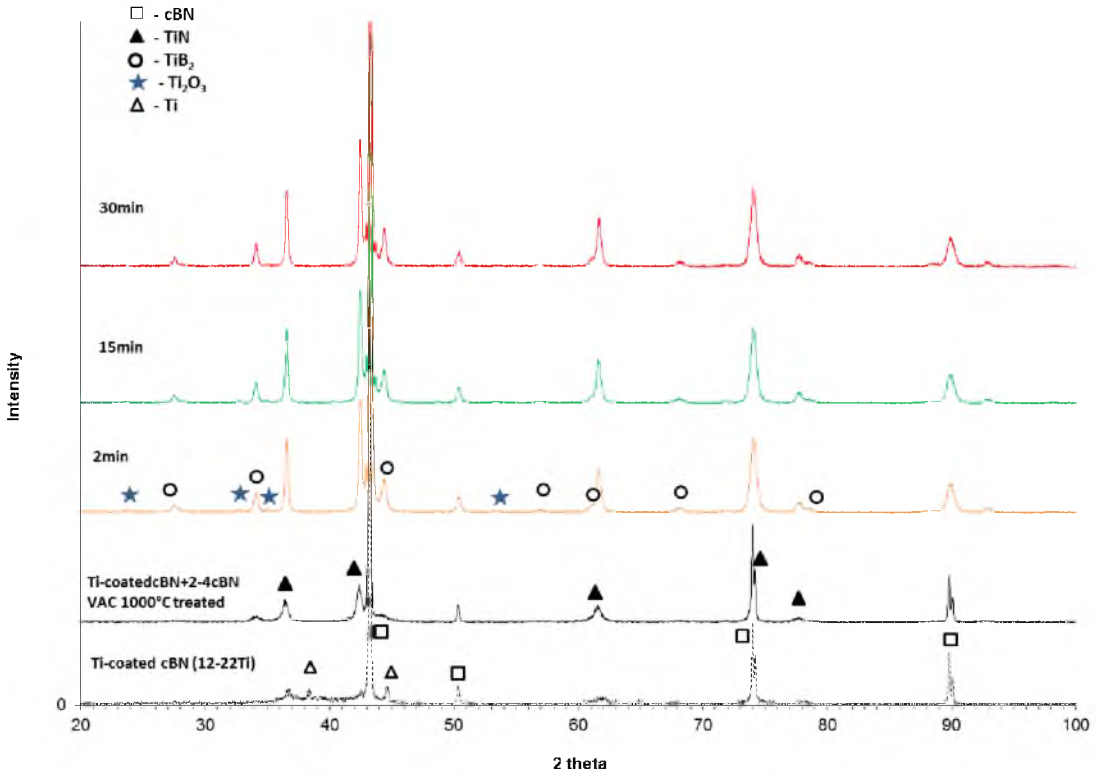

Figure 5-43. XRD patterns of PCBN HP/HT-sintered from Mix III (Ti-coated cBN).

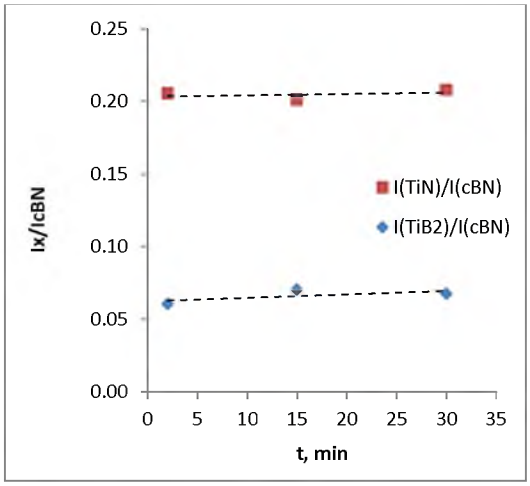

Figure 5-44. Intensity ratios of $I_{TiN(111)}/I_{cBN(111)}$ and $I_{TiB2(100)}/I_{cBN(111)}$ with respect to sintering time in PCBN (Ti-coated cBN).

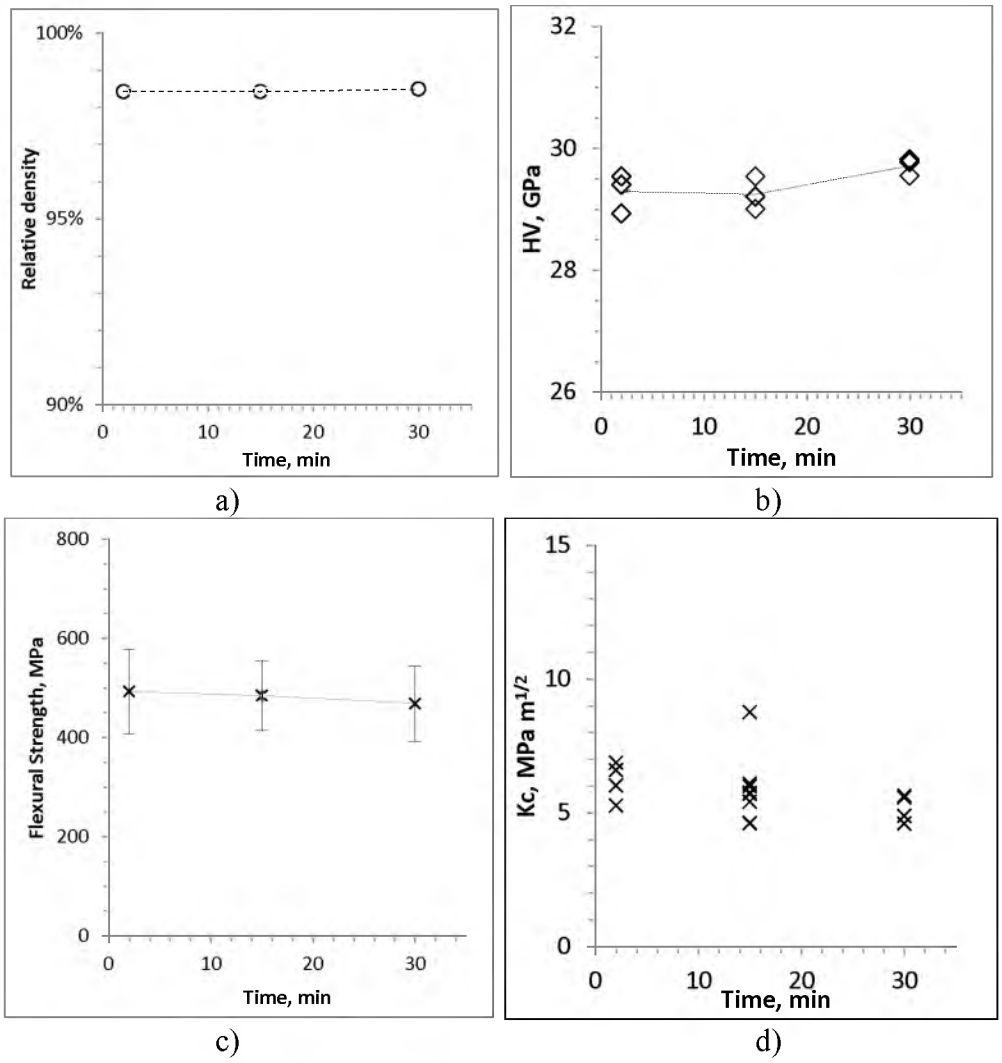

Figure 5-45. Effects of sintering time to PCBN HP/HT-sintered using Mix III (Ti-coated cBN): a) relative density; b) Vickers hardness; c) four-point-bend flexural strength; and d) indentation fracture toughness.

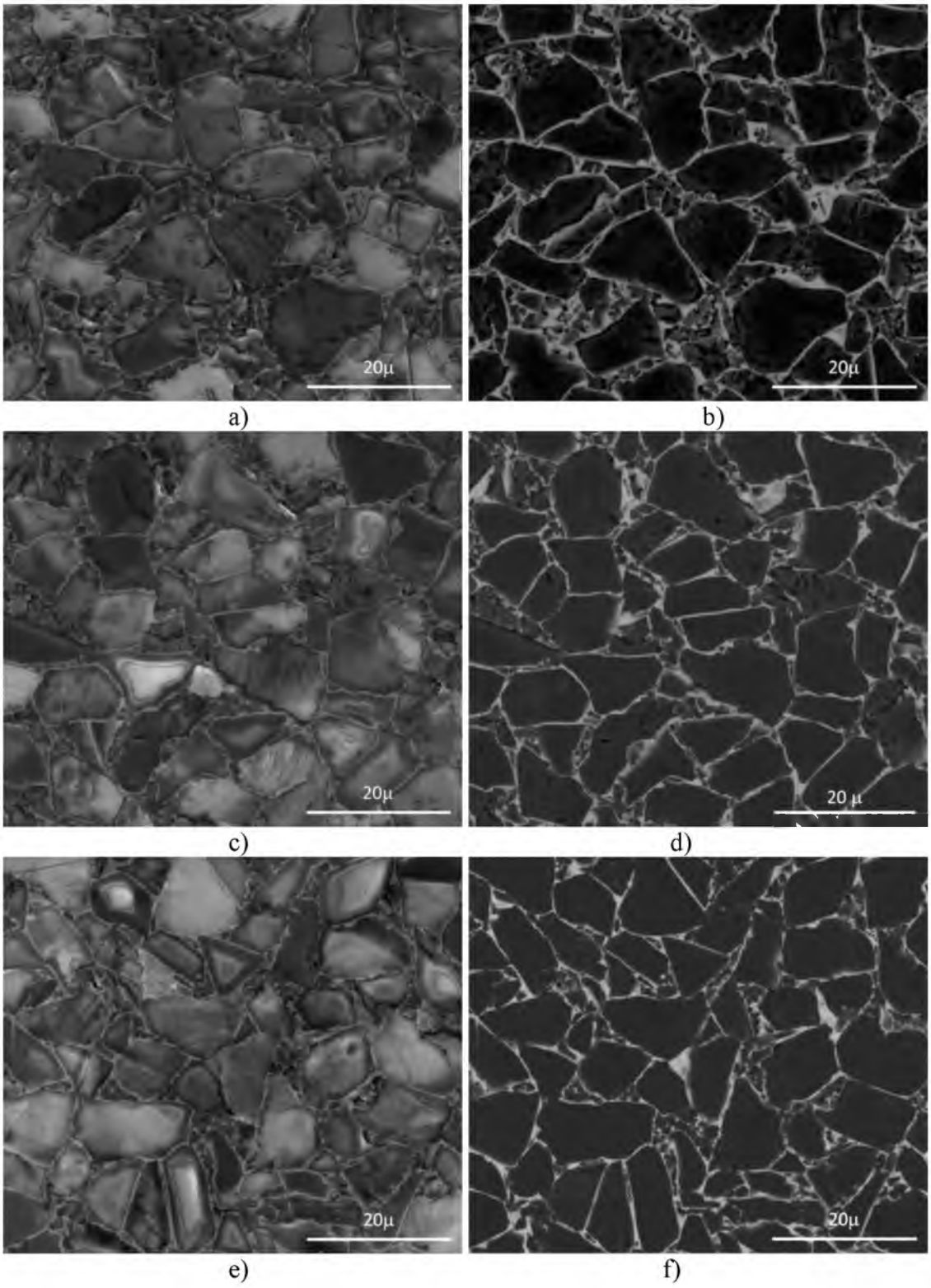

Figure 5-46. PCBN sintered using Mix III (Ti-coated cBN): a) SE and b) BSE images of 2 min, c) and d) 15 min, e) and f) 30 min sintering time in the 1350°C temperature range.

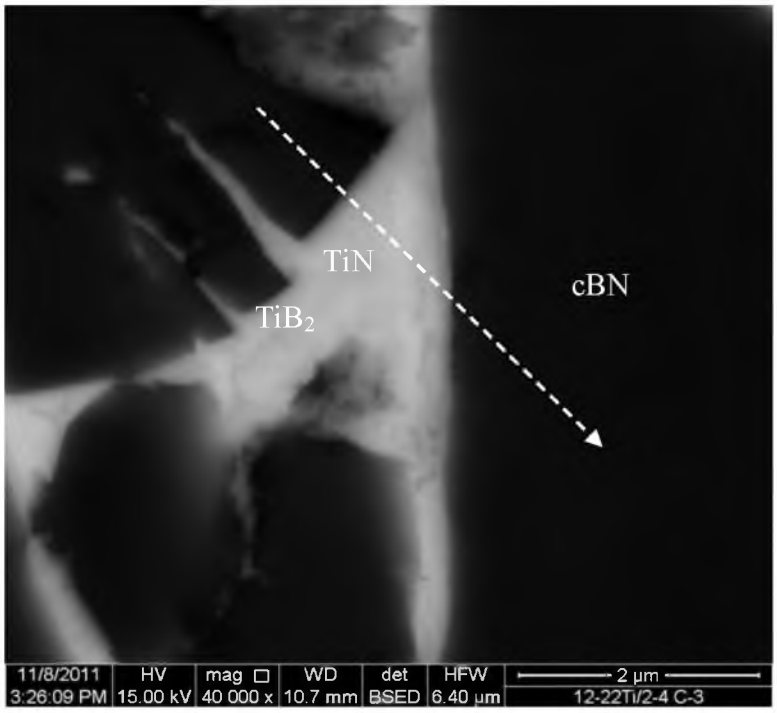

a)

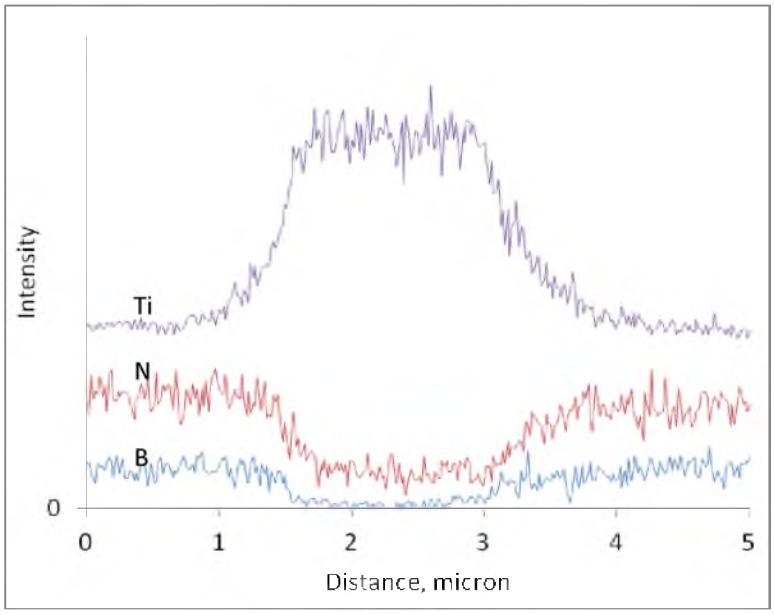

b)

Figure 5-47. SEM image shows reacted cBN and the Ti-coating resulting in a mixture of TiB_2 and TiN among cBN particles in PCBN (Ti-coated cBN) a) and x-ray line scan along the line indicated by the arrow b).

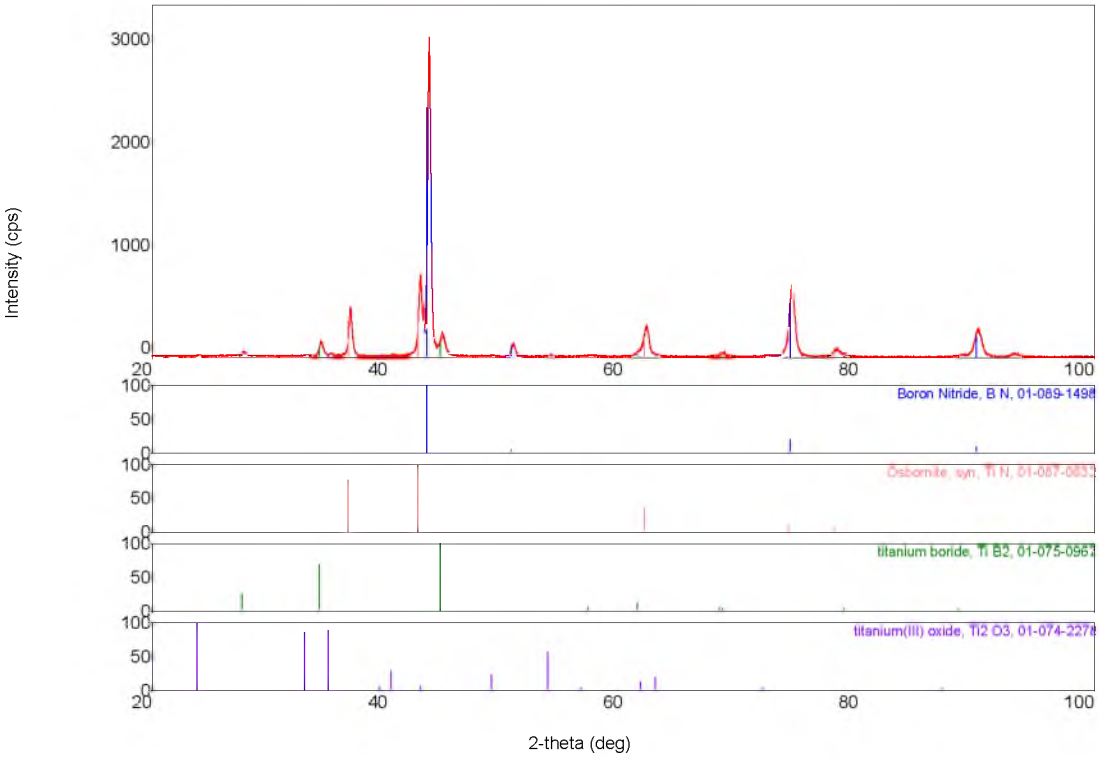

Compound	cBN	TiN	TiB_2	TiO_2
Wt%	83.9	12.5	3.1	0.5

Figure 5-48. XRD pattern of PCBN (Ti-coated cBN) sintered from Mix III.

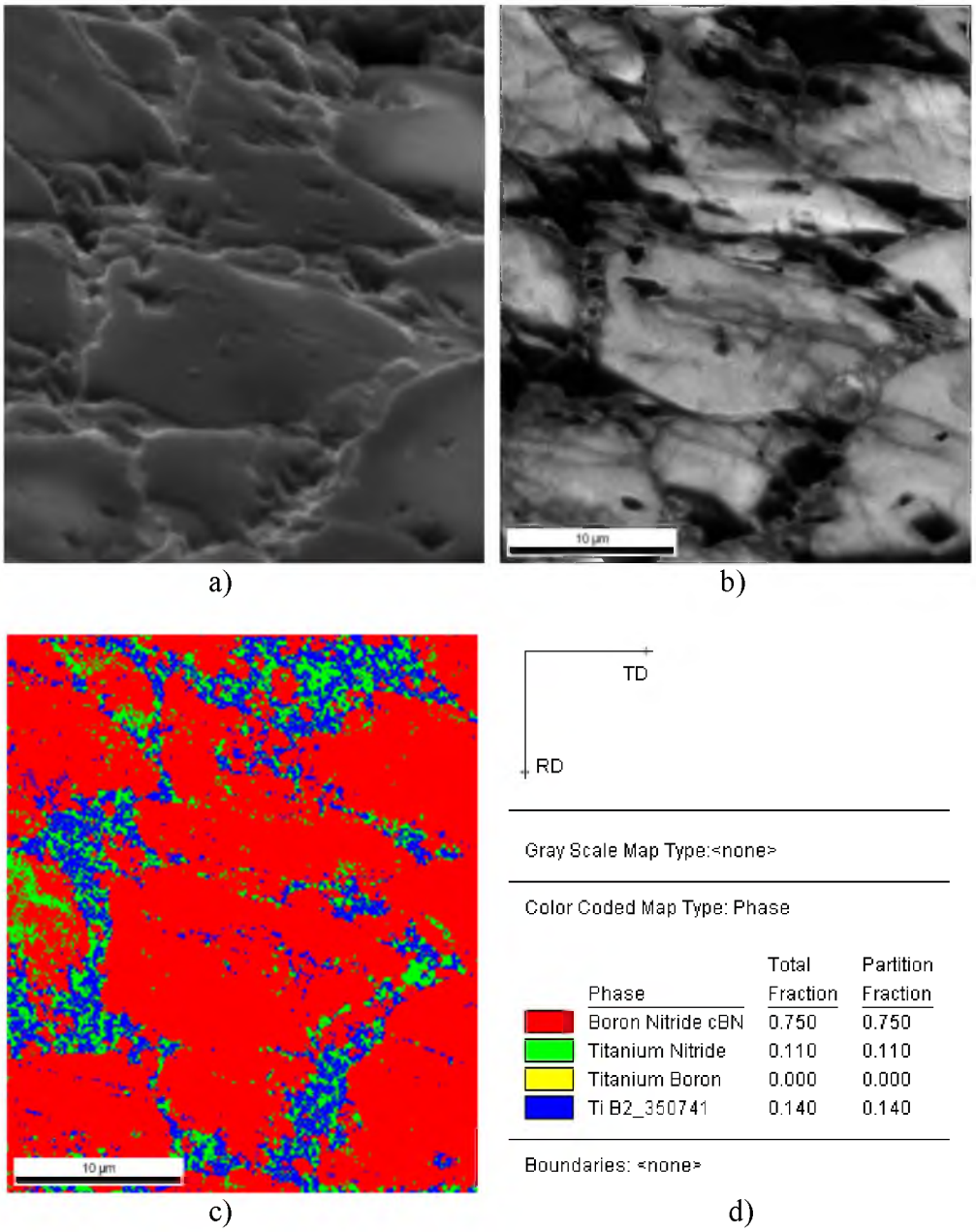

Figure 5-49. EBSD results of PCBN sintered at 1350°C for 15 min using Mix III (Ti-coated cBN): a) SEM image; b) EBSD image-quality map of the actual area analyzed; c) phase map; and d) area fraction of phases identified.

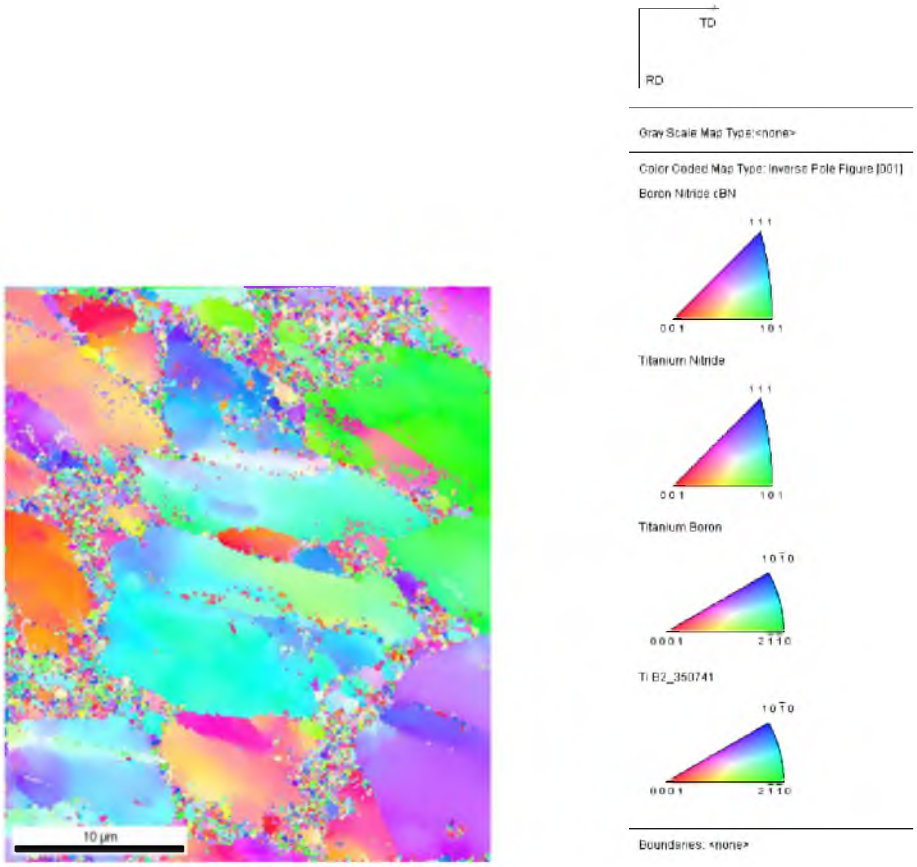

a) b)

Figure 5-50. EBSD results: a) orientation mapping and b) inverse pole figures of all phases.

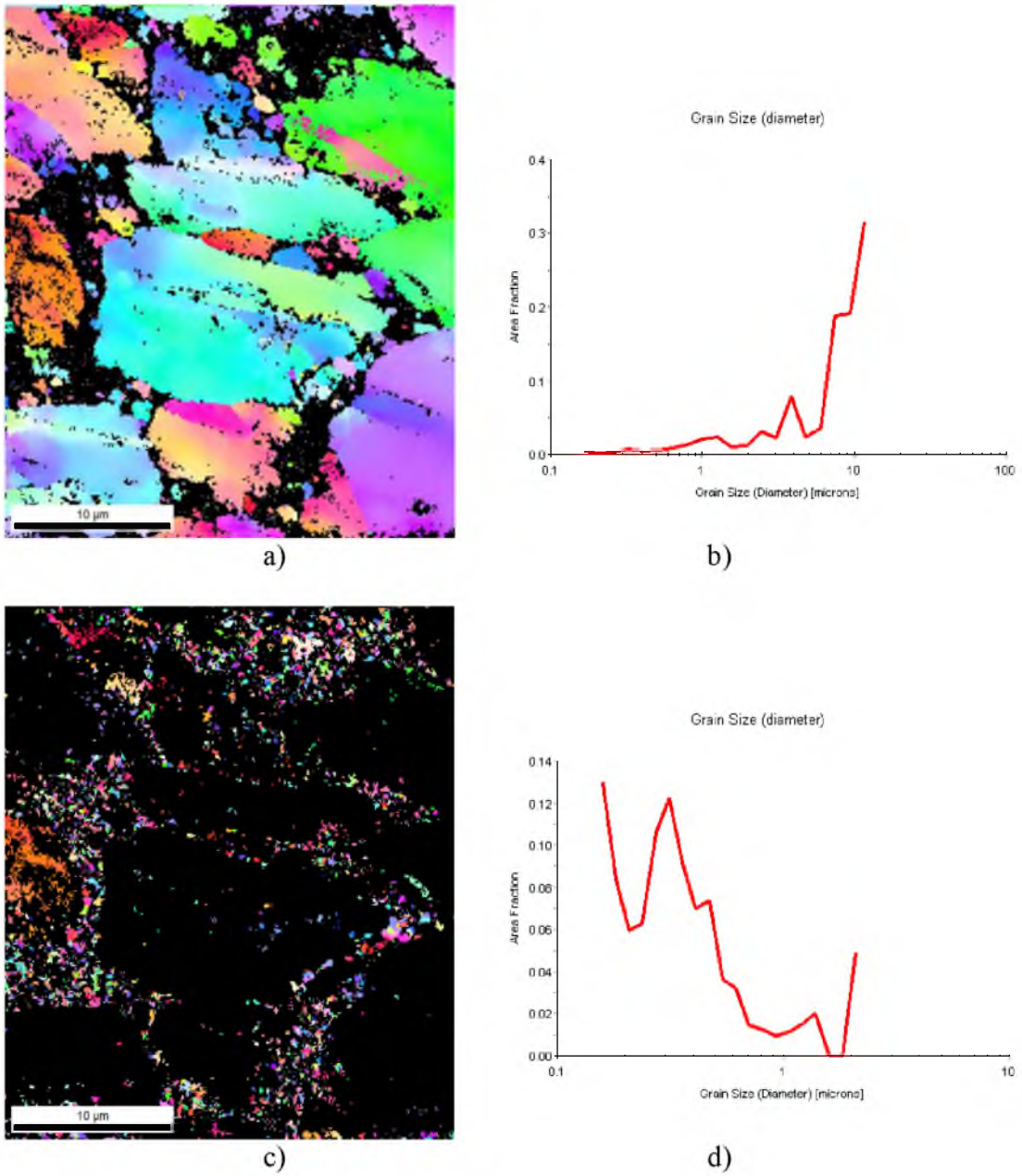

Figure 5-51. Individual phase mapping, grain size distribution and mismatch angle of: a) and b) cBN; c) and d) TiN; e) and f) TiB_2; and g) TiB.

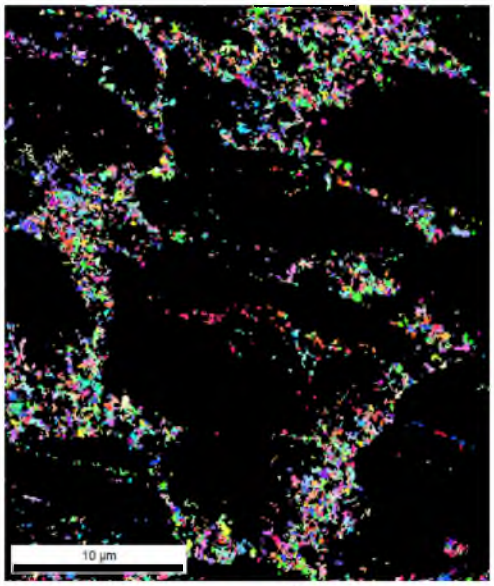

e)

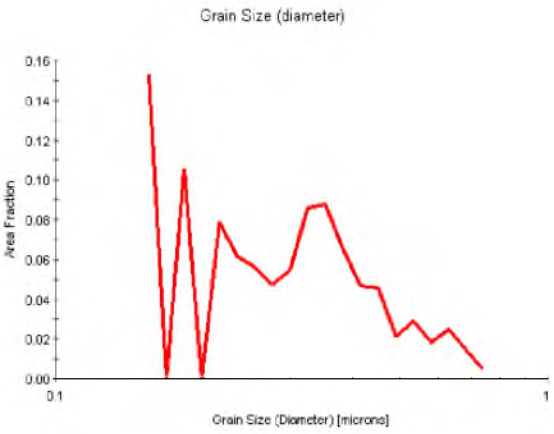

f)

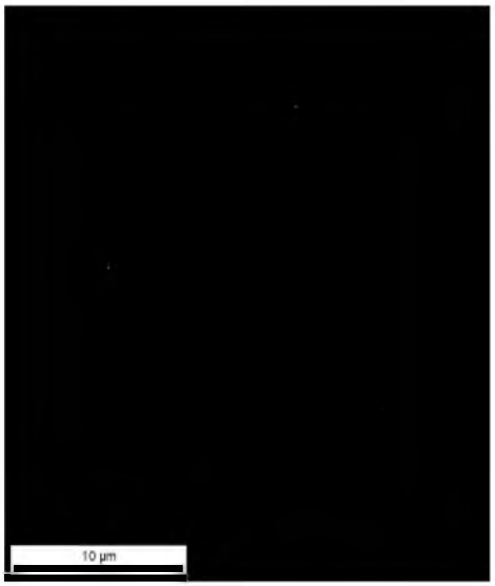

g)

Figure 5-51. Continued.

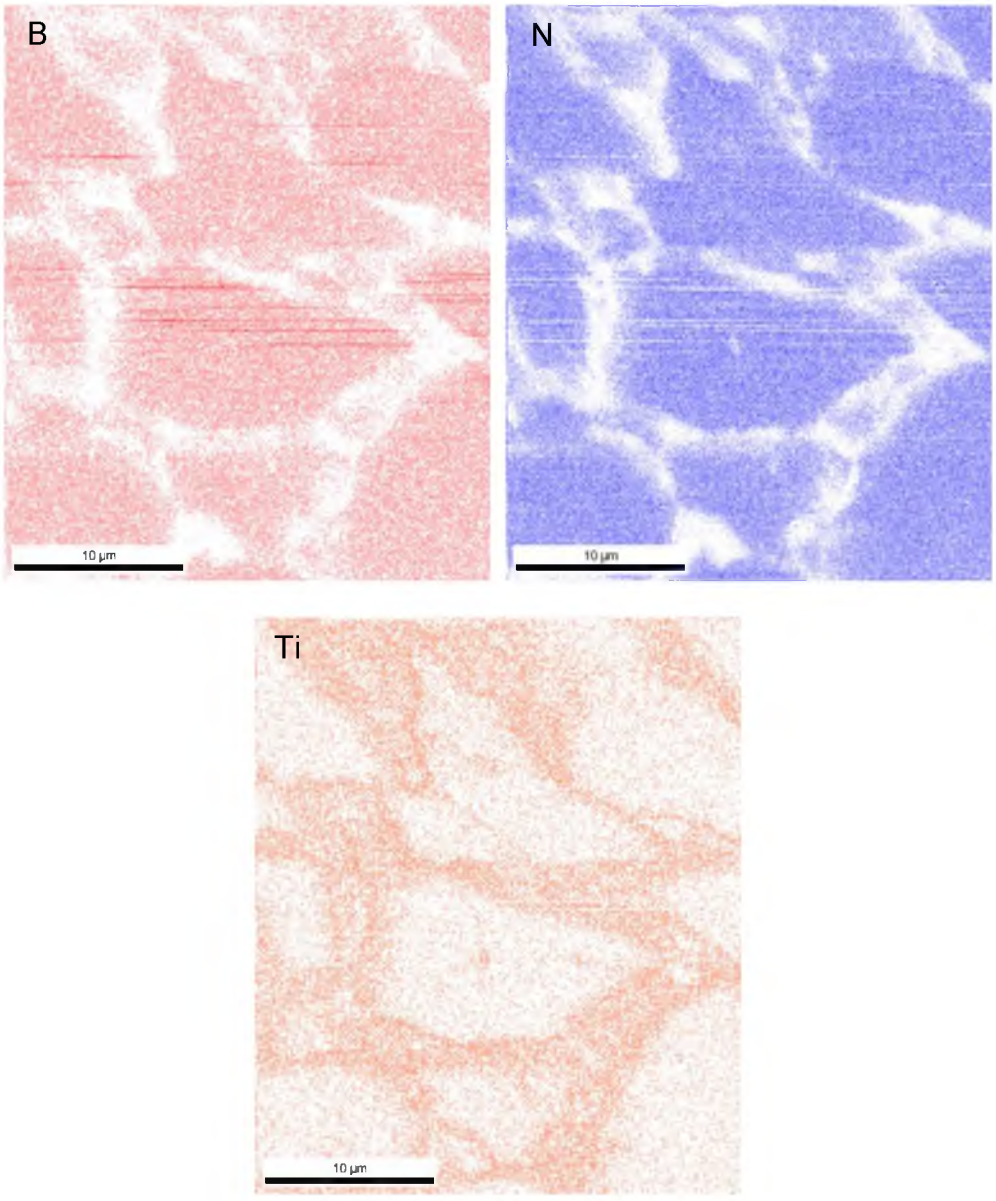

Figure 5-52. Boron (B), nitrogen (N), aluminum (Al), and oxygen (O) mapping collected simultaneously with the EBSD, in PCBN sintered at 1350°C for 15 min using Mix III (Ti-coated cBN).

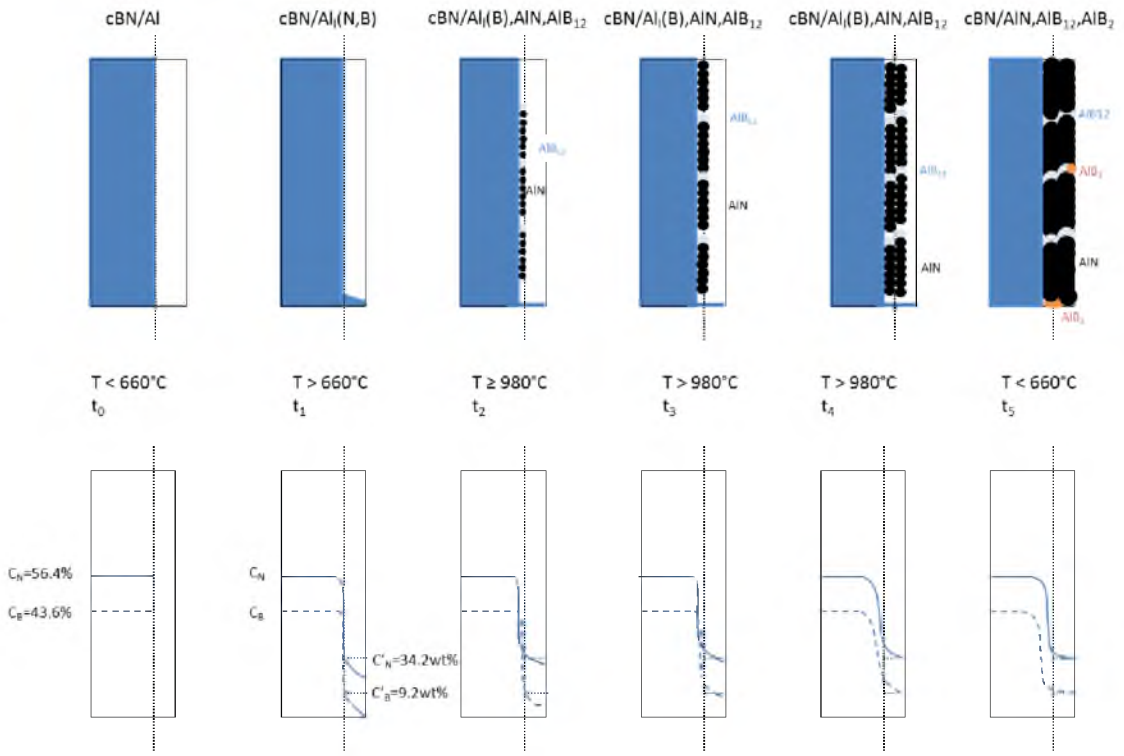

Figure 5-53. Schematic of reaction process and products of cBN+Al in HP/HT sintering, where C_B and C_N are wt% of B and N in cBN, respectively; C'_B and C'_N are their corresponding wt% ratios to Al; and time: $t_0 < t_1 < t_2 < t_3 < t_4 < t_5$.

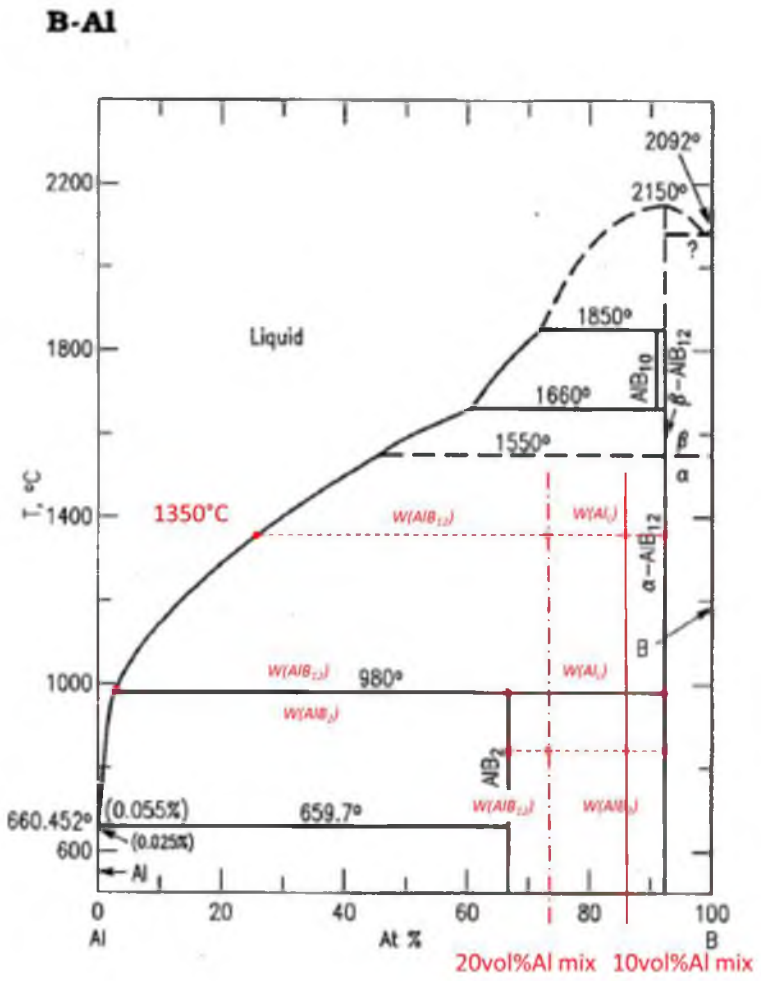

Figure 5-54. Starting Mix I (cBN+10vol%Al) and baseline cBN+20vol%Al compositions superimposed on Figure 2-6. B-Al phase diagram. (Reprinted with permission from the Am. Ceram. So., Fig. 8801,77 originally published by Carlson, O. N. Bull. Alloy Phase Diagrams, 11[6], 1990, 560-566.)

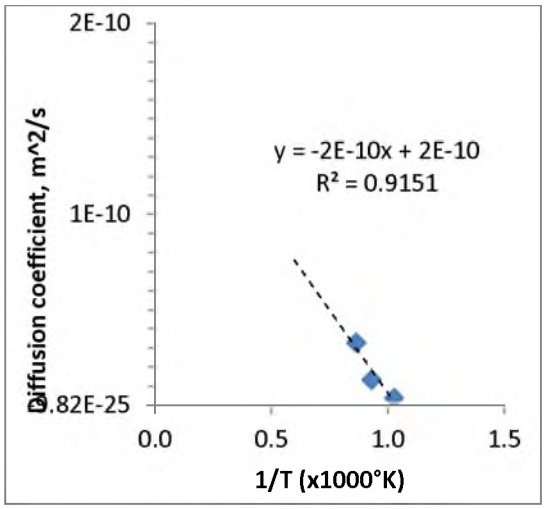

Figure 5-55. Estimated diffusion coefficient of B in α-Ti.

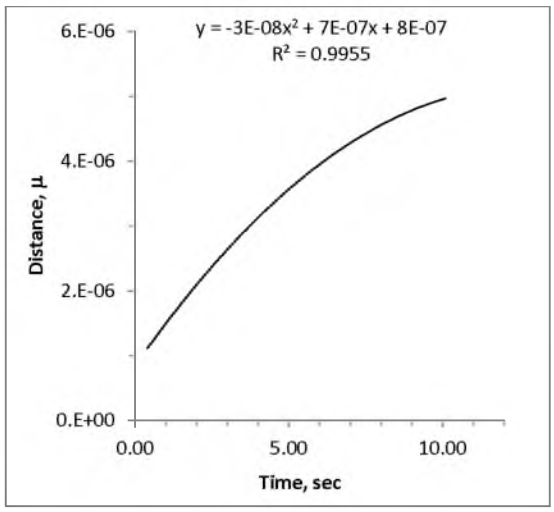

Figure 5-56. Calculated diffusion distance and time required to reach B = 31.3wt% for TiB_2 formation in pure Ti, using the diffusion coefficient of B in α-Ti at 882°C.

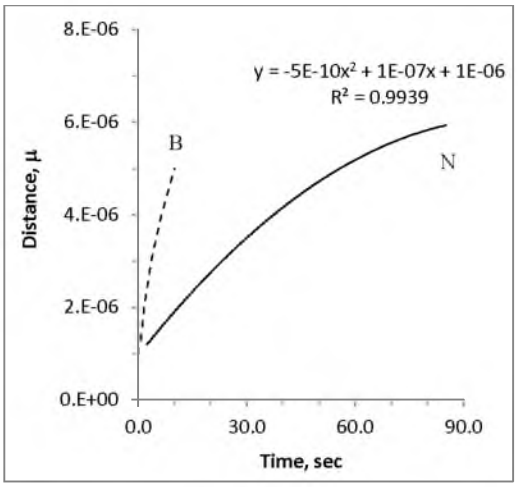

Figure 5-57. Calculated diffusion distance and time required to reach the N=22.6wt% for TiN formation in comparison to the calculated B diffusion model in Ti.

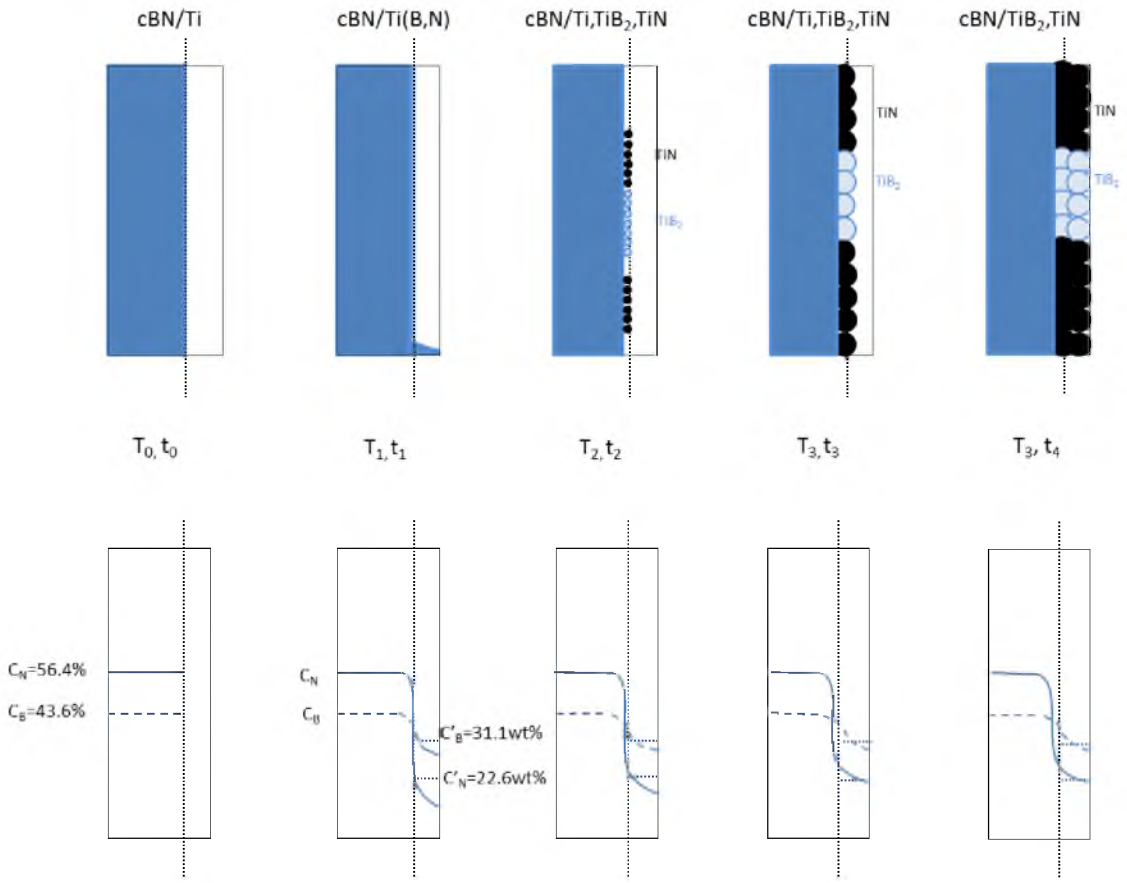

Figure 5-58. Schematic of reaction process and products of cBN+Ti in HP/HT sintering. C_B and C_N are wt% of N and B in cBN, respectively; C'_B and C'_N are their corresponding wt% in Ti; temperature $T_0 < T_1 < T_2 < T_3$; and time $t_0 < t_1 < t_2 < t_3 < t_4$.

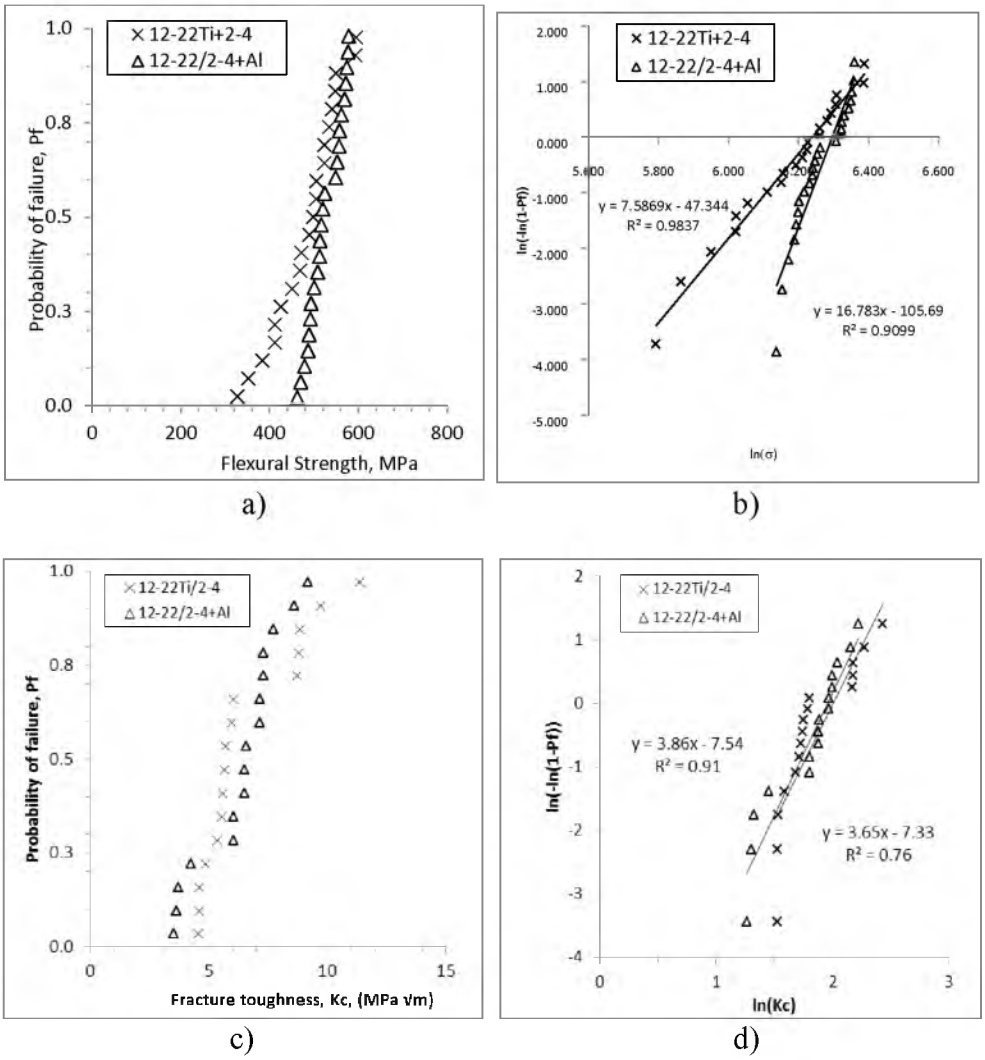

Figure 5-59. Comparison of PCBN (cBN-10Al) and PCBN (Ti-coated cBN): a) Weibull distribution of flexural strength values and b) corresponding Weibull modulus; c) Weibull distribution of fracture toughness; and d) corresponding Weibull modulus.

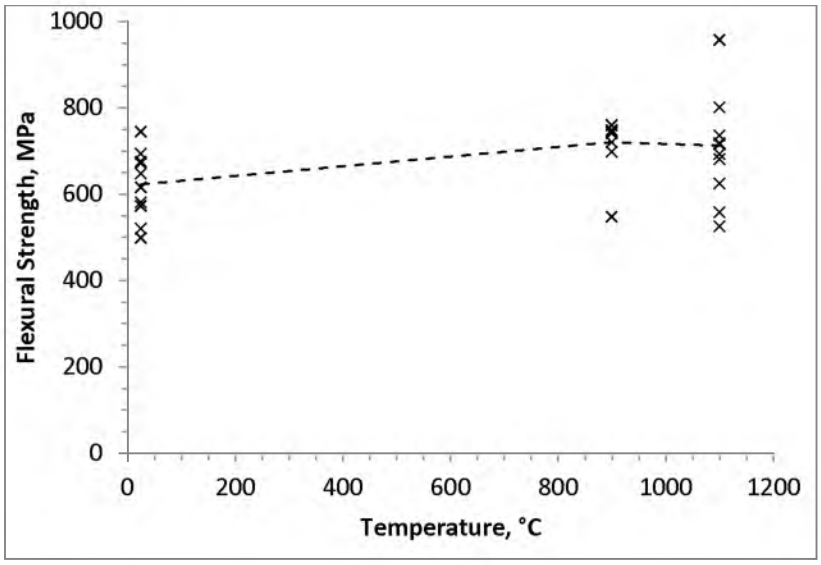

Temperature, °C	25	900	1100
Mean±1std dev, MPa	621.9 ± 78.9	720.2 ± 63.5	712.3 ± 114.6

Figure 5-60. Flexural strength of PCBN made of 10vol%Al at high temperatures.

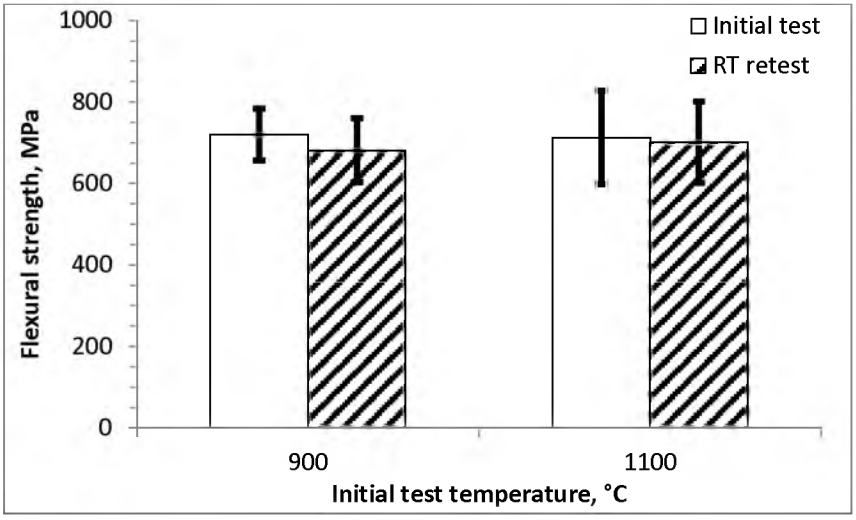

Initial test temperature	900°C	1100°C
Flexural strength	720.2 ± 63.5	712.3 ± 114.6
Retested at room temperature	681.4 ± 78.1	700.8 ± 99.2

Figure 5-61. Comparison of flexural strength values, of initially high-temperature tested and then retested after cooling down to room temperature of PCBN (90-10Al) samples.

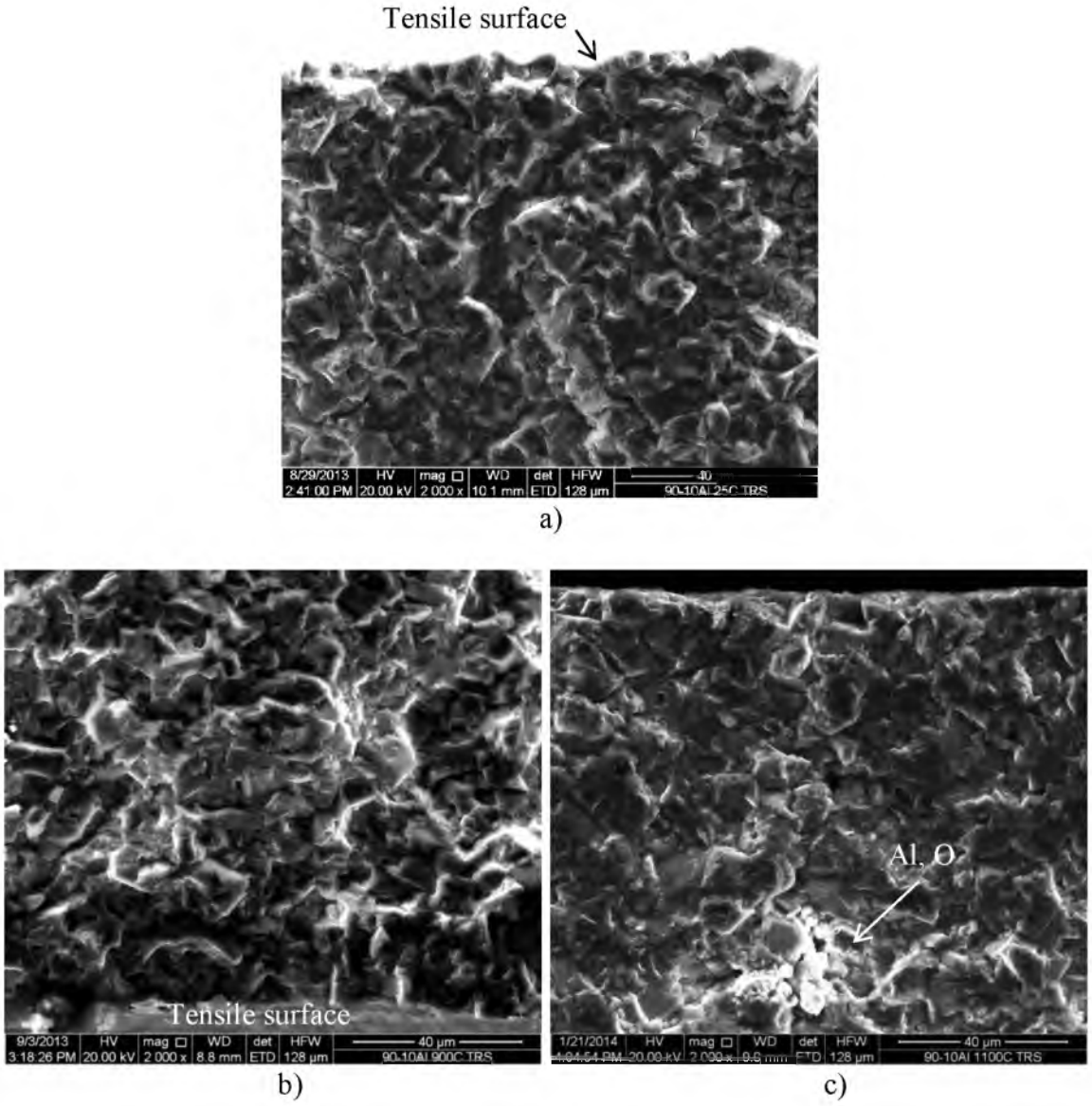

Figure 5-62. Fracture surface (close to the tensile surface) of PCBN (90-10Al) after three-point-bend test: a) at 25°C, b) at 900°C, and c) at 1100°C.

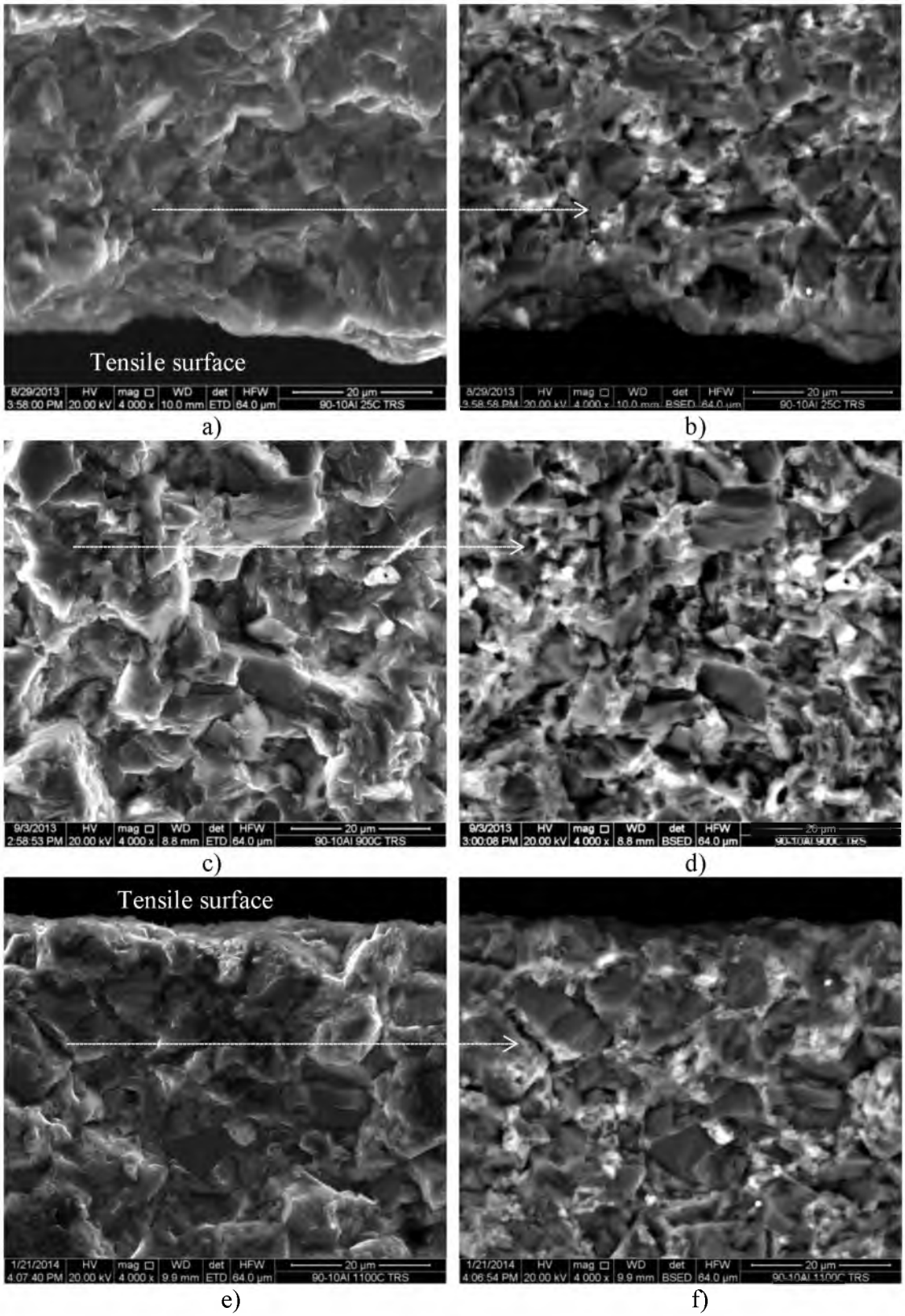

Figure 5-63. SE and corresponding BSE images of fracture surface of PCBN (90-10Al) after three-point-bend test: a) and b) at 25°C; c) and d) at 900°C; e) and f) at 1100°C .

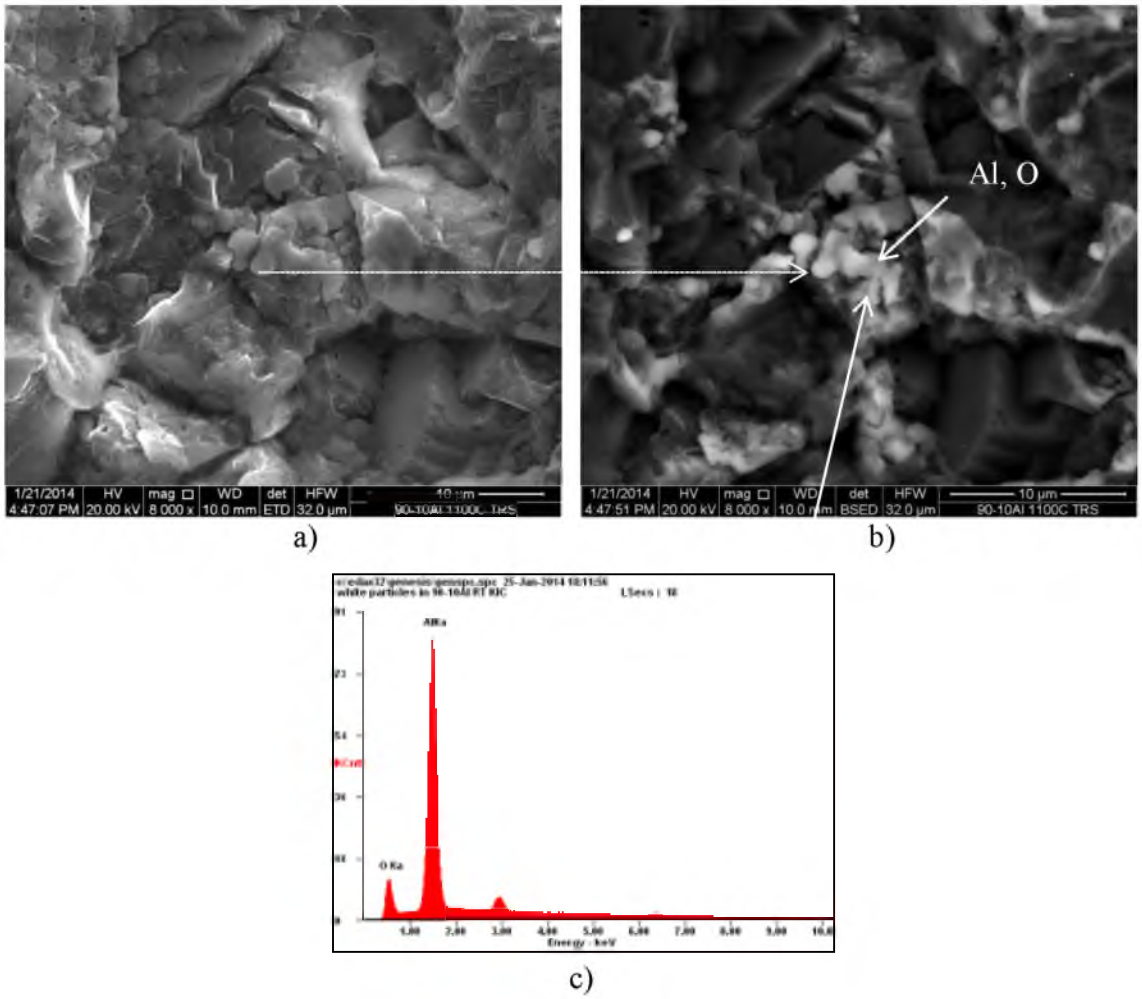

Figure 5-64. Fracture surface of PCBN (90-10Al) after three-point-bend test at 1100°C: a) SE image, b) corresponding BSE image and c) the EDS spectrum.

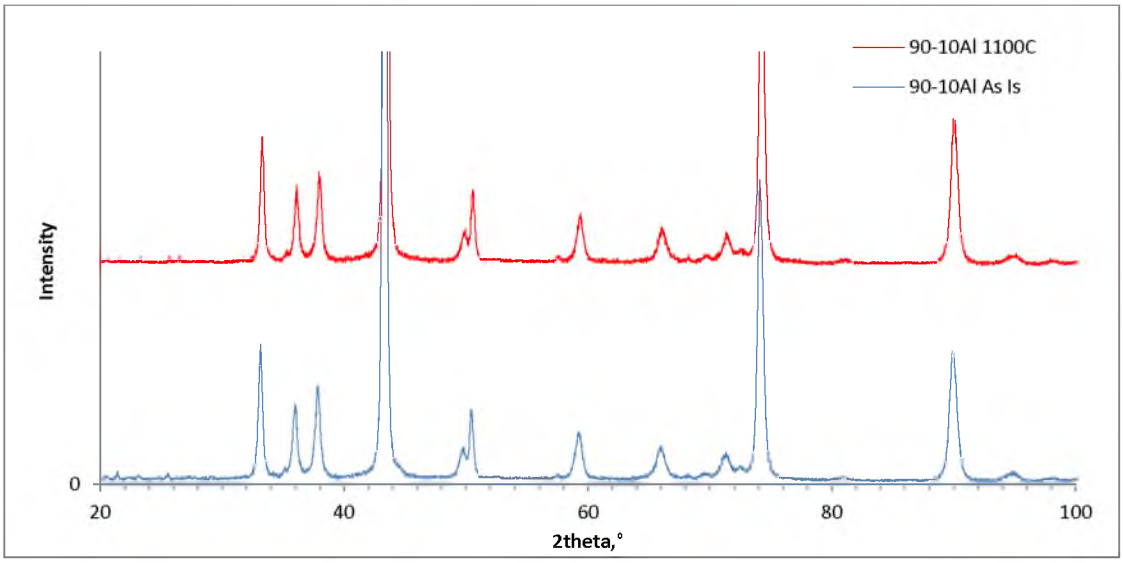

Compound	cBN	AlN	AlB_{12}
90-10Al as is, wt%	88.9	8.1	3.0
90-10Al 1100°C tested, wt%	80.4	10.7	8.9

Figure 5-65. XRD pattern collected on the PCBN (90-10Al) before and after the 1100°C flexural strength testing.

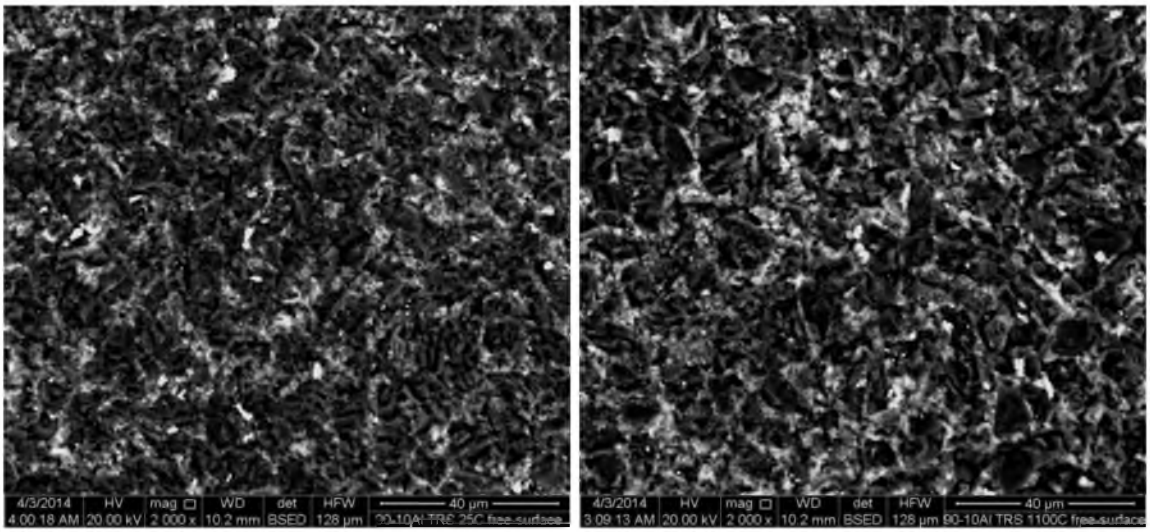

a) b)

Figure 5-66. SEM images of PCBN (90-10Al) bend-bar free-surface: a) before bending test and b) after test at 1100°C.

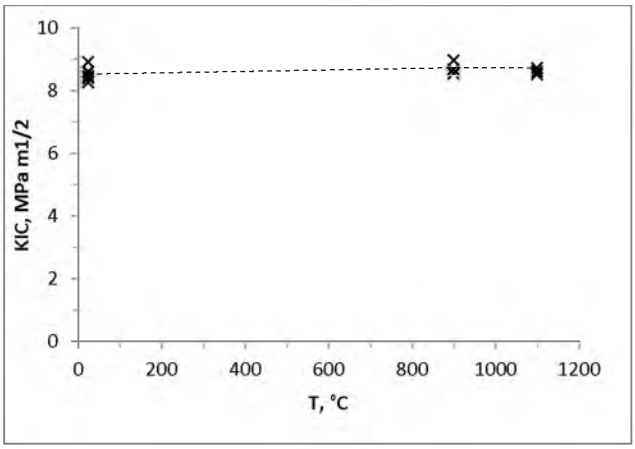

a)

Test ID	25°C	900°C	1100°C
1	8.60	8.667	8.511
2	8.46	8.965	8.604
3	8.39	8.537	8.716
4	8.90	-	-
5	8.58	-	-
6	8.26	-	-
Avg=	8.53	8.72	8.61

b)

Figure 5-67. Fracture toughness of PCBN (cBN+10vol%Al) tested by the diametral compression method at different temperatures: a) K_{IC} vs temperature plot and b) individual sample values.

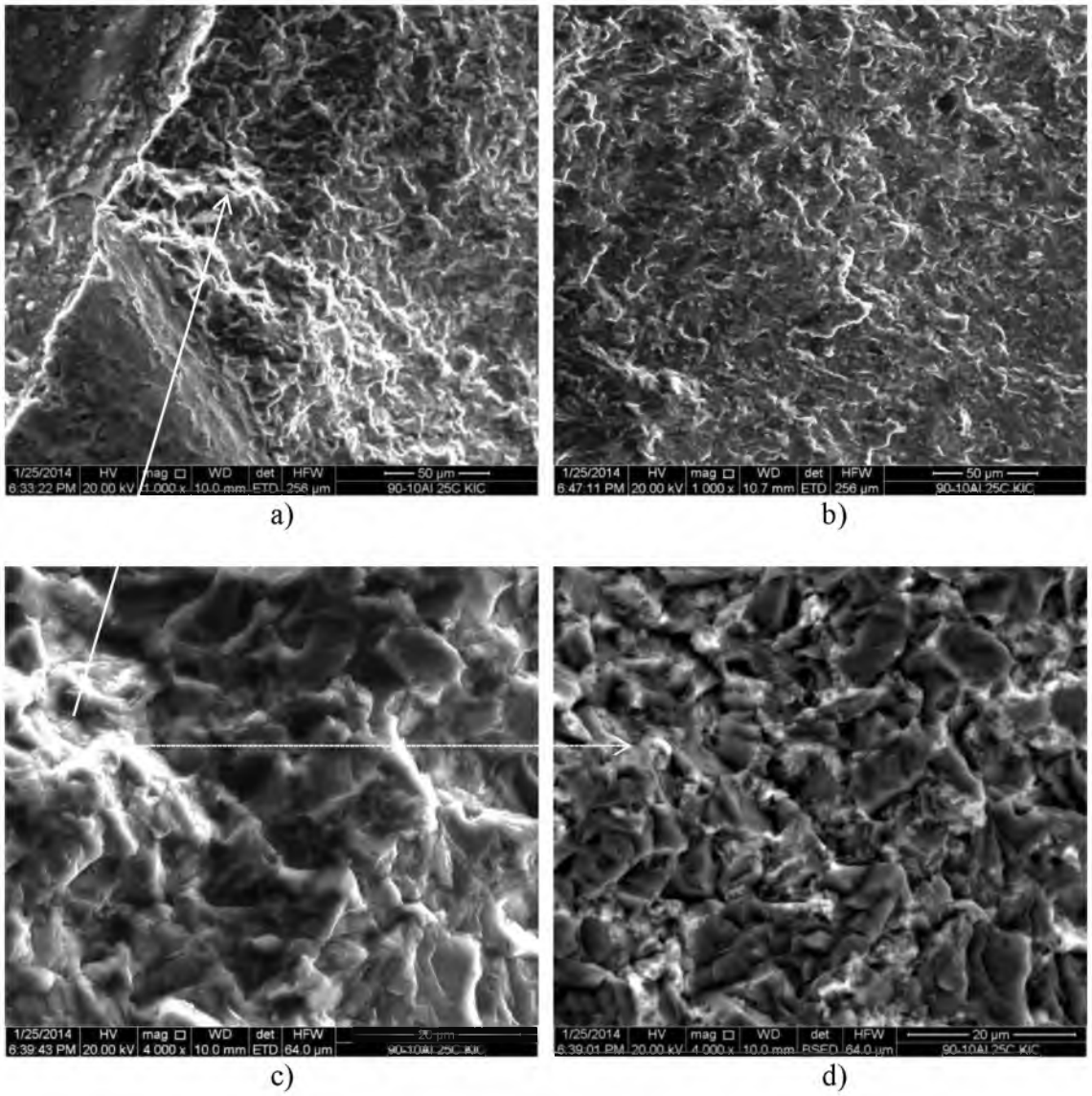

Figure 5-68. PCBN (90-10Al) after K_{IC} test at 25°C: a) fracture starting point; b) end of fracturing; c) magnified view and d) corresponding BSE image.

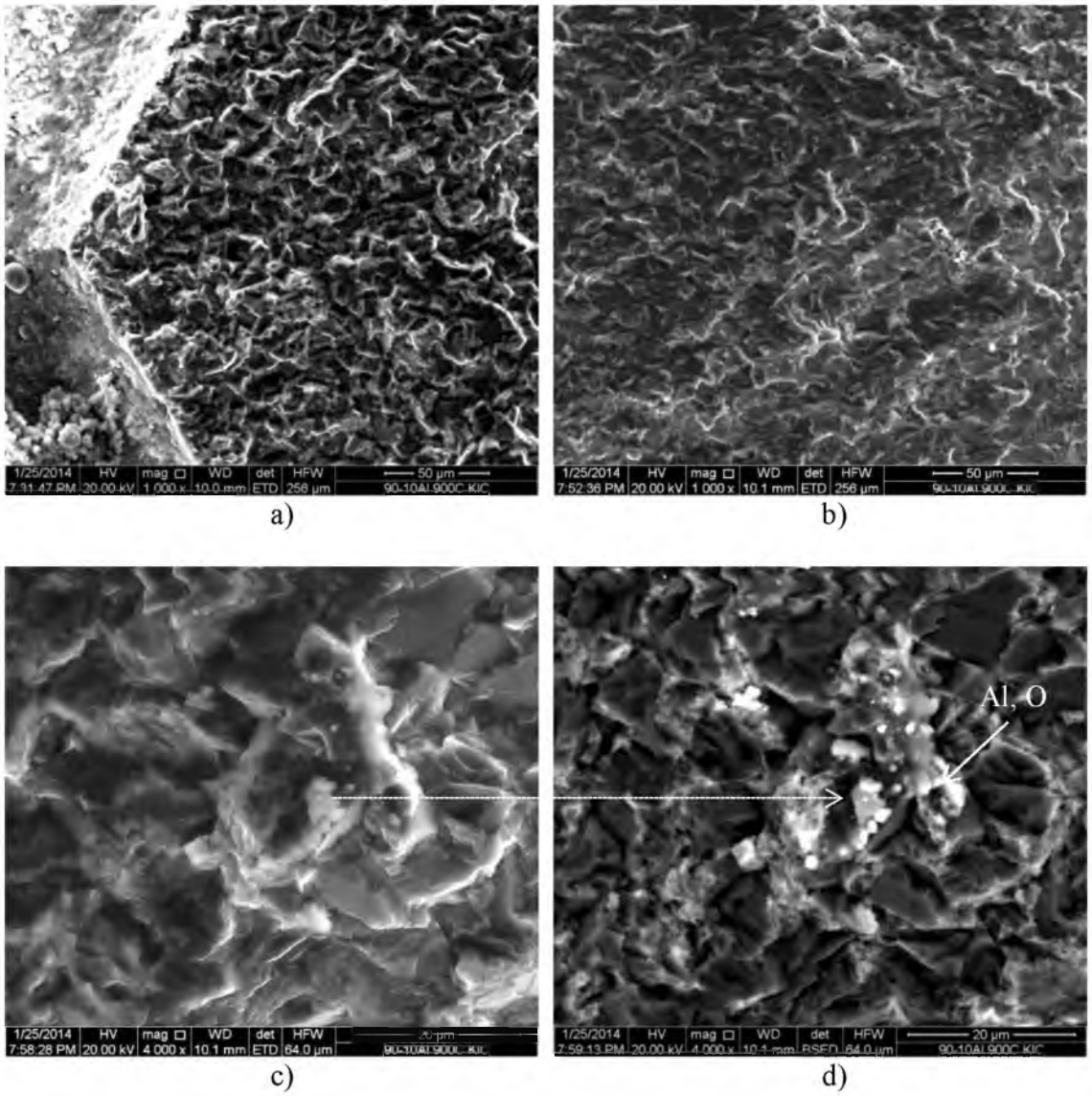

Figure 5-69. PCBN (90-10Al) after K_{IC} test at 900°C: a) fracture starting point; b) end of fracturing; c) typical fracture surface and d) corresponding BSE image.

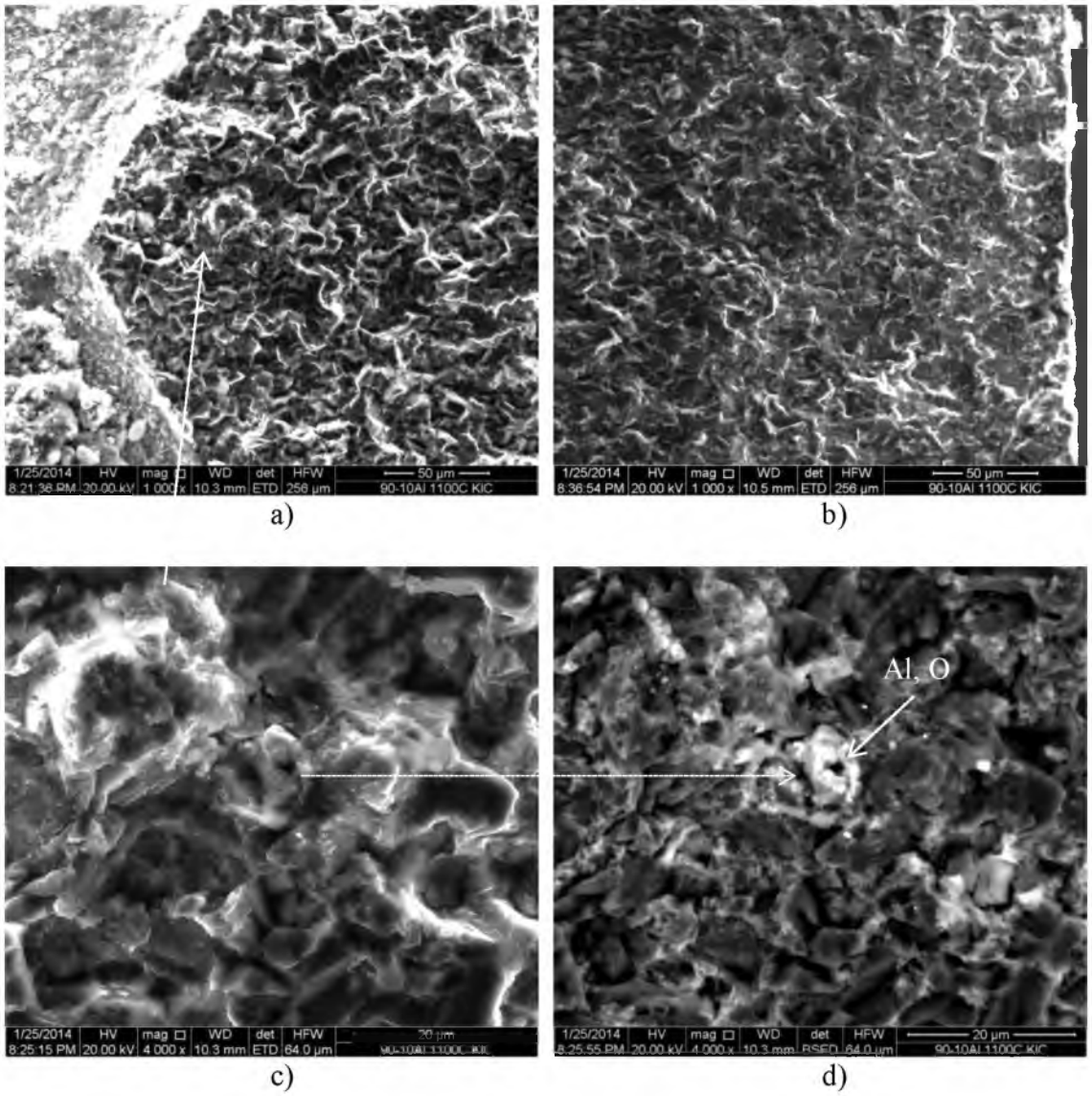

Figure 5-70. PCBN (90-10Al) after K_{IC} test at 1100°C: a) fracture starting point; b) end of fracturing; c) magnified view and d) corresponding BSE image.

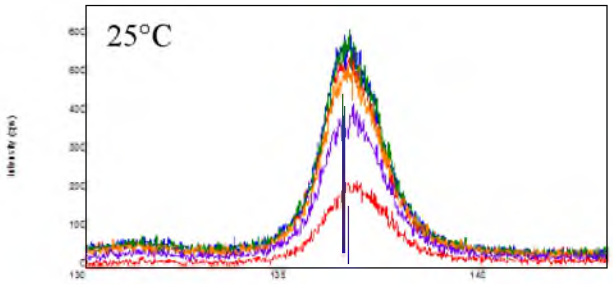

ψ(deg)	$(\sin(\psi))^2$	2θ(deg)
-60	-0.75	136.55
-36	-0.345	136.44
-24	-0.165	136.43
-12	-0.043	136.39

a)

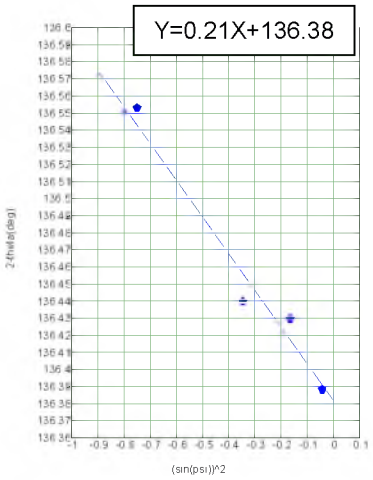

b)

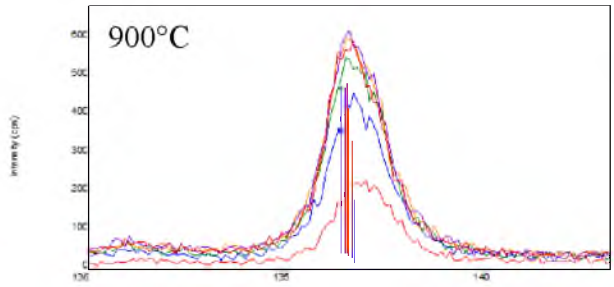

ψ(deg)	$(\sin(\psi))^2$	2θ(deg)
-65	-0.821	136.63
-51.4	-0.611	136.58
-37.8	-0.376	136.47
-10.6	-0.034	136.45

c)

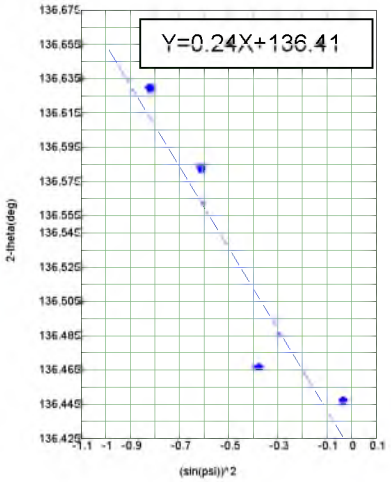

d)

Figure 5-71. Residual stress measurement on PCBN (90-10Al) three-point-bend bars tested at 25°C, 900°C, and 1200°C: a) c) e) cBN peak intensity plots; and b) d) f) $2\theta \sim sin^2(\psi)$ plots and linear regression results.

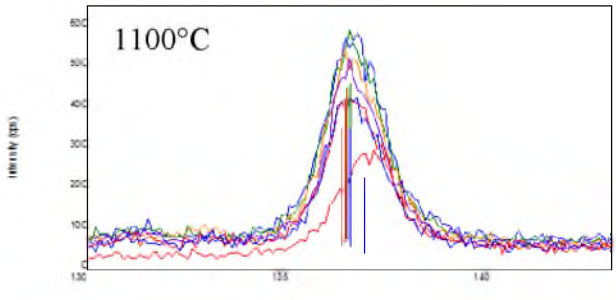

ψ(deg)	$(\sin(\psi))^2$	2θ(deg)
-53	-0.638	136.54
-41	-0.43	136.45
-29	-0.235	136.42
-17	-0.085	136.39

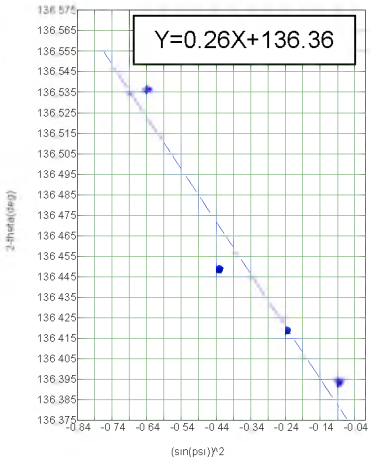

e) f)

Figure 5-71. Continued.

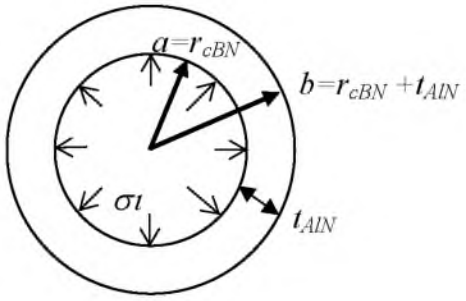

Figure 5-72. A simplified model for thermal-expansion stress estimate for cBN-AlN two phase.

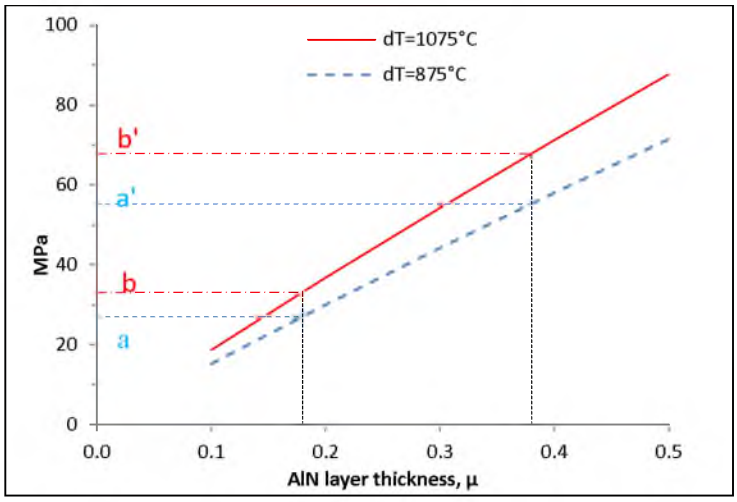

Temp difference, ΔT	875°C	1075°C
AlN t=0.18 μ	-27 MPa	-33 MPa
AlN t=0.38 μ	-55 MPa	-68 MPa

Figure 5-73. Thermal expansion stress estimated for cBN-AlN spherical interfaces at mean cBN 13.4μ (r_{cBN}=6.7μ).

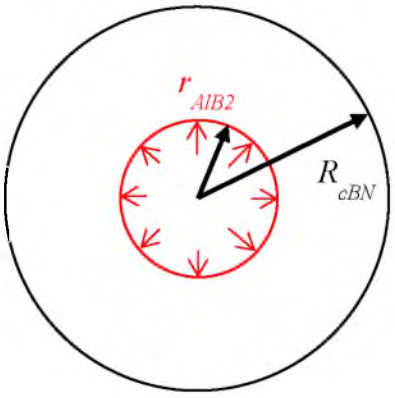

Figure 5-74. Modeling of the dilation effect of an AlB_2 disk surrounded by a cBN cylinder.

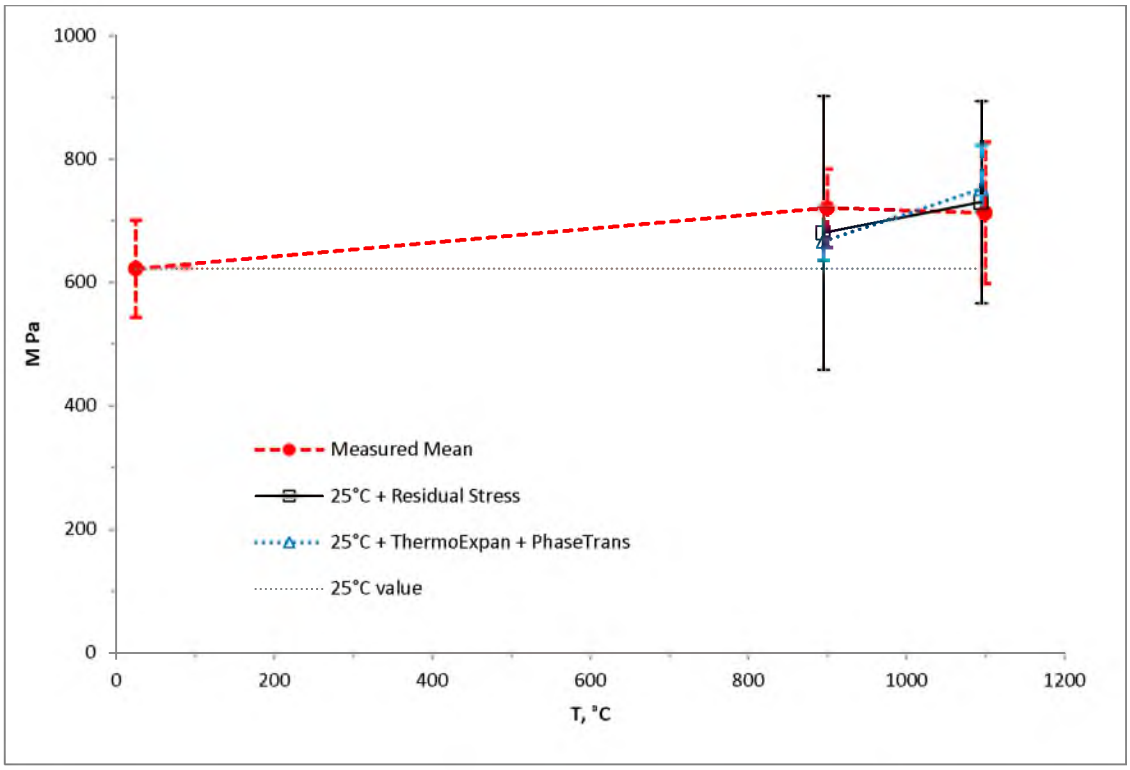

Figure 5-75. High temperature flexural strength measured for PCBN (90-10Al) at 25°C; 25°C + residual stress measured; and 25°C + thermal expansion modeled at 900°C; and 25°C + thermal expansion modeled + phase transformation at 1100°C, respectively.

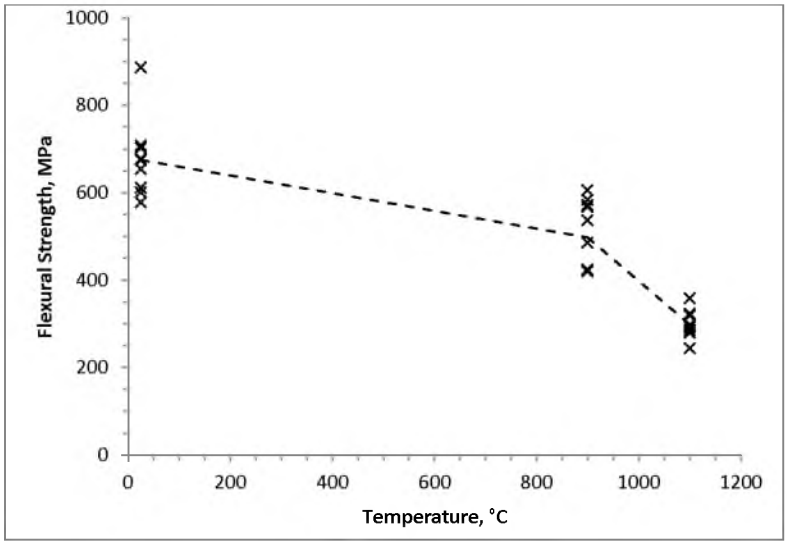

Temperature, °C	25	900	1100
Mean±1std dev, MPa	674.4 ± 85.7	497.1 ± 86.5	298.3 ± 30.1

Figure 5-76. Flexural strength of PCBN made of Ti-coated cBN at high temperatures.

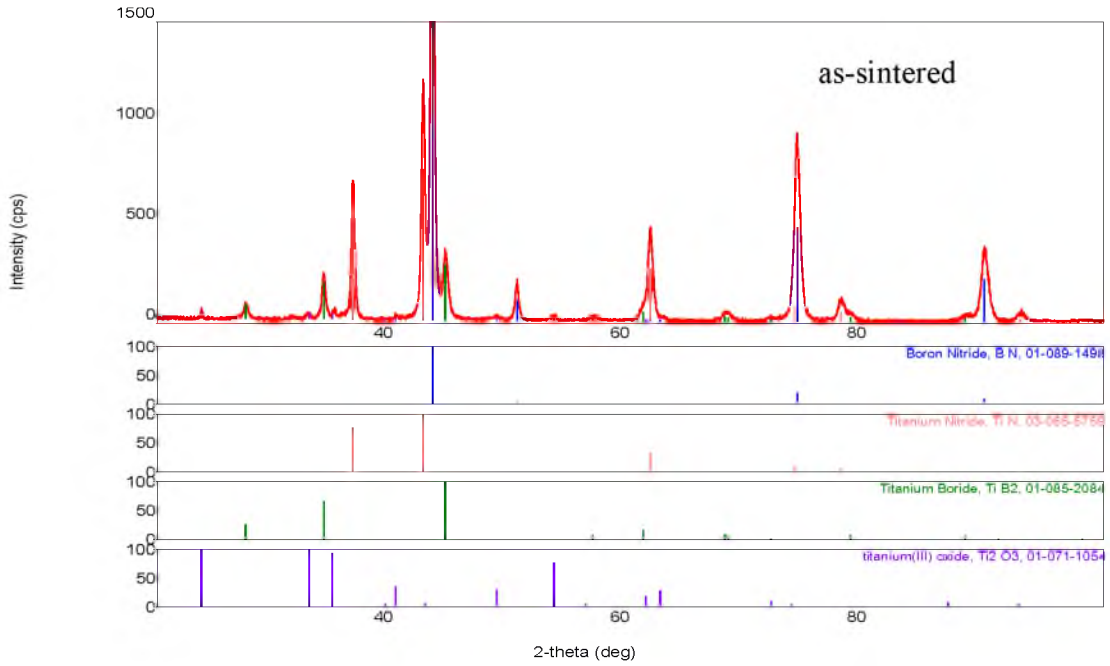

a)

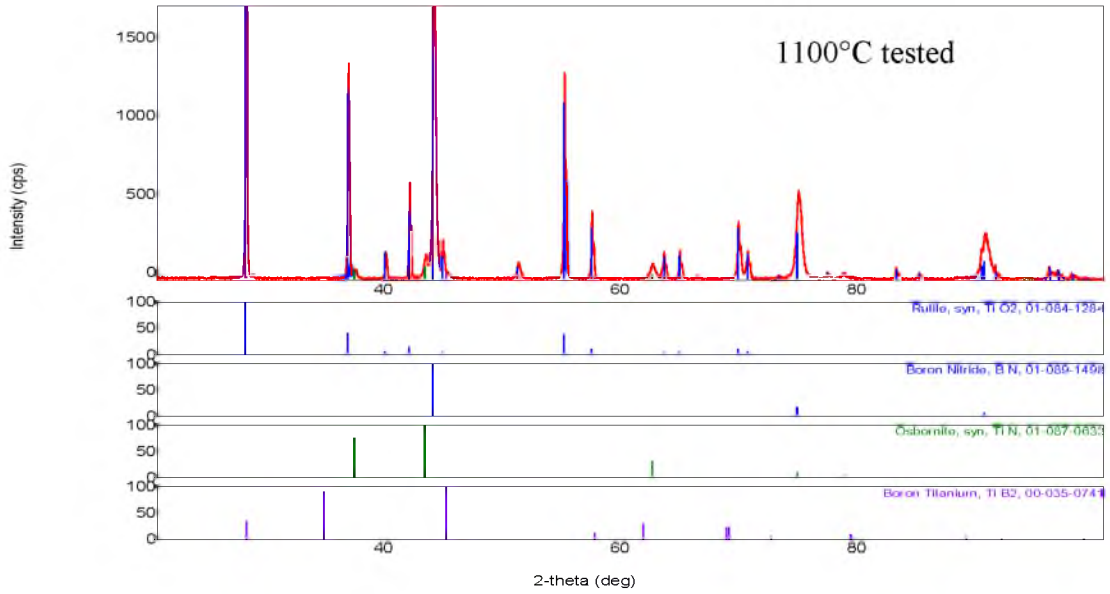

Compound	cBN	TiN	TiB_2	Ti_2O_3	TiO_2
25°C, wt%	87.7	8.4	3.0	0.9	-
1100°C, wt%	75.1	3.7	0.0	-	21.2

b)

Figure 5-77. XRD patterns collected on PCBN (Ti-coated cBN): a) at 25°C and b) after 1100°C testing.

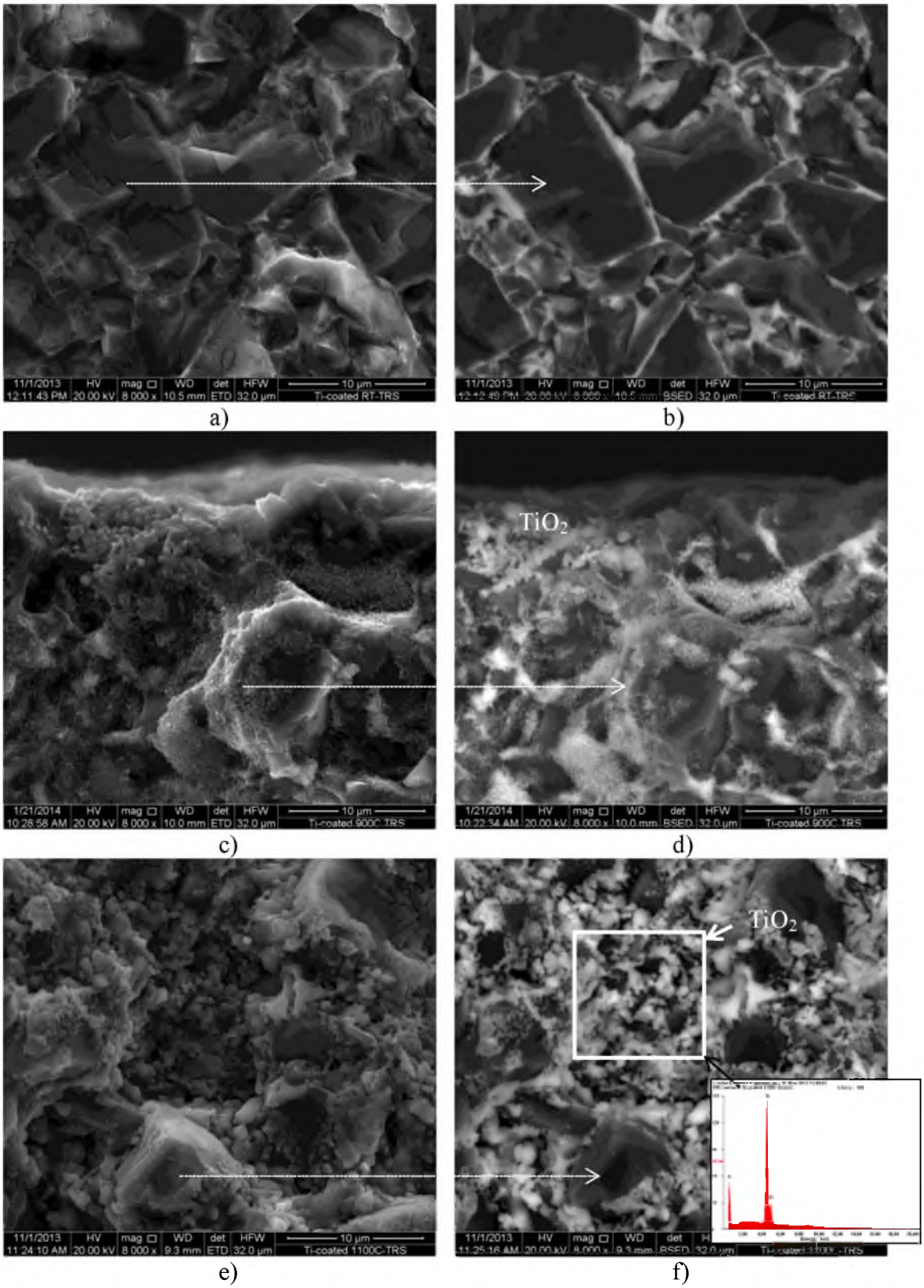

Figure 5-78. Fracture surface of PCBN (Ti-coated cBN) three-point-bend tested: a) SE image and b) corresponding BSE image at 25°C; c) and d) at 900°C; e) and f) at 1100°C.

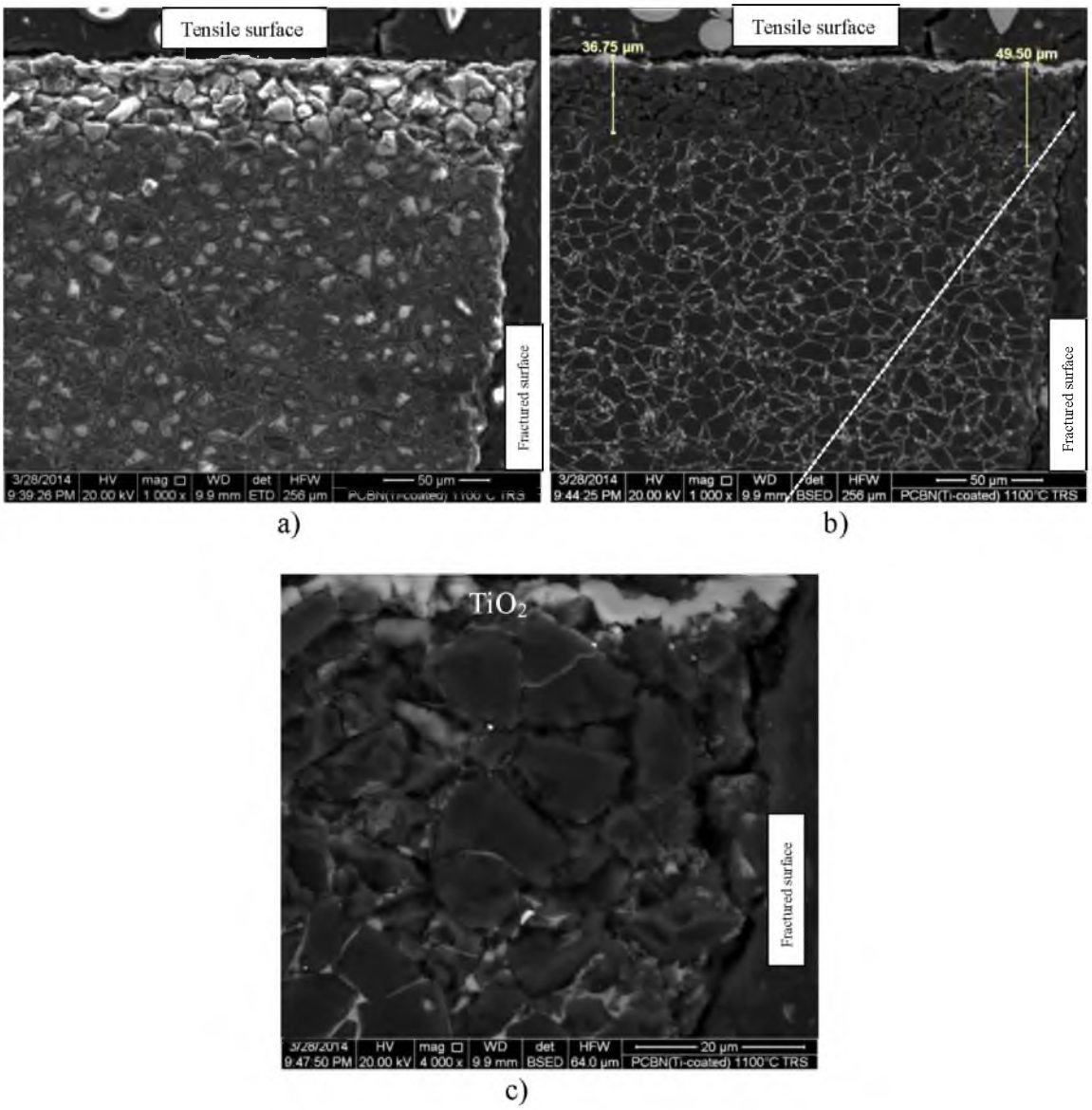

Figure 5-79. PCBN (Ti-coated cBN) bend-bars tested at 1100°C: a) SE image of the cross-section; b) corresponding BSE image; and c) enlarged view of the subsurface.

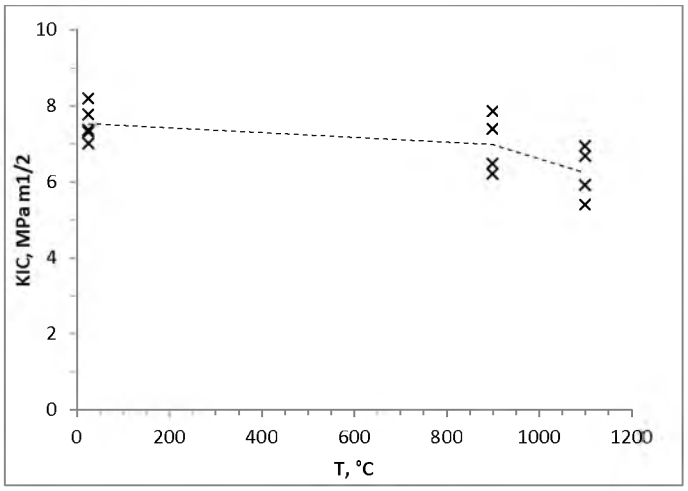

a)

Test ID	25°C	900°C	1100°C
1	7.01	6.54	7.01
2	7.31	7.44	6.74
3	7.76	7.91	5.45
4	7.36	6.27	5.98
5	8.19	-	-
Avg=	7.53	7.04	6.30

b)

Figure 5-80. Fracture toughness of PCBN (Ti-coated cBN), by the diametral compression method, tested at different temperatures, a) plot and b) individual test values.

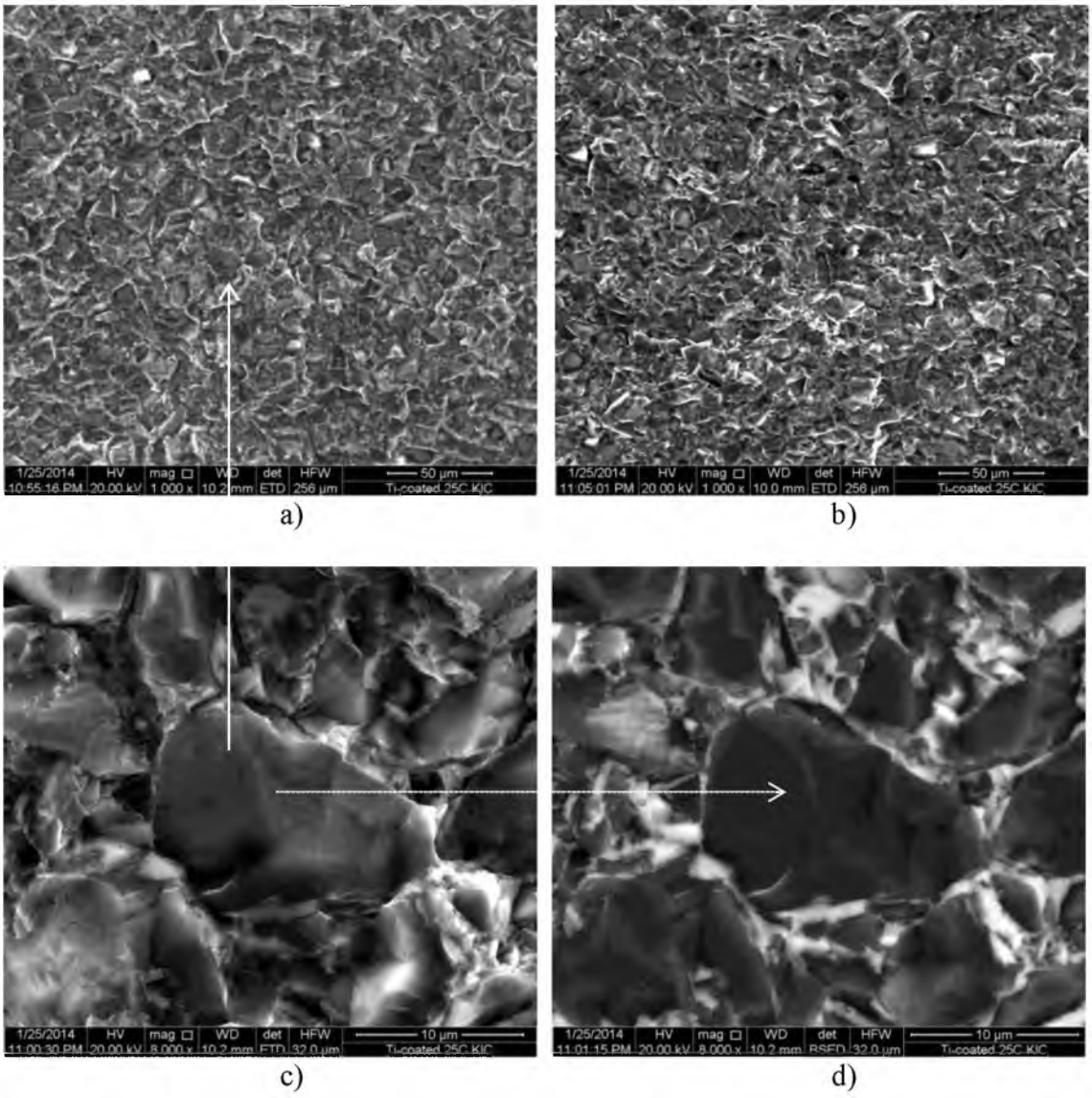

Figure 5-81. PCBN (Ti-coated cBN) after K_{IC} test at 25°C: a) fracture starting area; b) end of fracturing; c) magnified view and d) its corresponding BSE image.

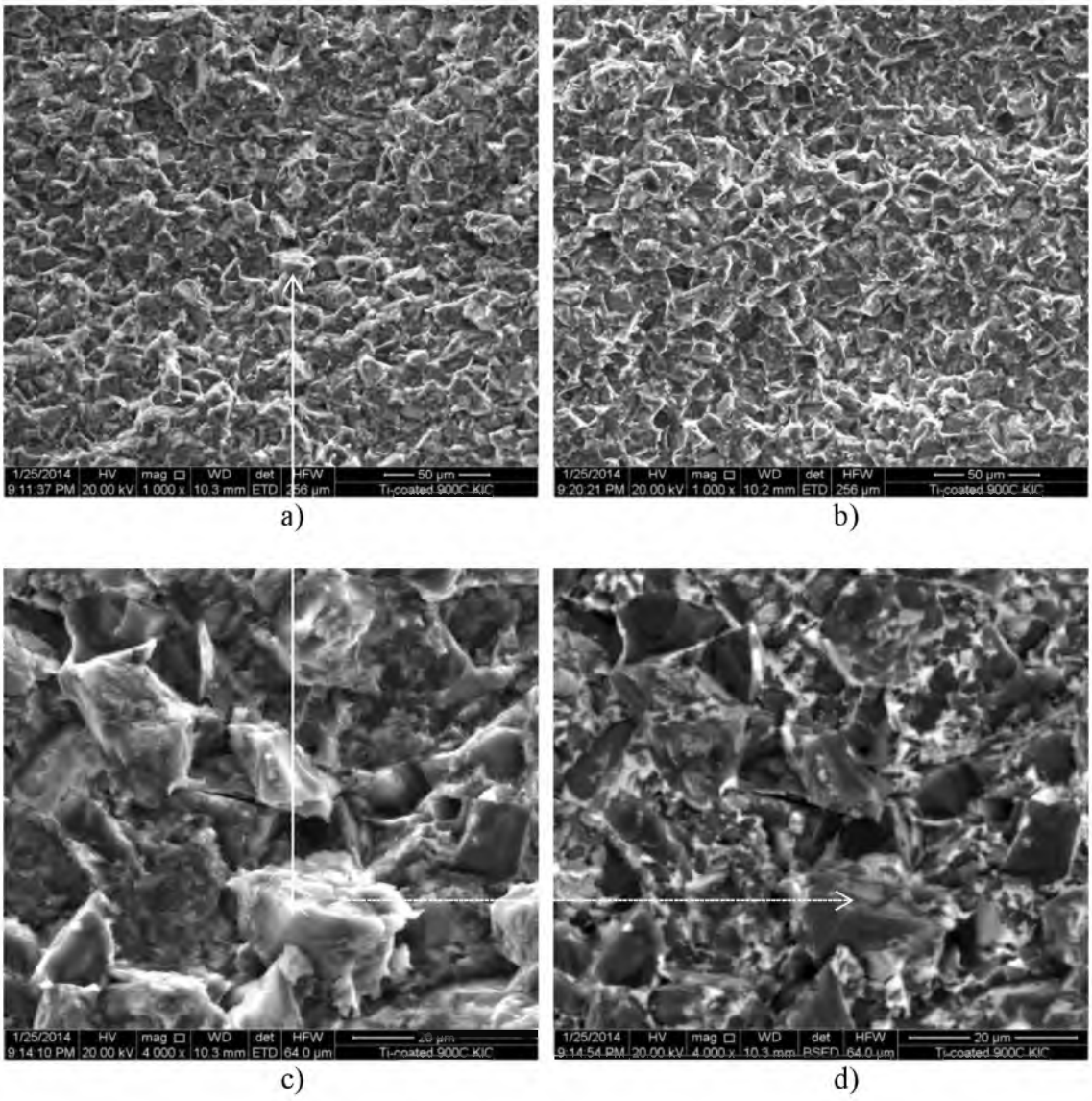

Figure 5-82. PCBN (Ti-coated cBN) after K_{IC} test at 900°C: a) fracture starting area; b) end of fracturing; c) magnified view of the starting area and d) its corresponding BSE image.

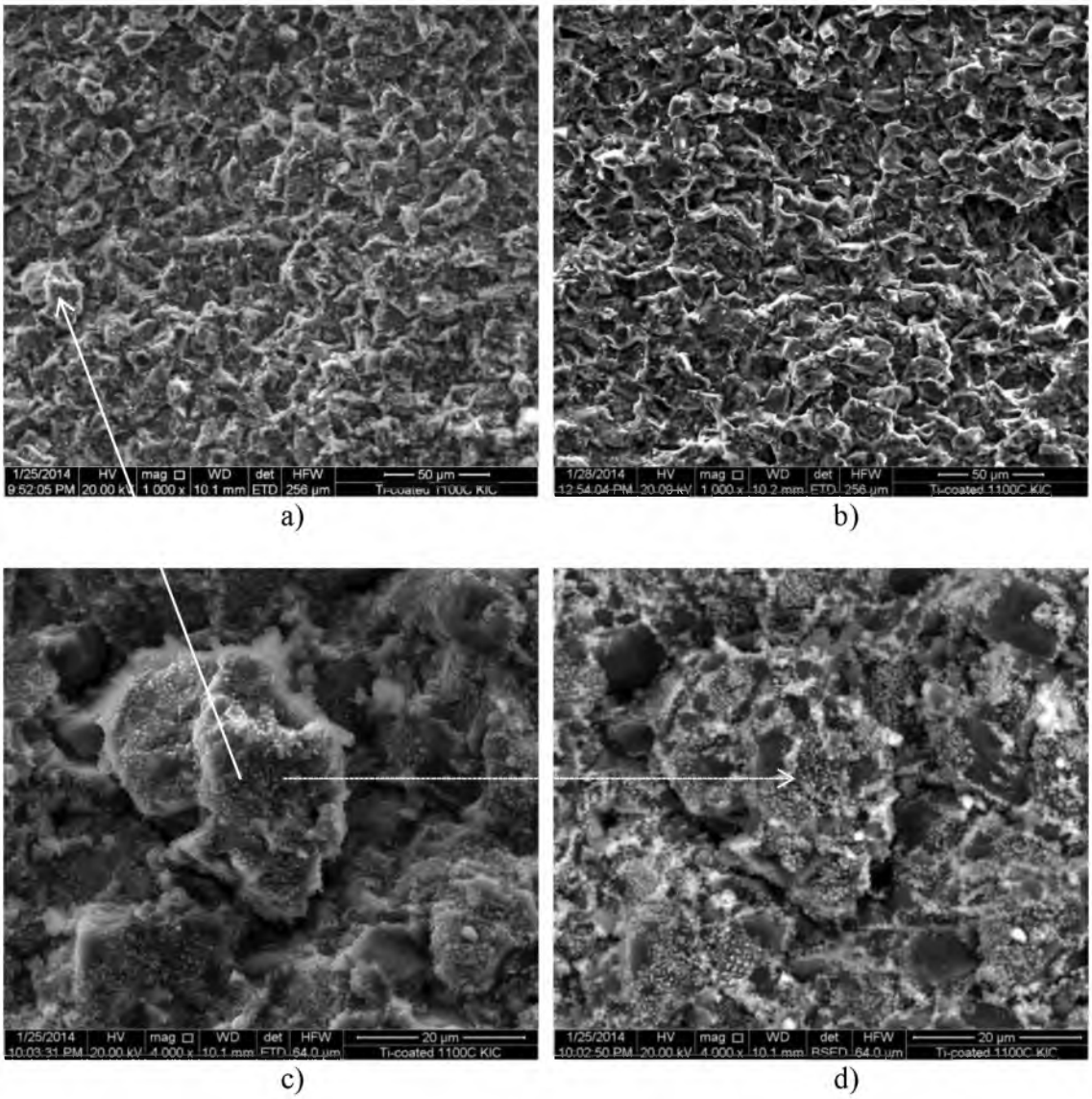

Figure 5-83. PCBN (Ti-coated cBN) after K_{IC} test at 1100°C: a) fracture starting area; b) end of fracturing; c) magnified view of the starting area and d) its corresponding BSE image.

Table 5-1. Diffraction data of major peaks for *hcp*-structured AlB_2, (ICDD 39-1482).

d	I/I_0	hkl	2θ
3.2503	12	001	27.42
2.6039	34	100	34.41
2.0325	100	101	44.54
1.5023	24	110	61.69

Table 5-2. Calculated reaction products in PCBN (cBN + 10vol%Al) using Equation 2-13.

Compound	Al	BN	AlN	AlB_{12}
Starting mix, vol%	10%	90%	-	-
Fully reacted, vol%	-	83.5%	11.9%	4.6%

Table 5-3. B and Al wt% detected by EDS in the B-rich Al-solution areas.

Element	B	Al	N	B/Al
EDS-1, wt%	72.6	17.2	10.2	4.2
EDS-2, wt%	75.8	15.3	8.9	5.0
AlB_{12} theoretical, wt%	*82.8*	*17.2*	-	*4.8*

Table 5-4. Equilibrium compositions of $Al_{(l)}$, AlB_{12}, and AlB_2 their Al consumptions at elevated temperatures in Mix I (cBN+10vol%Al), as calculated by the lever rule.

Phase	$Al_{(l)}$ (wt%)	AlB_{12} (wt%)	AlB_2 (wt%)
T = 1350°C	15.7	84.3	-
- *Al content*	*(0.10)*	*(0.51)*	
T > 980°C	13.5	86.5	-
- *Al content*	*(0.013)*	*(0.082)*	
T = 980°C	46.8	-	53.2
- *Al content*	*(0.006)*		*(0.007)*
T < 980°C	-	43.1	56.9
- *Al content*		*(0.0028)*	*(0.0034)*

Table 5-5. Calculated equilibrium composition, by lever rule, for PCBN HP/HT-sintered using Mix I (90+10vol%Al).

Compound	cBN	AlN	AlB_{12}	AlB_2
Wt%	86.34	10.17	3.47	0.02
Vol%	84.52	10.89	4.58	0.02

Table 5-6. Compounds and their area fractions detected by EBSD method in PCBN (90-10Al) sintered at 1245°C for 15 min.

Phase Lattice	cBN (cubic)	AlN (hexagonal)	AlB_{12} (tetragonal)	AlB_{12} (orthorhombic)	AlB_2 (hexagonal)
Area fraction	74.7%	15.8%	8.9%	0.1%	0.5%

Table 5-7. Compounds and their area fractions detected by EBSD in PCBN (90-10Al) sintered at 1420°C for 15 min.

Phase Lattice	cBN (cubic)	AlN (hexagonal)	AlB_{12} (tetragonal)	AlB_{12} (orthorhombic)	AlB_2 (hexagonal)
Area fraction	66.9%	20.2%	12.1%	0.2%	0.6%

Table 5-8. Calculated reaction products in PCBN (Ti-coated cBN).

Compound	Ti*	BN	TiN	TiB2
Start mix, vol%	11.5%	88.5%	-	-
Fully reacted, vol%	-	85.8%	8.5%	5.7%
Fully reacted, wt%	-	80.7%	12.4%	6.9%

*- calculated based on the assumption that the 15.8wt% of Ti-coating on coarse cBN consists of pure Ti.

Table 5-9. Compounds detected by EBSD method in PCBN (Ti-coated cBN).

Phase Lattice	cBN (cubic)	TiN (cubic)	TiB_2 (hexagonal)
Area fraction	75.0%	11.0%	14.0%

Table 5-10. Equilibrium molar ratios of AlB_{12} and Al-B liquid calculated by lever rule at 1350°C.

Composition	Al-B liquid	AlB_{12}
Mix I (cBN+10vol%Al)	8.9 at%	91.1 at%
Baseline(cBN+20vol%Al)	27.7 at%	82.2 at%

Table 5-11. Boundary conditions applied for calculation of B diffusion in Ti matrix.

Concentration		B wt%
Starting B in Ti	C_0	0.0%
Starting B in BN	C_s	43.6%
B in fully reacted TiB_2 at distance (x) in Ti	C_x	31.1%

Table 5-12. Boundary conditions used for estimated N diffusion Ti matrix.

Concentration		N wt%
Starting N in Ti	C_0	0.0%
Starting N in BN	C_s	56.4%
N in fully reacted TiN at distance (x) in Ti	C_x	22.6%

Table 5-13. Fracture toughness K_{IC} ($MPa \cdot m^{1/2}$) values of PCBN measured using diametral compression method at room temperature.

Test ID	Baseline cBN + 20vol%Al	Mix I cBN + 10vol%Al	Mix III Ti-coated cBN
1	7.11	8.60	7.01
2	7.05	8.46	7.31
3	7.50	8.39	7.76
4	7.65	8.90	7.36
5	7.85	8.58	8.19
6	7.15	8.26	-
7	7.16	-	-
Mean =	7.35	8.53	7.53
Std Dev =	0.31	0.22	0.46

Table 5-14. Fracture toughness K_C ($MPa \cdot m^{1/2}$) values of PCBN measured using Vickers indentation method at room temperature.

PCBN tested	Baseline cBN + 20vol%Al	Mix I cBN + 10vol%Al	Mix III Ti-coated cBN
1	7.1	8.2	6.1
2	8.1	6.9	6.5
3	9.0	8.4	6.8
4	8.1	7.4	9.9
Mean =	8.1	7.7	7.4

Table 5-15. Two-sample T-test comparison of flexural strength values obtained at 900°C and 1100°C to 25°C.

Comparison of mean	25°C to 900°C	25°C to 1100°C
Degree of freedom	20	22
Tails = 2, probability	0.05	0.05
α value	0.0033	0.0330
$T_{0.05(2),20}$	3.46	2.44
$T_{0.05(2),20}$ critical value	2.09	2.07
The null hypothesis	Rejected	Rejected

Table 5-16. Two-sample T-test comparing flexural strength values of room-temperature retested to the initially high-temperature tested.

Comparison	25°C-retested to 900°C	25°C-retested to 1100°C
Degree of freedom	15	16
Tails = 2, probability	0.05	0.05
α value	0.2996	0.8153
$T_{0.05(2),20}$	0.920	0.279
$T_{0.05(2),20}$ critical value	2.13	2.12
The null hypothesis	True	True

Table 5-17. Residual stress measurements on bending bars.

Bending test temperature	(as-is before test)	900°C	1100°C
Residual stress, M Pa	-568 ± 105	-626 ± 222	-676 ± 164
Change of residual stress, MPa	NA	-58	-108
Stress factor, MPa/deg	-2,641.2	-2,639.9	-2,643.9

6 CONCLUSION

Reaction products of PCBN HP/HT-sintered using 90vol% cBN and 10vol%Al as starting powder were comprised of AlB_{12} and 0.5vol% of AlB_2 in addition to AlN as the inter-cBN-granular phases.

The PCBN (90-10vol%Al) consisting of mostly AlB_{12} as the boride exhibited increased flexural-strength values from room temperature to 1100°C, contributed to by the high thermostability of cBN, AlN, and AlB_{12} as well as thermal stresses applied to the cBN particles. The flexural strength gained at high temperatures was largely retained after cooling down to room temperature, benefiting from the high compressive residual stresses applied to cBN particles.

The PCBN (90-10vol%Al) containing AlB_{12} as the major boride exhibited constant fracture toughness from room temperature to 1100°C measured by diametral compression method.

With the consistent room to high temperature thermostability, flexural strength, and fracture toughness, the PCBN (90-10vol%Al) is suitable for high temperature applications.

The titanium powder as a PCBN-sintering additive did not provide the high degree of densification attainable by Al powder in the HP/HT-sintering range of 5.5GPa and temperatures up to 1450°C.

The titanium-coating on cBN powder was shown to be an excellent sintering additive in providing a high degree of densification and reactions in HP/HT-sintering of PCBN, under 5.5GPa pressure and up to 1450°C temperature, and resulted in TiB_2 and TiN as the intergranular phases.

Oxidation of the intergranular TiB_2 and TiN phases in the PCBN made of Ti-coated cBN powder was observed at temperatures from 900°C to 1100°C during flexural strength and fracture toughness tests and led to reduced flexural strength and fracture toughness at high temperatures.

EBSD method was applied in detecting and mapping the 0.5vol% of fine and dispersive AlB_2, by lattice structure, as a reactive-sintering product in the PCBN microstructure consisting mostly of AlB_{12} as the major boride.

EBSD results revealed the reaction phases of AlN, AlB_{12}, AlB_2, TiN, and TiB_2 in the PCBN are fine, submicron sized, and randomly oriented as inter-cBN-granular phases.

APPENDIX

FLEXURAL STRENGTH VALUES

Table A-1. Three-point-bending strength and strain of PCBN (90-10Al) tested at 25°C.

Test No.	Peak Stress (MPa)	Strain at Break (mm/mm)
1	744.8	0.008
2	581.0	0.009
3	498.4	0.009
4	572.3	0.009
5	647.6	0.009
6	675.1	0.012
7	693.5	0.011
8	615.8	0.008
9	671.2	0.011
10	519.6	0.008
Mean	621.9	0.009
Std Dev	78.9	0.001

Table A-2. Three-point-bending strength, strain, sample weight change% (after test) of PCBN (90-10Al) tested at 900°C (corrected for the push rods' friction at the high temperature).

Test No.	Peak Stress (MPa)	Strain at Break (mm/mm)	ΔW $[(W_f-W_o)/W_o]$
1	740.6	0.012	-0.05%
2	745.3	0.024	-0.03%
3	743.7	0.025	-0.06%
4	547.3	0.015	-0.03%
5	741.1	0.017	-0.06%
6	748.2	0.025	-0.02%
7	759.8	0.027	-0.02%
8	758.8	0.037	-0.01%
9	697.5	0.021	-0.02%
10	719.8	0.05	0.01%
Mean	720.2	0.025	-0.03%
Std Dev	63.5	0.011	0.02%

Table A-3. Three-point-bending strength and strain of PCBN (90-10Al) retested at 25°C using unstressed remainder portion of bars initially tested at 900°C.

Test No.	Peak Stress (MPa)	Strain at Break (mm/mm)
1	737.7	0.013
2	522.9	0.024
3	726.6	0.014
4	705.4	0.014
5	750.4	0.020
6	651.7	0.026
7	675.0	0.013
Mean	681.4	0.018
Std Dev	78.1	0.006

Table A-4. Three-point-bending strength, strain, sample weight change% (after test) of PCBN (90-10Al) tested at 1100°C (corrected for the push rods' friction at the high temperature).

Test No.	Peak Stress (MPa)	Strain at Break (mm/mm)	ΔW, $[(W_f-W_o)/W_o]$
1	693.0	0.028	-0.21%
2	525.1	0.012	-0.10%
3	624.2	0.020	-0.03%
4	558.0	0.009	-0.08%
5	715.4	0.009	-0.11%
6	718.0	0.012	-0.03%
7	680.6	0.011	-0.13%
8	735.8	0.010	-0.12%
9	800.7	0.011	-0.05%
10	957.0	0.012	-0.06%
11	797.3	0.010	-0.05%
12	742.1	0.012	-0.09%
Mean	712.3	0.013	-0.09%
Std Dev	114.6	0.006	0.05%

Table A-5. Three-point-bending strength and strain of PCBN (90-10Al) retested at 25°C using unstressed remainder portion of bars initially tested at 1100°C.

Test No.	Peak Stress (MPa)	Strain at Break (mm/mm)
1	746.2	0.009
2	723.9	0.009
3	694.0	0.014
4	846.8	0.011
5	731.0	0.009
6	624.3	0.009
7	732.4	0.010
	508.0	0.013
Mean	700.8	0.011
Std Dev	99.2	0.002

Table A-6. Three-point-bending strength and strain of PCBN (Ti-coated cBN) tested at 25°C.

Test No.	Peak Stress (MPa)	Strain at Break (mm/mm)
1	577.7	0.009
2	653.8	0.010
3	610.6	0.009
4	707.7	0.010
5	886.0	0.010
6	677.0	0.010
7	654.3	0.010
8	674.7	0.010
9	701.3	0.010
10	601.4	0.009
Mean	674.4	0.010
Std Dev	85.7	0.000

Table A-7. Three-point-bending strength, strain, and sample weight change% (after test) of PCBN (Ti-coated cBN) tested at 900°C (corrected for the push rods' friction at the high temperature).

Test No.	Peak Stress (MPa)	Strain at Break (mm/mm)	ΔW, $[(W_f-W_o)/W_o]$
1	421.8	0.006	0.04%
2	536.5	0.012	0.11%
3	485.0	0.018	0.40%
4	604.8	0.010	0.07%
5	583.2	0.012	0.04%
6	566.6	0.016	0.05%
7	571.4	0.011	0.10%
8	424.4	0.046	0.06%
9	418.8	0.029	0.10%
10	358.5	0.010	0.06%
Mean	497.1	0.016	0.10%
Std Dev	86.5	0.012	0.11%

Table A-8. Three-point-bending strength, strain, and sample weight change% (after test) of PCBN (Ti-coated cBN) tested at 1100°C (corrected for the push rods' friction at the high temperature).

Test No.	Peak Stress (MPa)	Strain at Break (mm/mm)	ΔW, $[(W_f-W_o)/W_o]$
1	294.3	0.010	0.18%
2	243.7	0.055	0.14%
3	358.2	0.013	0.09%
4	322.3	0.048	0.47%
5	279.6	0.055	0.29%
6	296.0	0.073	0.13%
7	291.9	0.080	0.29%
8	293.5	0.055	0.12%
9	284.9	0.063	0.29%
10	318.5	0.114	0.13%
Mean	298.3	0.057	0.21%
Std Dev	30.1	0.030	0.12%

REFERENCE

1. Thomas, W. M., Nicholas, E.D., Christopher, N.J., Improvements Relating to Friction welding, European. Patent, 0615480 B1, Dec. 6, 1991.

2. Sorensen, C. D.; Nelson, T. W. Friction Stir Welding of Ferrous and Nickel Alloys. In *Friction Stir Welding and Processing*, Mishra, R. S.; Mahoney, M. W., Eds. ASM International: Materials Park, OH 44073, 2007; pp 111-121.

3. Zhu, X. K. C., Y.J., Numerical simulation of transient temperature and residual stress in frictional stir welding of 304L stainless steel. *J. Mat'l Proc. Tech* 2004, *146,* 263-272.

4. Reynolds, A. P. T., W., Gnaupel-Herold, T.; Prask, H., Structure, properties, and residual stress of 304L stainless steel friction stir welds. *Scripta Materialia* 2003, *48,* 1289-1294.

5. Lienert, T. J.; Stellwag, W. L.; Grimmett, B. B.; Warke, R. W., Friction stir welding studies on mild steel - Process results, microstructures, and mechanical properties are reported. *Welding Journal* 2003, *82* (1), 1S-9S.

6. Steel, R.; Liu, Q.; Yao, X.; Packer, S.; Leonhardt, T., FSW Tool Material Development for Joining High Melting Temperature Materials. In *7th Int'l FSW Symposium*, Awaji Island, Japan, 2008.

7. Nelson, T. W.; Sorensen, C. D.; Packer, S.; Felter, P. A. Friction Stir Welding Using a Superabrasive Tool, U.S. Patent, 6,648,206, Nov. 18, 2003.

8. Sorenson, C. D. N., T.W.; Parker, S., Tool Material Testing for FSW of High-Temperature Alloys. In *3rd Int'l Sym. on Friction Stir Welding*, Kobe, Japan, 2001.

9. Okamoto, K.; Hirano, S.; Inagaki, M.; Parker, S.; Sato, Y.; Kokawa, H.; Nelson, T.; Sorensen, C., Metallurgical and Mechanical Properties of Friction Stir Welded Stainless Steels. In *4th Int'l Sym on FSW,* Park City, 2003.

10. Mahoney, M.; Nelson, T. W.; Sorenson, C.; Packer, S., Friction stir welding of ferrous alloys: Current status. *Materials Science Forum 638-642* (2010), 41-46.

11. Sato, Y. S.; Muraguchi, M.; Kokawa, H., Tool wear and reactions in 304 stainless steel during friction stir welding. In *Materials Science Forum*, Dalian, 2010; Vol. 675 677, pp 731-734.

12. Fuller, C. B., Friction Stir Tooling: Tool Materials and Design. In *Friction Stir Welding and Processing*, Mishra, R. S.; Mahoney, M. W., Eds. ASM International: 2007; pp 7-35.

13. Perrett, J.; Martin, J.; Peterson, J.; Steel, R.; Packer, S., Friction Stir Welding of Industrial Steels. In *Friction Stir Welding and Processing VI,* Mishra, R.; Mahoney, M. W.; Sato, Y.; Hovanski, Y.; and Verma, R., Eds, John Wiley & Sons, Inc., 2011, pp 65-72.

14. Buffa, G.; Fratini, L., Friction stir welding of steels: Process design through continuum based FEM model. *Science and Technology of Welding and Joining* 2009, *14* (3), 239-246.

15. Zhu, X. K.; Chao, Y. J., Numerical simulation of transient temperature and residual stresses in friction stir welding of 304L stainless steel. *Journal of Materials Processing Technology* 2004, *146* (2), 263-272.

16. Prasanna, P.; Rao, B. S.; Rao, G. K. M., Finite element modeling for maximum temperature in friction stir welding and its validation. *International Journal of Advanced Manufacturing Technology* 2010, *51* (9-12), 925-933.

17. Arora, A.; Mehta, M.; De, A.; DebRoy, T., Load bearing capacity of tool pin during friction stir welding. *International Journal of Advanced Manufacturing Technology* 2012, 1-10.

18. Stahl, A. L.; Sorensen, C. D., Experimental Measurements of Load Distributions on Friction Stir Weld Pin Tools. In *Friction Stir Welding and Processing III*, Jata, K. V.; Mahoney, M. W.; Mishra, R. S.; Lienert, T. J., Eds. Willey, 2005; pp 179-190.

19. Wentorf, R. H., Jr., Cubic Boron Nitride, Past, Present, and Outlook, Abrasive Engineering Society Conference/Exhibition, Pittsburgh, PA, USA, *Abrasive Engineering Soc:* 1986; pp 27-31.

20. Bundy, F. P.; Hall, H. T.; Strong, H. M.; Wentorf, R. H., Man made diamonds. *Nature* 1955, *176*, 51-55.

21. Wentorf, R. H., Jr, Cubic form of boron nitride. *The Journal of Chemical Physics* 1957, *26*, 956.

22. Wentorf, R. H., Condensed systems at high pressures and temperatures. *Journal of Physical Chemistry* 1958, *63* (Nov.), 1934-1940.

23. Rogl, P., Materials science of ternary metal boron nitrides. *International Journal of Inorganic Materials* 2001, *3* (3), 201-209.

24. Haubner, R.; Wilhelm, M.; Weissenbacher, R.; Lux, B., Boron nitrides - Properties, synthesis and applications. *High Performance Non-Oxide Ceramics,* 2002, *102*, 1-45.

25. Wentorf, R. H., Cubic Boron Nitride Synthesis and Applications. In *New diamond science and technology;* Proceedings of the 2nd International Conference, Washington, DC, 1991; pp 1029-1037.

26. Shipilo, V. B.; Gameza, L. M.; Anichenko, N. G.; Gielisse, P. J., Investigation of the processes of crystallization and sintering of cubic boron nitride and its physical properties. *J. Wide Bandgap Mater.* 2000, *7* (3), 213-260.

27. Sirota, N. N.; Kofman, N. A., Polymorphous alpha-beta transformation of boron nitride. *Soviet Physics - Doklady* 1979, *24* (12), 1001-1002.

28. Wentorf, R. H., Jr., Synthesis of the cubic form of boron nitride. *Journal of Chemical Physics* 1961, (34), 809-812.

29. Will, G.; Nover, G.; von der Gonna, J., New experimental results on the phase diagram of boron nitride. *Journal of Solid State Chemistry* 2000, *154* (1), 280-285.

30. Belnap, J. D., Sintering of Ultrahard Materials. In *Sintering of Advanced Materials - Fundamentals and Processes*, Fang, Z. Z., Ed. Woodhead Publishing: 2010.

31. Huang, J. Y.; Zhu, Y. T., Advances in the synthesis and characterization of boron nitride. In *Defects and Diffusion in Ceramics*, Scitec Publications Ltd: Uetikon-Zuerich, 2000; Vol. 186-1, pp 1-32.

32. Bundy, F. P.; Wentorf, R. H., Jr. , Direct transformation of hexagonal boron nitride to denser forms. *Journal of Chemical Physics* 1963, *38*, 1144-1149.

33. Samantaray, C. B., Review of synthesis and properties of cubic boron nitride (c-BN) thin films. *International Materials Reviews* 2005, *50* (6), 313-344.

34. Vel, L.; Demazeau, G.; Etourneau, J., Cubic boron nitride: Synthesis, Physicochemical properties and applications. *Materials Science and Engineering: B* 1991, *10* (2), 149-164.

35. Yao, X., Thermal Behaviors of Polycrystalline Diamond and cubic Boron Nitride. In *Intertech 2003*, Industrial Diamond Association: Vancouver, Canada, 2003.

36. Rai, G., Matallurgy of CBN and Its Wear in High Speed Machining of Ferrous Materials. In *Proceeding of the International Conference on Machining of Advanced Materials*, Gaithersburg, MD, USA, 1993; pp 501-514.

37. Hibbs, L. E., Jr.; Wentorf, R. H. J., Borazon and diamond compact tools. *High Temp. High Pressures* 1974, *6* (4), 409-413.

38. Wentorf, R. H., Jr; Lai, A. D., Cubic Boron Nitride Compact and Method of its Production, U.S. Patent, 3,233,988, Feb. 8, 1966.

39. Wakatsuki, M.; Ichinose, K.; Aoki, T., Synthesis of polycrystalline cubic boron nitride (BN), *Materials Research Bulletin* 1972, *7* (9), 999-1003.

40. Hanneman, R. E.; Hibbs, L. E., Jr. Borazon Compact Cutting Tools, Tech. Paper No. MR73-143; *Society of Manufacturing Engineers,* 1973; 17.

41. Shul'zhenko, A. A.; Bozhko, S. A.; Bezhenar, N. P.; Belyankina, A. V.; Tovstogan, V. M., Sintering of cubic boron nitride with aluminum *Sverkhtverdye Materialy,* 1986, *8* (5), 17-21.

42. Walmsley, J. C.; Lang, A. R., A transmission electron microscope study of a cubic boron nitride-based compact material with AIN and AlB_2 binder phases. *Journal of Materials Science* 1987, *22* (11), 4093-4102.

43. Wentorf, R. H., High pressure chemistry. *Chemical Engineering* 1961, *Oct. 16*, 177-186.

44. Marshall, D. B. Reducing Fracture Tendencies in PCBN FSW Tools, *Base Effort Final Report for Office of Naval Research,* Code 332; Teledyne Scientific and Imaging LLC, Thousand Oaks, CA: July 25, 2010.

45. Corrigan, F. R. Direct Conversion Process for Making Cubic Boron Nitride from Pyrolytic Boron Nitride, U.S. Patent 4,188,194, Feb. 12, 1980.

46. Akaishi, M.; Satoh, T.; Ishii, M.; Taniguchi, T.; Yamaoka, S., Synthesis of translucent sintered cubic boron nitride. *Journal of Materials Science Letters* 1993, *12* (24), 1883-1885.

47. Sumiya, H.; Uesaka, S.; Satoh, S., Mechanical properties of high purity polycrystalline cBN synthesized by direct conversion sintering method. *Journal of Materials Science* 2000, *35* (5), 1181-1186.

48. Wang, Z. G.; Rahman, A.; Wong, Y. S., Tool wear characteristics of binderless CBN tools used in high-speed milling of titanium alloys. *Wear* 2005, *258* (5-6), 752-758.

49. Taniguchi, T.; Akaishi, M.; Yamaoka, S., Sintering of cubic boron nitride without additives at 7.7 GPa and above 2000 deg C. *Journal of Materials Research* 1999, *14* (1), 162-169.

50. Richerson, D. W., Phase Equilibria and Phase Equilibrium Diagrams. In *Modern Ceramic Engineering: Properties, Processing, and Use in Design*, CRC Taylor & Francis: 2006; Vol. Materials Engineering Series.

51. Tomlinson, P. N.; Wedlake, R. J., The Current Status of Diamond and Cubic Boron Nitride Composites. *Proc. Int. Conf on Recent Dev. in Special Steels and Hard Materials.* Comins, N. R.; Clark, J. B., Eds. 1983; pp 173-184.

52. Angseryd, J.; Elfwing, M.; Olsson, E.; Andren, H. O., Detailed microstructure of a cBN based cutting tool material. *International Journal of Refractory Metals & Hard Materials* 2009, *27* (2), 249-255.

53. Hooper, R. M.; Shakib, J. I.; Brookes, C. A., Microstructure and wear of TiC-cubic BN tools, *Materials Science and Engineering,* 105-106 (1998) 429-433.

54. German, R. M., Novel Sintering Techniques. In *Sintering Theory and Practice*. Wiley-Interscience: 1996.

55. Merzhanov, A.; Borovinskaya, I., Historical retrospective of SHS: An autoreview. *International Journal of Self-Propagating High-Temperature Synthesis* 2008, *17* (4), 242-265.

56. Wentorf, R. H. Cubic boron nitride synthesis and applications, *New Diamond Science and Technology, Proceedings*, 1991; pp 1029-37.

57. Astanin, V. V.; Imayeva, L. A., Two stage of interfacial reaction in B-Al composite. *Journal of Materials Science* 1994, *29* (1994), 3351-3357.

58. Rogl, P.; Schuster, J. C., Phase Diagrams of Ternary Boron Nitride and Silicon Nitride Systems. In *Monograph Series on Alloy Phase Diagrams*, ASM, Int'l: Materials Park, OH., 1992; pp 3-5.

59. Samsonov, G. V.; Neronov, V. A.; Lamikhov, L. K., The conditions, structure and some properties of phases in the Al-B System. *J. Less Common Met* 1979, *67* (2), 291-296.

60. Wang, X., The formation of AlB2 in an Al-B master alloy. *Journal of Alloys and Compounds* 2005, *403*, 1-2.

61. Mirkovic, D.; Grobner, J.; Schmid-Fetzer, R.; Fabrichnaya, O.; Lukas, H. L., Experimental study and thermodynamic re-assessment of the Al-B system. *Journal of Alloys and Compounds* 2004, *385*, 1-2.

62. Kharlamov, A. I.; Loichenko, S. V.; Nizhenko, V. I.; Kirillova, N. V.; Floka, L. I., Wetting of hot-pressed aluminum borides and borocarbides by molten aluminum and copper. *Powder Metallurgy and Metal Ceramics* 2001, *40* (1-2), 65-70.

63. Fjellstedt, J., Jarfors, A. E. W.; El-Benawy, T., Experimental Investigation and Thermodynamic Assessment of the Al-rich Side of the Al-B System. In *Materials & Design,* UK, Elsevier: UK, 2001; pp 443-449.

64. Czochralski, J. *Z.,* Moderne metallkunde in theorie und praxis, *Metallkunde* 1922, *14*, 278-281.

65. Benko, E., Equilibrium State in BN-Al Mixtures: Comparison of Calculated and Experimental Data. In *XIVth Int'l Sci. Conf Adv. Mat'l & Tech*, Zakopane, 1995; pp 49-52.

66. Bezhenar, N. P.; Konoval, S. M.; Bozhko, S. A.; Belyavina, N. N.; Markiev, V. Y., Relaxation interaction in cBN-Al system at high pressure. *Fiz. Tekh. Vys. Davlenii (Donetsk, Ukr.)* 2009, *19* (2), 41-47.

67. Benko, E., Wettability studies of cBN by AlTi. *Journal of Chemical Vapor Deposition* 1995, *4* (2), 164-170.

68. Xue, X. M.; Wang, J. T.; Zhao, F. M., Penetration and adhesion behavior of boron nitride by liquid aluminum. *Journal of Materials Science Letters* 1992, *11* (4), 199-201.

69. Fujii, H.; Nakae, H.; Okada, K., Application of wetting to fabrication of boron nitride/aluminum composites, *Miner. Met. Mater. Soc.*1993, 1001-1007.

70. Shen, P.; Fujii, H.; Nogi, K., Effect of temperature and surface roughness on the wettability of boron nitride by molten Al. *Journal of Materials Science* 2007, *42* (10), 3564-3568.

71. Sithebe, H. S. L.; McLachlan, D.; Sigalas, I.; Herrmann, M., Pressure infiltration of boron nitride preforms with molten aluminum. *Ceramics International* 2008, *34* (6), 1367-1371.

72. Sithebe, H. S. L.; McLachlan, D. S.; Sigalas, I. J.; Herrmann, M., Hot pressing of cBN ceramics with Al binder. *Advances in Science and Technology* 2006, *45*, 1364-1370.

73. Bezhenar, M.; Bozhko, S.; Bilyavina, N.; Krishtova, O.; Oleinik, G., The structure formation in reaction sintering of cubic boron nitride submicron and nanosized powders with aluminum at the stage of high-pressure infiltration. *Journal of Superhard Materials* 2008, *30* (1), 28-37.

74. Tomashik, V., B-N-Ti (Boron-Nitrogen-Titanium), Light Metal Ternary Systems: *Phase Diagrams, Part 4.* Springer Berlin Heidelberg: 2006; Vol. 11A4.

75. Klimczyk, P.; Benko, E.; Lawniczak-Jablonska, K.; Piskorska, E.; Heinonen, M.; Ormaniec, A.; Gorczynska-Zawislan, W.; Urbanovich, V. S., Cubic boron nitride

- Ti/TiN composites: Hardness and phase equilibrium as function of temperature. *Journal of Alloys and Compounds* 2004, *382* (1-2), 195-205.

76. Olevsky, F.; Mogilevsky, P.; Gutmanas, E. Y.; Gotman, I., Synthesis of in situ TiB_2/TiN ceramic matrix composites from dense BN-Ti and BN-Ti-Ni powder blends. *Metallurgical and Materials Transactions A* 1996, *27* (8), 2071-2079.

77. *Phase Equilibria Diagrams, Vol. X, Borides, Carbides, and Nitrides,* McHale A. Ed, The American Ceramics Society, 1994.

78. Ding, W. F.; Xu, J. H.; Fu, Y. C.; Xiao, B.; Su, H. H.; Xu, H. J., Interfacial reaction between cubic boron nitride and Ti during active brazing. *Journal of Materials Engineering and Performance* 2006, *15* (3), 365-369.

79. Ding, W. F.; Xu, J. H.; Shen, M.; Fu, Y. C.; Su, H. H.; Xiao, B., Solid-state interfacial reactions and compound morphology of cBN grain and surface Ti coating. *Vacuum* 2006, *81* (4), 434-440.

80. Seal, S.; Barr, T. L.; Sobczak, N.; Benko, E., X-ray photoelectron spectroscopy study of the chemical interaction between BN and Ti/TiN. *J. Vac. Sci. Technol., A* 1997, *15* (3, Pt. 1), 505-512.

81. Ma, X.; Li, C.; Du, Z.; Zhang, W., Thermodynamic assessment of the Ti-B system. *J. Alloys Compd.* 2004, *370* (1-2), 149-158.

82. Basu, B.; Raju, G. B.; Suri, A. K., Processing and properties of monolithic TiB_2 based materials. *International Materials Reviews* 2006, *51* (6), 352-374.

83. Wriedt, H.; Murray, J., The N-Ti (nitrogen-titanium) system. *Journal of Phase Equilibria* 1987, *8* (4), 378-388.

84. Pivkina, A., Reaction-bonded titanium nitride ceramics. *Journal of the European Ceramic Society* 1996, *16* (1), 35.

85. Rong, X. Z.; Yano, T., TEM investigation of high-pressure reaction-sintered cBN-Al composites. *Journal of Materials Science* 2004, *39* (14), 4705-4710.

86. Belnap, J. D., Sintering of Ultrahard Materials. In *Sintering of Advanced Materials - Fundamentals and Processes*, Fang, Z. Z., Ed. Woodhead Publishing: 2010.

87. Akaishi, M.; Kanda, H.; Sato, Y.; Setaka, N.; Ohsawa, T.; Fukunaga, O., Sintering behavior of the diamond-cobalt system at high temperature and pressure. *J. Mater. Sci.* 1982, *17* (1), 193-8.

88. Walmsley, J. C.; Lang, A. R., Characteristics of diamond regrowth in a synthetic diamond compact. *J. Mater. Sci.* 1988, *23* (5), 1829-34.

89. Akhmadi, E.; Minoru, A.; Itsuro, T., The bonding structure of the various high purity or binderless polycrystalline cubic boron nitride compacts sintered at 5 to 7GPa and 1600 to 2000 °C. *Materials Science Forum* 2010, *Vol. 654-656*, 2390-2393.

90. Benko, E.; Klimczyk, P.; Morgiel, J.; Wlochowicz, A.; Barr, T. L., Electron microscopy investigations of the cBN-Ti compound composites. *Materials Chemistry and Physics* 2003, *81* (2-3), 336-340.

91. Bezhenar, M. P.; Bozhko, S. A.; Bilyavina, N. M.; Krishtova, O. V.; Oleinik, G. S., The structure formation in reaction sintering of cubic boron nitride submicron and nanosized powders with aluminum at the stage of high-pressure infiltration. *Journal of Superhard Materials* 2008, *30* (1), 28-37.

92. Ueda, F.; Tazima, I.; Yageta, M. Titanium Aluminum Carbides and Titanium Aluminum Nitrides or Carbonitrides. U.S. Patent 5,328,875, July 12, 1994.

93. Ueda, F.; Yageta, M.; Tajima, I., Microstructure and mechanical properties of cBN-TiN composites. *Journal of Hard Materials* 1991, *2*, 3-4.

94. Collier, M.; Steel, R.; Nelson, T.; Sorensen, C.; Packer, S., Grade development of polycrystalline cubic boron nitride for friction stir processing of ferrous alloys. *Materials Science Forum* 2003, *426* (432), 3011-3016.

95. Diamond Innovations, BZN* Compacts Tool Blanks and Inserts. http://www.abrasivesnet.com/ en/product/mbs/bzn/index.htm (accessed Feb 20, 2005).

96. Element Six, An introduction to cutting tool materials. Accessed Feb 20, 2005 at: http://www.e6.com/en/resources/literature/Introduction%20to%20Cutting%20Tool%20Materials.pdf.

97. Iljin Diamond, cutting tool materials. http://www.iljindiamond.co.kr/ (accessed July 2, 2014).

98. Sumitomo Carbide cBN Diamond, PCD & PCBN grade. Accessed July 2, 2014 at: http://www.sumicarbide.com/cuttingtool_CBN.htm.

99. Takatsu, S.; Shimoda, H.; Otani, K., Effect of CBN content on the cutting performance of polycrystalline CBN tools. *Int. J. Refract. Hard. Mat. 2* (4), 175–178.

100. Brookes, C. A., The mechanical properties of cubic boron nitride - A perspective view. In *Science of Hard Materials*, Almond, A. E.; Brookes, C. A.; Warren, R., Eds. 1986; Vol. 75, pp 207.

101. Lahiff, C.; Gordon, S.; Phelan, P., PCBN tool wear modes and mechanisms in finish hard turning. *Robotics and Computer-Integrated Manufacturing* 2007, *23* (6), 638-644.

102. Huang, B. L.; Weiss, C.; Yao, X.; Belnap, D.; Rai, G., Fracture Toughness of Sintered Polycrystalline Diamond (PCD), *5th Int'l Conf on Adv. Part. Mat'ls & Pros.*, Metal Powder Industries Federation: West Palm Beach; FL; USA, 1997; pp 431-437.

103. Lammer, A., Mechanical properties of polycrystalline diamonds. *Materials Science and Technology* 1988, *4* (11), 949-55.

104. Luo, S. Y.; Liao, Y. S.; Tsai, Y. Y., Wear characteristics in turning high hardness alloy steel by ceramic and CBN tools. *Journal of Materials Processing Technology* 1999, *88* (1), 114-121.

105. Poulachon, G.; Albert, A.; Schluraff, M.; Jawahir, I. S., An experimental investigation of work material microstructure effects on white layer formation in PCBN hard turning. *International Journal of Machine Tools & Manufacture* 2005, *45* (2), 211-218.

106. Konig, W.; Neises, A., Wear mechanisms of ultrahard, non-metallic cutting materials. *Wear* 1993, *162-164* (A), 12-21.

107. Yerazunis, S.; Cornell, S. W.; Wintner, B., Dense random packing of binary mixtures of sphere. *Nature* 1965, *207* (10), 835-837.

108. German, R., *Powder Metallurgy Science.* 2nd ed.; Metal Powder Industries Federation: 1994.

109. Andreev, O. N.; Bezhenar, N. P., Cold pressing of CBN powders at high pressure. *Soviet Journal of Superhard Materials (USA)* 1991, *13* (1), 41-45.

110. Wachtman, J. B.; Cannon, W. R.; Matthewson, M. J., *Mechanical Properties of Ceramics*. 2nd ed.; John Wiley & Sons, Inc.: 2009.

111. McKie, A., Mechanical properties of cBN-Al composite materials. *Ceramics International* 2011, *37* (1), 1-8.

112. Carolan, D.; Petrovic, M.; Ivankovic, A.; Murphy, N., Fracture properties of PCBN as a function of loading rate. *Key Engineering Materials* 2010, *Vol. 417-418*, 669-672.

113. Carolan, D.; Petrovic, M.; Ivankovic, A.; Murphy, N., Fracture properties of PCBN as a function of loading rate. *Key Engineering Materials 417-418*, 669-672.

114. D'Evelyn, M. P.; Taniguchi, T., Elastic properties of translucent polycrystalline cubic boron nitride as characterized by the dynamic resonance method. *Diamond and Related Materials* 1999, *8* (8), 1522-1526.

115. Taniguchi, T.; Akaishi, M.; Yamaoka, S., Mechanical properties of polycrystalline translucent cubic boron nitride as characterized by the Vickers indentation method. *Journal of the American Ceramic Society* 1996, *79* (2), 547-549.

116. Palmqvist, S., Energy causing cracks at corners of Vickers indentations as measure of toughness of hard metals. *Archiv fuer das Eisenhuettenwesen* 1962, *33* (9), 629-634.

117. Anstis, G. R.; Chantikul, P.; Lawn, B. R.; Marshall, D. B., A critical evaluation of indentation techniques for measuring fracture toughness: I, direct crack measurements. *Journal of the American Ceramic Society* 1981, *64* (9), 533-538.

118. Takashi Taniguchi, M. A., Shinobu Yamaoka,, Mechanical properties of polycrystalline translucent cubic boron nitride as characterized by the Vickers indentation method. *Journal of the American Ceramic Society* 1996, *79* (2), 547-549.

119. Shetty, D. K.; Rosenfield, A. R.; Duckworth, W. H., Mixed-mode fracture in biaxial stress state--application of the diametral-compression (Brazilian disk) test. *Engineering and Fracture Mechanics* 1987, *26* (6), 825-840.

120. Shintani, K.; Ueki, M.; Fujimura, Y., Microstructure and mechanical properties of sintered cubic boron nitride. *J. Mater. Sci. Lett.* 1987, *6* (8), 987-9.

121. Harris, T. K.; Brookes, E. J.; Taylor, C. J., The effect of temperature on the hardness of polycrystalline cubic boron nitride cutting tool materials. *International Journal of Refractory Metals & Hard Materials* 2004, *22* (2-3), 105-110.

122. Novikov, N. V.; Sirota, Y. V.; Mal'nev, V. I.; Petrusha, I. A., Mechanical properties of diamond and cubic BN at different temperatures and deformation rates. *Diamond and Related Materials* 1993, *2* (9), 1253-1256.

123. Harris, T. K.; Brookes, E. J.; Taylor, C. J., The flow stress of PcBN cutting tool materials at high temperatures. *International Journal of Refractory Metals & Hard Materials* 2001, *19* (4-6), 267-273.

124. Carolan, D.; Petrovic, M.; Ivankovic, A.; Murphy, N., Fracture properties of PCBN as a function of loading rate and temperature, *Key Engineering Materials*, Nagasaki, Vol. 452-453, pp 457-460.

125. German, R. M., *Powder Metallurgy & Particulate Materials Processing.* Metal Powder Industries Federation, Princeton, NJ 08540: 2005.

126. Garshin, A. P.; Shvaiko-Shvaikovskii, V. E., Mechanism of beta-BN oxidation, *Sov. Powder Metall. Met. Ceram.* 1993, *8* (356), 656-661.

127. Williams, D. B.; Carter, C. B., *Transmission Electron Microscopy*. Springer: 2006.

128. Sitzman, S. D., Introduction to EBSD Analysis of Micro- to Nanoscale Microstructures in Metals and Ceramics, General Review, Meyendorf; Norbert; Baaklini, Eds. *Testing, Reliability, and Application of Micro- and Nano-Material Systems II*: 2004; pp 78-90.

129. Dingley, D., Progressive steps in the development of electron backscatter diffraction and orientation imaging microscopy. *J Microsc* 2004, *213* (Pt 3), 214-24.

130. Ladue, D.; Nowell, M., Using orientation imaging microscopy to measure particle size of sintered polycrystalline diamond. *Finer Points* 2007, *Winter 2007-2008*, 9-10.

131. Hsueh, C. H.; Becher, P. F.; Sun, E. Y., Analyses of thermal expansion behavior of intergranular two-phase composites. *Journal of Materials Science* 2001, *36* (1), 255-261.

132. Timoshenko, S. P., Two Dimensional Problems in Polar Coordinates. In *Theory of Elasticity*, 3rd Ed.; McGraw-Hill, Inc: 1987; p 68.

133. Oel, H. J.; Frechette, V. D., Stress distribution in multiphase systems: II, composite disks with cylindrical interfaces. *Journal of the American Ceramic Society* 1986, *69* (4), 342-346.

134. Cullity, B. D., Measurement of Residual Stress. In *Elements of X-ray Diffraction*, 2nd ed.; Addison-Wesley Publishing Comp.: 1978.

135. Rietveld, H. M., Profile refinement method for nuclear and magnetic structures. *J. Appl. Crystallogr.* 1969, *2* (Pt. 2), 65-71.

136. Wright, S.; Nowell, M., High-speed EBSD. *Advanced Materials & Processes* 2008, *166* (2), 29-31.

137. Standard Thermodynamic Properties of Chemical Substances, 5-4. In *CRC Handbook of Chemistry and Physics,* 87th Ed., Lide, D. R., Ed. Taylor & Francis: 2006-2007.

138. National Institute of Standard and Technology, Web SCD Database. http://www.ceramics.nist.gov/srd/scd/scdquery.htm (accessed July 2, 2014).

139. Neshpor, V. S.; Zaitsev, G. T.; Slovina, L. Y.; Nigovskii, A. N.; Treskovskii, V. V.; Neshpor, A. V.; Ordan'yan, S. S., Physical and mechanical properties of very hard polycrystalline ceramic materials. *Ogneupory* 1995, (9), 2-5.

140. Gosset, D.; Guery, M.; Kryger, B., Thermal Properties of Some Boron-rich Compounds B_nC and AlB_{12}. *AIP Conference Proceedings* 1991, *231* (1), 380-383.

141. Deppisch, C.; Liu, G.; Hall, A.; Xu, Y.; Zangvil, A.; Shang, J. K.; Economy, J., The crystallization and growth of AlB_2 single crystal flakes in aluminum. *Journal of Materials Research* 1998, *13* (12), 3485-3498.

142. Prikhna, T. A.; Kisly, P. S., Aluminium Borides and Carboborides. *AIP Conference Proceedings* 1991, *231* (1), 590-593.

143. Benko, E.; Wyczesany, A.; Barr, T. L., CBN-metal/metal nitride composites. *Ceramics International* 2000, *26* (6), 639-644.

144. Bezhenar, N. P.; Bozhko, S. A.; Klimenko, S. A.; Shulzhenko, A. A., Structure and Properties of a cBN-base Tool Material versus Production Conditions. In *Proceeding of the 14th International Plansee Seminar* Kneringer, G.; Rodhammer, P.; Wilhartitz, P., Eds. Plansee AG, Reutte, 1997; Vol. 2, pp 315.

145. Hall, H. T. High Pressure Press. U.S. Patent 3,159,876, Dec. 8, 1964.

146. Carter, L.; Yao, X.; Rai, G. Synthetic Gasket Materials for Use in High-pressure Presses. U.S. Patent 5,858,525, Jan 12, 1999.

147. Wentorf, R. H. Abrasive Material and Preparation Thereof. U.S. Patent, 2,947,617. Aug. 2, 1960.

148. Nowell, M. M.; Wright, S. I., Phase differentiation via combined EBSD and XEDS. *Journal of Microscopy* 2004, *213* (Pt 3), 296-305.

149. *Grade Properties Handbook.* Tungsten Carbide Manufacturer, 1980.

150. Garshin, A. P.; Shvaiko-Shvaikovskii, V. E., Mechanism of beta-BN oxidation. *Poroshkovaya Metallurgiya* 1992, *8* (356), 22-27.

151. Sachdev, H.; Haubner, R.; Nöth, H.; Lux, B., Investigation of the c-BN/h-BN phase transformation at normal pressure. *Diamond and Related Materials* 1997, *6* (2-4), 286-292.

152. Lavrenko, V. A.; Alexeev, A. F., Oxidation of sintered aluminium nitride. *Ceramics International* 1983, *9* (3), 80-82.

153. Whittaker, M. L.; Sohn, H. Y.; Cutler, R. A., Oxidation kinetics of aluminum diboride. *Journal of Solid State Chemistry 207*, 163-169.

154. Komratov, G. N., The oxidation kinetics of titanium carbide, nitride, and carbonitride powders in air. *Powder Metall. Met. Ceram.* 1998, *36* (9-10), 510-514.

155. Li, Z. H.; Zheng, H. F.; Zhu, Y. M.; Yuan, Q. M., Study on the performance of cBN abrasives with Ti coatings. *Key Engineering Materials* 2005, *280-283*.

156. Voitovich, V. B.; Lavrenko, V. A.; Adejev, V. M., High-temperature oxidation of titanium diboride of different purity. *Oxid. Met.* 1994, *42* (1-2), 145-61.

157. Zhang, G., Corrosion mechanism of boron nitride-aluminum nitride-titanium diboride (BN-AlN-TiB_2) conductive composite ceramics towards aluminum melt and ways to enhance its corrosion resistance. *Gongneng Cailiao* 1992, *23* (3), 175-8, 189.

158. Cullity, B. D., Crystal quality, Ch. 9 Structure of Polycrystalline Aggregates. In *Elements of X-ray Diffraction,* 2nd ed.; Addison-Wesley Publishing Comp.: 1978; pp 285-292.

159. Casanova, C. A. M.; Balzaretti, N. M.; Voronin, G.; da Jornada, J. A. H., Experimental study of plastic deformation during sintering of cubic boron nitride compacts. *Diamond and Related Materials* 1999, *8* (8-9), 1451-1454.

160. Sarma, B.; Ravi, C. K. S., Accelerated kinetics of surface hardening by diffusion near phase transition temperature: Mechanism of growth of boride layers on titanium. *Acta Materialia* 2011, *59* (10), 4216-4228.

161. Divinski, S. V.; Hisker, F.; Wilger, T.; Friesel, M.; Herzig, C., Tracer diffusion of boron in B-Ti and B-TiAl. *Intermetallics* 2008, *16* (2), 148-155.

162. Wlilliam D. Callister, J., *Materials Science and Engineering: An Introductin*, 5th ed. John Wiley & Sons, Inc: 200.

163. Bars, J.; David, D.; Etchessahar, E.; Debuigne, J., Titanium alpha-nitrogen solid solution formed by high temperature nitriding: diffusion of nitrogen, hardness, and crystallographic parameters. *Metallurgical and Materials Transactions A* 1983, *14* (8), 1537-1543.

164. Hultman, L., Thermal stability of nitride thin films. *Vacuum* 2000, *57* (1), 1-30.

165. Whitlock, M. C.; Schluter, D., Comparing Two Means. In *The Analysis of Biological Data*, Roberts and Company Publishers: Greenwood Village, 2009.

166. Mazdiyasni, K. S.; Ruh, R.; Hermes, E. E., Phase characterization and properties of AlN-BN composites. *Am. Ceram. Soc. Bull.* 1985, *64* (8), 1149.

167. Rice, R. W., Particle (and Grain) Effects on Elastic Properties, Crack Propagation, and Fracture Toughness of Ceramic Composites at ~22°C In *Mechanical*

Properties of Ceramics and Composites: Grain And Particle Effects, Marcel Dekker, Inc: 2000.

168. Rice, R. W., Grain Dependence of Microcracking, Crack Propagation. In *Mechanical Properties of Ceramic and Composites*, Marcel Dekker, Inc: 2000; pp 43-107.

169. Richerson, D. W., Toughening of Cermanics. In *Modern Ceramic Engineering: Properties, Processing, and Use in Design*, CRC Taylor & Francis 2006; Vol. Materials Engineering Series.

170. Guo, J. K.; Shi, J. L.; Zhang, Y. F.; Shi, Y.; Deng, Z. Y., The role of grain boundary stress in multiphase composed ceramics. In *Key Engineering Materials*, 1999; Vol. 161-163, 559-562.

171. Guo, J. K., Interphase of ceramics and stress design of ceramic grain boundary. *Key Engineering Materials* 1995, Vol. 108-110, 505-514.